Molecular Excited States Geometries From Resonance Raman Spectroscopy

A Thesis Submitted For The Degree Of Doctor Of Philosophy In The University Of London, University College London

by
Suzanne J. R. Allers

Christopher Ingold Laboratories
University College London
University of London

1996

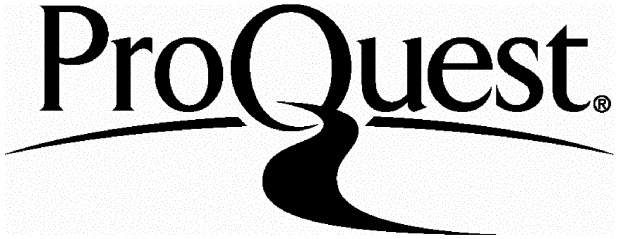

Abstract

This thesis is concerned with the application of two theoretical methods for finding structural changes in molecules in excited electronic states. Both methods, the Sum-over-States (SOS) method and the Overtone Transform (OT) method, utilise information from resonance Raman and electronic absorption spectroscopies.

The purpose of the work is twofold: first, to test the applicability of both methods in the case of a complex inorganic molecule, and second, to use the methods to find new structural information about the molecule in an excited electronic state.

A series of quadruply bonded metal-metal dimers serve as a vehicle for this dual aim. The partial characterisation of the $^1\delta\delta^*$ excited state by previous studies allows comparisons with the SOS and OT results to be made. Furthermore, the structural changes along the metal-metal co-ordinate in this state are of great interest.

Application of the SOS method to the metal-metal co-ordinate of the $[M_2X_8]^{n-}$ ions ($[Re_2Br_8]^{2-}$, $[Re_2I_8]^{2-}$ and $[Mo_2Cl_8]^{4-}$) in the $^1\delta\delta^*$ state has proved to be successful, and has allowed important conclusions to be drawn regarding the conversion between structural conformations in this state. It has been found that observation of a particular structure is dependent on the timescale of the experimental technique used. A comparative study of the $^1\delta\delta^*$ state of the compounds $Mo_2X_4(PMe_3)_4$ (X = Cl, Br or I) has provided insights into the effect of the ligands on metal-metal bonding in these systems.

An attempted application of the OT method to the same systems has been found to be unsuccessful. Investigations of this failure point to problems with the method of finding values for structural parameters.

The unusual behaviour of the ion $[Mo_2Br_8]^{4-}$ in the resonance Raman spectrum recorded in resonance with the $^1(\delta^* \leftarrow \delta)$ transition is reported and explanations for the observations are proposed.

Acknowledgements

I would firstly like to thank my parents and all my family for their unfailing support throughout my academic career and, above all, for helping me keep of a sense of perspective. I am also very grateful to a number of people at several institutions who have helped me at various stages of this project:

At UCL: Dr David Humphrey, for constant support and advice, for the preparation of some of the compounds studied in this work and for his help in the preparation of this thesis; Marcus Daniels, for providing a listening ear and for advice on all matters concerning e-mail; Dr Ian Bell, for advice on technical and experimental matters; Professor Clark and the Clark Research Group.

At Odense University: Christian Svendsen, for providing the collaboration which was vital to all of this work, for his patience in teaching me the finer points of Resonance Raman theory and for his invaluable help, advice and cheerful support at all times; Ole Mortensen, for his generous help and advice with the project and for enabling me to visit the Fysisk Institut in Odense.

At King's College: Dr Alan Collins for the use of the equipment to measure absorption spectra.

Finally, I wish to thank Lars for his help with a whole host of things, ranging from advice on programming and the use of his excellent 'Specman' software, to discussions on spectroscopy and advice on the content of this thesis. Most of all, however, I am deeply grateful to him for his patience, support and understanding without which this work would not have been completed.

Table Of Contents

List Of Figures

List of Tables

Chapter 1

Introduction

1.1 The Study of Excited States

Information on the structures and geometries of molecules in excited electronic states often provides insights into the bonding and reactivity of the species under study. In cases where the excited electronic state is also the reactive or transition state in, for example, a photochemical reaction, such information may be crucial to the understanding of the reaction process. Thus, the ability to characterise molecular structures in electronic states other than the ground state is widely sought.

The problem of accessing excited electronic states of molecules may be approached in two ways. A direct approach is to 'pump' the molecule into the excited state, and then attempt to use the normal spectroscopic characterisation techniques applied in the electronic ground state. Thus, excited state vibrational

spectra, transient absorption spectra and time-resolved Raman and infrared techniques may be used [for example 1.1, 1.2]. However, the application of such *direct* methods generally requires the generation of significant population of the excited state; furthermore, it is often necessary to record the spectrum within the lifetime of the state involved. Such experiments require sophisticated lasers and electronic equipment, and may not be applicable to very short-lived states. Thus, where this facility is either not available, or is inappropriate, other methods of probing excited electronic states of molecules must be found.

The alternative approach is to use *indirect* spectroscopic techniques which probe the excited electronic state, combined with theoretical methods which link the experimental observables to structural changes within the molecule. For example, careful analysis of vibronic structure on electronic absorption spectra (ABS) has long been used to estimate vibrational mode frequencies in the excited electronic state [1.3]. Frequently, however, for solid state samples in other than crystalline form, such structure is poorly resolved, and thus this method must be supplemented with information from other spectroscopic techniques. The Raman spectrum of a molecule recorded using an excitation frequency which lies within the contour of an electronic ABS band (resonance Raman, or RR) can also act a specific and sensitive probe of the excited electronic state. On resonance, the frequencies and linewidths of bands in a Raman spectrum remain dependent on ground state properties; however, the intensities of these bands contain information about structural changes in the molecule in the excited state.

The process of accessing this hidden information requires, however, not only the indirect experimental data, but also the manipulation of complex theoretical expressions for the RR intensities and/or ABS profile. The theoretical methods designed to simplify these expressions normally require some degree of approximation to be made about the molecule. However, the experimental data to which they apply are usually easily accessible.

This thesis is concerned with the second *indirect* type of approach to the problem of molecular excited state geometries. Specifically, it is concerned with recent applications of ABS and RR spectroscopy, together with a number of different theoretical methods, to elucidate changes in the vibrational normal co-ordinates of molecules in the resonant excited electronic state.

The theoretical methods which allow extraction of structural or geometric information about the excited electronic state from ABS or RR spectra, fall into three main categories: time-independent, time-correlator and time-dependent methods.

Time-independent methods: these treat the expressions for RR and ABS intensity in the frequency domain and concentrate on the relationships between ground and excited state vibrational wavefunctions. The Sum-over-States method (SOS), developed by Albrecht [1.4 - 1.8], analyses the contribution to the intensity from a number of vibronic levels of the excited electronic state.

Time-correlator methods: in the time-correlator approach, the expressions for RR and ABS intensity are Fourier-transformed to the time domain. Time-dependent vibrational operators for the ground and excited state are introduced, and so-called 'time-correlators' are defined for the RRS and ABS processes. The evaluation of these correlators can then proceed either via operator algebra and the use of known relationships between ground and excited state wavefunctions [1.9 - 1.11], or via the many-body approach of Tonks, Page and others [1.12, 1.13]

Time-dependent Methods: these methods, which also work in the time-domain, have been developed by Heller et al. [1.14 - 1.18]. In this approach, the RR and ABS intensities are written in terms of a time-dependent overlap between the final vibrational wavefunction and a moving wavepacket generated by the time propagation of the initial vibrational wavefunction on the potential energy surface of the excited electronic.

In principle, transformation of the problem into the time domain should reduce the computing time necessary for calculations.

This work is concerned with the application of a time-independent method and a time-correlator method. The former is a recent version of the SOS method and the latter is called the Overtone Transform (OT) method. These methods also differ in their approach to linking the ABS and RR processes: in the SOS method, the ABS profile and RR intensities are modelled separately and compared to experimental data; in the OT method, however, the expression for the RR intensities is developed in such a way as to be dependent on the ABS profile. Thus, the information contained in the ABS spectrum can be 'transformed' to give the RR intensities, which can then be compared to experimental data.

The aim of this study is twofold: first, by familiarisation with the two different theoretical methods (SOS and OT), to examine their underlying approximations, assumptions and experimental requirements. Consequently, an assessment of their general applicability to 'real' molecules can be made. In this way, obvious advantages and disadvantages of a particular method when dealing with a molecule with specific properties may be highlighted. The second aim is to apply both of these methods to the study of a small number of complex inorganic molecules, ideally ones with structurally interesting excited states on which some information is already available. In this way the molecules may act as test cases for the methods.

The molecules chosen for this purpose are some quadruply bonded dimetallic systems: $[M_2X_8]^{n-}$ ions (specifically $[Re_2Br_8]^{2-}$, $[Re_2I_8]^{2-}$ and $[Mo_2Cl_8]^{4-}$) and the series of compounds $Mo_2X_4(PMe_3)_4$ (X = Cl, Br or I). In particular, structural changes are investigated along the metal-metal (M-M) co-ordinate in the low lying $^1\delta\delta^*$ excited state, in which the formal M-M bond order is reduced from four to three. These compounds have been well characterised, and some estimates of the excited state geometry are available [1.19 - 1.21]. Thus, the

molecules can serve as vehicles for testing the applicability of the methods. At the same time, the successful application of one or both of the methods would provide additional insights into the nature of the metal-metal bonding in these species.

1.2 Structural Changes in Excited Electronic States

In this section, the parameters describing structural changes in excited electronic states will be introduced. Their effect on RR and ABS spectra will be discussed in sections 1.3 - 1.5 in terms of simple frequency-domain expressions, while more detailed account of their inclusion in the SOS and OT method formalisms is reserved for chapter 2.

The process of generating an excited electronic state of a molecule involves a change in the electronic quantum number, usually by stimulation via electromagnetic radiation. This change may also be accompanied by a change in the positions of the nuclei, which constitutes a change in the equilibrium geometry for a different arrangement of electrons within the molecule. Thus, geometric or structural changes in the molecule in an excited electronic state are expected.

In general, the treatment of the theory of ABS and RR scattering requires the use of the Born-Oppenheimer approximation to factor the vibronic states of a molecule into products of electronic states (denoted $|e\rangle$) and vibrational states (denoted $|v\rangle$). Thus, potential energy (PE) curves for each electronic state are introduced. These are, for non-linear molecules, $3N$ - 6 fold degenerate (where N is the number of atoms in the molecule), reflecting the number of vibrational degrees of freedom, or normal modes of vibration of the molecule. In the excited state, structural change can, in principle, occur along any of these normal

co-ordinates depending on the nature of the electronic transition. The following discussion focuses on **one** of these dimensions only.

(a) Linear Displacement (Bond Length Change) - Δ

This is the simplest type of structural change possible along a given normal co-ordinate of the molecule in the excited electronic state. It corresponds to a shift of the minimum of the PE curves of the two states along the normal co-ordinate, as depicted in Fig. 1.1.

In cases where the vibrational mode corresponding to this co-ordinate can be well-approximated by a local 'stretching' mode, the (dimensionless) parameter Δ can be related to a change in the bond length in the excited electronic state.

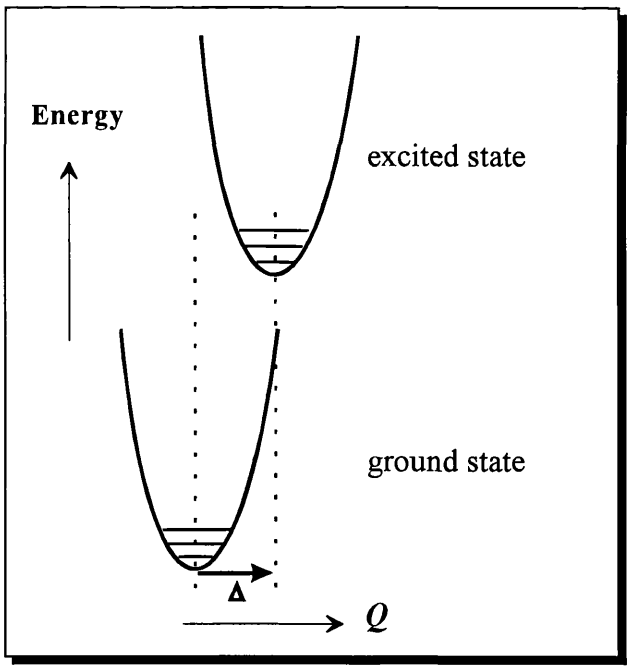

Fig. 1.1 Schematic representation of linear displacement along a normal co-ordinate (Q) in an excited electronic state. The displacement parameter is denoted Δ.

This type of structural change is termed 'linear electron-phonon coupling' and constitutes the primary change in a co-ordinate which can occur in the excited

state. It is usually incorporated into theoretical treatments by the addition of a linear term in the vibrational Hamiltonian:

$$H_e = H_g + E_{eg} + \sum_i \Delta Q_i \qquad (1.1)$$

where H_e is the excited-state vibrational Hamiltonian, H_g is the ground-state vibrational Hamiltonian, E_{eg} is the energy difference between the two states and Q_i is the (re-scaled) co-ordinate operator of normal mode i.

It should be noted that Δ can be non-zero only for totally symmetric modes: since the energy operator (H) in eqn. (1.1) must transform under the operations of the molecular point group as the totally symmetric representation, so only totally symmetric terms are possible on the right-hand side of eqn. (1.1). Thus, since Δ is dimensionless, a given normal co-ordinate Q_i can only appear if it is totally symmetric. Any displacement along a non-totally symmetric co-ordinate in the excited state would result in a change in the symmetry of the molecule in that state and hence is normally disallowed.

It should also be noted that linear displacements will only be significant for normal co-ordinates (modes) along which significant electronic redistribution occurs as a result of the electronic transition. The electronic potential energy along other modes is not expected to be affected significantly.

(b)Change in the frequency of a normal mode

This is the second type of structural change possible along a normal co-ordinate and corresponds to a change in the surface of the PE curve of the excited electronic state (as depicted in Fig. 1.2). Thus there is a change in the force constant of the normal mode, leading to a change in the frequency of the mode.

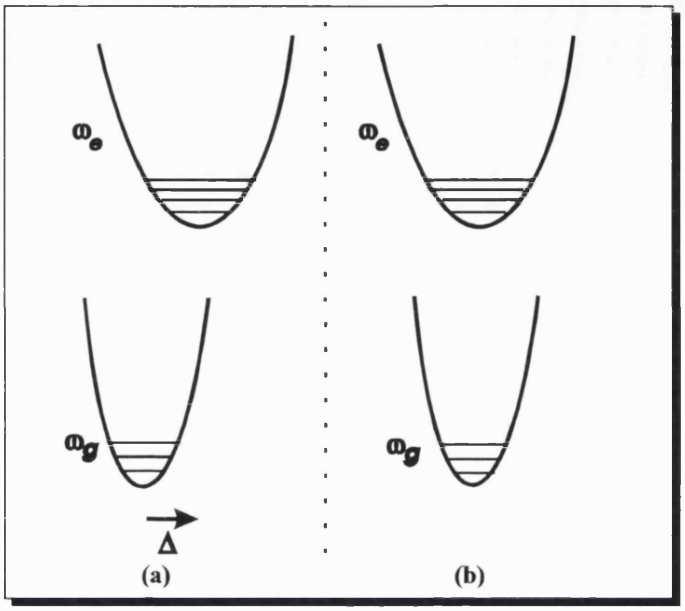

Fig. 1.2 Schematic representation of a frequency change along a normal co-ordinate in the excited electronic state for (a) a totally symmetric co-ordinate where linear displacement also occurs and (b) for a non-totally symmetric co-ordinate, or a totally symmetric co-ordinate where no displacement occurs. The mode frequencies are denoted ω_e (excited state) and ω_g (ground state) respectively.

A frequency change for a normal mode in the excited state is termed 'quadratic electron-phonon coupling' since it is described by the addition of a quadratic term to the vibrational Hamiltonian for the molecule. Its inclusion in theoretical treatments is more complex in general, and it can occur for any symmetry of vibrational mode.

(c) Mode-mixing / Duschinsky Rotation

This takes account of changes in the conformation of the normal co-ordinates of the molecule on promotion to the excited electronic state. In general, the co-ordinates of the ground state are described as 'normal' with respect to the ground state structure. In the excited state, these modes, defined for the ground state, may no longer be normal, but may 'mix', or appear to rotate (as depicted in Fig. 1.3).

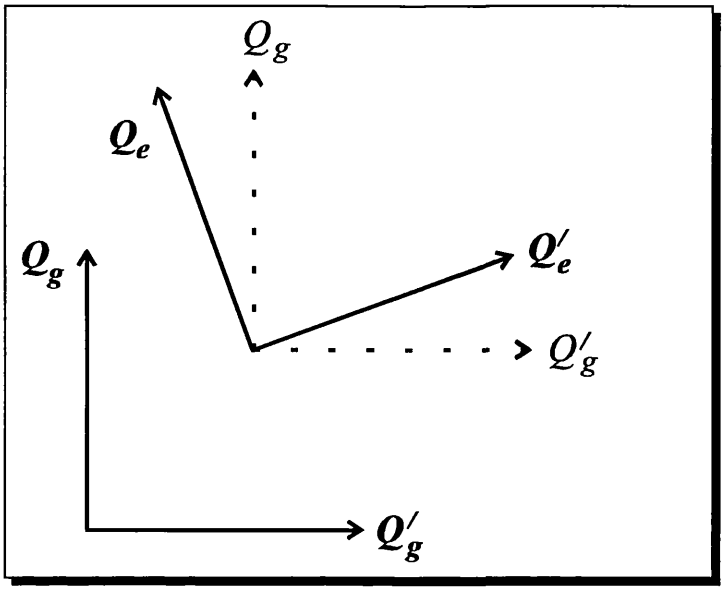

Fig. 1.3 Schematic representation of Duschinsky rotation of two normal co-ordinates in the excited electronic state. Q_g and Q'_g are normal co-ordinates of the ground electronic state, g. Q_e and Q'_e are normal co-ordinates of the excited electronic state, e.

Essentially, mixtures of the ground state normal co-ordinates are required to describe the co-ordinates which diagonalise the vibrational Hamiltonian of the excited electronic state. Since this effect appears to be a rotation of the co-ordinates, it is often termed 'Duschinsky rotation' [1.22].

Mode-mixing is also a manifestation of quadratic electron-phonon coupling, and is frequently represented by a parameter R, which may also incorporate mode frequency changes. Only modes of the same symmetry can mix in this way (provided the molecule does not change point group in the excited state), and the presence of this mixing greatly complicates the treatment of the problem, by preventing formal separation of mixing modes or co-ordinates into one-dimensional states.

(d) Non-Condon Coupling

This is not strictly a geometric change in the excited electronic state, but is a necessary additional parameter for a given mode/co-ordinate. In the course of the theoretical treatment, the Born-Oppenheimer (B-O) approximation is used and the electronic and nuclear wavefunction are separated. It is often assumed that the electronic transition moment, $M_{eg} = \langle e| \boldsymbol{r} | g\rangle$ (where g is the ground electronic state, e is the excited electronic state, and $\boldsymbol{r}$ is the dipole operator), is independent of the nuclear co-ordinates, Q. This is known as the Condon approximation.

However, M_{eg} retains a parametric dependence on the nuclear co-ordinates, Q. If M_{eg} for a given electronic transition is dependent on a given normal co-ordinate, Q_i, then that normal mode, i, is said to exhibit non-Condon (NC) coupling in this transition. The usual way of dealing with NC coupling is to expand M_{eg} as a Taylor series in the relevant co-ordinate(s), with only the first term retained as a parameter [1.4]. Alternative schemes, such as the Herzberg-Teller (HT) scheme [1.23, 1.4], interpret the NC coupling as a result of coupling between the excited state, $| e \rangle$ and another excited state $| s \rangle$ of the appropriate symmetry, via the vibrational mode Q_i.

These are the main parameters associated with changes in vibrational normal co-ordinates, i.e. nuclear positions and structure, in the excited electronic state. The aim of the theoretical methods is then to find values for these parameters for a given normal co-ordinate using information contained in the RR and ABS spectra. Thus in the next sections, the effect of these structural changes on RR and ABS spectra will be discussed.

1.3 The Raman Effect

When a molecule is irradiated with monochromatic light whose frequency, ω_L does not lie within the contour of an absorption band of the molecule, most of the light passes straight through without being affected. However, a small part of the

light will be scattered and, when analysed, this scattered light is found to consist of an elastically scattered part of frequency ω_L (Rayleigh scattering), and an inelastically scattered part, for which $\omega \neq \omega_L$: this latter part is referred to as Raman scattering.

This Raman effect was predicted by Smekal [1.24] in 1923 and subsequently discovered experimentally by C. V. Raman in 1928 [1.25]. Raman observed scattered light at frequencies $\omega_L \pm \omega_i$, where the ω_i correspond to changes in the rotational, vibrational or electronic energy of the molecule. The effect was discovered independently in the same year in Russia by Landesberg and Mandelstam [1.26], and named secondary radiation. However, the phenomenon became known as the Raman effect and, during the period following its discovery, much research was devoted to its investigation.

Initially, the scattered radiation was interpreted classically as arising from the oscillation of a dipole induced in the molecule by the oscillating electric field ($\boldsymbol{E}$) of the electromagnetic radiation. The induced dipole, μ_{ind}, can be expressed as a power series in the electric field:

$$\mu_{ind} = \boldsymbol{\alpha E} + \frac{1}{2!}\boldsymbol{\beta} \boldsymbol{E}^2 + \frac{1}{3!}\boldsymbol{\gamma E}^3 + ... \qquad (1.2)$$

where $\boldsymbol{\alpha}$ is the second-rank molecular polarisability tensor, $\boldsymbol{\beta}$ is the hyperpolarisability and $\boldsymbol{\gamma}$ is the second hyperpolarisability tensor. Only the first term is usually of significant magnitude, and hence eqn (1.2) can be written as:

$$\begin{bmatrix} (\mu_{ind})_x \\ (\mu_{ind})_y \\ (\mu_{ind})_z \end{bmatrix} = \begin{bmatrix} \alpha_{xx} & \alpha_{xy} & \alpha_{xz} \\ \alpha_{yx} & \alpha_{yy} & \alpha_{yz} \\ \alpha_{zx} & \alpha_{zy} & \alpha_{zz} \end{bmatrix} \begin{bmatrix} E_x \\ E_y \\ E_z \end{bmatrix} \qquad (1.3)$$

where the α_{ij} are the elements of the polarisability tensor, $\boldsymbol{\alpha}$.

In the classical treatment of the vibrational Raman effect, consideration of the dependence of the polarisability on the nuclear co-ordinates (via a Taylor series expansion) leads to the prediction of Raman scattered light of frequencies corresponding to internal vibrational frequencies of the molecule. In addition, it is seen that Raman bands appeared at both $\pm \omega_i$, with those of lower energy than that of the incident light being denoted Stokes Raman scattering, and those with energies higher than that of the incident light, anti-Stokes Raman scattering. It is also possible to derive a gross selection rule for a band due to a vibrational mode to be observed in a Raman spectrum: the polarisability of the molecule must change during the vibration for it to be Raman active.

Following the classical treatment, Plazcek [1.27] developed a theory on the intensities of Raman lines using a partial quantum-mechanical treatment. This treatment was particularly useful experimentally, as it allowed better understanding of Raman selection rules, for both rotational and vibrational bands. Thus the complementary nature of Raman and IR spectroscopies was highlighted.

A further advance in the study of Raman intensities was their interpretation in terms of bond polarisabilities within the molecule. The Bond Polarisability theory due to Wolkenstein [1.28] treated the overall molecular polarisability as the tensor sum of terms for the various bonds in the molecule. Thus Raman intensities could be related directly to chemical structures.

However, following the initial interest in the Raman effect and despite its potential as an analytical tool, it was eclipsed in usage by IR spectroscopy which proved to be easier to perform experimentally. The key problems associated with the experimental recording of a Raman spectrum resulted from it being a very weak effect, with only ~1 in 10^6 incident photons being inelastically scattered. The incident source standardly used was a mercury arc lamp, which proved to be quite weak, and thus the collection techniques for the scattered light were often unable to discriminate against the more intense Rayleigh light.

In the 1960s, however, the advent of lasers coupled with advances in the spectrometer optics and detection systems, allowed Raman spectra to become experimentally more accessible. In addition to the obvious advantages of power, wider wavelength range and monochromaticity of the laser excitation source, its directional properties and linear polarisation allowed measurements of depolarisation ratios and individual components of the polarisability tensor. Expressions for the depolarisation ratios (ρ) of Raman bands for freely rotating molecules in liquids and gases can be found easily from classical theory. ρ is defined as the ratio of the intensity of the light scattered with its electric vector perpendicular to that of the incident light ($I_{\perp}$) to the intensity of light scattered with its electric vector polarised parallel to the electric vector of the incident light ($I_{\parallel}$). The details of the derivation of these expressions will not be given here, since this work is concerned primarily with resonance Raman spectroscopy. A thorough treatment is given in chapter 4 of [1.29] and it can be seen that measurement of the depolarisation ratio of a Raman band can allow the determination of the symmetry of the vibration giving rise to that particular band.

In addition to these technical advances, much theoretical development in the field of Raman scattering (RS) took place, notably by Albrecht [1.4, 1.5], Shorygin [1.30] and others. The description of the Raman scattering process which emerged was one of the coherent (or simultaneous) absorption and emission of photons, involving a virtual intermediate state. This state is represented as a superposition of all the molecular eigenstates (see Fig. 1.4)

The net result of the virtual absorption/emission process is an upwards or downwards transition between levels in the ground state (either rotational or vibrational). In this work, and from here on, attention is restricted solely to the vibrational Raman effect. Thus the levels $|i\rangle$ and $|f\rangle$ in Fig. 1.4 differ in energy by a vibrational quantum.

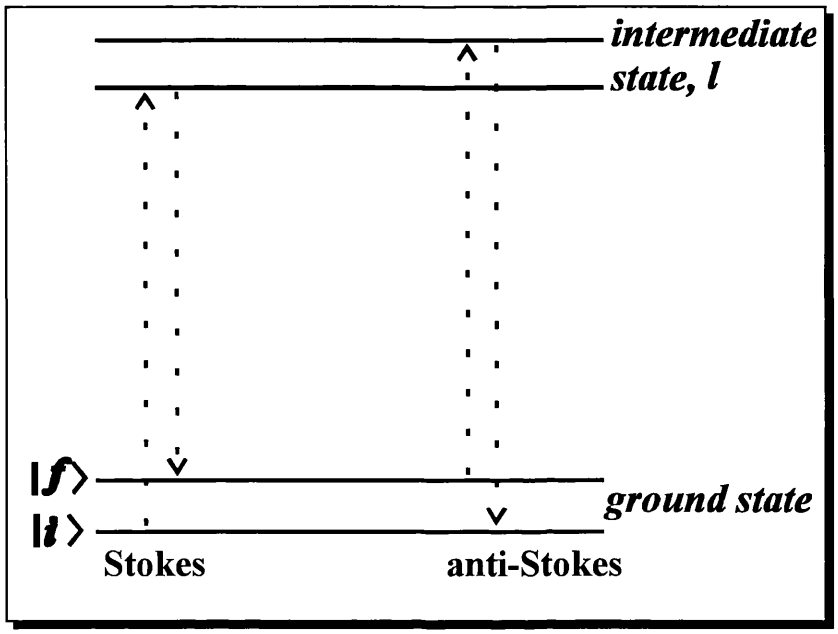

Fig. 1.4 Schematic representation of Raman scattering as a coherent two-photon process. The intermediate state is not a stationary state of the system and can be represented as a sum over all molecular eigenstates.

It can be seen from Fig. 1.4 that the two types of Raman scattering, Stokes and anti-Stokes scattering, correspond to excitation or de-excitation of a particular vibrational level. Thus, anti-Stokes scattering requires a significant initial population of an excited vibrational level and is therefore normally less intense than Stokes scattering, especially at low temperatures. The ratio of the intensities of corresponding Stokes and anti-Stokes bands is related to the relative populations of the initial vibrational states, and can thus be related to the temperature of the sample.

The intensity of the scattered radiation corresponding to a transition from a state $|\, i \,\rangle$ to a state $|\, f \,\rangle$ can be expressed in terms of the excitation frequency and the transition polarisability (or scattering tensor), $[\alpha_{\rho\sigma}(\omega_L)]_{fi}$, using Maxwell's equations. It is found that the total intensity scattered over 4π steradians is proportional to $|[\alpha_{\rho\sigma}(\omega_L)]_{fi}|^2$, where ρ and σ denote the polarisations of the incident and scattered light respectively.

The relationships between the elements of the transition polarisability, or scattering tensor, and the molecular eigenstates were found by Kramers and Heisenberg [1.31] using second order perturbation theory and modified by Dirac [1.32]. Thus:

$$[\alpha_{\rho\sigma}(\omega_L)]_{fi} = \left[\sum_l \frac{\langle f|r_\rho|l\rangle\langle l|r_\sigma|i\rangle}{\omega_{li} - \omega_L - i\Gamma_l} + \frac{\langle f|r_\sigma|l\rangle\langle l|r_\rho|i\rangle}{\omega_{li} + \omega_L - i\Gamma_l} \right] \qquad (1.4)$$

where r_ρ and r_σ are the electric dipole moment operators, Γ_l is a lifetime (damping) factor for state l and $\omega_{li} = \omega_l - \omega_i$, the frequency of the transition $|l\rangle \leftarrow |i\rangle$. ω_L is the frequency of the incident radiation.

Eqn. (1.4) is the Kramers-Heisenberg-Dirac (KHD) formula, upon which nearly all theories of Raman and RR intensities are based. In order to develop these theories further, several approximations and assumptions must now be made:

- The Born-Oppenheimer approximation is assumed to be valid for all molecular eigenstates. Thus the vibronic states, $|i\rangle$, $|f\rangle$ and $|l\rangle$ are factored into products of electronic and vibrational states:

$$|i\rangle \rightarrow |g\rangle|v_1\rangle; \quad |f\rangle \rightarrow |g\rangle|v_1 + n\rangle; \quad |l\rangle \rightarrow |e\rangle|v_2\rangle \qquad (1.5)$$

  where n denotes the degree of excitation in a mode following the Raman transition.

- The dipole operator matrix elements become :

$$\langle f|r_\rho|l\rangle \rightarrow \langle v_1 + n|\langle g|r_\rho|e\rangle|v_2\rangle$$

$$= \langle v_1 + n|(M_\rho)_{ge}|v_2\rangle$$

$$\langle l|r_\sigma|i\rangle \rightarrow \langle v_2|\langle e|r_\sigma|g\rangle|v_1\rangle$$

$$= \langle v_2|(M_\sigma)_{eg}|v_1\rangle \qquad \text{etc.} \qquad (1.6)$$

where $(M_\sigma)_{ge}$ etc. denote the pure electronic transition moments. These retain a parametric dependence on the vibrational co-ordinates, as described in section 1.2, giving rise to NC coupling.

In general, NC coupling is taken into account via a Taylor series expansion of $(M_\rho)_{ge}$ in the co-ordinate Q_i:

$$(M_\rho)_{ge}(Q) = (M_\rho^0)_{ge} + \sum_i \left(\frac{\partial M_\rho}{\partial Q_i}\right)_{ge,Q=0} Q_i + \ldots \qquad (1.7)$$

where i denotes the summation over vibrational co-ordinates. This first derivative is usually denoted m, the NC coupling parameter.

- The vibrational wavefunctions are generally assumed to be independent and normal, allowing the wavefunctions to be separated into the product of wavefunctions associated with particular normal modes or co-ordinates. Thus, at any time, a one-dimensional picture, as outlined in section 1.2, is used, corresponding to one particular co-ordinate of the system. A breakdown of this approximation can later be included for the case of RR scattering (RRS) by introduction of a mode-mixing parameter.

Following these rearrangements, eqn. (1.4) becomes:

$$[\alpha_{\rho\sigma}(\omega_L)]_{gv_1,g(v_1+n)} = \sum_{e,v_2} \frac{\langle v_1+n|(M_\rho)_{ge}(Q)|v_2\rangle\langle v_2|(M_\sigma)_{eg}(Q)|v_1\rangle}{\omega_{ev_2,gv_1} - \omega_L - i\Gamma_{ev_2}} + \frac{\langle v_1+n|(M_\sigma)_{ge}(Q)|v_2\rangle\langle v_2|(M_\rho)_{eg}(Q)|v_1\rangle}{\omega_{ev_2,gv_1} + \omega_L - i\Gamma_{ev_2}} \qquad (1.8)$$

and, after inclusions of NC coupling, this becomes:

$$[\alpha_{\rho\sigma}(\omega_L)]_{gv_1,g(v_1+n)} = \sum_e \sum_{v_2} (\omega_{eg} + \omega_{v_2v_1} - \omega_L - i\Gamma_{ev_2})^{-1}$$

$$\{(M^0_\rho)_{ge}(M^0_\sigma)_{eg}\langle v_1+n|v_2\rangle\langle v_2|v_1\rangle$$

$$+(M'_\rho)_{ge}(M_\sigma)_{eg}\langle v_1+n|Q|v_2\rangle\langle v_2|v_1\rangle$$

$$+(M^0_\rho)_{ge}(M'_\sigma)_{eg}\langle v_1+n|v_2\rangle\langle v_2|Q|v_1\rangle\}$$

$$+\sum_e \sum_{v_2} (\omega_{eg} + \omega_{v_2v_1} + \omega_L - i\Gamma_{ev_2})^{-1}$$

$$\{(M^0_\sigma)_{ge}(M^0_\rho)_{eg}\langle v_1+n|v_2\rangle\langle v_2|v_1\rangle$$

$$+(M'_\sigma)_{ge}(M^0_\rho)_{eg}\langle v_1+n|Q|v_2\rangle\langle v_2|v_1\rangle$$

$$+(M^0_\sigma)_{ge}(M'_\sigma)_{eg}\langle v_1+n|v_2\rangle\langle v_2|Q|v_1\rangle\} \quad (1.9)$$

Off-resonance, i.e. where the excitation frequency ω_L is much lower than the frequency difference of the electronic transition, $\omega_{ev_2,gv_1}(=\omega_{ev_2}-\omega_{gv_1})$, the denominators in eqn. (1.8) are large, irrespective of the state e.

Thus, the contributions to the scattered intensity arise from a large number of different intermediate states, each with the appropriate energy weighting. It is then possible to close the sum over v_2 in eqn. (1.9), since the v_2 then represents a complete set of orthonormal states:

$$\sum_{v_2} \langle v_2|v_2\rangle = 1 \quad (1.10)$$

Thus, the matrix elements in the first term in each sum reduce to

$$\langle v_1+n|v_1\rangle$$

and, since these are vibrational wavefunctions of the same electronic state, this integral will be zero unless $n = 0$. Thus, this term can only give rise to elastic (Rayleigh) scattering.

The matrix elements in the second and third terms of each sum in eqn. (1.9) become:

$$\langle v_1 + n|Q|v_1\rangle$$

which, if it is assumed that the vibrational wavefunctions are harmonic oscillators, yield first-order Raman scattering, with $n = \pm 1$. Thus, fundamental bands due to Raman active modes may be seen. Any overtones or combinations arise from consideration of higher terms in the expansion of the electronic transition dipole (eqn. (1.7)). Symmetry selection rules are most easily determined if it is remembered that $[\alpha_{\rho\sigma}]$ transforms as the product $\rho\sigma$: e.g. xy for α_{xy}, and thus the transition $| i \rangle \rightarrow | f \rangle$ is allowed if $\langle f|\alpha_{\rho\sigma}|i\rangle$ contains the totally symmetric representation for some ρ and σ.

Normal (off-resonance) Raman spectroscopy is now an invaluable characterisation, complementary to IR absorption spectroscopy [see for example 1.33, 1.34]. It has been widely used to study organic, inorganic and biochemical molecules and, through technical advances such as Raman microscopy, can allow structural analyses of molecules on surfaces [1.35].

1.4 The Resonance Raman Effect

As the frequency of the incident light, ω_L, approaches that of a transition to a defined electronic state (ω_{eg}), the denominator in the first term of eqn. (1.8) becomes very small. Consequently, the 'off-resonant' second term may be

neglected. The transition polarisability, $[\alpha_{\rho\sigma}]_{g(v_1+n),gv_1}$ becomes very large and intensity enhancement of Raman bands can be seen.

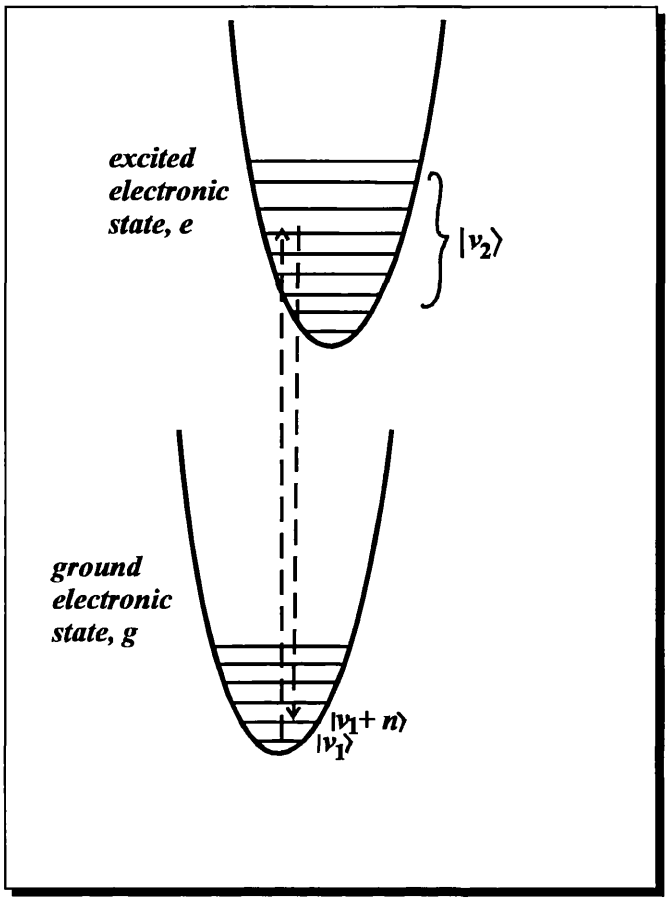

Fig. 1.5 Schematic diagram of the RR effect, where the intermediate level is now an excited electronic state, *e* lying at an energy $h\omega_{eg}$ above the ground state.

Therefore, concentrating on only the resonant part of eqns (1.8) and (1.9), it is generally the case on resonance that the contribution from a single excited electronic state is dominant, and thus the sum over *e* in these equations may be dropped. This is depicted in Fig. 1.5. In this case the vibrational sum runs over only a few vibrational levels of the excited electronic state, and the contribution from each must be summed.

Furthermore, it is usually necessary to treat the NC terms of eqns. (1.8) and (1.9) more explicitly on resonance, so that the behaviour of the intensities of bands due to modes of different symmetry may be understood. The usual

description of NC coupling invoked is the Herzberg-Teller (HT) scheme [1.23], where $(M'_{\rho})_{ge}$ in eqns. (1.7) - (1.9) describe vibronic coupling between the resonant excited electronic state, e, and another state, s, of the appropriate symmetry. Thus, eqn. (1.7) is written:

$$(M_{\rho})_{ge}(Q) = (M^0_{\rho})_{ge} + \sum_s \sum_i (M^0_{\rho})_{gs} \frac{h^i_{es}}{\omega_{es}} Q_i + ... \qquad (1.11)$$

where s denotes another excited electronic state to which a transition is allowed ($(M^0_{\rho})_{gs} \neq 0$), and $h^i_{es} = \langle e|\partial H/\partial Q_i|s\rangle_{Q_i=0}$.

This term is a measure of the strength of the vibronic coupling between states s and e via the co-ordinate Q_i. This HT description is only valid for weak coupling between non-degenerate states.

Thus, taking into account these considerations, eqn. (1.9) now becomes:

$$[\alpha_{\rho\sigma}(\omega_L)]_{g(v_1+n),gv_1} = A + B \quad (... + C + D) \qquad (1.12)$$

where

$$A = \sum_{v_2} (\omega_{eg} + \omega_{v_2 v_1} - \omega_L - i\Gamma_{ev_2})^{-1} (M^0_{\rho})_{ge} (M^0_{\sigma})_{eg} \langle v_1 + n|v_2\rangle\langle v_2|v_1\rangle \qquad (1.13)$$

and

$$B = \sum_{s\neq e} (M^0_{\rho})_{gs} (M^0_{\sigma})_{eg} \frac{h^i_{es}}{\omega_{es}} \sum_{v_2} \frac{\langle v_1 + n|Q_i|v_2\rangle\langle v_2|v_1\rangle}{\omega_{ev_2,gv_1} - \omega_L - i\Gamma_{ev_2}}$$

$$+ \sum_{s\neq e} (M^0_{\rho})_{ge} (M^0_{\sigma})_{sg} \frac{h^i_{se}}{\omega_{es}} \sum_{v_2} \frac{\langle v_1 + n|v_2\rangle\langle v_2|Q_i|v_1\rangle}{\omega_{ev_2,gv_1} - \omega_L - i\Gamma_{ev_2}} \qquad (1.14)$$

and C and D are higher order terms accounting for NC coupling between the ground state and other excited states, and for combination bands. These terms are small and usually negligible in comparison to the A and B terms [1.4].

A-term Scattering

Bands due to a vibrational mode may be enhanced by A-term scattering if two conditions are fulfilled:

(1) $(M_\rho^0)_{ge}$ and $(M_\sigma^0)_{eg}$ must be non-zero: i.e. the resonant electronic transition must be strongly allowed. Thus, resonance with a very weak band in the ABS spectrum would not be expected to produce significant A-term scattering.

(2) Non-orthogonality must subsist between the vibrational wavefunctions of the ground electronic state ($|v_1 + n\rangle$ and $|v_1\rangle$) and those of the excited electronic state ($|v_2\rangle$). Thus, the vibrational overlap integrals (Franck-Condon or FC factors)

$$\langle v_1 + n | v_2 \rangle \langle v_2 | v_1 \rangle$$

etc. must be non-zero for at least some values of v_2.

For totally symmetric vibrational modes, non-orthogonality can be achieved by either a displacement of the minimum in the PE curve along that co-ordinate, or a change in the curvature of the PE curve leading to a change in the frequency of that mode in the excited electronic state. Thus the two parameters Δ and ω_e, outlined in section (1.2), become important, and their magnitudes will determine the FC overlap factors and hence the intensities of RR bands due to these modes.

For non-totally symmetric modes, no displacement of the PE curve minimum in the excited electronic state is possible (provided the molecule does not change symmetry in the excited state), as explained in section 1.2. Thus, only

a significant frequency change for a given mode will allow bands due to that mode to be substantially enhanced via *A*-term scattering.

Thus, it is clear that the parameters Δ and ω_e for a mode in the excited electronic state are important in determining the FC factors and hence the RR intensities of bands due to that mode. For a totally symmetric co-ordinate, along which significant electronic redistribution occurs as a result of the electronic transition, Δ may be quite large. The FC factors above may then be large for several quanta of n, and thus many overtones can be seen in the RR spectrum. Therefore, the RR spectra of totally symmetric modes are characterised by long progressions, the length of which is determined by the size of Δ for that mode and, to a lesser extent, ω_e.

If a molecule contains more than one totally symmetric mode, all may show RR enhancement in this way. However, it is often the case that the electronic redistribution occurring during the transition is largely localised along one vibrational co-ordinate. Thus, geometric changes (and hence RR intensity enhancement) will be largest along this co-ordinate. However, if the treatment of each of the co-ordinates as individual, separable modes breaks down in the excited electronic state, then two totally-symmetric modes may mix. This 'mode-mixing' or Duschinsky rotation can be treated in the detailed theory of RR, and gives rise to another excited state parameter for each co-ordinate (see section 1.2). In this case, enhancement to both modes, and hence possibly a progression in both modes will occur (since a structural change has formally occurred along both co-ordinates). However, if enhancement to more than one totally-symmetric mode *is* seen in a RR spectrum, this does not indicate unequivocally that the two modes mix in the excited state: geometric change along both separable modes in the excited state could occur without the need for mode-mixing between them.

B-term Scattering

Scattering arising from the *B*-term mechanism is usually weaker than that arising from the *A*-term, because of the extra $1/(\omega_e - \omega_s)$ term in the denominators of eqn. (1.14). However, it is important where resonance occurs with a weak electronic transition (for which $(M^{\rho}_{\rho})_{ge} \sim 0$) or for non-totally symmetric modes for which near orthogonality of the vibrational wavefunctions of the ground and excited electronic states prevents scattering via the *A*-term mechanism.

The presence of *B*-term enhancement is incorporated parametrically as NC coupling in most RR theories (section 1.2), but its interpretation via the HT scheme requires that both the resonant transition, $|e\rangle \leftarrow |g\rangle$ and the transition $|s\rangle \leftarrow |g\rangle$ should be electric dipole allowed. The symmetries of the modes capable of coupling between states $|e\rangle$ and $|s\rangle$ may be ascertained by the normal symmetry selection rules which require h^i_{es} to be non-zero. It is notable that, for totally symmetric modes, this requires that $|e\rangle$ and $|s\rangle$ be of the same symmetry. In general, only one state, $|s\rangle$ contributes significantly to this kind of coupling and so the sum over *s* can be dropped.

The magnitude of *B*-term scattering is then determined by products of the kind

$$\langle v_1 + n|Q_i|v_2\rangle\langle v_2|v_1\rangle$$

and, in general the first integral will be non-zero only if $v_1 + n = v_2 \pm 1$, if the harmonic oscillator approximation is made to the (near orthogonal) vibrational wavefunctions of the ground and excited electronic states. Since the term $\langle v_2 | v_1 \rangle$ will only be non-zero for near orthogonal wavefunctions in the ground and excited state if $v_2 = v_1$, then $v_1 + n = v_1 \pm 1$, i.e. $n = \pm 1$. Thus, only fundamental bands are likely to be enhanced by *B*-term scattering. The actual magnitude of the overlap integrals may be affected by any other geometric change, e.g. mode-mixing or small frequency changes. Since these will also affect the degree

of orthogonality between the vibrational wavefunctions of the ground and excited electronic state, the above selection rule may also be slightly relaxed in these cases.

Thus, both totally symmetric and non-totally symmetric modes may be enhanced via this *B*-term mechanism, but the enhancement is likely to be weaker and confined to fundamental bands only. This type of scattering occurs in the RR spectrum of metallic porphyrin compounds in resonance with the so-called *Q* -band, where the nearby intense Soret band couples to the weak *Q*-transition via a mode of the appropriate symmetry [1.36].

It can be seen therefore that the magnitude of the geometric changes along a vibrational normal co-ordinate (Δ, ω_e, mode-mixing and NC coupling) will affect the intensities of bands due to that mode in the RR spectrum, either by affecting the magnitude of FC overlap integrals, or by producing *B*-term scattering. In general, geometric change (and hence intensity enhancement) will only occur for a given normal co-ordinate if there is significant electronic redistribution along that co-ordinate in the excited electronic state.

Thus, RR is a powerful technique for assigning, for example, bands due to totally symmetric modes [1.37], and can also help assign electronic transitions in the ABS spectrum [1.38]: if a particular mode shows strong resonance enhancement in the RR spectrum recorded with excitation frequency lying within the contour of a given ABS band, then the co-ordinate along which the electronic transition is largely localised may be identified.

It is possible to plot a Raman Excitation Profile (REP) for a band due to a vibrational mode: this is a plot of the intensity of that band in the RR spectrum as a function of the excitation frequency. It can be seen that the shape of such a profile generally follows that of the resonant ABS band, if geometric change occurs in the excited state along that co-ordinate. The actual shape and position

of the maximum of the REP are determined by the relative magnitude of some of the parameters of the excited electronic state, and these are detailed elsewhere [1.39, 1.40].

Many other effects can occur in resonance Raman scattering which have not been discussed in this simple outline. Thus, interference effects arising from resonance with more than one electronic state, or the effect of degeneracies of the electronic state or Jahn-Teller effects have not been considered, but are detailed elsewhere [1.39]. It has been the purpose of the preceding sections to outline the primary structural changes which can occur along a normal co-ordinate in an excited electronic state, and indicate how these changes can affect the intensities of bands in the RR spectrum. For this purpose, only simple frequency-domain expressions for RRS and ABS have been used. More detailed account of how these structural parameters are incorporated explicitly into expressions for RR intensities are reserved for chapter 2.

One notable change in the characteristics of Raman scattering which occurs on resonance is that the polarisability tensor, $\alpha_{\rho\sigma}$, is no longer symmetric. Thus, depolarisation ratios for a given mode may be different in the cases of on- or off-resonance. The details of this effect are thoroughly discussed elsewhere [1.29]. It is sufficient to note here that the degeneracies of the state involved in the resonant electronic transition become important. For a totally symmetric mode, in the case of resonance involving non-degenerate electronic states, only one diagonal component, say α_{zz}, of the polarisability tensor is generally non-zero. This is provided that the molecular point group symmetry is not C_i, C_s, C_1, C_2 or C_h. The component of the tensor which is non-zero will be that along which the electronic transition is polarised. Since the modes and transitions considered further in this work fall into the above category, only one component of the polarisability need be considered in further theoretical treatments.

1.5 Electronic Absorption Spectroscopy

The electronic ABS spectrum for a particular electronic transition will clearly also contain information about the structure of the excited electronic state. In the normal Franck-Condon (FC) picture of an electronic transition, the change in electronic state is usually accompanied by a change in the vibrational quantum number of a given mode, along which some geometric change occurs in the excited state. This is depicted in Fig. 1.6.

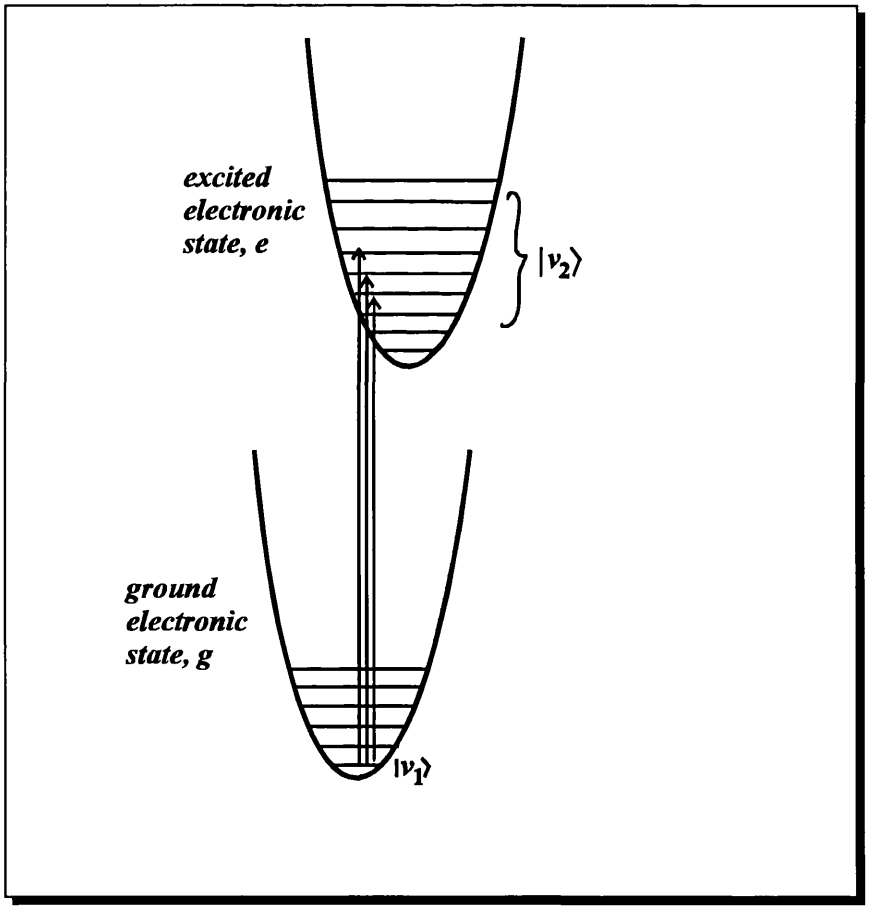

Fig. 1.6 FC picture of an electronic transition, with accompanying vibrational transitions in a given normal mode, Q.

Thus, the transition moment is defined (within the Born-Oppenheimer approximation) as:

$$\langle v_2 | (M_\rho)_{ge} | v_1 \rangle \qquad (1.15)$$

where e and g again denote the ground and excited electronic states, with vibrational states v_2 and v_1 respectively. If the Condon approximation is assumed, then $(M_\rho)_{ge} = (M^0_\rho)_{ge}$ then eqn. (1.15) becomes:

$$\langle v_2 | (M^0_\rho)_{ge} | v_1 \rangle = (M^0_\rho)_{ge} \langle v_2 | v_1 \rangle \qquad (1.16)$$

and thus, if the electronic transition is allowed, i.e. if $(M^0_\rho)_{ge} \neq 0$, vibrational transitions can also occur providing $\langle v_2 \mid v_1 \rangle$ is also non-zero.

The magnitude of the FC factors $\langle v_2 \mid v_1 \rangle$ for a given vibrational mode will depend on the overlap between the ground and excited state vibrational wavefunctions. In general, if the vibrational levels of the two states are nearly orthogonal, $\langle v_2 \mid v_1 \rangle = \delta_{v_2 v_1}$, and only transitions of the type $(v_1 =)0 \rightarrow (v_2 =)0$ and 1 -1 etc. will be seen.

Non-orthogonality between ground and excited state wavefunctions subsists for a given co-ordinate if there is significant geometric change along that co-ordinate in the excited state: e.g. for a totally symmetric co-ordinate, a linear displacement, denoted, Δ, or a change in the frequency of that mode, may occur. Thus, these structural parameters, as outlined in section 1.2, will affect the ABS spectrum in a similar way to that seen for RR scattering (section 1.4). Hence, progressions or vibronic structure may be observed on an electronic ABS band, usually in one or more totally symmetric modes along which there is structural change in the excited state.

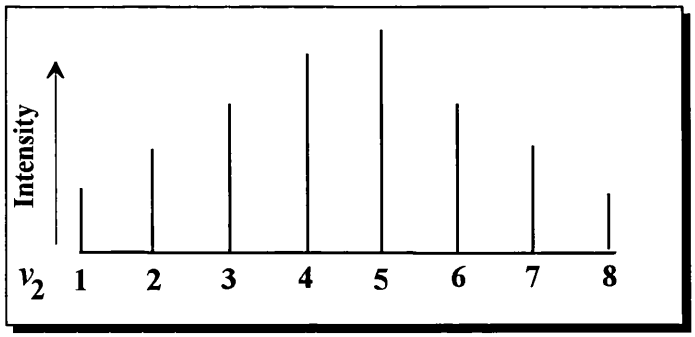

Fig. 1.7 Schematic diagram of vibronic progression from e.g. the $v_1 = 0$ level in a mode in an ABS band: the value of v_2 at which the intensity maximum occurs will depend on the extent of the structural changes along that co-ordinate in the excited state.

In addition, if NC coupling is taken into account, then eqn. (1.16) may be written:

$$\langle v_2 | (M_\rho^0)_{ge} + \sum_s (M_\rho^0)_{gs} \frac{h_{es}^i}{\omega_{es}} Q_i | v_1 \rangle$$

$$= \langle v_2 | (M_\rho^0)_{ge} | v_1 \rangle + \sum_s (M_\rho^0)_{gs} \frac{h_{es}^i}{\omega_{es}} \langle v_2 | Q_i | v_1 \rangle \qquad (1.17)$$

If the electronic transition is formally disallowed, then $(M^0_\rho)_{ge} = 0$; however, in some cases, the transitions become 'vibronically allowed' by coupling of the excited state to another nearby state (to which a transition from the ground state is allowed), via a normal co-ordinate of the appropriate symmetry. For example, the $^1B_{2u} \leftarrow {}^1A_{1g}$ band in benzene is formally forbidden, but 'steals' intensity from the nearby allowed $^1E_{1u} \leftarrow {}^1A_{1g}$ transition, via coupling through an E_{2g} vibration [1.41].

Intensity arising from this second NC mechanism can occur via coupling through totally symmetric modes or via non-totally symmetric modes, for which FC overlap integrals in the first term are usually zero.

Thus, it can be seen that geometric change along a normal co-ordinate in the excited electronic state will also manifest itself in the electronic ABS spectrum. It is often possible, by looking at the spacing between vibronic peaks of a mode progression in the ABS band, to estimate a value for ω_e (or $\tilde{\nu}_e$). However, further information on parameters such as Δ, or on mode-mixing and even NC coupling can be found by a more detailed theoretical treatment.

From the optical theorem of scattering [1.42], it has been found that the absorption intensity cross-section is also dependent on the molecular polarisability:

$$\sigma_{ABS} \propto Im[\alpha_{\rho\rho}(\omega_L)]_{ii}$$

where Im denotes the imaginary part and $[\alpha_{\rho\rho}(\omega_L)]_{ii}$ is given by the diagonal component of the resonant part of the KHD formula (eqn. (1.4) as:

$$[\alpha_{\rho\rho}(\omega_L)]_{i,i} = \sum_l \frac{\langle i|r_\rho|l\rangle\langle l|r_\rho|i\rangle}{\omega_{li} - \omega_L - i\Gamma_l} \qquad (1.18)$$

Thus, by exactly the same treatment as outlined in sections 1.3 and 1.4, this can be represented as:

$$[\alpha_{\rho\rho}(\omega_L)]_{gv_1,gv_1} = \sum_{v_2} \frac{\left|\langle v_1|(M_\rho^0)_{ge}|v_2\rangle\right|^2}{\omega_{eg} - \omega_{v_2v_1} - \omega_L - i\Gamma_{ev_2}} \qquad (1.19)$$

in the Condon approximation. NC coupling can be introduced further, as in the case of RR scattering. Therefore, it can be seen that the treatment of the ABS process is very similar to that for the RRS process, and that the same structural parameters of the excited state will be important in determining its final form.

1.6 Linking ABS and RRS

From sections (1.4) and (1.5) it can be seen that the RR and ABS processes can be linked at the theoretical level by the transition polarisability, $[\alpha_{\rho\sigma}(\omega_L)]_{fi}$. The magnitude of structural changes along a vibrational normal co-ordinate in the excited state (described by the parameters outlined in section 1.2) will affect both the ABS profile and the RR intensities of bands due to that mode.

Many theoretical methods have been developed to obtain explicit relationships between quantities which are experimentally observable, such as RR intensities or ABS profile, and the structural parameters for the co-ordinate in the

excited electronic state. A comparison of predicted and experimental values for observables then allows extraction of values for the parameters.
In general, the successful application of such a method requires:

- Application to a normal co-ordinate of a molecule which can be well-approximated to a local co-ordinate (e.g. assigned to a single bond stretching mode) such that the parameter values (such as displacement, Δ), can be interpreted in a meaningful way.

- Accurate experimental data for comparison or use in the method, e.g. intensity ratios of overtone bands in a progression due to a mode in the RR spectrum, or an REP for a given mode, as well as the resonant ABS spectrum.

- Clear and explicit relationships between these experimental observables and the desired structural parameters. Furthermore, these relationships should not require severe or restricting assumptions to be made about the molecule.

Much early work in the development of such theories was based on Albrecht's theory of Raman intensities [1.4 - 1.6]. The development of this work focused on the evaluation of the FC overlap integrals in eqns. (1.13) and (1.17) in terms of the structural parameters, using relationships defined earlier by Manneback [1.43]. The contribution of each vibrational level of the excited state to the total RR or ABS intensity is summed, thus leading to the term 'Sum-over-States' (SOS) for this approach.

This SOS approach has been widely used to study a number molecules including the ions S_2^- and Se_2^- in ultramarine [1.44], MnO_4^- [1.45], $[Mo_2X_8]^{4-}$ ions (X = Cl or Br) [1.46, 1.47], diruthenium bridged species [1.48] and cytochrome-*c* [1.49]. In most cases, however, only the REP for the fundamental band of the chosen vibrational mode was modelled and compared to the experimentally determined REP. Furthermore, only limited structural change was permitted in

the normal co-ordinate of interest in the excited electronic states, because of the need to simplify the theoretical treatment. Thus, NC coupling was generally ignored, together with mode-mixing and often mode frequency changes. Other studies allowed various combinations of parameters to be non-zero, but often required a zero-temperature approximation so that only the ground vibrational levels of the ground electronic state were initially occupied.

Time-correlator methods, which transform the expressions in sections 1.3 - 1.5 into the time-domain, use other methods of evaluating the overlap between ground and excited state vibrational wavefunctions. These methods were largely developed by Hizhnyakov and Tehver [1.9 - 1.11], and developed and used by Tonk, Page and others [1.12, 1.13, 1.50 - 1.56]. Again, frequently REPs for a mode and/or the relevant resonant ABS profile have been modelled and values for the parameters found. Often only certain combinations of parameter values have been allowed, or attention has been restricted to the fundamental RR band only.

Many of the above methods also utilise the so-called 'transform' method which further exploits the theoretical link between the ABS and RR process. In this method, expressions for RRS are developed which depend explicitly on the expression for the ABS profile, and on the structural parameters. Thus, the experimentally-determined ABS spectrum can be used as input into the calculation of the RR intensities, and computing times can be greatly reduced. This transform method is especially advantageous where there are many active modes in the RR spectrum: the method can focus on, and deliver parameter values for, one mode at a time, with the multimode information remaining implicit in the ABS spectrum.

It is the purpose of this work to focus on two recent theoretical developments: a version of the SOS method (time-independent), and the Overtone Transform method (OT) (time-correlator). Both methods are unusual in that they utilise RR intensity data for a mode in terms of the ratios of successive members of a progression in that mode, rather than using a less accurate REP.

The SOS method applies the basic ideas common to previous SOS applications, but allows full treatment of all possible structural changes along a co-ordinate in the excited electronic state. Furthermore, specific fast recursion relationships are employed to enable fast computing times for modelling calculations. The OT method again allows more structural parameters for a given mode to be taken into account in the treatment of Raman *overtone* bands than has been previously possible with similar methods

It is the aim of this work to outline the development of these two methods, such that their underlying assumptions and approximations may be assessed. In this way, the restrictions on the molecules studied may be found. Furthermore, the methods will be tested by application to normal modes of molecules for which all the assumptions are thought to hold, and for which some previous estimates of excited state structure are available (e.g. values for the frequency of the mode in the excited electronic state, from the ABS band). The experimental demands of the two methods can also be assessed, as can the procedures used in the relevant programs for finding optimum parameter values. In performing these tests on well-known inorganic compounds, it is further hoped that new information about the excited state may be obtained. The molecules chosen are the quadruply bonded dimetallic compounds, and attention is focused along the metal-metal (M-M) co-ordinate. The resonant excited state is the $^1\delta\delta^*$, which is also structurally of interest.

In the next section, the quadruply bonded M-M molecules will be introduced. The M-M co-ordinate and the $^1\delta\delta^*$ excited electronic state, which will serve as both test case and study for the rest of this work, will be described. Detailed account of the two theories, including their incorporation of structural parameters, will be discussed in chapter 2.

1.7 Metal-Metal Quadruply Bonded Compounds

This thesis is concerned with attempts to apply the theories outlined in the previous sections to a low lying excited electronic state of some quadruply bonded M-M compounds, and to consequently gain new insights into the M-M bonding in these species.

The recognition of a quadruple bond between metal atoms first occurred for the ion $[Re_2Cl_8]^{2-}$ in 1964 [1.59]. This compound had been prepared whilst studying preparative routes to the trinuclear cluster $[Re_3Cl_{12}]^{3-}$, which was already known to contain Re-Re double bonds [1.60]. The unusual royal blue compounds of composition $CsReCl_4$ and $KReCl_4.H_2O$ were isolated. At the same time, a number of Soviet authors purported to have found a variety of low oxidation state Re compounds of formulae such as $KHReCl_4$, H_2ReCl_4 [1.61]. In particular, one article reported the formation of an ion of formulation $[Re_2Cl_8]^{4-}$ [1.62] in which the eight Cl atoms were found to constitute a square prism and the Re-Re distance was 2.22 Å by X-ray crystallography. Meanwhile, an X-ray crystallographic study of the compound '$KReCl_4.H_2O$' revealed the presence of an ion of similar structure, shown in Fig. 1.8 [1.63], but in this case, the charge on the anion was found to be -2. It was then discovered that the correct formulation of the '$[Re_2Cl_8]^{4-}$' ion was in fact $[Re_2Cl_8]^{2-}$.

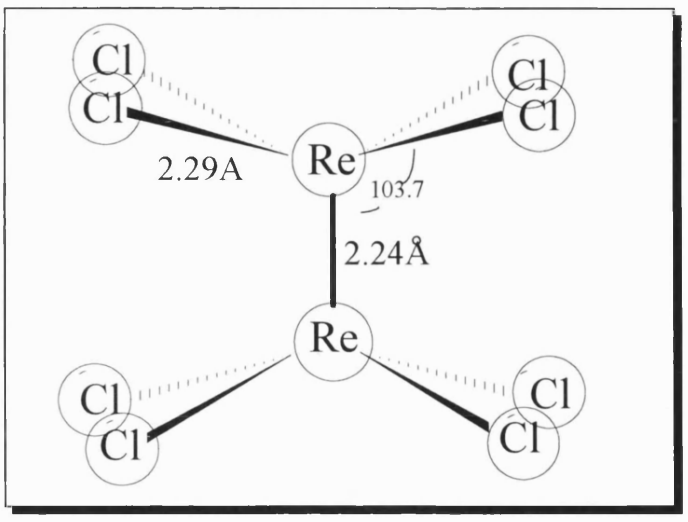

Fig. 1.8 Structure of the ion $[Re_2Cl_8]^{2-}$ as reported in the crystal structure of $K_2Re_2Cl_8.H_2O$

Following extensive studies of the chemistry of this new $[Re_2Cl_8]^{2-}$ ion [1.64], an explanation was proposed by Cotton [1.59, 1.65] for the exceptionally short Re-Re distance and overall structure of the ion, as well as its diamagnetism. This involved the formation of a quadruple M-M bond from the overlap of four of the five metal d orbitals on each metal atom (see below).

Following these reports, much work was carried out both on Re(III) systems [1.66, 1.67] and on similar compounds involving other metal atoms. Early reports of diamagnetic compounds of Mo(II), of composition '$(RCOO)_2Mo$' were later reinterpreted to show the presence of a quadruple Mo-Mo bond, e.g. in $Mo_2(O_2CCH_3)_4$. The chemistry of quadruply bonded dimolybdenum (Mo(II)) species was later extensively developed by Brencic, when the $[Mo_2Cl_8]^{4-}$ ion was prepared [1.68]; later, many compounds of the type $Mo_2X_4L_4$ (L = NMe_2, PR_3 etc.) were recognised [1.39]. These have the general structure depicted in Fig. 1.9.

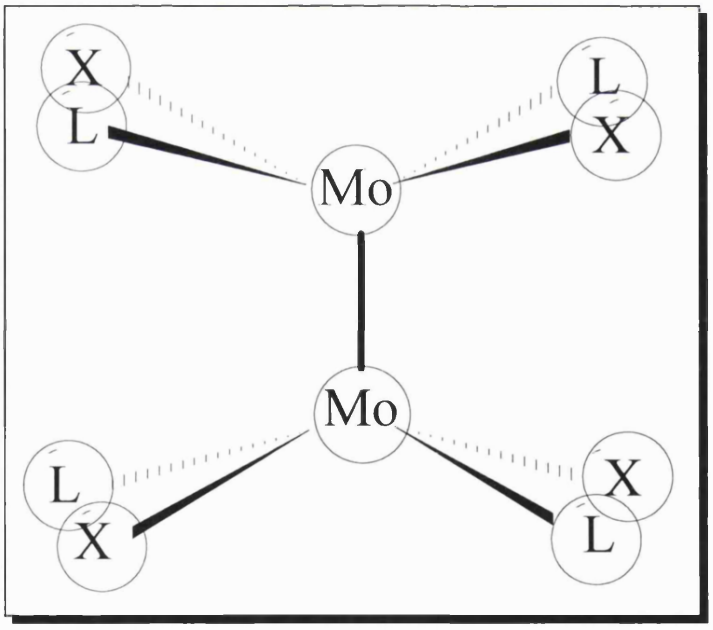

Fig. 1.9 General structure of quadruply bonded compounds of formula $Mo_2X_4L_4$

Around this time, the ion $[Tc_2Cl_8]^{3-}$ [1.70] was also reported, and this was later found to have a very short M-M distance (2.131 Å), even shorter than the corresponding Re-Re distance in $[Re_2Cl_8]^{2-}$.

The Metal-Metal Quadruple Bond

In the bonding picture described by Cotton [1.59], the quadruple M-M bond is formed from the overlap of metal d orbitals as the two metal atoms approach each other. The metal-metal axis is defined as the *z* -axis, and five non-zero overlaps are possible corresponding to d_{z^2} with d_{z^2}, d_{xy} with d_{xy} etc. The overlaps which give rise to the M-M bond are pictured in Fig. 1.10.

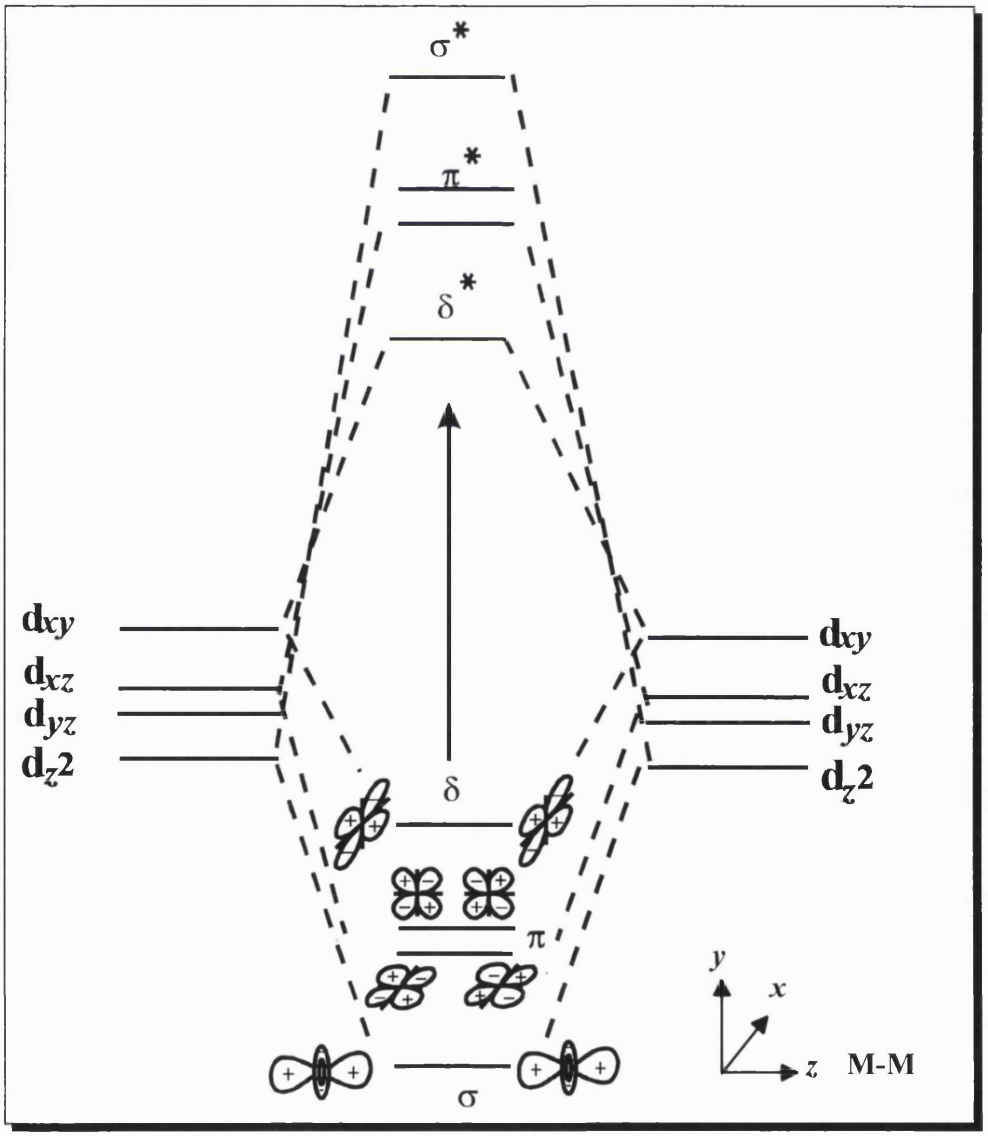

Fig. 1.10 Schematic diagram of the overlap of metal d orbitals which give rise to the M-M quadruple bond.

The overlap of the two d_{z^2} orbitals gives rise to both a σ bonding and σ^* antibonding orbital. The positive overlap of the d_{xz} orbitals on each metal atom gives rise to a π bond, as does the positive overlap of the d_{yz} orbitals, and these two form a degenerate pair. The corresponding π^* orbitals arise form negative overlap of these orbitals.

Finally, the sideways ('face-on') overlap of the d_{xy} orbitals forms the δ and δ^* orbitals. The remaining metal d orbitals, the $d_{x^2-y^2}$ orbitals, can in theory overlap to give M-M bonding orbitals. However, it is likely given their directionality along the M-L bonds that their primary interaction is with the set of four ligands on their own metal atom, thus contributing strongly to M-L bonding.

Thus, the energetic ordering of these M-M bonding orbitals is expected to be $\sigma < \pi < \delta < \delta^* < \pi^* < \sigma^*$, on account of the efficiency of overlap in each case. For compounds of Re(III) or Mo(II), each metal atom has the d^4 configuration and thus there eight electrons to be placed in the M-M bonding orbitals. This corresponds to a configuration of $\sigma^2\pi^4\delta^2$ with only bonding orbitals being filled, and a formal bond order of 4. This qualitative picture was later confirmed as correct by electronic structure calculation [1.71], the details of which will be discussed in chapter 3.

The presence of a δ bond can explain the observed eclipsed arrangement of the ligands in these compounds. The σ bond and pair of π bonds are cylindrically symmetric. However, the efficiency of δ-overlap maximises when the torsion angle, χ, defined in Fig. 1.11, is zero, i.e. when the ligands on the two metals lie in an eclipsed conformation.

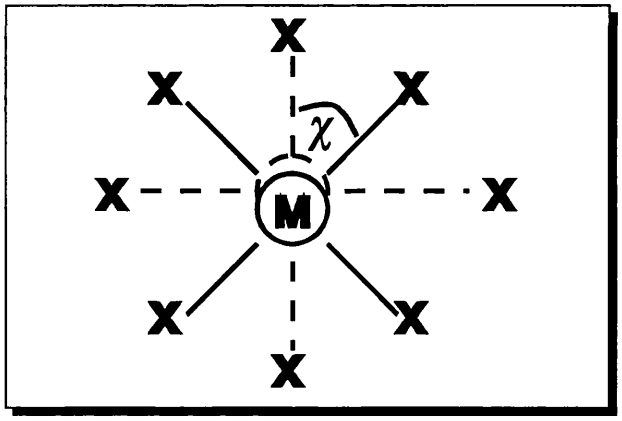

Fig. 1.11 Definition of the torsion angle, χ in metal-metal quadruply bonded systems (shown here for $\chi = 45^0$ in $[M_2X_8]^{n-}$ system).

Any rotation away from this eclipsed conformation will cause a loss of δ bond energy. It has been shown that the δ-overlap depends on cos 2χ [1.72] and that a rotation of 22.5^0 will cause a loss of only 30% of the overlap. In the limit where $\chi = 45^0$, the δ bond disappears and a staggered conformation is adopted. Clearly, repulsions between the ligands on different metal atoms are minimised in the staggered conformation. However, the requirement of an eclipsed structure for effective M-M δ bonding appears to impose frequently a value of 0^0 for χ.

With this picture of the quadruple bond, it is simple to describe M-M bonds of lower bond orders [1.73]. Thus, bond orders of 3.5 and 3.0 can be achieved by the removal of one or two electrons from the δ bonding orbital respectively, giving configurations corresponding to $\sigma^2\pi^4\delta^1$ and $\sigma^2\pi^4$. The addition of one or two electrons to the δ^* orbital also produces bond orders of 3.5 and 3.0 respectively, corresponding to $\sigma^2\pi^4\delta^2(\delta^*)^1$ and $\sigma^2\pi^4\delta^2(\delta^*)^2$. Thus, $[Tc_2Cl_8]^{3-}$ is seen to have a bond order of 3.5, and the configuration $\sigma^2\pi^4\delta^2(\delta^*)^1$, while the ion $[Os_2Cl_8]^{2-}$ has a bond order of 3, and a configuration $\sigma^2\pi^4\delta^2(\delta^*)^2$. Many other examples of compounds with even lower bond orders are seen for later transition metals, and in some cases the ordering of the energy levels is perturbed by interaction with the ligands. Thus, for example, the compounds

$Ru_2(O_2CR)_4$ have configurations $\sigma^2\pi^4\delta^2(\delta^*)^2\pi^2$, while the compounds $Ru_2(RNCHNR)_4$ have the configurations $\sigma^2\pi^4\delta^2(\pi^*)^4$.

The field of M-M quadruply bonded species has grown enormously following the early work and there is now a vast quantity of literature on both these early discovered species and on compounds containing other metals or other types of ligand. In particular, a large number of compounds with bidentate bridging or chelating ligands, such as RCO_2^- have been isolated. The topic is now the subject of a large text book by Cotton, who first proposed the original description of the M-M quadruple bond [1.74].

Other characteristics of M-M quadruple bonds

The vast amount of work published on these compounds has brought to light some characteristic features of multiple metal-metal bonds. In general it has been seen that attempts to correlate formal bond order of the bond with its length have been unsuccessful and that it is necessary to take into account the entire set of intra-ligand bonds and repulsions when considering the molecule. Any change in formal positive charge on the metal atoms, which may accompany a change in formal bond order, must also be considered, since this may affect the overlap of the d orbitals on each metal atom.

Structural studies on a large number of quadruply bonded compounds have revealed a characteristic form of disorder in their crystals. The effect was first discovered in $K_4Mo_2Cl_8.2H_2O$ [1.68], where 93% of the $[Mo_2Cl_8]^{4-}$ ions were seen to have their M-M axis oriented in one direction, while 7% had their M-M axis oriented in a perpendicular direction. A similar effect was seen in $(TBA)_2Re_2Cl_8$ [1.75], with the ratios being 74% and 26%. In some other cases, both of the possible secondary orientations for the M-M axis are occupied, e.g. $(TBA)_2Re_2I_8$ [1.76]. It is thought that the precise ratios of favoured orientations is a result of the positioning of the counter-ions in each case [1.77]. It has also been proposed that an internal flip of the M_2 unit between orientations within the

quasi-cubic cage of ligands is possible, but experimental evidence for such a process remains scarce.

Other studies have focused on the diamagnetic anisotropy of the M-M multiple bonds [1.78] or on estimations of the M-M bond energies from thermochemical [1.79] or spectroscopic [1.80] means. These latter calculations have proven to be problematic, as assumptions regarding M-L bond strengths are frequently required.

It is clear that the branch of inorganic chemistry involving multiply bonded, and in particular quadruply bonded, dimetallic species is now vast. However, despite the simple qualitative picture of the M-M quadruple bond described above, more quantitative insights into the nature of the M-M bonding, and in particular, the δ bond, remain elusive. Generally this is a result of the complexity of these large molecules. In this work, an attempt to gain further insights into the δ bond in complexes of configuration $\sigma^2\pi^4\delta^2$ will be made, by attempting to elucidate structural changes along the M-M axis in the excited state formed by the $^1(\delta^* \leftarrow \delta)$ transition (the $^1\delta\delta^*$ state). Thus, this low-lying state, to which the lowest energy allowed transition from the ground state occurs, will be probed by RR and ABS spectroscopy, and the OT and SOS methods applied to evaluate geometric changes.

The work is focused on a number of simple quadruply bonded compounds: the ions $[Re_2Br_8]^{2-}$, $[Re_2I_8]^{2-}$ and $[Mo_2Cl_8]^{4-}$, and the compounds $Mo_2X_4(PMe_3)_4$ (X = Cl, Br or I), which all have the configuration $\sigma^2\pi^4\delta^2$ in the ground state, and a simple eclipsed structure similar to those in Figs. 1.8 and 1.9. In general, the $[M_2X_8]^{n-}$ ions are seen to be largely separate from the appropriate counter-ions or accompanying water molecules, with only a slight effect of differing counter-ions on the M-M bond length. Further discussion of previous work on the $^1\delta\delta^*$ state of these compounds is reserved for chapters 3 and 4, where the application of the SOS method to the relevant ABS and RR data is reported.

1.8 Plan for Rest of Thesis

The aim of this work is then, as described in the preceding sections, to elucidate structural changes along the M-M co-ordinate of a number of quadruply bonded dimetallic compounds in the $^1\delta\delta^*$ excited electronic state, by application of ABS and RR spectroscopy together with the SOS and OT methods. Furthermore, the methods themselves will be tested by this procedure, and their general applicability assessed on the basis of their inherent assumptions, and on their ability to produce agreement with excited state structural data, where available.

To this end, an outline of the theory behind the SOS and OT methods is described in chapter 2, and the assumptions and restrictions inherent to the methods are highlighted. The types of experimental data required by the methods is also discussed.

Following this, in chapter 3, the application of the SOS method to the $^1\delta\delta^*$ state of the $[M_2X_8]^{n-}$ ions ($[Re_2Br_8]^{2-}$, $[Re_2I_8]^{2-}$ and $[Mo_2Cl_8]^{4-}$) is reported. The suitability of these molecules for study by this method is assessed, and details given of the collection of experimental data and the procedure for finding values for structural parameters of the excited electronic state. The values of these parameters are discussed and, as a result, important insights into the nature of the $^1\delta\delta^*$ state are achieved. Further insights are obtained after a similar application of the SOS method to the $^1\delta\delta^*$ state of the compounds $Mo_2X_4(PMe_3)_4$ (X = Cl, Br or I), which is detailed in chapter 4. Following the elucidation of values for structural parameters of the $^1\delta\delta^*$ state, the trends in these values for all the molecules studied are discussed.

In chapter 5, an attempt to apply the OT method the study the same $^1\delta\delta^*$ state of the $[M_2X_8]^{n-}$ ions is reported. Again, the suitability of these molecules for study is assessed, and a new procedure for finding values for structural parameters using the available calculational program is introduced. The subsequent failure of

the OT method is investigated by investigating the assumptions of the method, the accuracy of the experimental data, and the procedure for finding values for the parameter. General conclusions about the applicability of this method in its current form are then made.

In chapter 6, the unusual temperature dependent behaviour of a compound thought to be $Cs_4Mo_2Br_8$ (containing the $[Mo_2Br_8]^{4-}$ ion) is reported. This compound was initially investigated as a possible subject for study by the SOS method. However, after identification of two very similar species in the sample, one of which shows unusual temperature dependence in its RR spectrum, it was no longer possible to apply these methods to the study of the $^1\delta\delta^*$ excited state. Consequently, a thorough investigation of the sample has been made, with an attempt to identify both species present.

Finally, in Appendices A1 - A5, a discussion of the experimental methods of RR and ABS spectroscopy, together with details of programs used in data manipulation or other calculational procedures is given.

Chapter 2

Theoretical Methods for Studying Excited States

2.1 General and Introduction

Spectroscopic methods which probe an excited electronic state of a molecule produce spectra which contain information about the structure of the molecule in that excited electronic state. As detailed in chapter 1, the resonant electronic absorption band (ABS) and the pattern and intensities of vibrational bands in the RR spectrum reflect structural changes along the vibrational co-ordinates of the molecule in the excited state.

Much of this information remains concealed in the spectra and is not directly observable. Only in high resolution, low temperature single-crystal ABS spectra can information such as vibrational mode wavenumbers in the excited electronic state sometimes be obtained directly. Where such data are not available, it remains difficult to access information regarding the structure of the excited state. For this reason, theoretical methods must be used to link the two

RR and ABS processes in a manner dependent on the structural parameters of the excited electronic state. Comparison of calculated and experimental RR and ABS data will then allow extraction of values for these unknown parameters.

Several theoretical methods have been developed for this purpose. These methods differ in the assumptions and approximations employed in the theory and also in the extent of the structural changes which can be accommodated within the theoretical framework. Many also require comparison with experimental data in different forms.

As discussed in sections 1.1 and 1.6, the methods can be divided into three main types: time-independent, time-correlator and time-dependent methods. All methods develop the molecular polarisability, $[\alpha_{\rho\sigma}(\omega_L)]$, as the central link between the ABS and RR processes.

Time-independent methods e.g. Sum-over-States [2.1-2.4] concentrate on evaluating the overlap integrals between the ground and excited state vibrational wavefunctions (FC factors). In the **Time-correlator** approach [2.5-2.8], the KHD formula is written as a half-Fourier transform in the time-domain and time-dependent vibrational energy operators are then introduced. The **Time-dependent** methods also transform the problem into the time domain and focus on the propagation of the ground state vibrational wavepacket on the potential surface of the excited electronic state [2.9 - 2.11].

This work is concerned with the application of two recently developed methods: the first, the Sum-Over-States (SOS) method, is time-independent, while the second, the Overtone Transform (OT) method uses the time-correlator approach. The methods also differ in their use of the experimental RR and ABS data. The SOS method is a '**pure simulation**' method, in which ABS spectra and RR data for certain vibrational modes are generated for a given set of values of the structural parameters relating to these modes. These values can then be refined after comparison with the equivalent experimental data. By contrast, the

OT method is a **transform** method, in which information on all the modes held in the ABS spectrum is 'read' and 'transformed' to give the RR data for a single mode, without being treated explicitly. Values for the structural parameters are also required to be input to the calculations.

RR data is, in general, utilised in one of two forms. First, the REP of a vibrational mode (plot of intensity of a band due to the mode as a function of the excitation frequency) may be used. If significant structural change occurs along that co-ordinate in the excited state then this REP is often seen to follow pattern of the resonant ABS band.

Alternatively, the relative intensity ratios of members of a progression in the mode, at a given laser excitation frequency, may be used. This type of data, which is easier to obtain with a high standard of accuracy than the REP (Appendix A1) is the preferred choice for this work.

Both methods reviewed in this chapter are based on the KHD expression for the molecular polarisability which is developed in different ways to incorporate the structural parameters of the excited electronic state. The ABS and RRS cross-sections are then given as a function of these parameters.

The KHD expression is found by considering the response of the molecule to the electric field of the incident light via second order perturbation theory. The two methods develop this expression in different ways, employing different assumptions and approximations, to produce final equations relating the ABS and RR band intensities to the unknown structural parameters. The application of the two methods then requiresdifferent forms of the appropriate experimental data.

It is the purpose of this work to review and compare these two methods, to investigate fully any implications of their assumptions and approximations and to assess their performance by application to a number of well-characterised inorganic molecules. To this end, this chapter aims to set out the basic theory

behind the two methods and show how the link to the parameters is made, without any attempt to comment on their development. Greater detail on the theory can be found in the primary references. The assumptions and approximations employed in the methods will, however, be considered in detail in order that and resulting restrictions on the nature of molecules studied by the two methods may be clearly seen. Any practical limitations of application arising from demands on the experimental data will also be discussed, both here and in subsequent chapters.

2.2 The SOS Method: Basic Equations and Assumptions

The SOS method starts with definitions of the rotationally averaged ABS and RRS cross-sections in terms of various components of the molecular polarisability tensor $[\alpha_{\rho\sigma}(\omega)]$. These tensor components are then expanded in the familiar KHD form. Following the introduction of some assumptions and approximations, $[\alpha_{\rho\sigma}(\omega)]$ can be related to multidimensional overlap integrals or Franck-Condon (FC) factors which are dependent on the parameters of the excited electronic state. These FC factors are evaluated using recursion relationships together with a second quantization formalism whereby the normal co-ordinate operators of the excited state are expressed in terms of those of the ground electronic state. Finally, the resonant ABS profile and RR band intensities can be generated and compared to the experimental measurements: parameter values are then refined until a good fit to both is achieved simultaneously.

The rotationally averaged ABS cross-section is given by the optical theorem [2.12] as:

$$\langle\sigma_{ABS}\rangle = \frac{4\pi\alpha}{3}\omega_L \mathrm{Im}[\alpha_{xx} + \alpha_{yy} + \alpha_{zz}]_i \qquad (2.1)$$

where α is the fine structure constant, ω_L is the angular frequency of the incident light, c is the speed of light (in units of cm^{-1}) and Im denotes the imaginary part. The trace parts of the molecular absorption tensor in this case are defined by the resonant part of the KHD formula (see chapter 1):

$$[\alpha_{\rho\rho}(\omega_L)]_{ii} = \sum_l \frac{\langle i|r_\rho|l\rangle\langle l|r_\rho|i\rangle}{\omega_{li} - \omega_L - i\Gamma_l} \tag{2.2}$$

Only the resonant part has been assumed to be significant when ω_L approaches ω_{li}. Here, $|i\rangle$ and $|l\rangle$ are the initial and final molecular states in the absorption process, the angular frequency gap between them being ω_{li}. r_ρ is the ρth element of the dipole operator and Γ_l is a phenomenological lifetime factor of the state l.

The rotationally averaged RRS cross-section, $\langle\sigma_{RR}\rangle$ can be expressed [2.13] in terms of three rotational invariants, Σ^0, Σ^1 and Σ^2 of the molecular polarisability tensor, with the tensor components also defined by the resonant part of the KHD formula as:

$$[\alpha_{\rho\sigma}(\omega_L)]_{fi} = \sum_l \frac{\langle f|r_\rho|l\rangle\langle l|r_\sigma|i\rangle}{\omega_{li} - \omega_L - i\Gamma_l} \tag{2.3}$$

with $|f\rangle$ being the final state in the Raman transition $|f\rangle \leftarrow |i\rangle$. The equations for the rotationally invariants (Σ^0, Σ^1 and Σ^2) are complex and reduce to various different forms for different polarisations of incident light. While it is possible to treat all of these cases via the SOS method, the most common case of application in this work has been to the Raman intensities of totally symmetric vibrational modes, in resonance with a transition between non-degenerate electronic states. The polarisation of the scattered light is scrambled before detection. In this situation, only one diagonal tensor element is dominant, and the RRS cross-section is given by:

$$\langle\sigma_{RR}\rangle = \frac{\alpha^2\omega_L\omega_s^3}{c^4}\left[\left|\alpha_{\rho\rho}(\omega_L)\right|_{fi}^2\right] \tag{2.4}$$

It should be emphasised that the SOS method is not restricted to the treatment of totally symmetric vibrational modes: for brevity, this is the only case detailed here and it remains the only case required for subsequent use of the SOS method in this work. However, the method itself remains generally applicable to Raman transitions involving other symmetries of vibrational modes.

At this point, several assumptions and approximations are introduced in order to simplify the problem of calculating the above cross-sections, and to allow an explicit dependence on the structural parameters of the excited state to be obtained.

The adiabatic Born-Oppenheimer approximation is assumed to be valid for the ground and excited molecular states. Only a single excited electronic state is assumed to be in resonance with the ground state and all states are assumed to be non-degenerate and bound. Thus, the general molecular state $|l\rangle$ can be written as a product of a nuclear ($|v_2\rangle$) and an electronic ($|e\rangle$) part; likewise, the ground molecular states $|i\rangle$ and $|f\rangle$ can be factored as $|g\rangle|v_1\rangle$ and $|g\rangle|v_1 + n\rangle$ respectively, where n is the overall degree of vibrational excitation in the ground electronic state g after the Raman process. Therefore, (2.3) becomes

$$[\alpha_{\rho\rho}(\omega_L)]_{v_1,v_1+n} = \sum_{e,v_2} \frac{\langle v_1+n|\langle g|r_\rho|e\rangle|v_2\rangle\langle v_2|\langle e|r_\rho|g\rangle|v_1\rangle}{\omega_{eg} + \omega_{v_2v_1} - \omega_L - i\Gamma_{e,v_2}} \quad (2.5)$$

where ω_{eg} and $\omega_{v_2v_1}$ are the electronic and vibrational frequency differences respectively, and the dipole operator operates on the electronic co-ordinates only.

For a molecule with N vibrational degrees of freedom, the states $|v_1\rangle$ and $|v_1 + n\rangle$ represent the N dimensional states

$$|v_1\rangle = |(v_1)_1, (v_1)_2 \ldots\ldots\ldots (v_1)_N\rangle \quad (2.6)$$

and

$$|v_1+n\rangle = |(v_1+n)_1,(v_1+n)_2.....(v_1+n)_N\rangle \qquad (2.7)$$

respectively, where n is the degree of excitation of the molecule in any given mode after the Raman process.

Taking account of the real nature of the electronic transition moment $(M_\rho)_{ge} = < g|\ r_\rho|\ e >$, and assuming at present that this transition moment is independent of the nuclear co-ordinates (the Condon approximation), then (2.5) can be rewritten as:

$$[\alpha_{\rho\rho}(\omega_L)] = \sum_e \alpha_{\rho\rho}\{(v_1+n), v_1, e;\ \omega_L\} \qquad (2.8)$$

where

$$\alpha_{\rho\rho}\{(v_1+n), v_1, e; \omega_L\} = \sum_{v_2} \frac{\langle v_2|(M_\rho^0)_{ge}|v_1+n\rangle\langle v_2|(M_\rho^0)_{ge}|v_1\rangle}{\omega_{eg}+\omega_{v_2v_1}-\omega_L-i\Gamma_{ev_2}} \qquad (2.9)$$

and where $(M_\rho)^0_{ge}$ denotes the Condon approximation for the transition moment (equivalent to Albrecht's A-term [2.1]). NC coupling, or the dependence of the electronic transition moment, $(M_\rho)_{ge}$ on the nuclear co-ordinates will be treated in detail in the next section.

At this stage it can be seen that the FC factors such as $\langle v_2|(M_\rho^0)_{ge}|v_1+n\rangle$ must be evaluated and that NC coupling must be formally introduced in the electronic transition moments in these matrix elements. The first step in this process is to derive general recursion relationships for FC factors in terms of the excited state parameters. Following this, NC coupling can be introduced.

For simplicity, the derivation of generalised recursion relationships for multidimensional FC factors

$$\langle s|(M_\rho^0)_{ge}|t\rangle$$

will be given, where | s > and | t> are taken to be vibrational states of the excited and ground electronic states respectively. Since, in the Condon limit, $(M_\rho)^0_{ge}$ is a constant the matrix elements become

$$(M_\rho)^0_{ge}\langle s|t\rangle$$

In order to find recursion relationships for these <s | t > factors, the vibrational Hamiltonians of the ground and excited electronic states are written within the harmonic approximation as:

$$H_g = \frac{\hbar}{2}(P^T.\omega_g.P + Q^T.\omega_g.Q) \qquad (2.10a)$$

and

$$H_e = \frac{\hbar}{2}(P_e^T.\omega_e.P_e + Q_e^T.\omega_e.Q_e) + \omega_{eg} \qquad (2.10b)$$

respectively. Here, P and Q are column vectors representing the dimensionless momentum and co-ordinate operators respectively, ω_g and ω_e are diagonal matrices consisting of the normal mode angular frequencies for electronic states g and e, and ω_{eg} is the electronic frequency difference between the two states. T denotes transposition.

The dimensionless momentum and co-ordinate operators of the ground and excited electronic states are taken to be related by:

$$P_e = (R^{-1})^{\mathrm{T}}.P \qquad (2.11a)$$

and

$$Q_e = R.(Q - \Delta) \qquad (2.11b)$$

where R is the matrix describes both mode frequency changes, if applicable and Duschinsky rotation (mode mixing) between the co-ordinates of the two electronic states. Δ is the dimensionless displacement parameter. Thus, R is

dependent on ω_e, and ω_g, the angular mode frequencies for a given mode in the states *e* and *g* respectively and will not reduce to the identity matrix in the absence of mode mixing.

In order to continue to evaluate the multidimensional FC factors, relationships between the normal co-ordinates of the ground and excited electronic states and between the annihilation and creation operators of the two states are sought.

Two column vectors are defined:

$$a = (2)^{-\frac{1}{2}}(Q + \mathrm{i}P) \tag{2.12a}$$

and

$$b = (2)^{-\frac{1}{2}}(Q_e + \mathrm{i}P_e) \tag{2.12b}$$

where the *i*th component of *a* and *b* are the step-down operators of the *i*th mode of the ground and excited states respectively. The equivalent creation operators, $a^\dagger$ and $b^\dagger$, are the usual Hermitian conjugates of the components of *a* and *b*.

Using equations (2.11) and (2.12), relationships which relate (a, $a^\dagger$) and (b, $b^\dagger$) can be found:

$$\mathrm{i}(b^\dagger - b) = \mathrm{i}R^{-1}(a^\dagger - a) \tag{2.13}$$

and

$$(b^\dagger + b) = R(a^\dagger + a - \sqrt{2}\,\Delta) \tag{2.14}$$

where the $\sqrt{2}$ factor has been included to facilitate further calculation. Solving these for $b^\dagger$ gives:

$$b^\dagger = L_+ \,.\, a^\dagger + L_- \,.\, a - l_0 \tag{2.15}$$

and solving for b gives:

$$b = L_- . a^\dagger + L_+ . a - l_0 \tag{2.16}$$

where the matrices $L_\pm$ are defined by:

$$L_\pm = \tfrac{1}{2}(R \pm (R^{-1})^T) \tag{2.17}$$

and the vector l_0 is given by:

$$l_0 = 2^{-\frac{1}{2}} R.\Delta \tag{2.18}$$

Eliminating $a^\dagger$ from (2.15) and (2.16) gives:

$$b = D_1.b^\dagger + D_2.a + D_3.l_0 \tag{2.19}$$

where the D matrices are given by

$$D_1 = L_- . L_+^{-1} \tag{2.20}$$

$$D_2 = L_+ - (L_- . L_+^{-1} . L_-) \tag{2.21}$$

$$D_3 = (L_- . L_+^{-1}) - I \tag{2.22}$$

Hence, looking now at an FC factor of the type:

$$(s_k + 1)^{\frac{1}{2}} \langle s_1, s_2 ..... s_{k+1} .. s_N | t_1, t_2 ..... t_N \rangle \tag{2.23}$$

Since $\langle j | b = (j+1)^{\frac{1}{2}} \langle j+1 |$ then (2.23) is equal to

$$\langle s_1, s_2 \ldots\ldots s_k \ldots s_N | b_k | t_1, t_2 \ldots\ldots t_N \rangle \tag{2.24}$$

and from (2.19)

$$b_k = \sum_{j=1}^{N} (D_1)_{kj} b_j^{\dagger} + \sum_{j=1}^{N} (D_2)_{kj} a_j + \{D_3 . l_0\}_k \tag{2.25}$$

Substituting (2.25) into (2.24), the FC matrix becomes

$$(s_k + 1)^{\frac{1}{2}} \langle s_1, s_2 \ldots . s_{k+1} \ldots s_N | \; t_1, t_2 \ldots\ldots t_N \rangle =$$

$$\sum_{j=1}^{N} \{D_1\}_{kj} (s_j)^{\frac{1}{2}} \langle s_1 \ldots . s_{j-1} \ldots s_N | t_j \ldots . t_N \rangle$$

$$+ \sum_{j=1}^{N} \{D_2\}_{kj} (t_j)^{\frac{1}{2}} \langle s_1 \ldots\ldots s_N | t_1 \ldots\ldots t_{j-1} \ldots\ldots t_N \rangle$$

$$+ \{D_3 . l_0\}_k \langle s_1 \ldots . s_N | t_1 \ldots . t_N \rangle \tag{2.26}$$

A similar procedure, eliminating b from (2.13) and (2.14) [2.14], allows a definition of the $a^{\dagger}$ operator in terms of D matrices which are also combinations of the $L_{\pm}$ matrices, and since $a^{\dagger}$ acts to the right on only ground state vibrational functions, FC factors of the kind:

$$(t_{k+1})^{\frac{1}{2}} \langle s_1 \ldots s_N | t_1 \ldots t_{k+1} \ldots . t_N \rangle \tag{2.27}$$

can be expressed as:

$$(t_{k+1})^{\frac{1}{2}} \langle s_1 \ldots s_N | t_1 \ldots t_{k+1} \ldots t_N \rangle =$$

$$\sum_{j=1}^{N} \{D_4\}_{kj} (s_j)^{\frac{1}{2}} \langle s_1 \ldots s_{j-1} \ldots s_N | t_1 \ldots t_N \rangle$$

$$+ \sum_{j=1}^{N} \{D_5\}_{kj} (t_j)^{\frac{1}{2}} \langle s_1 \ldots s_N | t_1 \ldots t_{j-1} \ldots, t_N \rangle$$

$$+ \{D_6 . l_0\}_k \langle s_1 \ldots s_N | t_1 \ldots t_N \rangle \tag{2.28}$$

where the D matrices are given by:

$$D_4 = L_+^T \tag{2.29}$$

$$D_5 = -L_+^{-1} \,.\, L_- \tag{2.30}$$

$$D_6 = L_+^{-1} \tag{2.31}$$

From the above recursion relationships, presented here only in outline, it is possible to calculate any vibrational occupation number configuration of $\langle s_1 \ldots s_N | t_1 \ldots t_N \rangle$ by relating them back to the $\langle 0_1 \ldots 0_N | 0_1 \ldots 0_N \rangle$ matrix element which is known to have the analytical form [2.15]:

$$\langle 0_1 \ldots 0_N | 0_1 \ldots 0_N \rangle = \det[R^T.R]^{\frac{1}{4}} \det[\mathrm{M}]^{-\frac{1}{2}} \exp[-\tfrac{1}{2}\Delta^T.R^T.R.\Delta] \times \exp[\tfrac{1}{4} v^T.\mathrm{M}^{-1}.v] \tag{2.32}$$

where the matrix M is given by:

$$\mathrm{M} = (1/2)\,(R^T.\,R + I) \tag{2.33}$$

and the vector v is given by:

$$v = R^T.R.\Delta \tag{2.34}$$

Thus, at this point it can be seen that FC factors for the Condon case can be computed from the multidimensional recursion relationships for evaluating matrix elements such as $\langle s_1 \ldots s_N | t_1 \ldots t_N \rangle$. Furthermore, these recursion relationships have produced an explicit dependence on the parameters of the excited electronic state (ω_e (through R), Δ etc.). It then remains only to consider NC coupling to allow

NC FC-factors to be calculated, and hence the $\alpha_{\rho\sigma}$ tensor elements, which lead to the RRS and ABS cross-sections, to be computed.

2.3 The SOS method: NC Coupling and Final Equations

NC coupling is included to take account of the dependence of the electronic transition moment, $(M_\rho)_{ge}$ on the nuclear co-ordinates. In this study, only linear NC coupling is included (giving rise to a term equivalent to Albrecht's B-term [2.1]). The transition moment is assumed to be real and linearly dependent on the dimensionless co-ordinate. Thus, in one dimension:

$$(M_\rho)_{ge}(Q_g) = (M_\rho)^0_{ge}(1 + 2^{\frac{1}{2}} m Q_g) \tag{2.35}$$

where m denotes a linear NC coupling factor. From (2.12), and the equivalent expression for $a^\dagger$, Q_g can be written as:

$$Q_g = 2^{-\frac{1}{2}}(a^\dagger + a) \tag{2.36}$$

and thus:

$$(M_\rho)_{ge}(Q_g) = (M^0_\rho)_{ge}(1 + m(a^\dagger + a)) \tag{2.37}$$

Expanding this treatment to include the N vibrational dimensions of the molecule, the transition dipole moment can be described by a Taylor series to first order. Thus, denoting $(M_\rho)_{ge}$ as M for simplicity,

$$M(Q_g) = (M(0) + \sum_i \left(\frac{\partial M(Q)}{\partial Q_i}\right)_{Q_i = 0} Q_i \tag{2.38}$$

where the i indicates the i^{th} co-ordinate. This is applicable to both totally and non-totally symmetric modes.

This expression for M can be substituted into the FC factors $\langle s_1 \ldots s_N | M | t_1 \ldots t_N \rangle$ and thus these NC FC-factors can be related to the Condon FC-factors $M^0 \langle s_1 \ldots s_N | t_1 \ldots t_N \rangle$ for which recursion relationships have already been developed. This lengthy relationship will not be detailed here [see 2.14]: it is subsequently used via substitution in the matrix elements in (2.9) to relate the NC polarisability tensor, α^{NC} of the eth electronic state to the equivalent Condon tensor, α^{C}. This in turn is derived from (2.9) using the Condon FC-factors and the recursion relationships found previously. Thus, denoting

$$\alpha^{C}\{(v_1+n), v_1; \omega_L\} = \sum_{v_2} \frac{\langle v_2 | M^0 | v_1 + n \rangle \langle v_2 | M^0 | v_1 \rangle}{\omega_{eg} + \omega_{v_1 v_2} - \omega_L - i\Gamma} \qquad (2.39)$$

where the polarisation indices have been dropped for simplification, and writing $v_1 = v$ and $(v_1 + n) = V$, the final relationship can be found as:

$$\begin{aligned}
\alpha^{NC}\{V, v; \omega_L\} = {} & \alpha^{C}(V, v; \tilde{\omega}_L) \quad + \\
& + \sum_k m_k^1 \{ v_k^{\frac{1}{2}} \alpha^{C}(V, (v_k - 1); \tilde{\omega}_L = \omega_L + \omega_k \\
& \quad + (v_k + 1)^{\frac{1}{2}} \alpha^{C}(V, (v_k + 1); \tilde{\omega}_L = \omega_L - \omega_k) \\
& \quad + (V_k^{\frac{1}{2}} \alpha^{C}((V_k - 1), v; \tilde{\omega}_L = \omega_L) \\
& \quad + (V_k + 1)^{\frac{1}{2}} \alpha^{C}((V_k + 1), v; \tilde{\omega}_L = \omega_L)\} \\
& + \sum_{j,k} m_j^1 m_k^1 \{ V_k^{\frac{1}{2}} v_k^{\frac{1}{2}} \alpha^{C}(v_j - 1, v_k - 1; \tilde{\omega}_L = \omega_L + \omega_k) \\
& \quad + (V_j + 1)^{\frac{1}{2}} v_k^{\frac{1}{2}} \alpha^{C}(V_j + 1, v_k - 1; \tilde{\omega}_L = \omega_L + \omega_k) \\
& \quad + V_j^{\frac{1}{2}} (v_k + 1)^{\frac{1}{2}} \alpha^{C}(V_j - 1, v_k + 1; \tilde{\omega}_L = \omega_L - \omega_k) \\
& + (V_j + 1)^{\frac{1}{2}} (v_k + 1)^{\frac{1}{2}} \alpha^{C}(V_j + 1, v_k + 1; \tilde{\omega}_L = \omega_L - \omega_k)\}
\end{aligned} \qquad (2.40)$$

where $\tilde{\omega}_L$ is a shifted laser frequency and only linear NC terms have been included for brevity. Only vibrational occupation numbers which are changed relative to those of α^{NC} are given explicitly.

Thus a relationship is finally obtained between the NC polarisability α^{NC} and the Condon polarisability, α^{C}, which can be computed form the recursion relationships developed earlier. These recursion relationships provide the dependence on the parameters of the excited electronic state. Finally, the ABS and RRS cross-sections can be computed from the α^{NC} via (2.1) and (2.3).

Before comparison of calculated and experimental data, however, account must be taken of ensemble effects in the sample. The scatterers are assumed to be independent of each other during the optical process and only thermal and inhomogeneous broadening effects are taken into account. Thermal effects are dealt with by a Boltzmann distribution of initial states such that the ABS and RRS cross-sections become:

$$\frac{1}{W}\sum_i \exp\left[-\frac{\hbar\omega_i}{kT}\right]\langle\sigma_{ABS}\rangle \tag{2.41}$$

and

$$\frac{1}{W}\sum_i \exp\left[-\frac{\hbar\omega_i}{kT}\right]\left\langle\frac{d\sigma}{d\omega d\Omega}\right\rangle \tag{2.42}$$

respectively, where W is the partition function. In the condensed phase (solution), local perturbations alter both the energies and states of the molecule, hence altering the scattering tensor. The energy perturbation is the more important on resonance, and so the spectra are effectively 'folded' along the frequency axis with a particular distribution $P(\omega)$ giving:

$$\frac{\int_0^\infty d\omega P(\omega)\langle\sigma_{ABS}\rangle}{\int_0^\infty d\omega P(\omega)} \tag{2.43a}$$

and

$$\frac{\int_0^\infty d\omega P(\omega)\langle\sigma_{RR}\rangle}{\int_0^\infty d\omega P(\omega)} \tag{2.43b}$$

where ω is conveniently taken to be ω_{eg}, the electronic transition frequency. In most cases of inhomogeneous broadening, $P(\omega)$ is taken to be a Gaussian lineshape with spread s:

$$P(\omega) = \frac{1}{\sqrt{(2\pi s^2)}} \exp\left[\frac{(\omega - \omega_{eg})^2}{2s^2}\right] \tag{2.44}$$

and s can be fitted as a parameter.

From the above theory, the multidimensional ABS and RRS cross-sections can be calculated in terms of a number of parameters of the excited electronic state. The treatment is general and does not necessarily focus on one vibrational mode at a time, although this is usually the case in practice as often only one vibrational mode shows RR enhancement in resonance with a given electronic ABS band.

Starting from estimates of the values of the parameters for this co-ordinate (ω_e (or $\tilde{\nu}_e$), Δ, m, R) and for any other co-ordinate if necessary, relative RR cross-sections (i.e. relative intensities for members of the mode progression at a given excitation frequency) can be calculated. Values of ω_{eg} and Γ are also required, the latter being treated as a parameter. Values for parameters such as these are often given in units of cm^{-1}, but are converted to angular frequency units for the purpose of calculations. In general, it is assumed that a sufficient number of states, v_2, have been included in the summing procedure if convergence in the calculated values of the RRS cross-sections has been reached. Using the same

parameter values, the ABS profile can be calculated, scaled (normalised) and compared to the experimental ABS. Comparison between the experimental and calculated data is visual and refinement of the parameter values is continued until the best **simultaneous** fit to both types of data is achieved.

2.3 The SOS Method: Review of Assumptions and Approximations

In the previous two sections, an overview of the theory behind the SOS method was presented and the procedure for calculating the excited state structural parameter outlined. However, within the theory, several assumptions and approximations are used. The implications of these for the nature of the molecule to be studied must be assessed.

The full adiabatic B-O approximation is assumed to be valid for both the ground and excited states. Only a single excited electronic state is considered - if more than one electronic state is in resonance with the ground state, then the total polarisability is a sum of the contributions from both states. Thus cross-terms will appear in the RRS expression, and these are usually avoided by assuming a single resonant excited state. The B-O approximation means that there must be no non-adiabatic couplings in the excited electronic state. Thus, Jahn-Teller couplings, spin-orbit coupling or degeneracies must all be absent. The excited electronic state must also be bound.

The other major approximation of the SOS method is the harmonic approximation: - the normal co-ordinates of both the ground and excited electronic states cannot be highly anharmonic. However, non-zero temperatures, mode-mixing and any magnitude of change in the wavenumber of a mode in the excited state are all tolerated by the SOS method. Furthermore, it is possible to obtain simultaneously values for structural parameters for more than one vibrational mode, should they show intensity enhancement in the RR spectrum.

Finally, it should be noted that the initial assumption of a sample of randomly oriented molecules precludes the use of single-crystal RR and ABS data.

2.5 The OT Method: Basic Equations and Assumptions

As in the previous case of the SOS method, the OT theory starts with initial definitions of the ABS and RRS cross-sections in terms of the molecular polarisability, $[\alpha_{\rho\sigma}(\omega)]$. However, in this case, the half-Fourier transform of the KHD expression for $[\alpha_{\rho\sigma}(\omega)]$ is taken and RR and ABS correlators defined in the time domain. These are related to the excited state parameters via operator algebra and the Manneback equations for calculating overlap integrals (FC factors). Finally, a transform between the ABS and RR correlators is obtained.

The sample is assumed to consist of randomly oriented molecules. The Raman scattering occurs from an initial eigenstate *i* to a final molecular eigenstate, *f*, upon excitation with laser frequency ω_L. Under these conditions, with the light scattered in all polarisations over 4π steradians, the RRS cross-section per molecule is [2.1]:

$$\langle\sigma_{RR}\rangle = \frac{8\pi(\omega_L - \omega_{fi})^4}{9c^2\hbar^2} \sum_{\rho,\sigma} \left| [\alpha_{\rho\sigma}(\omega_L)]_{fi} \right|^2 \qquad (2.45)$$

in which $[\alpha_{\rho\sigma}(\omega_L)]_{fi}$ is the *f,i*th matrix element of the molecule based $\rho\sigma$th Cartesian tensor element of the molecular polarisability, and ω_{fi} is the angular frequency of the transition. This definition differs from that used in the SOS method in the nature of the terms preceding the molecular polarisability. These differences arise from different unit systems but will not affect any comparison with relative intensity ratios.

At the same time, the general expression for the linear absorption (ABS) cross-section, $\sigma_{ABS}(\omega_L)$ from the *i*th molecular level is found from the optical theorem [2.12] as:

$$\sigma_{ABS}(\omega_L) = \frac{4\pi\omega_L}{3} \sum_{\rho} \mathrm{Im}[\alpha_{\rho\rho}(\omega_L)]_{ii} \qquad (2.46)$$

Again, some prefactors in this definition differ from those in the SOS definition, due to different unit systems. However, unless absolute cross-sections are sought (normalised spectra being used in all cases here) then these differences will be inconsequential. In general, and on resonance with an electronic transition, $[\alpha_{\rho\sigma}(\omega_L)]_{fi}$ is given by the resonant part of the KHD formula (eqn. (1.4)):

$$[\alpha_{\rho\sigma}(\omega_L)]_{fi} = \sum_{l} \frac{\langle f|r_\rho|l\rangle\langle l|r_\sigma|i\rangle}{\omega_{li} - \omega_L - i\Gamma_l} \qquad (2.47)$$

where the sum is over all molecular eigenstates and Γ_l represents a damping factor. For the ABS cross-section, $[\alpha_{\rho\rho}(\omega_L)]_{ii}$ is given by (2.47) with $f = i$ and $\rho = \sigma$.

The first step in the development of (2.47) is then to take the half-Fourier transform of the complex denominator and write $[\alpha_{\rho\sigma}(\omega_L)]_{fi}$ in the time domain. Thus, making use of the integral:

$$i\int_0^\infty d\tau\, e^{i\tau\omega_L} e^{-i\tau(\omega_{li} - i\Gamma_l)} = \frac{1}{\omega_{li} - \omega_L - i\Gamma_l} \qquad (2.48)$$

then $[\alpha_{\rho\sigma}(\omega_L)]_{fi}$ can be written as:

$$[\alpha_{\rho\sigma}(\omega_L)]_{fi} = i\int_0^\infty d\tau\, e^{i\tau\omega_L} \sum_{l} e^{-i\tau(\omega_{li} - i\Gamma_l)} \langle f|r_\rho|l\rangle\langle l|r_\sigma|i\rangle \qquad (2.49)$$

The sum on l can be closed after introduction of a non-Hermitian Hamiltonian, H, which consists of a full molecular Hamiltonian and a damping operator. Thus, if $\langle l | H^{\dagger} = \langle l | (\omega_l + i\Gamma_l)$ and $H | i \rangle = \omega_i | i \rangle$ then (2.49) reads

$$[\alpha_{\rho\sigma}(\omega_L)]_{fi} = i\int_0^{\infty} d\tau \, e^{i\tau\omega_L} \langle f | \rho e^{-i\tau H^{\dagger}} \sigma e^{i\tau H} | i \rangle \qquad (2.50)$$

where ρ now denotes r_ρ, the ρth element of the dipole operator, r. The above equation can be written as the Fourier transform of a time-correlator, $[A_{\rho\sigma}]_{fi}$ for the transition from i to f:

$$[\alpha_{\rho\sigma}(\omega_L)]_{fi} = \int_{-\infty}^{\infty} d\tau \, e^{i\tau\omega_L} [A_{\rho\sigma}]_{fi} \qquad (2.51)$$

where

$$[A_{\rho\sigma}]_{fi} = i\theta(\tau) \langle f | \rho e^{-i\tau H^{\dagger}} \sigma e^{i\tau H} | i \rangle \qquad (2.52)$$

where $\theta(\tau)$ is the Heaviside step function.

The OT method allows treatment of one single vibrational normal co-ordinate at a time. In essence, attention is focused on the normal mode (or co-ordinate) which is enhanced in the RR spectrum. Structural changes can be calculated for this co-ordinate after comparison of calculated and experimental RR data regarding this mode, and of the calculated and experimental multimode ABS spectrum. Thus, the multimode nature of the molecule is retained implicitly in the ABS spectrum.

The B-O approximation is introduced only in the normal co-ordinate of the chosen vibration. This 'limited adiabatic' approach allows considerable generality in the 'non-Raman' subspace of modes - i.e. it is possible to focus on a transition and resonance enhancement in a given vibrational mode without

considering explicitly the other N-1 vibrational modes (for a molecule with N degrees of vibrational freedom). Thus, variable damping parameters and non-adiabatic effects involving these co-ordinates are possible. However, Duschinsky rotation, or mode-mixing, between the Raman mode and the (N -1) remaining modes is then strictly forbidden.

Thus, focusing on one vibrational co-ordinate only, the harmonic approximation is invoked in both the ground and excited electronic states, with vibrational Hamiltonians H_1 and H_2 respectively:

$$H_1 = T_1 + V_1 = \omega_g(a_1^\dagger a_1 + \tfrac{1}{2}) \tag{2.53a}$$

$$H_2 = T_2 + V_2 = \omega_e(a_2^\dagger a_2 + \tfrac{1}{2}) \tag{2.53b}$$

in which the $a_i^\dagger$ and a_i are the usual creation and annihilation operators and the eigenkets are $|v_1\rangle$ and $|v_2\rangle$ respectively. ω_g and ω_e are the angular frequencies of the chosen mode in the ground and excited electronic states respectively.

For the nth overtone transition of the mode in the ground state then:

$$|i\rangle = |g\rangle|v_1\rangle \tag{2.54a}$$

$$|f\rangle = |g\rangle|v_1 + n\rangle \tag{2.54b}$$

and likewise for the resonant excited electronic state

$$|l\rangle = |e\rangle|v_2\rangle \tag{2.54c}$$

where, for (2.54a) and (2.54c), the partitioning of the molecular Hamiltonian is recognised:

$$H \rightarrow H_g + H_1 \quad \text{with} \quad H_g|g\rangle = \omega_g|g\rangle \tag{2.55a}$$

$$H \rightarrow H_e + H_2 \quad \text{with} \quad H_e|e\rangle = \omega_e|e\rangle \tag{2.55b}$$

in which H_g and H_e are not just the electronic Hamiltonians evaluated at the ground and excited state equilibrium positions of the Raman mode, but also include the N-1 non-Raman space. The sum over molecular eigenstates then also recognises the factoring of state space:

$$\sum_{l} \rightarrow \sum_{e} \sum_{v_2} \tag{2.56a}$$

and likewise

$$\Gamma_l \rightarrow \Gamma_e + \Gamma_v \tag{2.56b}$$

where the Γ_v denotes the average damping factor over all vibrational levels of the excited electronic state. This will henceforth be denoted Γ and will be assumed to represent damping from the Raman subspace only, and to be constant for all v_2.

Finally, the RRS cross-section is partitioned:

$$\langle \sigma_{RR} \rangle_{fi} = \langle \sigma_{RR} \rangle_{(v_1+n),v_1} \tag{2.56c}$$

Within these approximations and with these assumptions, the sum over v_2 in (2.49) can be closed. While the sum over e remains, it is usually assumed that only a single excited electronic state is in resonance with the ground electronic state, thus avoiding cross terms in the final RRS cross-section.

Thus:

$$[\alpha_{\rho\sigma}(\omega_L)]_{g(v_1+n),\, gv_1} = i\int_0^\infty d\tau\, e^{i\tau\omega_L} e^{-\tau\Gamma} \sum_e \{ e^{-i\tau(\omega_{eg} - i\Gamma_e)} \times$$

$$\langle v_1 + n | (M_\rho)_{ge} e^{-i\tau H_2} (M_\sigma)_{eg} e^{i\tau H_1} | v_1 \rangle \} \tag{2.57}$$

where

$$(M_\rho)_{ge} = \langle g|\rho|e\rangle \text{ and } (M_\sigma)_{eg} = \langle e|\sigma|g\rangle \tag{2.58}$$

Thus, relating back to the Raman correlator we obtain:

$$[\alpha_{\rho\sigma}(\omega_L)]_{v_1+n,\,v_1} = \int_{-\infty}^{\infty} d\tau\, e^{i\tau\omega_L}[A_{\rho\sigma}(\tau)]_{v_1+n,\,v_1} \tag{2.59}$$

where $[A_{\rho\sigma}(\tau)]_{v_1+n,\,v_1}$ is now given by:

$$[A_{\rho\sigma}(\tau)]_{v_1+n,\,v_1} = i\theta(\tau)e^{-\Gamma\tau}\sum_e e^{-i\tau(\omega_{eg}-i\Gamma_e)}\times$$

$$\langle v_1+n|(M_\rho)_{ge}e^{-i\tau H_2}(M_\sigma)_{eg}e^{i\tau H_1}|v_1\rangle \tag{2.60}$$

Returning to (2.46) for the ABS cross-section, the same treatment and approximations give:

$$\langle\sigma_{ABS}(\omega_L)\rangle_{v_1v_1} = \frac{4\pi\omega_L}{3}\sum_\rho \mathrm{Im}[\alpha_{\rho\rho}(\omega_L)]_{v_1,v_1} \tag{2.61}$$

in the limited adiabatic approximation, where:

$$[\alpha_{\rho\rho}(\omega_L)]_{v_1,v_1} = \int_{-\infty}^{\infty} d\tau\, e^{i\tau\omega_L}[A_{\rho\rho}(\tau)]_{v_1,v_1} \tag{2.62}$$

and the ABS correlator is given by:

$$[A_{\rho\rho}(\tau)]_{v_1,v_1} = i\theta(\tau)e^{-\Gamma\tau}\sum_e e^{-i\tau(\omega_{eg}-i\Gamma_e)}\langle v_1|(M_\rho)_{ge}e^{-i\tau H_2}(M_\rho)_{eg}e^{i\tau H_1}|v_1\rangle \tag{2.63}$$

This can be seen to be just the diagonal (v_1, v_1) matrix element of the ρρth Cartesian tensor component of the vibronic absorption correlator. The task is then to relate this to the off-diagonal (v_1+n, v_1) correlator in (2.60).

Before preceding further, account is taken of the ensemble averaging over all initial states, recognising both the thermal distribution of molecules as well as possible site inhomogeneity leading to a distribution of the ω_{eg} values. This problem will not be treated explicitly here, but is detailed in ref [2.7].

2.6 The OT Method: Excited State Parameters and Transform Equations

The task is then to link the nth order RR correlator to the ABS correlator and to introduce NC coupling and an explicit dependence on the remaining excited state structural parameters (ω_e and Δ) for the mode of interest.

Non-Condon coupling is introduced only in the Raman active mode; only linear terms are considered. Thus:

$$(M_\rho)_{ge} = (M_\rho)^0_{ge}[1 + m(a + a^\dagger)] \qquad (2.64)$$

where m is the linear NC coupling parameter, and $a^\dagger$ and a are the raising and lowering operators of the ground state harmonic potential in the Raman active mode. $(M_\rho)^0_{ge}$ continues to contain implicitly all the N-1 nuclear co-ordinates in an unconstrained Condon and NC role.

At this stage, attention is restricted to totally symmetric vibrational modes only, and, since only non-degenerate electronic states are being considered, only one diagonal component of the polarisability tensor will be dominant. Thus, ρ =

σ, and all polarisation indices are dropped. In order to simplify notation, the following abbreviations are introduced:

$$M = [1 + m(a + a^{\dagger})],\ B \equiv e^{-i\tau H_2},\ C \equiv e^{i\tau H_1} \tag{2.65}$$

and thus:

$$\langle v_1 + n|(M)_{ge}\, e^{-i\tau H_2}(M)_{eg}\, e^{i\tau H_1}|v_1\rangle = \left|(M)^0_{ge}\right|^2 \langle v_1 + n|MBMC|v_1\rangle \tag{2.66}$$

From equation (2.60), the *n*th order RR correlator now becomes:

$$A_n^{NC}(\tau) = i\theta(\tau)e^{-\Gamma\tau}\sum_e e^{-i\tau(\omega_{eg} - i\Gamma_e)}\left|(M)^0_{ge}\right|^2 \langle v_1 + n|MBMC|v_1\rangle \tag{2.67}$$

in which $[A_{\rho\rho}(\tau)]_{v_1+n,\, v_1}$ now equates to $A_n^{NC}(\tau)$

Now, given that:

$$\langle n| = \langle 0|(a_1)^n (n!)^{-\frac{1}{2}} \tag{2.68}$$

then the abbreviation $(a_1)^n \circ A_n(1)$ is introduced. Furthermore, it is now assumed that $v_1 = 0$ for the chosen mode - in effect this a 'zero-temperature' approximation, assuming that only the ground vibrational level in the mode of interest is occupied at the experimental temperature.

Equation (2.67) now becomes:

$$A_n^{NC}(\tau) \approx i\theta(\tau)(n!)^{\frac{1}{2}}e^{-\Gamma\tau}\sum_e e^{-i\tau(\omega_{eg} - i\Gamma_e)}\left|(M)^0_{ge}\right|^2 \langle 0|A_n(1)MBMC|0\rangle \tag{2.69}$$

and the NC absorption correlator (2.63) becomes:

$$A_0^{NC}(\tau) \approx i\theta(\tau)e^{-\Gamma\tau}\sum_e e^{-i\tau(\omega_{eg}-i\Gamma_e)}\left|(M)_{ge}^0\right|^2\langle 0|MBMC|0\rangle \qquad (2.70)$$

At this point, the nth order NC Raman correlator is related to nth, (n+1)th and (n-1)th order Condon Raman correlators (M = 0), denoted A_n^C, A_{n+1}^C and A_{n-1}^C respectively. In doing so, use is made of linear relationship between the two sets of raising and lowering operators of the harmonic potentials of the ground and excited state PE curves. These relationships involve the excited state parameters ω_e and Δ via the Manneback relationships [2.16]. The procedure adopted is first to transform the M operator into a function of a_2 and $a_2^\dagger$, the lowering and raising operators of the harmonic potential of the excited electronic state, e. Using commutation relationships and the Manneback equations, a relationship can be found between the NC and Condon correlators in terms of quantities dependent on the unknown excited state structural parameters. The details of this procedure are not given here, but can be found elsewhere [2.7]. In this review of the OT method, it is the resulting equations which are important. It should, however, be noted that no further assumptions or approximations are introduced by the above procedure.

Thus, the NC correlators, A_n^{NC} are related to the Condon correlators, A_n^C through:

$$A_n^{NC}(\tau) = \left[1 + \frac{mp}{q+r}(e^{i\tau\omega_e} + e^{-i\tau\omega_e} - 2)\right]A_n^C(\tau)$$

$$+ m(n+1)^{\frac{1}{2}}\left[1 + \frac{q}{q+r}e^{i\tau\omega_e} + \frac{r}{q+r}e^{-i\tau\omega_e}\right]A_{n+1}^C(\tau)$$

$$+ mn^{\frac{1}{2}}\left[1 + \frac{q}{q+r}e^{-i\tau\omega_e} + \frac{r}{q+r}e^{i\tau\omega_e}\right]A_{n-1}^C(\tau) \qquad (2.71)$$

The absorption correlator is then obtained using n = 0 as:

$$A_0^{NC}(\tau) = \left[1 + \frac{mp}{q+r}(e^{i\tau\omega_e} + e^{-i\tau\omega_e} - 2)\right] A_0^C(\tau)$$

$$+ m\left[1 + \frac{q}{q+r}e^{i\tau\omega_e} + \frac{r}{q+r}e^{-i\tau\omega_e}\right] A_1^C(\tau) \qquad (2.72)$$

where the parameters p, q and r are given by:

$$p = -\delta\left(\frac{\pi c}{\hbar}\right)^{\frac{1}{2}} \mu^{\frac{1}{2}} \tilde{\nu}_e^{\frac{1}{2}}$$

$$q = \frac{\tilde{\nu}_e + \tilde{\nu}_g}{2(\tilde{\nu}_e \tilde{\nu}_g)^{\frac{1}{2}}}$$

$$r = \frac{\tilde{\nu}_e - \tilde{\nu}_g}{2(\tilde{\nu}_e \tilde{\nu}_g)^{\frac{1}{2}}} \qquad (2.73)$$

in which δ is the displacement of the equilibrium position of the PE curves (in pm), μ is the reduced mass of the Raman oscillator (in a.m.u.), and $\tilde{\nu}_e$ and $\tilde{\nu}_g$ are the Raman mode wavenumbers in the excited and ground states (in cm^{-1}) respectively, with $\omega = 2\pi c\tilde{\nu}$).

At this stage, the NC Raman and ABS correlators have been related to the Condon correlators via the desired excited state parameters. Recursion relationships for the nth order Condon correlators ($A_n^C(\tau)$) in terms of the zero-order ($A_0^C(\tau)$) correlator have previously been published [2.6].

Using these relationships, it can be seen for n even ($= 2k$):

$$A_{2k}^C(\tau) = [(2k)!]^{\frac{1}{2}} \sum_{s=0}^{k} \frac{\varepsilon^{2s}\zeta^{k-s}}{(k-s)!2^{k-s}(2s)!} A_0^C(\tau) \qquad (2.74a)$$

and for n odd ($n = 2k+1$)

$$A_{2k+1}^{C}(\tau) = [(2k+1)!]^{\frac{1}{2}} \sum_{s=0}^{k} \frac{\varepsilon^{2s+1} \zeta^{k-s}}{(k-s)! 2^{k-s} (2s+1)!} A_0^{C}(\tau) \qquad (2.74b)$$

where:

$$\varepsilon = \bar{\varepsilon} \frac{e^{-i\tau\omega_e} - 1}{1 - d e^{-i\tau\omega_e}} \text{ and } \bar{\varepsilon} = \frac{p}{q} \qquad (2.75a)$$

and

$$\zeta = d \frac{e^{-2i\tau\omega_e} - 1}{1 - \delta^2 e^{-2i\tau\omega_e}} \text{ and } d = \frac{r}{q} \qquad (2.75b)$$

and thus

$$d = \frac{r}{q} = \frac{\tilde{\nu}_e - \tilde{\nu}_g}{\tilde{\nu}_e + \tilde{\nu}_g} \qquad (2.76)$$

At this stage, the following relationships are known:

- The *n*th order NC Raman correlators in terms of the *n*th, (*n*-1)th and (*n*+1)th order Condon correlators and the structural parameters:

$$A_n^{NC} \Leftrightarrow A_n^{C},\ A_{n+1}^{C} \text{ and } A_{n-1}^{C} \qquad \text{.....via (2.71)}$$

- The 0th order NC (ABS) correlator in terms of the 0th order Condon correlator and the structural parameters:

$$A_0^{NC} \Leftrightarrow A_0^{C} \qquad \text{.....via (2.72)}$$

- Previously published relationships for the *n*th order Condon correlators in terms of the 0th order Condon correlators:

$$A_n^{C} \Leftrightarrow A_0^{C} \qquad \text{....via (2.74)}$$

The A_n^{NC} correlators can thus be related to the A_0^{NC} correlator via multiple operations of the type (2.71) and (2.74). What is then required is a simpler relationship between A_0^{NC} and A_0^{C} (a simpler version of (2.72). Given this, the A_n^{NC} correlators could be related to the A_0^{NC} correlator via (2.71) and (2.72), with A_0^{NC} being available from the ABS profile. Finally, the Raman correlator, A_n^{NC} could then be directly related to A_0^{NC} (the ABS correlator) via (2.71) and the transform formalised.

In order to obtain this simpler $A_0^{NC} \Leftrightarrow A_0^{C}$ transformations explicitly in terms of the structural parameters, several assumptions and approximations are invoked and detailed algebraic rearrangements made. Again, as this work aims to present an overview of the theory, the details of these manipulations will be omitted here and only the assumptions, approximations and resulting equations quoted. Further details may be found elsewhere [2.7].

Using the approximations:

$$d^2 << 1,\ md << 1, m^2 << 1 \tag{2.77}$$

and assuming further that:

$$\varepsilon \approx \bar{\varepsilon}(e^{-i\tau\omega_e} - 1)(1 + de^{-i\tau\omega_e}) \tag{2.78a}$$

and

$$\zeta \approx d(e^{-2i\tau\omega_e} - 1) \tag{2.78b}$$

and further introducing the notation:

$$\beta \equiv e^{-i\tau\omega_e},\ \ k_e \equiv \frac{n_e}{2},\ k_0 \equiv \frac{(n_o - 1)}{2}$$

where n_e and n_o denote even and odd numbers respectively, together with:

$$x \equiv 2m\bar{\varepsilon},\ \ k_{e_s} \equiv \frac{k_e - s}{2s+1},\ k_{o_s} \equiv \frac{k_o - s}{2s+2}$$

and approximating $(1 + d\beta)^j$ as $(1 + jd\beta)$, then the final form of the relationships $A_n^{\mathrm{NC}} \Leftrightarrow A_0^{\mathrm{NC}}$ are given below.

For $n = n_e$ (even):

$$A_{n_e}^{\mathrm{NC}}(\tau) = (n_e!)^{\frac{1}{2}} \sum_{s=0}^{k_e} \frac{\bar{\varepsilon}^{2s} d^{k_e-s}(k_e+s-1)!}{2^{k_e-s}(2s)!} \sum_{t=0}^{k_e+s-1} \frac{(-1)^t}{t!(k_e+s-1-t)!}$$

$$\times \sum_{u=0}^{k_e-s} \frac{1}{u!(k_e-s-u)!}$$

$$\times \{[(2s)d + k_{e_s}x]\beta^{n_e-t-u+1} + [1 - 2s(d - \frac{m}{\bar{\varepsilon}}) - k_{e_s}x]\beta^{n_e-t-u}$$

$$+[(2s)\frac{m}{\bar{\varepsilon}} - 1 - k_{e_s}x]\beta^{n_e-t-u} + k_{e_s}x\beta^{n_e-t-u-2}\}A_0^{\mathrm{NC}}(\tau) \tag{2.79}$$

and for $n = n_o$ (odd):

$$A_{n_o}^{\mathrm{NC}}(\tau) = (n_o!)^{\frac{1}{2}} \sum_{s=0}^{k_o} \frac{\bar{\varepsilon}^{2s+1} d^{k_o-s}(k_o+s)!}{2^{k_o-s}(2s+1)!} \sum_{t=0}^{k_o+s} \frac{(-1)^t}{t!(k_o+s-t)!}$$

$$\times \sum_{u=0}^{k_o-s} \frac{1}{u!(k_o-s-u)!}$$

$$\times \{[(2s+1)d + k_{o_s}x]\beta^{n_o-t-u+1} + [1 - (2s+1)(d - \frac{m}{\bar{\varepsilon}}) - k_{o_s}x]\beta^{n_o-t-u}$$

$$+[(2s+1)\frac{m}{\bar{\varepsilon}} - 1 - k_{o_s}x]\beta^{n_o-t-u-1} + k_{o_s}x\beta^{n_o-t-u-2}\}A_0^{\mathrm{NC}}(\tau) \tag{2.80}$$

The $A_0^{\mathrm{NC}}(\tau)$ correlators can be found directly from the experimental ABS spectrum. Following the above manipulations, (2.62) becomes:

$$\alpha_0^{NC}(\omega) = \int_{-\infty}^{\infty} d\tau\, e^{i\tau\omega} A_0^{NC}(\tau) \tag{2.81}$$

where $\omega_L \equiv \omega$.

It is known from (2.46) that the Imaginary part of α_0^{NC} leads to the ABS spectrum:

$$\mathrm{Im}\left[\alpha_0^{NC}(\omega)\right] = \frac{3}{4\pi\omega}\langle\sigma_{ABS}(\omega)\rangle = \frac{ABS(\omega)}{\omega} \tag{2.82}$$

Usually, $\alpha_0^{NC}(\omega)$ is denoted $\Phi(\omega)$, the complex polarisability, which can be found from the ABS spectrum from:

$$\alpha_0^{NC}(\omega) \equiv \Phi(\omega) = \frac{2}{\pi} P \int_0^{\infty} \frac{ABS(\omega')}{(\omega')^2 - \omega^2}\, d\omega' + i\frac{ABS(\omega)}{\omega} \tag{2.83}$$

Since the operator β in (2.79) and (2.80) simply shifts the frequency of the Fourier kernel:

$$\int_{-\infty}^{\infty} d\tau\, e^{i\tau\omega}\beta^s .. = \int_{-\infty}^{\infty} d\tau\, e^{i\tau(\omega - s\omega_e)} \tag{2.84}$$

then the Fourier transform of the Raman correlator, $A_n^{NC}(\tau)$ will produce a Raman polarisability whose frequency argument is downshifted by an amount $s\omega_e$ from the laser frequency, ω.

Thus, the Fourier transform of (2.79) and (2.80) give, for $n = n_e$ (even):

$$\alpha_{n_e}^{NC}(\tau) = (n_e!)^{\frac{1}{2}} \sum_{s=0}^{k_e} \frac{\bar{\varepsilon}^{2s} d^{k_e - s}(k_e + s - 1)!}{2^{k_e - s}(2s)!} \sum_{t=0}^{k_e + s - 1} \frac{(-1)^t}{t!(k_e + s - 1 - t)!}$$

$$\times \sum_{u=0}^{k_e - s} \frac{1}{u!(k_e - s - u)!}$$

$$\times \{[(2s)d + k_{e_s}x]\Phi(1) + [1 - 2s(d - \frac{m}{\bar{\varepsilon}}) - k_{e_s}x]\Phi(0)$$

$$+[(2s)\frac{m}{\bar{\varepsilon}} - 1 - k_{e_s}x]\Phi(-1) + [k_{e_s}x]\Phi(-2)\} \tag{2.85}$$

where $\Phi(j) = \Phi[\omega - (n_e - t - u + j)\omega_e]$

For $n = n_o$ (odd):

$$\alpha_{n_o}^{NC}(\tau) = (n_o!)^{\frac{1}{2}} \sum_{s=0}^{k_o} \frac{\bar{\varepsilon}^{2s+1} d^{k_o - s}(k_o + s)!}{2^{k_o - s}(2s+1)!} \sum_{t=0}^{k_o+s} \frac{(-1)^t}{t!(k_o + s - t)!}$$

$$\times \sum_{u=0}^{k_o - s} \frac{1}{u!(k_o - s - u)!}$$

$$\times \{[(2s+1)d + k_{o_s}x]\Phi(1) + [1 - (2s+1)(d - \frac{m}{\bar{\varepsilon}}) - k_{o_s}x]\Phi(0)$$

$$+[(2s+1)\frac{m}{\bar{\varepsilon}} - 1 - k_{o_s}x]\Phi(-1) + [k_{e_s}x]\Phi(-2)\} \qquad (2.86)$$

where $\Phi(j) = \Phi[\omega - (n_o - t - u + j)\omega_e]$.

From these transform equations, the nth order RRS cross-section is obtained from (2.45) as:

$$RRS_n(\omega) = \text{const.}\left|\alpha_n^{NC}(\omega)\right|^2 \qquad (2.87)$$

with the constant only required for absolute measurements.

It is now possible to relate the ratios of Raman band intensities in a progression of the mode to the $\Phi(\omega)$ function, which is directly available from the ABS spectrum and to obtain values for the parameters $\tilde{\nu}_e$ (= ω_e / $2\pi c$), δ, and m for that mode.

The general procedure followed in this work, in order to find values for these three parameters, was to record the relative band intensities of the first four harmonics of the vibrational mode in the RR progression as well as the resonant ABS band. These ratios are given by:

$$\frac{\mathrm{RRS}_{n=2}}{\mathrm{RRS}_{n=1}} = \frac{\left|\alpha_2^{\mathrm{NC}}(\omega)\right|^2}{\left|\alpha_1^{\mathrm{NC}}(\omega)\right|^2} \qquad \text{etc...} \qquad (2.88)$$

and this can be compared with the calculated values based on the ABS spectrum and pre-defined estimates of $\tilde{\nu}_e$, δ and m. In practice, a range of allowed values of the three parameters is specified and the function

$$F(\omega_e, \delta, m) = \sum_{i=2}^{4} \left[\left(\frac{\left|\alpha_i^{\mathrm{NC}}(\omega, \delta, \omega_e, m)\right|^2}{\left|\alpha_1^{\mathrm{NC}}(\omega, \delta, \omega_e, m\right|^2} \right)_{\mathrm{calc}} - \left(\frac{\mathrm{RRS}_i(\omega)}{\mathrm{RRS}_1(\omega)} \right)_{\mathrm{expt}} \right] \qquad (2.89)$$

is calculated at $\omega = \omega_L$ (the laser frequency). A minimum in this function is then sought as the values of the parameters are varied.

2.7 The OT Method: Review of Assumptions and Applications

In the previous two sections, an overview of the theory behind the OT method was presented and the procedure for finding the excited state structural parameters for a given vibrational mode was outlined. However, several assumptions and approximations are employed in this theory and the implication of these for the nature of the molecule, the normal mode and the excited state able to be studied by this method must be examined.

The introduction of the limited B-O approximation in section 2.5 allows attention to be focused on a single vibrational normal co-ordinate and mode (the 'Raman' mode) at a time. Structural changes along this co-ordinate in the resonant excited electronic state give rise to the intensity enhancement of the mode in the RR spectrum and possibly vibronic structure in the ABS spectrum. However, this

is not always resolved, especially in powder or solution media. The contribution of the other modes is carried implicitly in the ABS during the transform process.

Thus, the OT method is at its most useful in cases where a number of vibrational modes affect the RR and ABS spectra, and where the ABS spectrum is complicated. By focusing on one mode at a time, while retaining the multimode character of the ABS spectrum, the OT method should allow values of structural parameters along each co-ordinate to be obtained sequentially. However, even in the case where significant structural changes in the excited state occur along one mode only, the OT method should still deliver excited state geometric changes along that co-ordinate.

At the start of section 2.6, it was assumed that the vibrational normal co-ordinate under study was totally symmetric under the operations of the molecular point group and that the resonant electronic states were non-degenerate. Thus, at present, the OT method is restricted to application to totally symmetric vibrational modes.

With the introduction of the limited B-O approximation (section 2.5), it was assumed that no mode-mixing (Duschinsky rotation) involving the Raman mode was present. Thus, the mode chosen for study must not mix strongly with other normal modes in the excited state. A necessary condition for the presence of mode-mixing between two modes in an excited electronic state is the appearance of simultaneous resonance enhancement of bands due to both the modes in the RR spectrum recorded with an excitation frequency lying within the ABS band. However, this is not a sufficient condition for mode-mixing to occur, although it may be taken as an indication of the possibility of its presence.

It should be noted that mode-mixing in the N - 1 dimensional non-Raman subspace is not precluded by this limited B-O approximation.

In formulating (2.69) and (2.70) it was assumed that the 'effective zero temperature' approximation is valid for the mode of interest. In effect this requires, $\omega_g >> kT$ for this vibrational mode. This is usually considered the case of the population of the $v = 1$ vibrational level is less than 1% of that of the $v = 0$ level at the experimental temperature, i.e.:

$$\frac{N(v=1)}{N(v=0)} = \frac{\exp(-3\hbar\omega_g/2kT)}{\exp(-\hbar\omega_g/2kT)} \leq 0.01 \qquad (2.90)$$

This assumption does not normally prove to be restrictive for the study of inorganic species, although for lower frequency modes (where, for example heavy metal atoms are vibrating) an experimental consequence may be that spectra must be recorded at ca. 80 K .

The excited electronic state is assumed to be single and non-degenerate. While the sum on e is never formally closed, cross terms in the final Raman intensities arising from a total polarisability being a sum of contributions from different excited states, will appear if this is not assumed:

$$\mathrm{RRS}_{total} \propto \left|[\alpha_n^{\mathrm{NC}}]_1 + [\alpha_n^{\mathrm{NC}}]_2\right|^2 \qquad (2.91)$$

for two excited electronic states 1 and 2.

Furthermore, non-adiabatic effects involving the vibrational mode of interest must be absent and the potential surface of both ground and excited electronic states are assumed to be harmonic. Thus, degenerate excited states or dissociative co-ordinates cannot be treated by this method.

In producing (2.79) and (2.80) the approximation:

$$d^2 = \left|\frac{\tilde{\nu}_e - \tilde{\nu}_g}{\tilde{\nu}_e + \tilde{\nu}_g}\right| << 1 \qquad (2.92)$$

was assumed to be valid for the mode of interest. This is usually held to be the case if the fraction is less than or equal to 0.01. An obvious problem with this assumption is that $\tilde{\nu}_e$ is an unknown and so for 'blind' cases, where no estimate of this parameter is available, the value of d cannot be found. However, in practice an estimate of $\tilde{\nu}_e$ can usually be found from vibronic structure on a low-temperature ABS spectrum.

This assumption can, however, prove to be quite restrictive. For example, the totally symmetric S-S stretch of the S_2^- ion in ultramarine is known to have a value of $\tilde{\nu}_g$ = 540 cm^{-1} and a value of $\tilde{\nu}_e$ = 400 cm^{-1} for the $^2\Pi_{1/2u}$ excited electronic state [2.17]. Thus, $d^2 \gg 0.02$ and the above assumption is seen to be invalid.

Similarly, the change in the wavenumber of the I-I stretch of the I_2 molecule in the first excited state is seen to be too large for this approximation to be valid [2.18]. This case is unsuitable for study by the OT method for a second reason: the excited state potential is anharmonic and so the assumption regarding the nature of the excited electronic state also does not hold. Hence, despite these diatomic molecules being among the simplest and the most useful molecules available to test the OT method, their study is precluded by the invalidation of the assumptions of the method.

One further assumption of the OT method is that the damping parameter, Γ_v in the Raman subspace, is assumed to be independent of v. The effect of this approximation is difficult to assess, but if inappropriate for a system, it may be expected that the quality of any fit to the experimental data will be reduced. It should be noted, however, that complete generality is allowed in the non-Raman subspace.

It is notable that the use of Eqn. (2.73), which defines the role of the excited state parameters in the theory, requires the displacement parameter, δ, to be computed in pm. This presupposes that the Raman mode may be

approximated to a pseudo-diatomic stretch, with the oscillator being of known reduced mass. While this is often the case, it may prove to be too severe an approximation for many vibrational modes of inorganic molecules, where a contribution from more than one local mode to the Raman mode might be expected.

Finally, NC coupling is assumed to be significant only to the linear term, i.e. terms of the order of m^2 are neglected. Thus, for cases where it is known that strong NC coupling is present, the OT method may again be unsuitable for application.

It should be further noted that the RRS and ABS cross-sections are taken to be averages over all molecular orientations, and thus data from single crystals cannot be used.

All OT calculations were performed using a program written by D. Oprescu of University College London. This program utilised the detailed theory outlined above, together with a search routine for finding values of the parameters. The implications of this search routine for the procedure of finding values, as well as for the performance of the method as a whole, will be discussed in more detail in chapter 5, where initial attempts at application of this OT method will be presented.

Chapter 3

Application of the SOS Method to the Structure of the $^1A_{2u}$ Excited State of $[M_2X_8]^{n-}$ Ions

(M = Re, Mo; X = Cl, Br, I)

The SOS method is the first of the two methods, outlined in chapter 2, which is used to connect RR intensity and electronic absorption (ABS) data in order to extract values for some structural parameters of the resonant excited electronic state. For a chosen vibrational normal co-ordinate of a molecule, the method can, in principle, deliver values for the following parameters:

- The wavenumber of the mode in the resonant excited state, $\tilde{\nu}_e$
- The displacement along the normal co-ordinate, Δ
- The linear non-Condon coupling parameter, m

The phenomenological lifetime factor, Γ, and the general zero-zero transition energy between the ground and excited electronic states (denoted ω_{eg} in chapter 2 and $E_{0\text{-}0}$ here) are also treated as parameters. The parameters used in this method are similar to those used in the OT method; however, in the latter method, values for Γ and $E_{0\text{-}0}$ are 'read' from the absorption spectrum during the transform process.

The experimental data required by the SOS method are the appropriate electronic absorption spectrum (ABS) and RR intensity data. The latter may be used in two forms: (a) the relative intensities of overtone bands in a mode progression, or (b) an REP for the chosen vibrational mode, using excitation lines across the resonant ABS band. Where possible, REPs are avoided as the source of RR intensity data since the accuracy obtained for relative intensity measurements of bands recorded *within* a single spectrum (i.e. overtone bands) is generally higher. A more detailed treatment of the errors involved in recording RR data is given in Appendix A1.

Close inspection of the theoretical assumptions of the SOS method in chapter 2 allowed a greater insight into its applicability: while claimed to be widely applicable, it can be seen from section (2.3) that some common inorganic species may prove to be problematic subjects for study by this method. These include cases where two electronic states are close in energy or where the excited electronic state is known to be highly anharmonic.

In this chapter, an account is given of the application of the SOS method to a class of compounds for which it is thought that all the assumptions and restrictions of the method hold. Specifically, the well-characterised metal-metal (M-M) co-ordinate of quadruply bonded dimetallic species in the $^1\delta\delta^*$ excited electronic state is studied. Thus the aim is both to assess the performance of the method and to obtain new information about the structure of these species in this excited electronic state.

In the next section details will be given about the $[M_2X_8]^{n-}$ species, while their adherence to the restrictions imposed by the method is assessed in section 3.2. Details of the method of calculation of the the SOS parameters are also given in 3.2, while the experimental data and results are presented in sections 3.3 and 3.4 respectively, and discussed in sections 3.5 and 3.6.

3.1 The $[M_2X_8]^{n-}$ Ions

The $[M_2X_8]^{n-}$ ions ($[Re_2X_8]^{2-}$ (X = F, Cl, Br or I); $[Mo_2X_8]^{4-}$ (X = Cl or Br)) are the most widely studied of the species known to contain quadruple metal-metal bonds. The metal-metal bonding scheme in such species, first formulated for $[Re_2Cl_8]^{2-}$ [3.1, 3.2], was outlined in section (1.7): a $\sigma^2\pi^4\delta^2$ configuration describes the electronic ground state and the presence of δ-overlap between the d_{xy} orbitals of the two metal atoms explains the eclipsed arrangement of ligands about the two metal centres. Electronic structure calculations using SCF-Xα-SW methods for the $[Mo_2Cl_8]^{4-}$ [3.3, 3.4] and $[Re_2Cl_8]^{2-}$ [3.5, 3.6] ions have verified the essential qualitative correctness of this $\sigma^2\pi^4\delta^2$ description of the ground ($^1A_{1g}$) electronic state. The symmetry of the structure of all the $[M_2X_8]^{n-}$ ions in the ground state was revealed to be D_{4h} by X-ray crystallography [3.1, 3.2; 3.7, 3.8]. The eight halide atoms lie at the corners of a square prism with the two MX_4 units being held cofacially in an eclipsed manner by a short quadruple metal-metal bond and with MMX angles of ca. 105° in each case. The structure is shown schematically in Fig. 3.1.

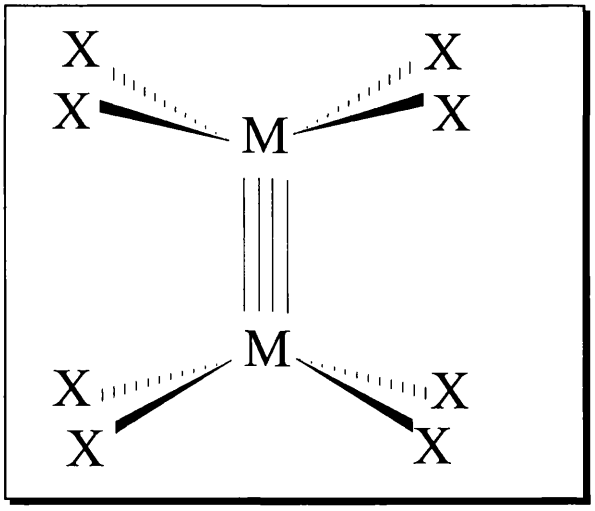

Fig. 3.1 : Structure of the $[M_2X_8]^{n-}$ ions

The vibrations of the molecule in this D_{4h} symmetry span the irreducible representations $3a_{1g}$ (R) + b_{1g} + $3e_g$ (R) + a_{1u} + $2b_{1g}$(R) + $2a_{2u}$(IR) + b_{1u} + $2b_{2u}$ + $3e_u$(IR), with the three Raman active a_{1g} modes being assigned to local ν(MM), ν(MX) stretches and to a δ(MMX) bending mode [3.9 - 3.11].

The ions form salts with a variety of cations, with TBA and Cs^+ being the most common for $[Re_2X_8]^{2-}$ ions. For the $[Mo_2Cl_8]^{4-}$ ion, $(NH_4)^+$, Cs^+, K^+ and Rb^+ salts are known. The identity of the counter-ion has a slight effect on the M-M bonding in these ions. For example, *r*(MoMo) in $(NH_4)_5Mo_2Cl_9.H_2O$ (which contains the $[Mo_2Cl_8]^{4-}$ ion and an additional mole of NH_4Cl) is 2.15 Å, compared with 2.14 Å for the compound $K_4Mo_2Cl_8$. This effect, which arises from the differing sizes of the cations, is also apparent in the values of the ν_1 (ν(MM)) mode wavenumber, with ν_1 being 338 cm^{-1} in the NH_4^+ salt and 346 cm^{-1} in the K^+ salt [3.12]. However, it appears that the main influence of the counter-ions on the $[M_2X_8]^{n-}$ ions in the crystals is to determine the relative occupations of the three possible perpendicular orientations for the M-M bond in the unit cell. It has recently been proposed that the positioning of the counter-ions relative to the partially positively-charged M-M unit may be responsible for the differing populations of the three orientations in different salts of these ions [3.13].

The electronic absorption spectrum of the $[Re_2Cl_8]^{2-}$ ion has been studied in most detail, first in solution [3.14] and later at low temperatures on a single crystal [3.15]. Several bands were reported in the region 200-800 nm and assignments based on an SCF-Xα-SW calculation were proposed [3.6]. The allowed transition of longest wavelength, centred at around 680 nm, was assigned on the basis of polarisation measurements to the $[^1A_{2u} \leftarrow {}^1A_{1g}]$ ($\delta^* \leftarrow \delta$) transition. With the symmetries of the δ-orbital and the δ^*-orbital being b_{2g} and b_{2u}, respectively, the polarisation of this transition is, as expected for a transition between almost pure metal orbitals, along the M-M axis (i.e. *z*-polarised). Qualitatively similar electronic spectra were seen for $[Re_2Br_8]^{2-}$ [3.15], $[Re_2F_8]^{2-}$ [3.16], $[Re_2I_8]^{2-}$ [3.16], $[Mo_2Cl_8]^{4-}$ [3.17] and $[Mo_2Br_8]^{4-}$ [3.18]. In each case the band of longest wavelength was assigned to the $[^1A_{2u} \leftarrow {}^1A_{1g}](\delta^* \leftarrow \delta)$ transition and these assignments received support from REP studies on the $[Re_2X_8]^{2-}$ ions [3.19, 3.20], the $[Mo_2Cl_8]^{4-}$ ion [3.12] and the $[Mo_2Br_8]^{4-}$ ion [3.21]. In these studies it was observed that the REP of the ν_1 mode, assigned to the local (totally symmetric) metal-metal stretch (ν(MM)), followed the contour of the $^1A_{2u} \leftarrow {}^1A_{1g}$

absorption band. As explained in section (1.4), this observation indicates the presence of significant geometric change along the M-M co-ordinate in the excited electronic state and thus confirms that the electronic transition takes place between orbitals which are largely metal in character.

The structure of the molecule in this $^1A_{2u}$ ($^1\delta\delta^*$) state has long been of interest. Vibronic structure on the $^1A_{2u} \leftarrow {}^1A_{1g}$ band observed in the single-crystal electronic absorption spectra of $(TBA)_2Re_2Cl_8$, $(TBA)_2Re_2Br_8$ and $K_4Mo_2Cl_8.2H_2O$ at low temperature was seen to have an average spacing of 249±1 cm^{-1} [3.22], 255 ± 1 cm^{-1} [3.15] and 336± 2 cm^{-1} [3.23], respectively. This structure was attributed in each case to a progression in ν_1 in the $^1A_{2u}$ state and thus these values are assigned to the wavenumbers of that mode in the $^1\delta\delta^*$ state (denoted $\tilde{\nu}_e$ henceforth, with the reference to only the ν_1 mode implicit). The corresponding values of the wavenumber of the ν_1 mode in the ground electronic state, denoted $\tilde{\nu}_g$, are 274 [3.11], 275 [3.20] and 346 cm^{-1} [3.12] from Raman spectroscopy.

Since the δ-bond is formally eliminated by the $^1(\delta^* \leftarrow \delta)$ transition, the requirement that the halides adopt a strained, eclipsed (D_{4h}) structure in the $^1\delta\delta^*$ excited state is removed. It may then be possible for the molecule to twist about the M-M axis to some degree and thus to adopt a staggered or partially staggered D_{4d} or D_4 structure as shown in Fig. 3.2.

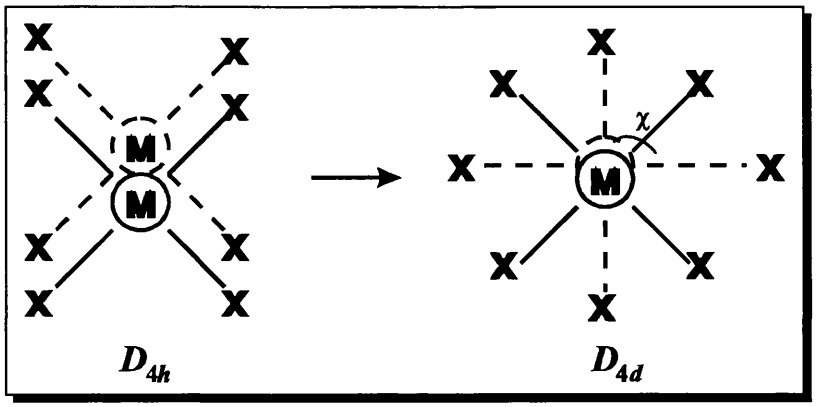

Fig. 3.2 Diagram showing the possible rotation of the ligands in an $[M_2X_8]^{n-}$ ion about the M-M axis to give a staggered structure; in D_{4h}, $\chi = 0°$, in D_{4d}, $\chi = \pi/4$.

Theoretical studies on the $[Re_2X_8]^{n-}$ ion [3.24] suggest that the staggered structure of D_{4d} symmetry is energetically preferred in the $^1A_{2u}$ state. Spectra of the $^1(\delta \leftarrow \delta^*)$ emission of this, and other quadruply bonded M-M compounds, have produced several, often contradictory, interpretations. Initially, the emission spectra of the ions $[Re_2Cl_8]^{2-}$, $[Re_2Br_8]^{2-}$ and $[Mo_2Cl_8]^{4-}$[3.25] in the solid-state at 1.3 K, using excitation within the $^1(\delta^* \leftarrow \delta)$ absorption band, were reported. It was found that the absorption and emission bands are not mirror images and do not overlap significantly at the frequency of the 0-0 transition. Consequently, it was thought that the emission must arise from an excited state other than the $^1\delta\delta^*$. The equivalent emission spectrum of the compound $Mo_2Cl_4(P^nBu_3)_4$ was also reported [3.26]. This compound has a D_{2d} structure typical of $M_2X_4L_4$ species (section 1.7) and it is thought that the large (P^nBu_3) ligands may prevent any twisting about the M-M axis, such as that depicted in Fig. 3.2, in the excited electronic state. The emission spectrum of this compound, as well as those of the series of compounds $Mo_2X_4(PMe_3)_4$ (X = Cl, Br or I) [3.27] show good overlap and mirror symmetry with the $^1(\delta^* \leftarrow \delta)$ absorption band in each case. Thus it was proposed [3.26-3.28] that the emitting state in this case was the *untwisted* (D_{2d}) $^1\delta\delta^*$ state; by contrast, the emission in the $[M_2X_8]^{n-}$ ions was then assigned to the twisted (D_{4d}) $^1\delta\delta^*$ excited state, hence explaining the lack of mirror symmetry between the absorption and emission bands.

However, more recently, an emission spectrum of the $[Re_2Cl_8]^{2-}$ ion in the solid-state at ~ 80 K was reported to show a mirror-image relationship and good overlap with the $^1(\delta^* \leftarrow \delta)$ absorption band [3.29]. Thus it was proposed that, for the $[M_2X_8]^{n-}$ ions, the emitting state is also of eclipsed (D_{4h}) geometry, at least in the solid-state. In fluid solution, however, it is thought that twisting may still occur: a kinetic study [3.30] of the $[Re_2Cl_8]^{2-}$ and $[Mo_2Cl_8]^{4-}$ ions proposed that, in solution, a transient, assigned to the twisted $^1\delta\delta^*$ excited state, is formed in fewer than 20 ps.

Recently, a time-resolved resonance Raman (TR^3) study of the $^1A_{2u}$ states of $[Re_2Cl_8]^{2-}$ and $[Re_2Br_8]^{2-}$ in solution was performed [3.31]. In this study, the ions were pumped to the $^1A_{2u}$ state and this state was then probed to obtain a RR spectrum. This excited state RR spectrum showed a value of $\tilde{\nu}_e$ of 262 cm^{-1} for both ions, notably different from the values found from vibronic progressions in single-crystal absorption spectra at ca. 80 K (249±1 and 255±1 cm^{-1}, respectively). By contrast, the sterically hindered $Mo_2Cl_4(PMe_3)_4$ complex, of D_{2d} structure, which is thought not to torsionally distort, showed a value of $\tilde{\nu}_e$ in the TR^3 study in solution very close to that found from vibronic structure in the ABS spectrum. The change in the Re-Re bond length on going from the ground to the $^1A_{2u}$ excited state, denoted δ(M-M), where M = Re, has previously been estimated for $[Re_2Cl_8]^{2-}$ using empirical rules relating band wavenumbers for a pseudo-diatomic species and bond lengths [3.32]. These gave a value of 3.7 pm for the bond length change in solution and 8.1 pm in the single-crystal under cryogenic conditions. The differences between the values of the parameters in the two environments were ascribed to the prevention of relaxation to the staggered state in the rigid crystal environment at ca. 80 K. It was also suggested that the difference in the timescale between the vibronic ABS experiment and the nanosecond TR^3 study may be important in determining whether a relaxed, staggered excited state is observed. It is reasonable to expect that the bond length of a staggered $^1\delta\delta^*$ excited state would be shorter than the equivalent length in the eclipsed $^1\delta\delta^*$ excited state, since the inter-ligand repulsion would be greatly reduced in the former structure.† Likewise, the wavenumber of the ν(MM) stretch would be expected to be higher in the excited state of staggered geometry. Thus, it appears that the value of $\tilde{\nu}_e$ and δ(M-M) (which can be found from the dimensionless displacement, Δ, calculated in the SOS method) for the ν_1 mode in the $^1A_{2u}$ state may be indicative of the excited state conformation adopted.

†A similar effect is seen for the compound $(PPN)_2Os_2Cl_8$ in which there is a filled δ^* orbital and hence no preference for an eclipsed structure. Two crystal forms are seen, one staggered and the other eclipsed, with the latter form showing a longer Os-Os bond length [3.33].

Previously, vibronic analysis of ABS bands has only been possible for structured low temperature spectra recorded in the solid-state. The SOS method, which uses 'vibronic' analysis of ABS and RR data, is applicable in both solid state and solution. Thus, an SOS study of these ions using data recorded in both the solid-state and, where possible, in solution, should provide new information on the role of the crystal environment and/or the experimental timescale in determining the excited state geometry observed. Furthermore, values of $\tilde{\nu}_e$ and δ(M-M) for the ν_1 mode are available without resort to empirical rules.

Moreover, agreement of the SOS-calculated values of parameters with previous estimates or measurements in the appropriate environment would indicate some success in the application of the SOS method in these cases. A summary of the ground state structural information for the $[M_2X_8]^{n-}$ ions is shown in Table 3.1, while the available excited-state structural information is summarised in Table 3.2.

	$[Re_2Cl_8]^{2-}$	$[Re_2Br_8]^{2-}$	$[Re_2I_8]^{2-}$	$[Mo_2Cl_8]^{4-}$		
				$K_4Mo_2Cl_8$	$K_4Mo_2Cl_8.2H_2O$	$(NH_4)_5Mo_2Cl_9.H_2O$
$\tilde{\nu}_g$/cm^{-1}	275[3.20]	276[3.20]	257[3.20]	346[3.12]	-	338[3.12]
r(M-M) /Å	2.22[3.1,3.2,3.22, 3.34]	2.23[3.34 - 3.35]	2.25[3.7]	-	2.14[3.8]	2.15[3.35]

Table 3.1: Summary of the ground state structural information relating to the M-M co-ordinate of the $[M_2X_8]^{n-}$ ions.

	$[Re_2Cl_8]^{2-}$		$[Re_2Br_8]^{2-}$		$K_4Mo_2Cl_8$
	CH_2Cl_2 (295 K)	crystal (14 K)	CH_2Cl_2 (295 K)	crystal (14 K)	crystal (14 K)
$\tilde{\nu}_e$/cm^{-1}	262[3.31]	249 ±1 [3.22,3.35]	262[3.31]	255 ± 1[3.15] (-3.7 %)	336 ± 2[3.23]
δ(M-M) /pm	3.7[3.31]	8.1[3.31]	3.7[3.31]	8.1[3.31] (7.6 %)	-

Table 3.2: Summary of the available structural information relating to the M-M co-ordinate of the $[M_2X_8]^{n-}$ ions in the $^1\delta\delta^*$ excited electronic state. Figures in parentheses indicate percentage changes in the value relative to that of the ground state.

3.2 Application of the SOS Method: Suitability of $[M_2X_8]^{n-}$ Ions for SOS Study

In order to serve as a test for the SOS method, the ν_1 mode of these ions and the resonant $^1\delta\delta^*$ excited state must adhere to the theoretical restrictions and assumptions outlined in section (2.3). In this way, any failure of the calculation can be attributed solely to a problem with the implementation of the SOS method, rather than to the breakdown of the approximations.

The $^1\delta\delta^*$ excited state of these ions is generally well separated from any other excited electronic state (the $^1(\delta^* \leftarrow \delta)$ transition is a single band in the ABS spectrum in each case) and strong non-adiabatic couplings to other electronic states are not expected. Furthermore, since both the ground ($^1A_{1g}$) and excited ($^1A_{2u}$) states are both spin and orbitally non-degenerate, spin-orbit coupling, which may otherwise have been large for such atoms as Re, is not present. Similarly, Jahn-Teller effects are not present. Thus the assumptions concerning the validity of the Born-Oppenheimer approximation and the nature of the excited electronic state appear to hold. There is also no reason to expect that the ν_1 co-ordinate will have a strongly anharmonic or dissociative potential in the excited electronic state†. It is therefore expected that the harmonic approximation will be valid.

It should be pointed out that the SOS method is capable of dealing with the situation where the molecule changes point group in the excited electronic state (e.g. D_{4h} to D_{4d}); in this case, the symmetries of the vibrational modes must be referenced to the common subgroup or dynamic point group.

Application of the SOS Method

The SOS method aims to fit the electronic absorption profile (ABS) of the resonant electronic transition and the relative intensity ratios of the first four harmonics of the chosen normal mode (in this case ν_1) in the RR spectrum. These

† Estimations of anharmonicity constants from RR progressions in this mode are very small [3.20]

ratios must be corrected for all frequency-dependent factors except the molar scattering parameter, as described in Appendix A1. However, in this case, no correction for ν^4 scattering was performed, since this is included in the SOS calculation. The ratios are averaged over several spectra and a standard deviation of less than 10% was generally achieved. Further details of the collection, measurement and manipulation of the experimental data are given in Appendices A1- A3.

In fitting the experimental data, the SOS calculation uses a *single* set of values for the parameters $\tilde{\nu}_e$, Δ, m, (for the ν_1 normal co-ordinate) Γ and $E_{0\text{-}0}$ to fit simultaneously both types of data. If necessary, Duschinsky mixing involving the ν_1 mode can be included.

The SOS calculations in this study were carried out using a program written in C++ [†] to generate RR and ABS data through the relationships detailed in chapter 2. The general procedure of a calculation is to inspect closely the ABS curve (or its first derivative) for a rough estimate of values of ν_e (if there is any vibronic structure), $E_{0\text{-}0}$ and Γ. Using these, together with estimates of Δ and m, and if necessary, including Duschinsky rotation, the ABS profile and RR intensity ratios are generated via the transition polarizability, $[\alpha]_{fi}$, and these are compared visually to the experimental data. The parameter values are then modified accordingly and the calculation repeated. This method is shown schematically in Fig. 3.3.

Clearly this method will not guarantee a unique solution - with several parameters to fit and the equations used to calculate the ABS and RR data being complicated functions of these parameters, there will exist several sets of parameter values which provide a good fit to the experimental data. It should be possible to discount some of these sets on the basis of physically unreasonable parameter values, e.g. a negative value for Δ where the electronic transition is of the type which takes an electron from a bonding to an anti-bonding orbital is not

[†] Carried out by C. Svendsen at the Fysisk Institut, Odense University, Denmark

expected. It must be recognised, however, that the set of parameters found by the above method is influenced by previous estimates of the magnitudes of some of the parameter values from experimental or other data. While the uniqueness of the final fit cannot be guaranteed, it nevertheless provides the best simultaneous fit to two types of experimental data using parameter values within a physically sensible range.

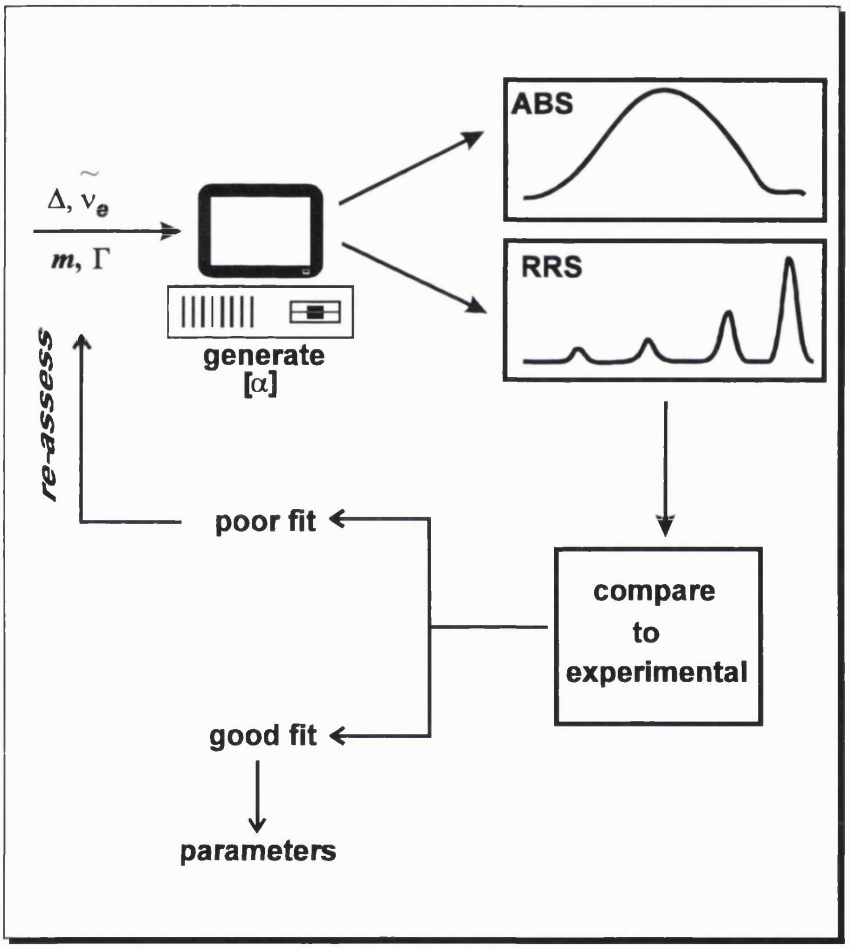

Fig. 3.3 : Schematic diagram of SOS method

Later additions to the SOS calculational procedure involved checking the solution set of parameter values by running a concurrent search programme aimed at finding the best fit to the ABS data from a pre-specified range of possible values for the parameters. A Monte-Carlo type fitting function and procedure were defined and once the 'best fit' was found, the method of steepest descent was used for refinement. Use of such a method requires that the values of some or all of the parameters are varied slightly about the initial minimum in the fitting

function until an absolute minimum is found. The results of this numerical fitting procedure were found to produce parameter values extremely close to those found by the visual fitting method. Obviously, such a search procedure introduces problems of its own and must be conducted in a way which is consistent with the magnitude of the errors in the experimental data. The intrinsic problems of such a search method are discussed in greater detail in chapter 5, since, in the OT method, only a numerical fitting routine is used to obtain the values for the parameters of interest. Further problems arise in the OT case, however, because of the unsophisticated method of finding minima in the fitting function. Furthermore, the large spacing between adjacent points in the ABS spectrum, necessitated by the need to 'read' as well as fit it, mean that only a coarse search of widely spaced values for the parameters is possible. In the case of the SOS method, not only is this numerical search procedure more sophisticated, but it is also used only as a secondary check of the visual fit to the experimental data. Furthermore, the ABS data usually consists of a larger number of closely spaced points allowing a tighter search of possible parameter values to be carried out.

One further factor in the SOS calculation is the number of vibrational states of the excited electronic state over which the sum in equation (2.40) is taken. The procedure adopted in this study was to include a sufficient number of states so as to reach convergence on the values of the relative intensity ratios of the RR spectrum.

3.3 Experimental Details

The compounds $(TBA)_2Re_2Br_8$ [3.36, 3.37], $(TBA)_2Re_2I_8$ [3.38] and $(NH_4)_5Mo_2Cl_9.H_2O$ (which contains the $[Mo_2Cl_8]^{4-}$ ion) [3.8] were prepared by standard literature methods[†] .

UV/Visible Absorption Spectra

Transparent alkali halide pressed disks of each of the compounds were prepared as detailed in Appendix A2. The alkali halide compounds used were KBr

[†] The help of Dr. D. G. Humphrey is gratefully acknowledged

($[Re_2Br_8]^{2-}$), CsI ($[Re_2I_8]^{2-}$) and KCl ($[Mo_2Cl_8]^{4-}$). UV/Visible spectra were recorded at ~ 77 K in the region of the $^1(\delta^* \leftarrow \delta)$ transitions as detailed in Appendix A2.

As discussed in Appendix A3, the baseline of the ABS spectra recorded on pressed disks rises towards the blue end of the spectrum as a result of ν^4 scattering. Further deviations arise due to dispersion effects. For all the spectra recorded here, a baseline was deducted to give a 'flat' spectrum taking into account both of these contributions. Since no strong vibronic structure was observed on any of the ABS bands, it is not expected that the deduction of this baseline will affect seriously the quality of the data or the fitting procedure.

The ABS spectra of all three compounds, in the region of their $^1(\delta^* \leftarrow \delta)$ transitions are shown in Figs. 3.4 ($[Re_2Br_8]^{2-}$), 3.5 ($[Re_2I_8]^{2-}$) and 3.6 ($[Mo_2Cl_8]^{4-}$) respectively. Correction for baseline scattering and dispersion has already been performed.

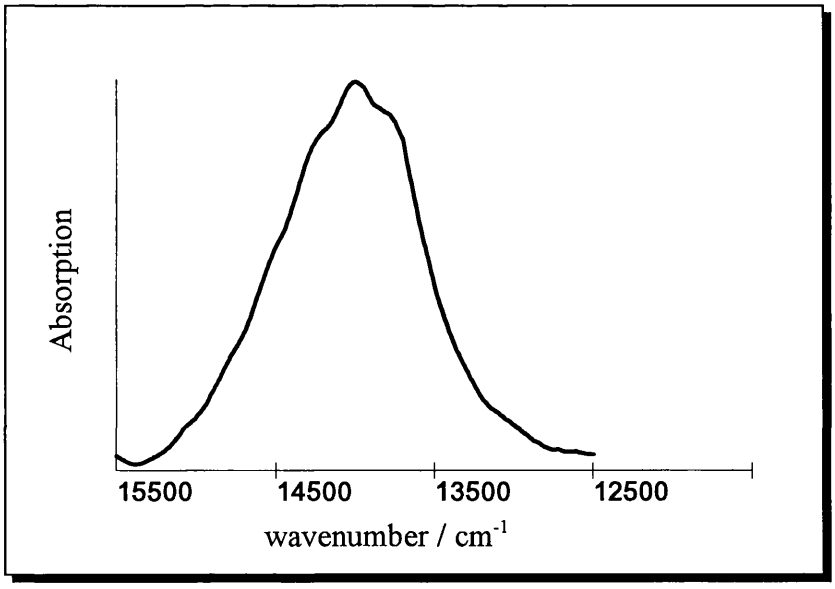

Fig. 3.4 UV/Vis absorption spectrum of $(TBA)_2Re_2Br_8$ in the region of its $^1(\delta^* \leftarrow \delta)$ transition. The sample was held as a pressed KBr disk at ~ 77 K. Correction for baseline scattering and dispersion effects has been performed.

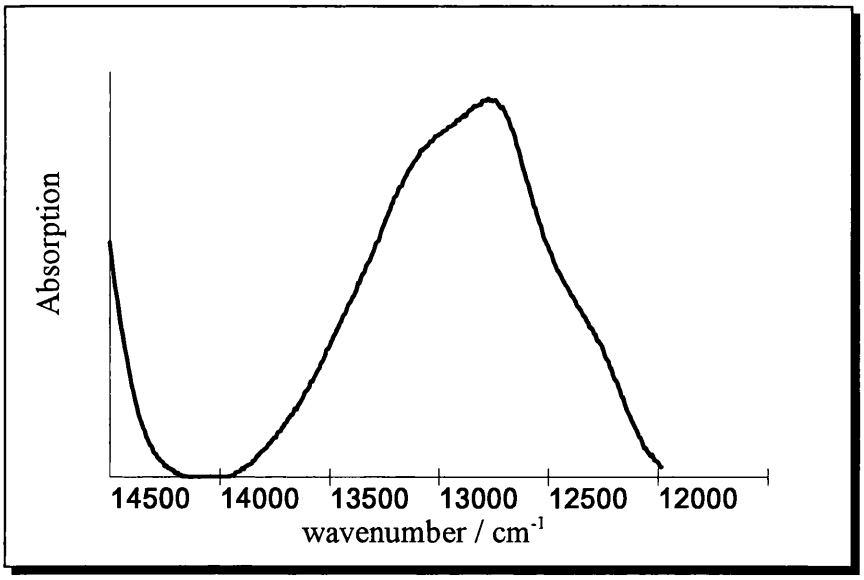

Fig. 3.5 UV/Vis absorption spectrum of $(TBA)_2Re_2I_8$ in the region of its $^1(\delta^* \leftarrow \delta)$ transition. The sample was held as a pressed CsI disk at ~ 77 K. Correction for baseline scattering and dispersion effects has been performed.

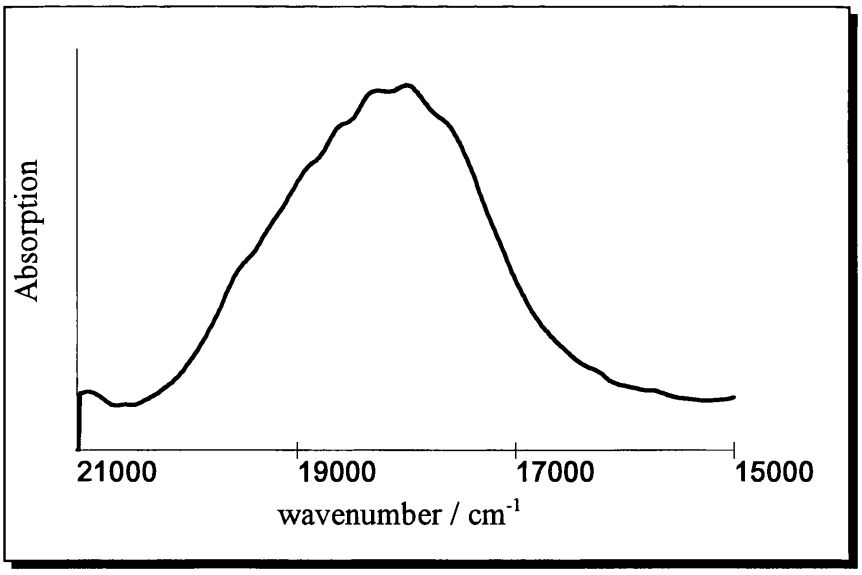

Fig. 3.6 UV/Vis absorption spectrum of $(NH_4)_5Mo_2Cl_9.2H_2O$ in the region of its $^1(\delta^* \leftarrow \delta)$ transition. The sample was held as a pressed KCl disk at ~ 77 K. Correction for baseline scattering and dispersion effects has been performed

The $[Re_2Br_8]^{2-}$ ion is the only ion studied which is sufficiently stable in solution to allow ABS and RR spectra to be recorded. A solution of $(TBA)_2Re_2Br_8$ (0.2 mM)

in acetonitrile was prepared and an ABS spectrum recorded at 295 K in the region of the $^1(\delta^* \leftarrow \delta)$ transition. This spectrum is shown in Fig. 3.7.

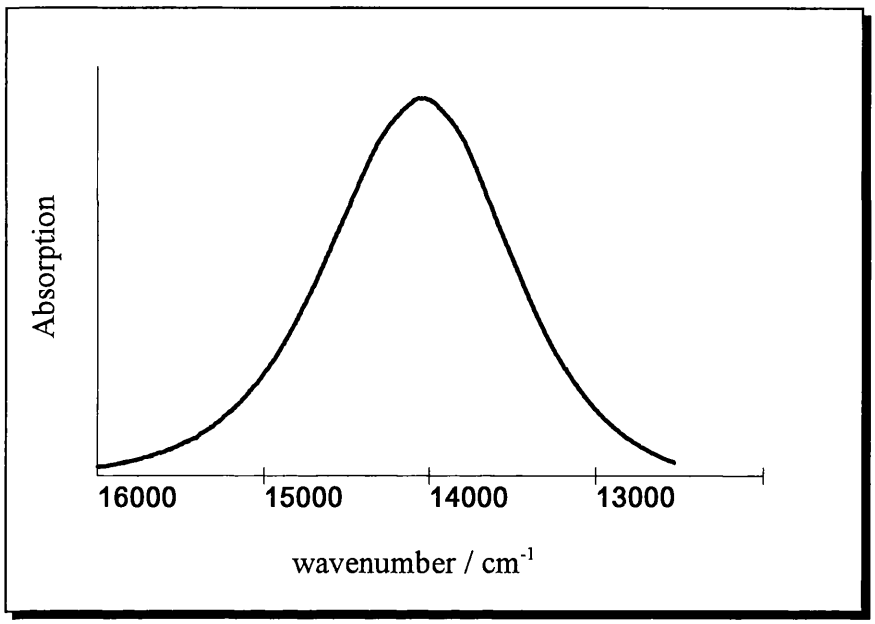

Fig. 3.7 UV/Vis absorption spectrum of $(TBA)_2Re_2Br_8$ in the region of its $^1(\delta^* \leftarrow \delta)$ transition. The sample was held in acetonitrile solution (0.2 mM) at 295 K.

All spectra were used in the calculation in the form of *x-y* data points in cm^{-1} units. Since the fit to the data is visual, there is no limit on the number of points allowed in the ABS spectrum and the spectra were thus converted from nm units to evenly spaced cm^{-1} points, normalised and used in the SOS calculations.

RR Spectra

The procedure for recording RR spectra and measuring accurately the relative intensity ratios of the successive members of a progression are detailed in Appendix A1. RR spectra of each of the compounds $(TBA)_2Re_2Br_8$, $(TBA)_2Re_2I_8$ and $(NH_4)_5Mo_2Cl_9.H_2O$ were recorded using a laser excitation wavenumber falling within the observed $^1(\delta^* \leftarrow \delta)$ ABS band; where possible, the wavenumber was chosen so as to avoid masking of the higher overtones of the ν_1 progression by

fluorescence. Thus, the excitation wavenumbers ($\tilde{\nu}_0$) used in each case were 15,453 cm^{-1} (Kr^+) for $[Re_2Br_8]^{2-}$, 13,297 cm^{-1} (Kr^+) for $[Re_2I_8]^{2-}$, and both 19,345 cm^{-1} (Ar^+) and 19,200 cm^{-1} (Kr^+) for $[Mo_2Cl_8]^{4-}$. For the Re(III) ions, only one excitation wavenumber produced a RR spectrum with a sufficiently long progression in the ν_1 mode to enable an SOS study to be made. For the $[Mo_2Cl_8]^{4-}$ ion, two excitation wavenumbers were used so as to provide a check of the consistency of the SOS method in fitting two sets of RR intensity ratios for a single compound, recorded with different $\tilde{\nu}_0$ values. It should be noted that, owing to strong fluorescence, it has not yet been possible to obtain a RR spectrum of the $[Re_2Cl_8]^{2-}$ ion with a sufficiently long progression in ν_1 to allow accurate fitting via the SOS method.

Samples were held in a pressed halide disk and spectra were recorded at ~77 K. These spectra are shown in Figs 3.8 ($[Re_2Br_8]^{2-}$), 3.9 ($[Re_2I_8]^{2-}$), 3.10 ($[Mo_2Cl_8]^{4-}$, $\tilde{\nu}_0$ = 19,345 cm^{-1}) and 3.11 ($[Mo_2Cl_8]^{4-}$, $\tilde{\nu}_0$ = 19,200 cm^{-1}) respectively. For $[Re_2Br_8]^{2-}$, a spectrum of a solution of $(TBA)_2Re_2Br_8$ in acetonitrile (1.0 mM) at 295 K was also recorded and is shown in Fig. 3.12.

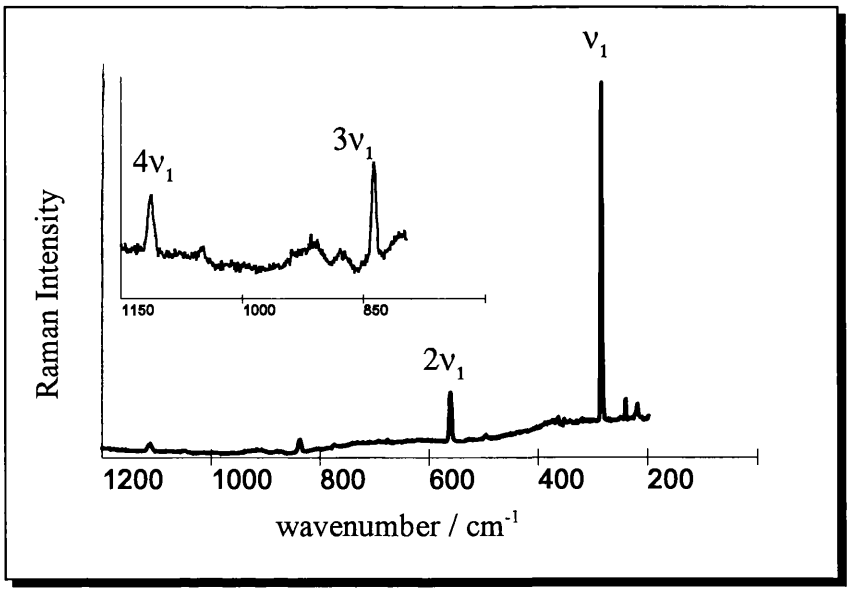

Fig. 3.8 RR spectrum of $(TBA)_2Re_2Br_8$ as a pressed KBr disk at ~ 77K.

Excitation wavenumber ($\tilde{\nu}_0$) : 15,453 cm^{-1}

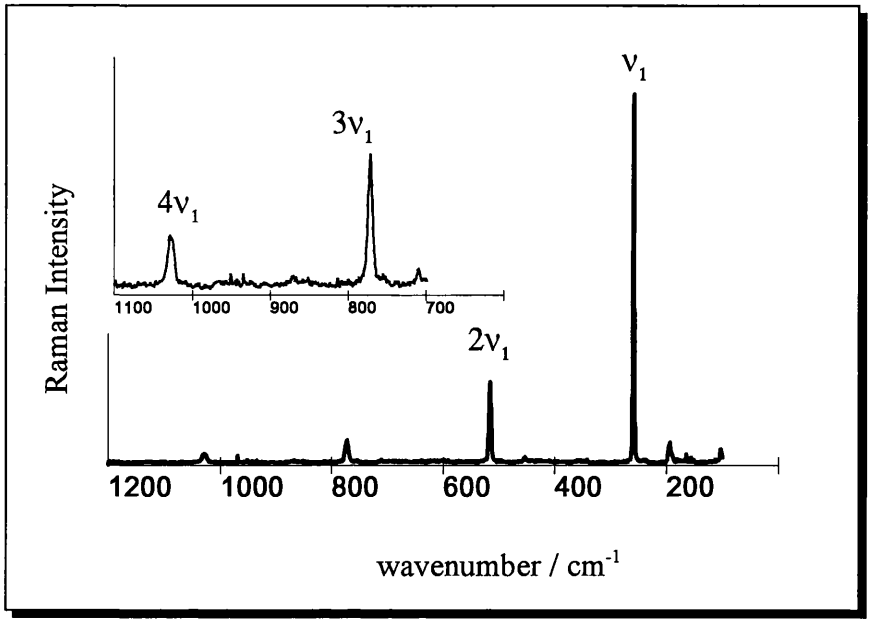

Fig. 3.9 RR spectrum of $(TBA)_2Re_2I_8$ as a pressed CsI disk at ~ 77K. Excitation frequency ($\tilde{\nu}_0$) 13,297 cm^{-1}.

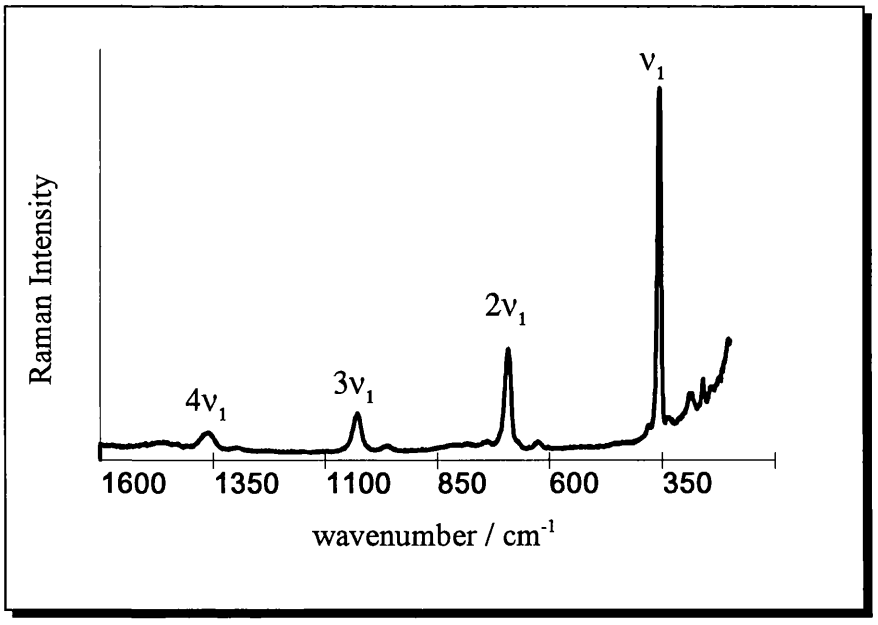

Fig. 3.10 RR spectrum of $(NH_4)_5Mo_2Cl_9.H_2O$ as a pressed KCl disk at ~ 77K. Excitation frequency ($\tilde{\nu}_0$) 19,345 cm^{-1}.

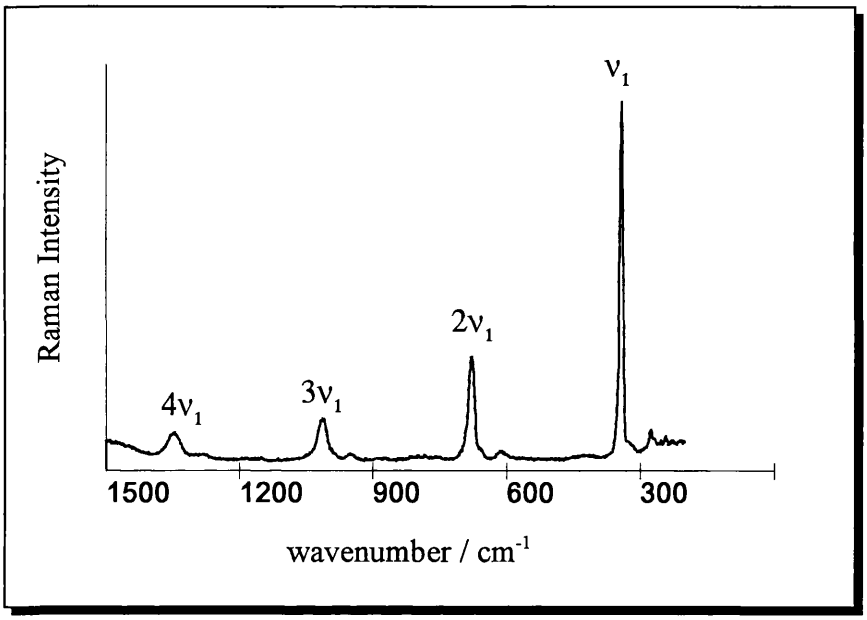

Fig. 3.11 RR spectrum of $(NH_4)_5Mo_2Cl_9.H_2O$ as a pressed KCl disk at ~ 77K. Excitation frequency ($\tilde{\nu}_0$) 19,200 cm^{-1}.

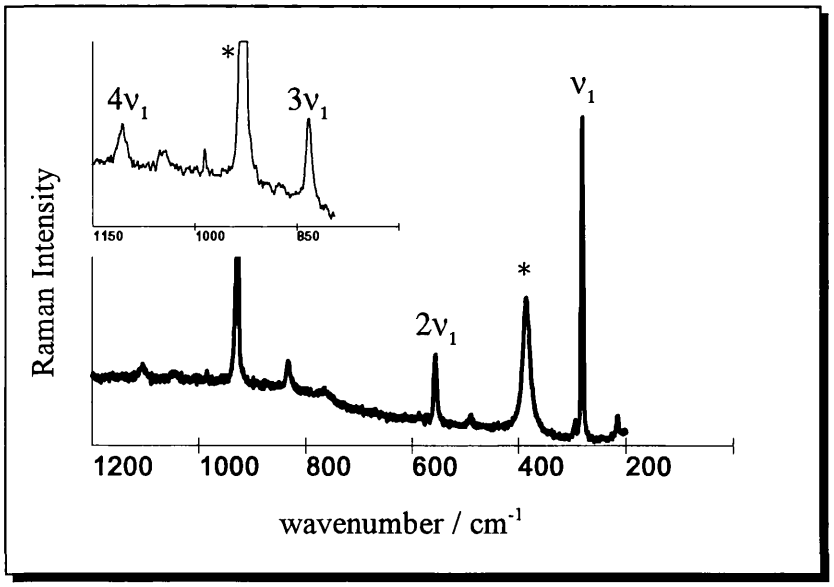

Fig. 3.12 RR spectrum of $(TBA)_2Re_2Br_8$ in acetonitrile solution (1.0 mM) at 295 K. Excitation frequency ($\tilde{\nu}_0$) 15,453 cm^{-1}. Starred peaks denote solvent bands

From these spectra, the relative intensity ratios of the first four members of the $n\nu_1$ progression were measured, as detailed in Appendix A1. Correction for

spectral response of the instrument and averaging over six spectra were performed. The measured and corrected intensity ratios for each of the spectra are shown in Table 3.3:

	$[Re_2Br_8]^{2-}$ disc,77 K	$[Re_2Br_8]^{2-}$ CH_3CN, 295 K	$[Re_2I_8]^{2-}$ disc,77 K	$(NH_4)_5Mo_2Cl_9.H_2O$ disc,77 K	
$\tilde{\nu}_0$ / cm^{-1}	15,453	15,453	13,288	19,200	19,435
$I(\nu_1)$	100	100	100	100	100
$I(2\nu_1)$	38.0	43.7	41.8	59.8	52.6
$I(3\nu_1)$	21.4	27.4	20.8	38.6	30.9
$I(4\nu_1)$	11.8	22.2	14.4	32.8	21.4

Table 3.3 Intensity ratios of the members of the $n\nu_1$ progression in the RR spectra of the $[M_2X_8]^{n-}$ ions (corrected for spectral response). **Errors** ≤ 10%.

3.4 Results

The SOS calculations were carried out on the data shown in section 3.3. For each set of ABS and RR data, a set of parameter values, corresponding to the best fit to the experimental data, was found: these parameter values are shown in Table.3.4. In this table the values in parentheses are the percentage changes in the parameter from its ground state value. *s* denotes the spread of the Gaussian distribution, $P(\omega)$ (or $P(\tilde{\nu})$ in wavenumbers), required to take account of thermal and inhomogeneous broadening in the solution spectrum recorded at 295 K (see 2.2). The phenomenological lifetime factor, Γ, takes account of homogeneous broadening and multimode effects.

	$[Re_2Br_8]^{2-}$	$[Re_2Br_8]^{2-}$	$[Re_2I_8]^{2-}$	$[Mo_2Cl_8]^{4-}$
	CH_3CN	disc	disc	disc
$\tilde{\nu}_g$ / cm^{-1}	276	276	257	338
$\tilde{\nu}_e$ / cm^{-1}	255 (-7.6%)	255 (-7.6%)	240 (-6.6%)	336 (-0.6%)
Δ	2.2	2.2	2.1	3.4
δ / pm	8.1 (3.6%)	8.1(3.6 %)	7.9 (3.5%)	15.4 (7.1%)
m	0.08	0.08	0	0
Γ / cm^{-1}	225	225	280	280
s / cm^{-1}	75	0	0	0
T / K	295	77	77	77
$E_{0\text{-}0}$ / cm^{-1}	13,580	13,520	12,420	16,345

Table 3.4 Calculated parameter values for the ν_1 co-ordinate for the $^1\delta\delta^*$ state of $[M_2X_8]^{n-}$ ions using ABS and RR intensity data

The corresponding fits of the calculated and experimental ABS profiles are shown in Figs. 3.13 - 3.16. The calculated RR intensity ratios are shown in Table 3.5, and show good agreement with the measured ratios in Table 3.3.

	$[Re_2Br_8]^{2-}$	$[Re_2Br_8]^{2-}$	$[Re_2I_8]^{2-}$	$[Mo_2Cl_8]^{4-}$	
	disc, 77 K	CH_3CN, 295 K	disc, 77 K	disc, 77 K	
$\tilde{\nu}_0$ / cm^{-1}	15,453	15,453	13,288	19,200	19,435
$I(\nu_1)$	100	100	100	100	100
$I(2\nu_1)$	37.4	46.6	42	59.7	54.3
$I(3\nu_1)$	20.2	27.9	21.4	37	36.9
$I(4\nu_1)$	13.3	19.3	11.7	28.1	24.4

Table 3.5 Calculated RR intensity ratios for $[M_2X_8]^{n-}$ ions

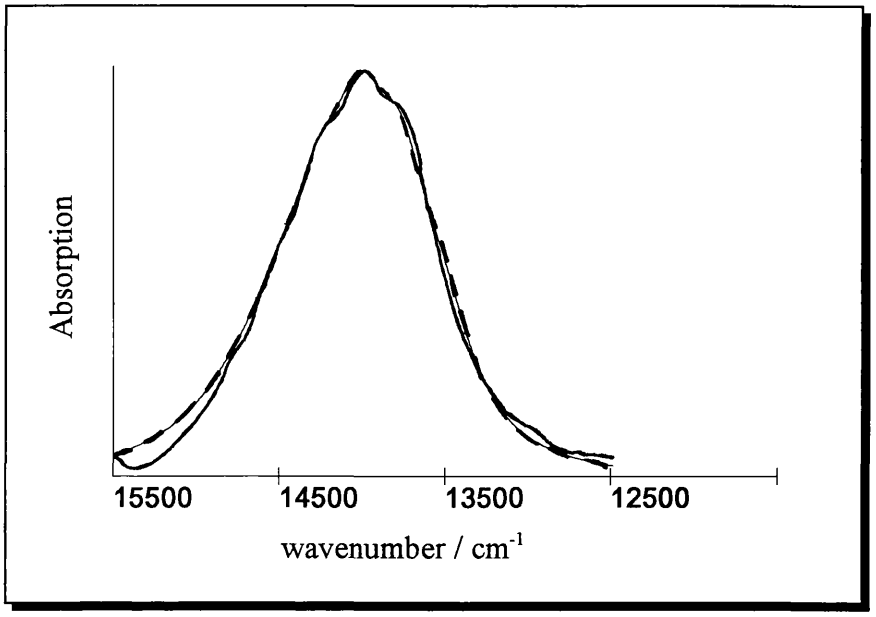

Fig. 3.13 Comparison of the experimental (—) and calculated (---) normalised ABS profiles for $[Re_2Br_8]^{2-}$ in the solid state at ~ 77 K.

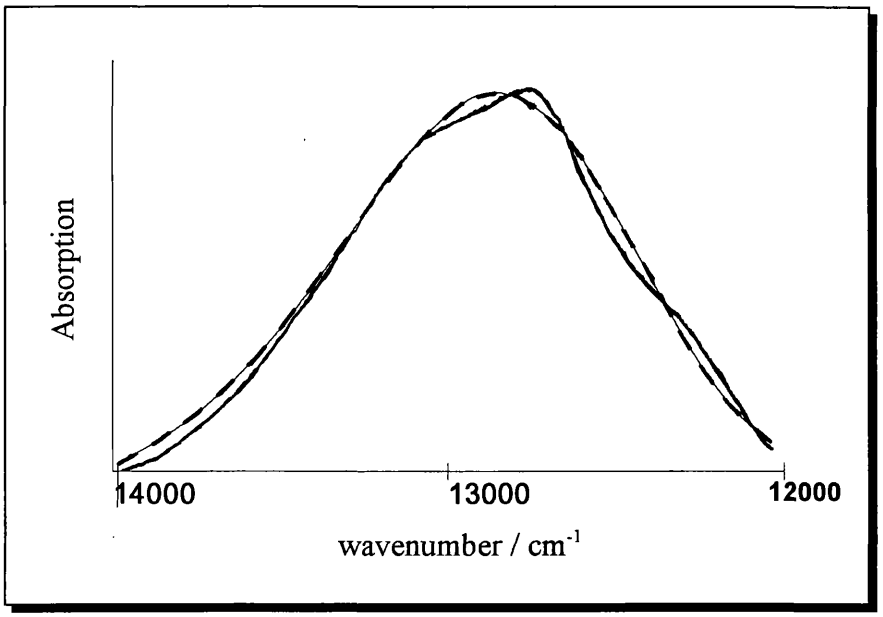

Fig. 3.14 Comparison of the experimental (——) and calculated (---) normalised ABS profiles for $[Re_2I_8]^{2-}$ in the solid state at ~ 77 K

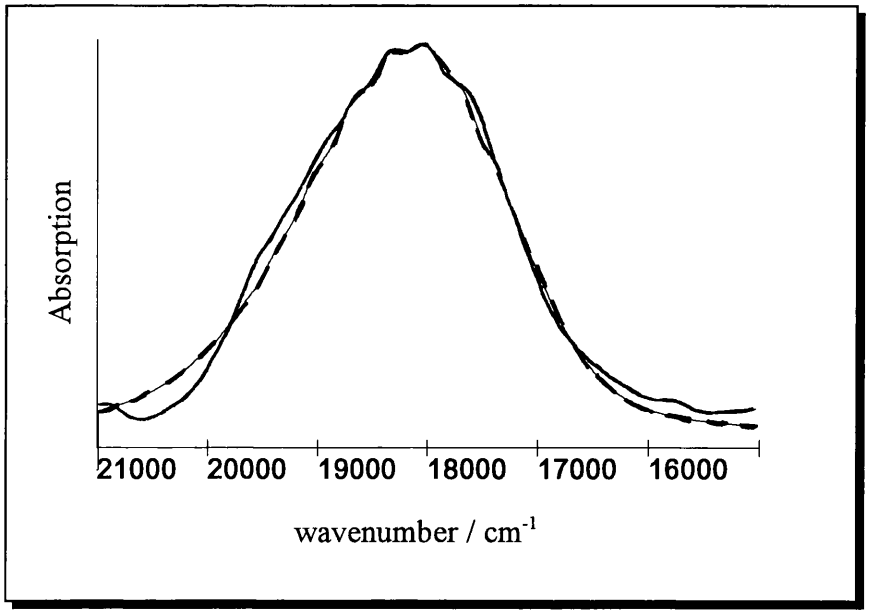

Fig. 3.15 Comparison of the experimental (——) and calculated (---) normalised ABS profiles for $[Mo_2Cl_8]^{2-}$ in the solid state at ~ 77 K.

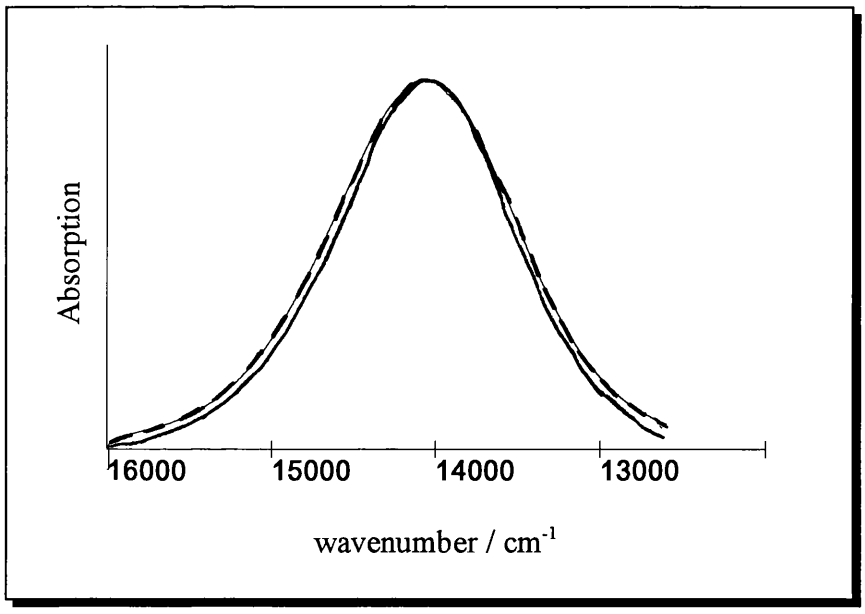

Fig. 3.16 Comparison of the experimental (——) and calculated (---) normalised ABS profiles for $[Re_2Br_8]^{2-}$ in solution at 295 K.

The errors on the value of any parameter in Table 3.4 can be estimated by keeping all the other parameters at constant values and changing the value of the particular parameter until the fit is significantly worsened. In this way it is estimated that $\tilde{\nu}_e$ is known to ± 3 cm^{-1} and Γ to ± 10 cm^{-1}.

Table 3.4 contains a value for a dimensionless displacement, Δ, along the ν_1 normal co-ordinate. Clearly, to be meaningful, this value must be converted to a bond length change. If it is assumed that the ν_1 mode and co-ordinate may be adequately represented by a local ν(MM) stretch, then a 'pseudo-diatomic' approximation can be used. The reduced mass of the vibrating species is then assumed to be that of an M_2 diatomic and the conversion [3.39]

$$\Delta = \left(\frac{\omega_g \mu}{\hbar}\right)^{\frac{1}{2}} \delta(\text{M-M}) \qquad (3.1)$$

can be made, where $\omega_g = 2\pi c\tilde{\nu}_g$ is the angular frequency of the ν_1 mode, μ is the reduced mass of the M_2 vibrating species (in kg) and δ(M-M) is the M-M bond length change in metres. The merit of this diatomic approximation will be assessed in further detail in chapter 4. At this stage, Eq. 3.1 is assumed to provide a useful conversion to a meaningful bond length change along the M-M axis. The error in δ(M-M) can be estimated using the above method for estimating the error in Δ: it is estimated that δ(M-M) is known to $\pm$ 0.5 pm.

It should be noted that it was not necessary in any case to include Duschinsky mixing involving the ν_1 mode and any other totally symmetric mode such as ν(MX). Addition of such mixing was not found to significantly improve the fit to either type of data.

3.5 Discussion

From Table 3.4, it can be seen that the general trend in the values of $\tilde{\nu}_e$ and δ(M-M) is one which shows an increase in the M-M bond length and a decrease in the wavenumber of the ν_1 mode in the $^1\delta\delta^*$ excited state. This is consistent with the electronic transition being one which takes an electron from a bonding to an antibonding orbital. Two important features can be seen in Table 3.4:

(1) The parameter values $\tilde{\nu}_e$ and δ(M-M) for the $[Re_2Br_8]^{2-}$ ion are calculated to be the same for the solid-state (~ 77 K) and solution (295 K) calculations

(2) The percentage changes in the wavenumber of the ν_1 mode $\{(\tilde{\nu}_e - \tilde{\nu}_g)/\tilde{\nu}_e\}$ and in the M-M bond length $\{\delta(M\text{-}M)/ r(M\text{-}M)\}$ are seen to be fairly uniform for the two Re(III) ions. The same percentage changes are markedly different for the $[Mo_2Cl_8]^{4-}$ ion for which a very large percentage change in the bond length and very small percentage change in the ν_1 mode wavenumber are seen. The value of $\tilde{\nu}_e$ = 336 cm^{-1} for this ion is in good agreement with that found from vibronic structure on single-crystal electronic absorption spectra of the K^+ salt of this ion at 80 K[3.23]. Furthermore, a luminescence study of this ion, as the $(enH_2)^{2+}$ salt, showed that the separation of the maximum of the $^1(\delta^* \leftarrow \delta)$ absorption and corresponding emission band is approximately twice as large for the $[Mo_2Cl_8]^{4-}$ ion as for the $[Re_2Cl_8]^{2-}$ ion [3.25]. This parameter can give a qualitative indication of the magnitude of Δ, or δ(M-M), which would therefore be expected to be larger for this $[Mo_2Cl_8]^{4-}$ ion than for the $[Re_2Cl_8]^{2-}$ ion. While such spectroscopic measurements may be expected to vary slightly for different salts of the $[Mo_2Cl_8]^{4-}$ ion, similar behaviour for the $(NH_4)^+$ ion would be expected. Thus the unusual values for $\tilde{\nu}_e$ and δ(M-M) for the Mo(II) ion shown in Table 3.4 can be supported from other experimental evidence and are unlikely to result from inappropriate theoretical models.

These two features will be discussed below.

(1) Comparison of the structure of the $^1\delta\delta^*$ state of the $[Re_2Br_8]^{2-}$ in solution (295 K) and in the solid state (77 K)

The results in Table 3.4 show a value of $\tilde{\nu}_e$ = 255 cm^{-1} and δ(M-M) = 8.1 pm for the $[Re_2Br_8]^{2-}$ ion in the $^1\delta\delta^*$ state calculated using both solution data (295 K) and solid state data (80 K). As mentioned in section 3.1, a TR^3 study of this ion in solution[3.31] found a value of $\tilde{\nu}_e$ = 262 cm^{-1} and a corresponding value for

δ(M–M) of 3.7 pm was calculated on the basis of empirical force constant rules, based on an M_2 diatomic approximation for the ν_1 vibrational mode.

The value $\tilde{\nu}_e$ = 255 cm^{-1} is in agreement with that observed from vibronic structure on the low-temperature single crystal electronic absorption spectrum of the $^1(\delta^* \leftarrow \delta)$ transition [3.15]. The observation in the TR^3 study of a different $\tilde{\nu}_e$ value for the same ion in solution was attributed to the presence of a torsional distortion of the molecule about the M-M axis in solution to adopt a staggered, D_{4d} structure in the $^1\delta\delta^*$ state: since steric repulsion between the now-staggered halide atoms is reduced, this excited state may be expected to show a shorter M-M bond length than the corresponding eclipsed (D_{4h}) excited state. Hence the value of δ(M–M)(D_{4d}) will be less than that of δ(M–M)(D_{4h}). Furthermore, with the metal atoms in closer proximity in the staggered $^1\delta\delta^*$ excited state, the value of $\tilde{\nu}_e$ is then expected to be higher than that seen for the $^1\delta\delta^*$ excited state of the ion in the solid state ABS spectrum at low temperatures. It was also thought that the shorter timescale of the vibronic experiment may preclude the observation of a relaxed structure in the $^1\delta\delta^*$ state, owing to the barrier to rotation imposed by the rigid crystal environment.

The results in Table 3.4, however, suggest that the structure observed in the SOS study of the $^1\delta\delta^*$ state of the $[Re_2Br_8]^{2-}$ in solution is identical to that in the solid state. The results in both media match that found from the low-temperature solid-state ABS spectrum, which is thought to be characteristic of an eclipsed conformation for the excited state. Accordingly, from the SOS results, the $^1\delta\delta^*$ state observed in solution must also be assigned to an eclipsed (D_{4h}) geometry.

As a result of analysing both ABS and RR data, the SOS method can allow the evaluation of an excited state in solution on the same timescale as that of the usual vibronic analysis of low-temperature solid-state ABS spectra. The

ABS process takes place 'vertically' in nuclear space (according to the Franck-Condon principle). In order for phase coherence between the incident and scattered photons in the RR process to be retained, conventional RR scattering must also take place in a time shorter than the lifetime of the vibronic state(s) involved in resonance, i.e. before any vibrational decay has taken place.

Tubino et al [3.40] have shown from a study of the RR scattering of molecular I_2 that the lifetimes of the resonant vibronic states in the RR process are strongly dependent on the molecular environment. In the gas phase, at low pressure, the lack of non-radiative or collisional decay routes means that the lifetimes, and hence the timescale of RR scattering, may be as long as 10^{-8} - 10^{-11}s. However, in condensed media, or in a high pressure gas, strong interactions between the molecule and its environment produce many damped multiphonon processes which can accompany electronic ABS. The lifetimes of the vibronic states are shortened ($< 10^{-12}$ s), and the ABS band is broadened as a result.

Thus, the use of condensed medium-RR data in the SOS method means that the excited state observed via this method will always be one in which no vibrational relaxation has taken place, and in this case, it is expected that the timescale of observation is $< 10^{-12}$s.

The result of the SOS study for the $[Re_2Br_8]^{2-}$ ion is thus that, even in solution, a different structure of the ion in the $^1\delta\delta^*$ state is observed on this 'vibronic' timescale, in comparison with that observed in a nanosecond TR^3 experiment. The agreement between the values of the structural parameters for the excited state in solution with those found in the solid-state point to the assignment of an eclipsed geometry for this state in both media. It therefore appears that an eclipsed (D_{4h}) excited state is initially prepared by optical ABS and RR, even in solution.

In drawing the above conclusion, it has been assumed that the change in the solvent for the $[Re_2Br_8]^{2-}$ ion between the TR^3 study (where CH_2Cl_2 was used)

and the SOS study (where CH_3CN was used) does not affect significantly the structure of the excited state. It was not possible to record the RR spectra for the SOS study in dichloromethane because of the presence of an intense solvent band at 282 cm^{-1} which obscures the ν_1 fundamental band at 276 cm^{-1}. Proper separation of these bands to allow intensity measurements would require a concentration of $(TBA)_2Re_2Cl_8$ at which self-absorption would be significant (Appendix A1).

However, several observations indicate that the solvent has little effect on the $^1\delta\delta^*$ excited state. Firstly, the $^1(\delta^* \leftarrow \delta)$ ABS maximum shifts only 25 cm^{-1} on changing between the two solvents, indicating that no significant change in the excited state takes place on this timescale. Secondly, the transient ABS spectrum of the $^1\delta\delta^*$ state, recorded on a nanosecond timescale, is seen to be identical in both solvents [3.31]. The RR spectrum in each solvent shows no progression in a torsional mode, and it is also seen that the transient kinetics of the $^1\delta\delta^*$ state of the structurally similar compound $Mo_2Cl_4(PBu_3)_4$ are insensitive to this change in solvent [3.30]. In light of these observations, a direct comparison between the results based on solutions in the two solvents has been made.

This study then allows a more complete picture of the nature and dynamics of the $^1\delta\delta^*$ state to be drawn. One interpretation is that the potential energy of the $^1\delta\delta^*$ state is a function of the torsion angle, χ of the ligand groups on the metal centres (see Fig. 3.2). Thus, there is a shallow minimum at $\chi = 0°$ and a lower energy configurational minimum at $\chi = \pi/4$ where the halide atoms lie in a staggered geometry†. This is represented in Fig. 3.17.

†The retention of a minimum at $\chi = 0$, despite there being formally no δ bond in this state may reflect the inadequacy of the $\sigma^2\pi^4\delta^1\delta^{*1}$ description of this state. It is likely that there is a contribution from some other configuration, possibly one with some δ bonding character, and that this may provide a barrier to rotation about the M-M axis.

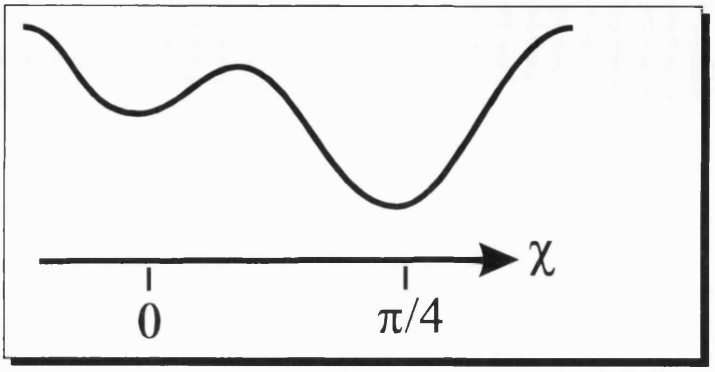

Fig. 3.17 - Schematic representation of the potential energy of the $^1\delta\delta^*$ excited state in the dimension of the torsional co-ordinate.

In the dimension of the metal-metal co-ordinate (ν_1), the potential energy of the state is then also dependent on χ as well as on the M-M bond distance, r, as shown in Fig. 3.18. r is expected to be larger for the eclipsed configuration.

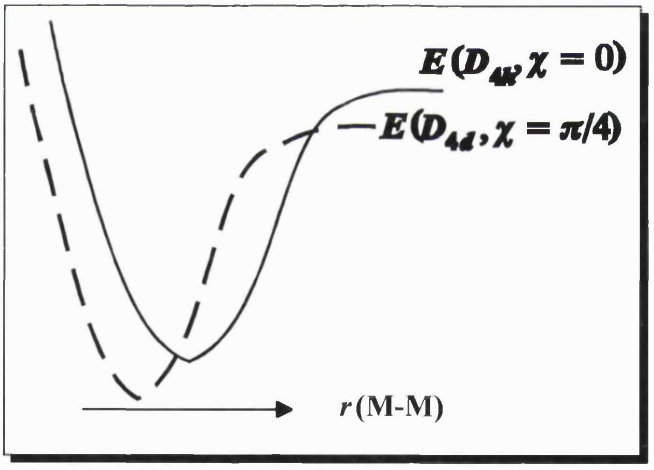

Fig. 3.18 - Schematic representation of the periodic potential energy of the $^1\delta\delta^*$ excited state in the dimension of the M-M co-ordinate, showing its dependence on χ

Apparently, only the D_{4h} minimum (the solid line in Fig. 3.18) is probed by the ABS and conventional RR processes. However, on a longer timescale, the local D_{4d} minimum can be reached, either by direct excitation above the barrier in the χ co-ordinate and then decay to the lower energy minimum, or by thermal repopulation of higher vibrational levels of this low-frequency mode followed by

vibrational decay into the D_{4d} minimum. Thus, when the excited state is probed nanoseconds after excitation (via the TR^3 experiment), the relaxed D_{4d} minimum is observed, and hence different values of $\tilde{\nu}_e$ and r(MM) are found.

It is not possible using the SOS method to estimate the timescale of the vibrational relaxation concurrent with twisting about the M-M axis. However, it is notable that a previous kinetics study of the $[Re_2Cl_8]^{2-}$ and $[Mo_2Cl_8]^{4-}$ ions in solution found that a transient absorption, which was attributed to the staggered $^1\delta\delta^*$ excited state, appeared in fewer than 20 ps [3.30]. This study also showed the presence of two long-lived transients after excitation of the compound $Mo_2Cl_4(PBu_3)_4$ to the $^1\delta\delta^*$ state. On the basis of the large steric bulk of the PBu_3 ligand, which is thought to prevent any twisting about the M-M axis, the first of these transients with a 4 - 9 ns lifetime was assigned to the eclipsed $^1\delta\delta^*$ excited state. The second transient, with a lifetime of 90 - 115 ns, was assigned to a distorted chemical intermediate of the molecule to which the $^1\delta\delta^*$ state relaxed. In view of the above model for the potential of the $^1\delta\delta^*$ excited state, it could be argued that, since rotation about the M-M axis in this case may only be partial, or may take longer than for the $[M_2X_8]^{n-}$ ions, then the first transient may be assigned to the eclipsed $^1\delta\delta^*$ state, and the second, which has a low oscillator strength to the ground state, could be assigned to a partially staggered conformation of $^1\delta\delta^*$ state. Thus, the 'two-step' decay process of the $^1\delta\delta^*$ state can be observed on a longer timescale for these sterically hindered compounds. However, without similar TR^3 studies of this ion, and with no evidence to indicate that such twisting is even possible with the large PBu_3 ligands, then such an interpretation must remain speculative.

The behaviour of the $^1\delta\delta^*$ state of the $[M_2X_8]^{n-}$ ions in the solid state on these longer timescales cannot be predicted. In these cases, the crystal environment may raise the barrier to rotation and the eclipsed structure may persist. Alternatively, only partial staggering may be possible. However, the lack of mirror image symmetry between the ABS and luminescence bands for these

ions, even in the solid state, may point to some relaxation to a partially staggered structure in the excited state on longer timescales.

One alternative model for the excited state is that there exists, below the $^1\delta\delta^*$ state of D_{4h} geometry, a separate $^1\delta\delta^*$ electronic state, of D_{4d} geometry. A transition from the ground electronic state to the latter state has a very low oscillator strength, thus accounting for the observation of only a single band in the ABS spectrum in this region. However, interaction between the two states is sufficiently strong to allow relaxation from the former, which is initially populated upon excitation, to the latter. This relaxation takes place on the timescale of the pump-probe TR^3 experiment, but is still unobservable via either the optical absorption or RR experiments.

While this explanation can explain adequately the SOS results, the coupling between two excited state so close in energy is likely to be non-adiabatic. Thus, a breakdown of the Born-Oppenheimer approximation might be expected. If this were the case, however, some failure of the SOS method, the theory of which involves the Born-Oppenheimer approximation, would also be expected. All the experimental data was, however, able to be fitted within the standard SOS model. It is therefore likely that the former explanation, involving a single $^1\delta\delta^*$ state with a double minimum in the potential, is the more plausible.

This 'double minimum' potential model can also explain the unexpected absence of bands due to even quanta of the torsional mode in the RR spectrum in solution. In a similar case, that of the $\pi - \pi^*$ transition in ethylene, where the molecule relaxes from an eclipsed ground state structure to a staggered conformation in the excited state, a progression in even quanta of the torsional mode can be seen in the RR spectrum in solution [3.41]. In the case of the $[Re_2Br_8]^{2-}$ ion, the RR experiment is able to probe the only the eclipsed excited state. Since there is no displacement along the torsional co-ordinate in the excited

state, then no progression in the torsional mode is expected to be observed in either the RR or ABS spectra.

These results therefore show that, rather than the $^1\delta\delta^*$ state of the ion *necessarily* being of either eclipsed (D_{4h}) or staggered (D_{4d}) geometry, the potential energy of the $^1\delta\delta^*$ state can be represented by a function of the torsion angle, χ and thus, both structures (D_{4h} and D_{4d}) may be adopted. The observation of one or other of these structures is then critically dependent on the nature of the experiment used to probe the excited electronic state. It appears that, in solution, the optical ABS and RR experiments probe an eclipsed structure, while the nanosecond TR[3] method probes the staggered, relaxed structure. In the solid state, it is believed that twisting about the M-M axis may not be possible, and that the eclipsed structure may persist for the $^1\delta\delta^*$ state, even after vibrational decay has occurred. However, with only ABS and conventioanl RR experimental data available, these results are unable to determine if this is the case.

Therefore, it is proposed that the results of an SOS calculation on these species will reflect structural changes relevant to observation of an *eclipsed* $^1\delta\delta^*$ state. Direct comparison should therefore be possible between parameter values for these systems and those for systems where torsional distortion about the M-M axis is thought to be prevented (even in solution) by the presence of bulky ligands (e.g. $Mo_2X_4(PMe_3)_4$ compounds).

(2) Trends in the magnitudes of the $\tilde{\nu}_e$ and δ(M-M) parameters

While the results of the above calculations on the $[Re_2Br_8]^{2-}$ ion in two different media provide a clear conclusion about the structure of the $^1\delta\delta^*$ state, comparisons of trends in the magnitudes (or percentage changes) in the various excited state parameters *between* members of a series such as $[Re_2X_8]^{2-}$ (X= Br or I), or between the Mo(II) and Re(III) ions are more problematic.

In these cases, careful consideration must be given to the numerous, often interrelated factors which may affect not only the electronic structure and bonding in the ground and excited states, but also the vibrational analyses. For example, although the two series of ions $[Re_2X_8]^{2-}$ and $[Mo_2X_8]^{4-}$ are structurally and electronically similar, and their ground electronic states may both be described by the $\sigma^2\pi^4\delta^2$ configuration of the M-M quadruple bond, care must be taken when comparing the M-M bonding parameters in the $^1\delta\delta^*$ state. The different nature of the metal atoms, as well as their differing formal oxidation states, together with the change in overall charge of the ion and number and size of the counter-ions in the unit cells, mean that sweeping generalisations about the difference in the M-M bonding in these ions are hazardous.

Even within a series of compounds where the metal remains the same and only the halide changes (a 'halide series'), e.g. $[Re_2X_8]^{2-}$ or the $Mo_2X_4(PMe_3)_4$ compounds (X = Cl, Br or I), simple comparisons must be made with caution. The description of the M-M bonding in these systems, given in chapter 1, is, without doubt, an oversimplification, though helpful in providing a qualitative understanding of these systems. The effect of the halide ions on the M-M bonding, and hence on the changes in the M-M co-ordinate in the $^1\delta\delta^*$ excited state must be considered. It is therefore necessary at this stage to re-examine the sensitivity to the halide of structural and spectroscopic measurements and calculations which are diagnostic of the M-M bonding in these systems.

3.6 Re-examination of M-M bonding: the role of the halides

Many studies have focused on the assessment of the role of the ligands, especially halides, in metal-metal bonding in quadruply bonded dimers. The description of the quadruple M-M bond, given in section 1.7 [3.1], which treats the δ-bond as arising from overlap of pure metal d_{xy} orbitals, is, at least, simplistic, although qualitatively extremely helpful. However, even simple electronic structure

calculations [3.5, 3.6] have predicted up to 23% ligand character in the δ-bonding orbital.

In addition to electronic structure calculations, measurements of the energy and intensity of the $^1(\delta^* \leftarrow \delta)$ transition, the M-M bond length (r(M-M)) and the wavenumber of the ν_1 mode ($\tilde{\nu}_g$), assigned to the totally symmetric ν(MM) stretch, are often used to characterise the M-M bonding in a particular compound. The sensitivity of these 'diagnostic' values to the nature of the halide in a series such as $[Re_2X_8]^{2-}$ or $Mo_2X_4(PMe_3)_4$ (X = Cl, Br or I) may therefore also allow some insight into the role played by the halide ligands in the general M-M bonding.

The behaviour of these four observables as a halide series (such as $[Re_2X_8]^{2-}$ or $Mo_2X_4(PMe_3)_4$ (X = Cl, Br or I)) is traversed (i.e. Cl - Br - I), is summarised in Table 3.6, which also contains data for the ion $[Mo_2Cl_8]^{4-}$. As the halide becomes more reducing, so the energy of the $^1(\delta^* \leftarrow \delta)$ transition decreases, and its intensity increases. On the other hand, r(M-M) and $\tilde{\nu}_g$ are less sensitive to a change in the identity of the halide.

The effects of the halide on the nature of the M-M bonding, as seen from the observations summarised in Table 3.6, and from electronic structure calculations, are discussed below.

Compound	$\tilde{\nu}$ [$^1(\delta^* \leftarrow \delta)$] / cm^{-1}	ε_{max} [$^1(\delta^* \leftarrow \delta)$] / $M^{-1}cm^{-1}$	r(M-M) /Å	$\tilde{\nu}_g$ / cm^{-1}
$[Re_2Cl_8]^{2-}$	14,700 [3.14]	2,340	2.222 [3.44]	276 [3.20]
$[Re_2Br_8]^{2-}$	14,000 [3.42]	2,980	2.226 [3.35]	276 [3.20]
$[Re_2I_8]^{2-}$	12,800 [3.17]	-	2.245 [3.7]	257 [3.20]
$[Mo_2Cl_8]^{4-}$	19,610 [3.18]	960	2.15 [3.35]	338 [3.12]
$Mo_2Cl_4(PMe_3)_4$	17,090 [3.43]	3,110	2.13 [3.45]	355 [3.44]
$Mo_2Br_4(PMe_3)_4$	16,720 [3.43]	4,060	2.125 [3.43]	353 [3.43]
$Mo_2I_4(PMe_3)_4$	15,720 [3.43]	5,250	2.127 [3.43]	343 [3.43]

Table 3.6 A comparison of the wavenumber and intensity of the $^1(\delta^* \leftarrow \delta)$ transition in solution, the M-M bond length, r(M-M) and $\tilde{\nu}_g$ for the ν_1 mode across the series $[Re_2X_8]^{2-}$ and $Mo_2X_4(PMe_3)_4$ (X = Cl, Br or I).

Electronic Structure Calculations and Bond Lengths

Several electronic structure calculations using a variety of techniques have been performed on $[M_2X_8]^{n-}$ ions [3.3 - 3.6, 3.46 - 3.48], the compounds $Mo_2X_4(PR_3)_4$ (X = Cl, Br or I, R = alkyl) [3.49, 3.51] and quadruply bonded carboxylate species of the type $Mo_2(O_2CR)_4$ [3.52, 3.53]. These calculations estimate the energy separation of, and percentage atomic contributions to the M-M and M-L valence molecular orbitals. While they are frequently unable to estimate correctly the transition energies between states (as a result of neglecting electron correlation and/or configuration interaction terms), the energetic separation of the valence orbitals predicted in these studies have been supported in some cases by PES measurements [3.49].

Obviously such structure calculations for these large and electron-rich molecules must involve approximation and will therefore have some deficiencies. However, the relative magnitudes of the contributions to the M-M bonding orbitals from the different atoms, and the energetic ordering of the orbitals

predicted will provide a useful insight into the sensitivity of the M-M bonding to the ligands in such molecules.

For all the molecules studied, the HOMO is confirmed as the predominantly metal-based δ-orbital, with the LUMO being the δ*. The general ordering of the M-M valence MOs is depicted in Fig. 3.19 with the $\delta > \pi > \sigma$ order confirmed.

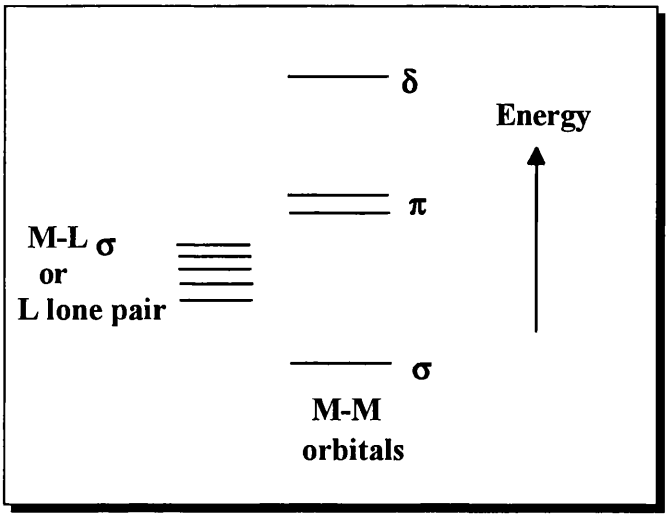

Fig. 3.19 Schematic ordering of the M-M bonding orbitals in quadruply bonded dimetallic species, as predicted from electronic structure calculations.

In general, all the M-M bonding orbitals in each species are predicted to contain some percentage ligand character, with up to 23% (Cl in the δ orbital of $[Re_2Cl_8]^{2-}$ [3.47]) or as little as 11% (Cl in the δ orbital of $[Mo_2Cl_8]^{4-}$[3.4]). The precise mixture of ligand orbitals with M-M orbitals depends not only on the molecular geometry, but also on the energetic proximity of the M-L bonding or L lone pair orbitals (of the correct symmetry) to the M-M bonding manifold. Fig. 3.19 also shows a typical region in which M-L bonding and/or L lone pair orbitals are predicted to occur.

This variable contribution of the ligands to the M-M bonding orbitals is easily demonstrated by the series $Mo_2X_4(PR_3)_4$ (X = Cl, Br or I) [3.50]. Initially,

for X = Cl, the Cl lone pair orbitals (of which some have the correct symmetry for mixing with the M-M δ bond) lie between the M-M σ and M-M π bonding regions. As the halide becomes more reducing, so the X lone pair orbitals increase in energy relative to the M-M bonding orbitals, and contribute more to the M-M π (X = Br) and finally M-M δ (X = I) bonding orbitals. This is reflected in the calculated percentage halide contributions to the M-M δ bond increasing in the order X = Cl (11%) < Br (17%) < I (26%) (see Table 3.7). Furthermore, a large percentage Br contribution to the M-M π bond is observed for X = Br. For all these compounds, the phosphorus lone pair orbitals are too low in energy to contribute to the M-M bonding manifold.

	$Mo_2Cl_4(PH_3)_4$		$Mo_2Br_4(PH_3)_4$		$Mo_2I_4(PH_3)_4$	
	%M	%X	%M	%X	%M	%X
δ	75	11	69	17	60	26
δ*	78	14	70	22	53	40

Table 3.7 Calculated percentage atomic contributions to the δ and δ* M-M bonding orbitals for the series of compounds $Mo_2X_4(PH_3)_4$ (X = Cl, Br or I) [3.50].

Although the figures from calculations using different models are not strictly comparable, those for $Mo_2(O_2CH)_4$ [3.52], $[Mo_2Cl_8]^{4-}$ [3.4], and $[Re_2Cl_8]^{2-}$ [3.47] are shown in Table 3.8.

	$Mo_2(O_2CH)_4$		$[Mo_2Cl_8]^{4-}$		$[Re_2Cl_8]^{2-}$	
	%M	%O	%M	%Cl	%M	%Cl
δ*	86	14	93	7	67	21
δ	89	3	89	11	62	23

Table 3.8 Calculated percentage atomic contributions to the M-M δ and δ* bonding orbitals of $Mo_2(O_2CH)_4$, $[Mo_2Cl_8]^{4-}$, and $[Re_2Cl_8]^{2-}$.

In some cases, e.g. $Mo_2(O_2CR)_4$, M-M π bonding character is distributed through several MOs, each of which may also have some Mo-O σ or π bonding character. Thus, the interaction between the M-L and M-M bonding manifolds can be considerable: specifically in this case it is thought that Mo-O π and Mo-Mo π interactions greatly stabilise and lower the energy of the Mo-Mo π bonding orbitals [3.46,3.53]. Overall, a distribution of M-M bonding charge (especially π bonding) over several orbitals can be seen for both the $Mo_2(O_2CR)_4$ and $Mo_2X_4(PH_3)_4$ molecules, and to some extent for the $[Re_2Cl_8]^{2-}$ ion.

Thus it is clear that the earlier simplistic model of M-M bonding as arising purely from overlap of metal d orbitals requires some modification, and that contributions from, and interactions with M-L bonding orbitals or L lone pair orbitals can lead to significant ligand character in the M-M bonding orbitals.

It might be expected that such variable percentage contribution of the metal d orbitals to the δ bond across a halide series such as $Mo_2X_4(PR_3)_4$ (X = Cl, Br or I) would be reflected in a variation of the M-M bond length. However, as seen in Table 3.6, *r*(MoMo) is found to be very similar for such a series (with R = PMe_3). One suggested explanation for this observation is that the M-M σ bond composition is calculated across this series to be relatively insensitive to X. If this is the most dominant component of the M-M quadruple bond, then the overall bond length might also be expected to be less sensitive to X. However, it is thought that the M-M π bond will be at least as significant in determining the M-M bond length in quadruply bonded dimers [3.54]; the composition of this MO is calculated to be strongly sensitive to X.

However, when the overlap populations (Mulliken populations) for the M-M σ, π and δ bonding orbitals are calculated (for $Mo_2X_4(PH_3)_4$; X = Cl, Br or I), as well as the **total** overlap population for the whole bond, it is seen that the *percentage* contribution of the δ overlap to the *total* bond overlap is less sensitive to X (12% X = Cl, 11, X = Br, 10%, X = I) [3.50]. Thus, while the composition

of the δ bonding orbital may change as X becomes more reducing, the contribution of the δ bonding electron density to the total M-M bond is relatively uniform across the series [3.50, 3.51]. This trend, combined with the similar behaviour of the σ and π orbitals, may result in a uniformity of the M-M bond length across the series.

The question then arises as to whether or not the *change* in the M-M bond length, *r*(MM), on formally eliminating the δ bond during the $^1(\delta^* \leftarrow \delta)$ transition, will also be insensitive to the ligands in these, and other, compounds. With the percentage contribution of the metal atoms to the δ bonding MO in a halide series estimated to vary as X varies, it might be expected that differing percentage changes in M-M bond length in the $^1\delta\delta^*$ state might be observed.

Energies and Intensities of $^1(\delta^* \leftarrow \delta)$ Transitions

A strong sensitivity to the ligands of the energies and intensities of the $^1(\delta^* \leftarrow \delta)$ transition for many quadruply bonded species, is generally observed (see Table 3.6). Initial attempts to relate the higher $^1(\delta^* \leftarrow \delta)$ energy with increasing δ-bond strength were thwarted by the apparently contradictory trend in the intensities of these transitions [3.43]. Thus, as a halide series such as $Mo_2X_4(PMe_3)_4$ (X = Cl, Br or I) is traversed, the transition is seen to red shift in energy, but also to increase in intensity.

A comprehensive study of the trends in the energies and intensities of the $^1(\delta^* \leftarrow \delta)$ transition across a number of quadruply bonded dimetallic systems has been given by Hopkins, Gray and Miskowski [3.42]. It was concluded that the relative energies of the four states arising from having two electrons in the δ/δ^* orbital manifold (the $^1(\delta)^2$, $^3\delta\delta^*$, $^1\delta\delta^*$ and $^1(\delta^*)^2$) are strongly dependent on the magnitude of a two-electron correlation term, *K*: this gives rise to the splitting of the triplet and singlet $\delta\delta^*$ states. Furthermore, being a measure of

electron-electron repulsion, this term typically decreases on going from a second row to a third row transition metal species as a result of the nephelauxetic effect. Inclusion of configuration interaction (CI) between the $^1(\delta)^2$ and $^1(\delta^*)^2$ states, which have the same symmetry, was seen to be important in determining the final energy of the $^1(\delta^* \leftarrow \delta)$ transition. These two factors (K and CI) explained the consistent underestimation of the transition energy by simple SCF calculations in which only orbital energies were calculated.

It was also noted that the halide atoms in such species as $[Re_2X_8]^{2-}$ and $Mo_2X_4(PMe_3)_4$ possessed a filled $p(\pi)$ orbital of the same symmetry as the δ-orbital (b_{2u} for D_{4h} molecular symmetry). These orbitals lie below the M-M δ-bonding manifold, as seen from the electronic structure calculations (as discussed above). Thus a ligand-to-metal-charge-transfer (LMCT) transition is possible which has the same polarisation as the $^1(\delta^* \leftarrow \delta)$ transition and involves the promotion of an electron from this ligand $p(\pi)$ orbital to the δ^* orbital. This LMCT transition will lie at higher energy than the $^1(\delta^* \leftarrow \delta)$ transition and is likely to have high intensity (characteristic of LMCT transitions). Owing to the symmetry matching of the LMCT excited state with the $^1\delta\delta^*$ excited state, it is possible for the two states to mix, via CI, as depicted in Fig. 3.20.

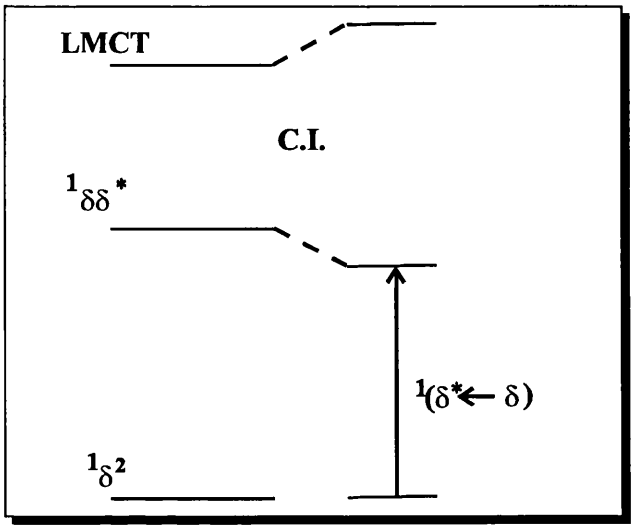

Fig. 3.20 CI involving the high-lying LMCT state and the $^1\delta\delta^*$ excited state for M-M quadruply bonded species.

Through this CI mixing, the $^1(\delta^* \leftarrow \delta)$ transition moves lower in energy and is able to 'steal' intensity from the very strongly allowed LMCT transition.

Two points about this mixing must be noted: first, it is likely that it is relatively small in all cases, due to the large energy separation of the $^1(\delta^* \leftarrow \delta)$ and LMCT transitions. It can be seen that the $^1(\delta^* \leftarrow \delta)$ transition is still predominantly a transition between metal δ and δ^* orbitals: only the ν_1 (ν(MM)) vibrational mode shows a significant progression in the ABS or RR spectra in all of the molecules studied. Furthermore, a large amount of excited state coupling of the type proposed, might be reflected in significant non-Condon coupling for totally symmetric vibrational modes (see section 1.4). This is not observed for the compounds studied here.

Secondly, as the halide becomes more reducing (X = Cl $\rightarrow$ Br $\rightarrow$ I) for a series of compounds such as $[M_2X_8]^{n-}$ ions or $Mo_2X_4(PMe_3)_4$ compounds, so the X $p(\pi)$ orbitals move closer in energy to the M-M bonding orbitals and the LMCT transition consequently decreases in energy, in accordance with the trend in optical electronegativities. Thus CI of the kind shown in Fig. 3.20 will be more effective. This can then explain the red-shifting and increase in energy of the $^1(\delta^* \leftarrow \delta)$ transition across these series of compounds as the halide becomes more reducing.

By contrast to the halide-containing species, the carboxylate compounds, $Mo_2(O_2CR_3)_4$ show high energy $^1(\delta^* \leftarrow \delta)$ transitions of low intensity. In these cases, the LMCT transition from the oxygen-bound ligand would occur at a much higher energy than the equivalent LMCT transition in a halide-containing species. Thus, the mixing depicted in Fig. 3.20 is weaker in these cases. These species are believed to show the 'intrinsic' energy and intensity of a $^1(\delta^* \leftarrow \delta)$ transition,

where the breaking of the weak δ-overlap is reflected in an inherently low intensity.

It is clear from the above discussion that the ligands in a quadruply bonded dimetallic molecule can affect the M-M δ bonding. Thus, a dependence of the orbital composition of the δ and δ^* orbitals, and of the spectroscopic parameters relating to the $^1(\delta^*\leftarrow\delta)$ transition, on the ligands are seen. However, often structural parameters, such as *r*(MM), remain largely insensitive to a change in the ligands. Furthermore, resonance with the $^1(\delta^*\leftarrow\delta)$ transition consistently produces significant enhancement in only the ν_1 (ν(MM)) mode in the RR spectrum.

All these factors must be taken into account when attempting to understand trends in the structural changes in the $^1\delta\delta^*$ state of these molecules. While the orbitals involved in the resonant transition, and the transition itself, contain ligand contributions, the ground state structure along the M-M axis appears to be relatively insensitive to this varying ligand character. The question then arises as to whether the structural changes accompanying the formal elimination of the δ bond will show any sensitivity to the nature of the ligands in the molecule.

A further consideration in such comparisons between molecules is the relative merit between the compounds of the approximation of the ν_1 normal mode to an M_2 diatomic stretch. Some G-matrix mixing of the ν(MM) and ν(MX) totally symmetric *local* modes seems likely for many of these systems where the MMX angle is > 90°. Even if the mixing itself is independent of the nature of X, the resulting reduced mass required for the simple $\Delta \rightarrow \delta$ conversion (Eq. 3.1) will acquire a strong halide dependence. This problem will be discussed

further in chapter 4, where the effect of the halide on the ability to draw structural comparisons between molecules on the basis of a study of the ν_1 co-ordinate will be considered.

3.7 Conclusions

The SOS study of the $[M_2X_8]^{n-}$ ions has shown that the method can be applied successfully in cases in which the criteria laid down by the theory are met. The experimental data available for these species have been sufficient to allow good agreement between the values of $\tilde{\nu}_e$ for $[Re_2Br_8]^{2-}$ and $[Mo_2Cl_8]^{4-}$ and those calculated previously from other experimental data [3.15, 3.23]. Furthermore, the relative magnitudes of the values of δ(M-M) for these ions are in agreement with a previous emission study on these complexes [3.25]. The visual fitting procedure has thus been successful, as has a single-mode approximation. Duschinsky mixing involving the ν_1 mode has not been required to fit the experimental data.

Furthermore, the method has been seen to be applicable to experimental data recorded in solution as well as to the better-resolved low temperature solid-state data. As a result of fitting simultaneously two types of experimental data, the method has been found to be more generally applicable to the problem of elucidation of excited state structures than a previous study based on the SOS approach to REPs only [3.55].

Conclusions about the nature of the $^1\delta\delta^*$ state and the M-M bonding in these systems on the basis of their calculated parameter values, however, have been more difficult to obtain. This is largely a reflection of the vast number of factors which must be taken into account if the bonding in the ground and excited electronic states is to be described accurately. However, conclusions have been reached from the comparison of the results for the $[Re_2Br_8]^{2-}$ ion in the solid-state and in solution: this comparison is independent of any halide-dependent factors

which may affect the interpretation of the parameter values (sections 3.5 and 3.6). It has been proposed that the potential energy of the $^1\delta\delta^*$ state of these $[M_2X_8]^{n-}$ ions is a function of the torsion angle, χ, about the M-M axis, and that both a D_{4h} (eclipsed) and a D_{4d} (staggered) geometry for this ion are possible. Importantly, the observation of one or other of these excited state geometries appears to be critically dependent on the experimental technique, with both optical absorption and conventional RR experiments unable to probe the staggered, D_{4d} excited state structure. Nanosecond TR[3] experiments, however, appear to be able to probe this vibrationally relaxed structure in solution. Thus the structure of these ions in the $^1\delta\delta^*$ excited state in solution is now better understood.

It is also clear that more general conclusions about the M-M bonding and δ-interactions in these compounds, and comparisons of structural changes accompanying the breaking of the δ bond between different compounds can only be made after many ligand-dependent factors influencing the bonding, electronic and vibrational structure, are considered. These have been discussed in section 3.6. In order for further conclusions to be drawn, a similar SOS study of the $^1\delta\delta^*$ excited state of the complete series of compounds $Mo_2X_4(PMe_3)_4$ (X = Cl, Br or I), which have also been well studied, is detailed in chapter 4. Following the calculation of excited state values of the structural parameters for these systems, the general trends for all the $[M_2X_8]^{n-}$ and $Mo_2X_4(PMe_3)_4$ compounds can be reviewed and more detailed account of the halide-dependence of trends observed can be made.

Chapter 4:

Application of the SOS Method to the Structure of the $^1B_2$ Excited State of $Mo_2X_4(PMe_3)_4$ Compounds (X = Cl, Br or I):

insights into the eclipsed $^1\delta\delta^*$ excited state of quadruply bonded metal dimers

In chapter 3, the SOS method was successfully applied to the $^1A_{2u}$ ($^1\delta\delta^*$) excited electronic states of some $[M_2X_8]^{n-}$ ions and values for structural parameters along the M-M co-ordinate in this electronic state were found. From the results on the $[Re_2Br_8]^{2-}$ ion, for which experimental data were available in both solution and in the solid-state, it can now be concluded that the timescale of the optical absorption (ABS) and conventional RR experiments permit observation of an eclipsed (D_{4h}) $^1\delta\delta^*$ excited electronic state structure, and that the potential energy of this state can be represented as a function of the torsion angle, χ, of the ligand groups about the M-M axis.

However, the process of drawing conclusions about the M-M bonding in these ions, on the basis of their excited state values of $\tilde{\nu}_e$ (the wavenumber of the ν_1 mode in the excited state) and δ(M-M) (the bond length change along the M-M

co-ordinate in the excited state), is complicated by many interrelated, and often halide-dependent, factors which vary among the ions and prevent direct comparisons from being drawn between them. To this end, an analogous study of the $^1\delta\delta^*$ state of the well studied series of compounds, $Mo_2X_4(PMe_3)_4$ (X = Cl, Br or I) is detailed in this chapter. It is hoped that this study will show the effect of the nature of the halide atom on M-M bonding in the $^1\delta\delta^*$ excited state and allow better interpretation of the values of the structural parameters of this state for all the quadruply bonded dimetallic species studied so far.

4.1 The $Mo_2X_4(PMe_3)_4$ Compounds (X = Cl, Br or I)

The set of compounds $Mo_2X_4(PMe_3)_4$ (X = Cl, Br or I) are structurally analogous to the $[M_2X_8]^{n-}$ ions, with four of the halide atoms replaced by four PMe_3 ligands, giving a D_{2d} molecular point group for $M_2X_4P_4$ skeleton in the ground electronic state [4.1, 4.2]. The ligands are arranged in the usual eclipsed manner, as a result of the δ-bond between the metal centres (section 1.7). The M-M bonding in the ground electronic state is then described by the usual $\sigma^2\pi^4\delta^2$ configuration. The structure of the molecules is shown in Fig. 4.1.

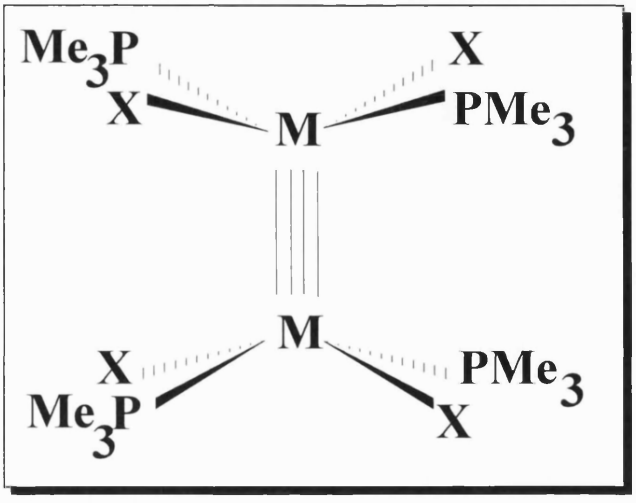

Fig. 4.1 Structure of the $Mo_2X_4(PMe_3)_4$ compounds

For the D_{2d} molecular point group, the $M_2X_4P_4$ skeletal vibrations of the molecule span the irreducible representations $5a_1 + a_2 + 2b_2 + 4b_2 + 6e$, with the five a_1 Raman active modes assigned to the ν(MoMo) stretch (ν_1), the ν(MoX) stretch (ν_2), the ν(MoP) stretch (ν_3), the δ(MoMoX) bend (ν_4) and the δ(MoMoP) bend(ν_5) [4.3]. However, with the MoMoX angles in these compounds being larger (~113 - 115°) [4.1, 4.2] than those in the $[M_2X_8]^{n-}$ ions (~ 105°) [4.4 - 4.7], it seems even more likely that the approximation of the ν_1 normal mode to a ν(MoMo) stretch is inappropriate, and that G-matrix mixing between the ν(MoMo) stretch and the ν(MoX) stretch will be appreciable.

In section (3.6), the results of electronic structure calculations on the analogous $Mo_2X_4(PH_3)_4$ compounds [4.8 - 4.10], were seen to indicate that the halides may also exert some influence on the actual M-M bonding, through orbital contribution to the M-M bonding orbitals. Specifically, the contribution of the halide to the M-M δ-bond was calculated to increase in the order X = Cl < Br < I. However, for the analogous series, $Mo_2X_4(PMe_3)_4$ (X = Cl, Br or I), the M-M bond length is seen to be insensitive to the identity of X (see Table 3.6).

The $^1\delta\delta^*$ excited electronic states of these $Mo_2X_4(PMe_3)_4$ compounds have also been studied in some detail. The $^1(\delta^* \leftarrow \delta)$ transition maximises at 17,090 cm^{-1} (X = Cl [4.2]), 16,720 cm^{-1} (X = Br [4.2]) and 15,720 cm^{-1} (X = [4.2]). The concomitant increase in intensity of this transition with the red-shifting of the energy as the halide becomes more reducing have been explained [4.11] as arising from increasing CI mixing between the $^1\delta\delta^*$ excited state and and LMCT excited state at a higher energy (section 3.6).

The mirror-image of this $^1(\delta^* \leftarrow \delta)$ absorption band with the strong $^1(\delta \leftarrow \delta^*)$ emission band in a glass at ~ 77 K [4.12, 4.13] was taken to indicate that the structure of the molecule remained eclipsed (D_{2d}) in the $^1\delta\delta^*$ excited state. Even when in solution, where twisting about the MM axis in the $^1\delta\delta^*$ state is thought to

be possible for $[M_2X_8]^{n-}$ ions, it is thought that the steric bulk of the trimethylphosphine (PMe_3) groups prevent torsional distortion from occurring. It is now proposed that, as in the case of the $[M_2X_8]^{n-}$ ions (section 3.7), the potential energy of this $^1\delta\delta^*$ excited state can be described as a function of the torsion angle, χ (see Fig. 4.2) but with a much higher barrier to rotation about the M-M axis to reach the staggered D_2 minimum:

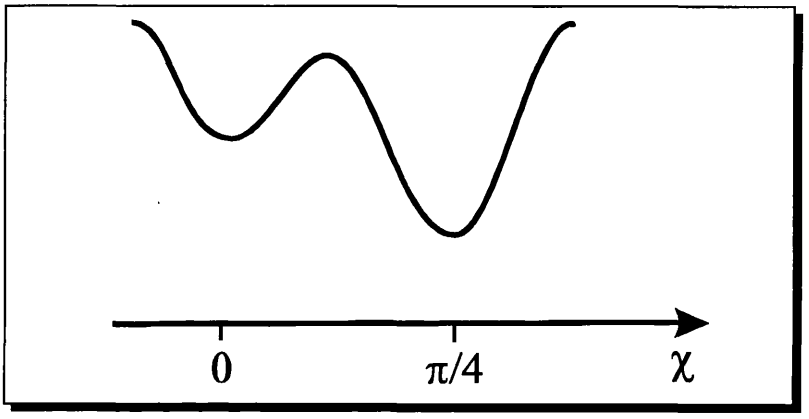

Fig. 4.2 : Potential energy of the $^1\delta\delta^*$ excited state of $Mo_2X_4(PMe_3)_4$ compounds in the dimension of the torsional co-ordinate.

Thus, as expected a TR^3 study of the $^1\delta\delta^*$ excited state [4.14] in solution found values of ∇_e for the ν_1 mode of $Mo_2Cl_4(PMe_3)_4$ very similar to that found from vibronic structure on solid-state absorption spectra of the $^1(\delta^* \leftarrow \delta)$ transition at low temperature [4.12], indicating that vibrational relaxation from the D_{2d} eclipsed minimum to the D_2 staggered minimum cannot be observed, even on the timescale of this experiment. The contrasting behaviour of these sterically hindered compounds to that of the $[M_2X_8]^{n-}$ ions has often been used to argue the presence of a staggered D_{4d} $^1\delta\delta^*$ excited state for the latter species. Following the SOS study in chapter 3, however, it can be seen that the present study on the timescale of conventional ABS and RR spectra will probe only the eclipsed $^1\delta\delta^*$ structure in every case.

As in the case of the $[M_2X_8]^{n-}$ ions, the ν_1 co-ordinate of these $Mo_2X_4(PMe_3)_4$ species in the $^1\delta\delta^*$ excited state is a suitable subject for study via

the SOS method. The $^1(\delta^* \leftarrow \delta)$ electronic transition is well-resolved and isolated in each case, and again there are no spin-orbit coupling or Jahn-Teller effects, the ground and excited states being both spin and orbitally non-degenerate. Other non-adiabatic effects and anharmonicities are also thought to be negligible. The only question remaining in the interpretation of the parameters is the description of the ν_1 normal mode as a pure ν(MM) diatomic stretch. This will affect the conversion of the dimensionless displacement parameter, Δ to δ(M-M), a bond length change. The possibility of Duschinsky mixing involving ν_1 (with perhaps the ν_2 mode) can be included in the SOS calculation. All the required experimental data are easily available and are detailed in the next section.

4.2 Experimental Data and the SOS Calculations

As for the $[M_2X_8]^{n-}$ ions, the experimental data fitted in the SOS calculation were the $^1(\delta^* \leftarrow \delta)$ ABS profile and the relative intensities of the first four members of the $n\nu_1$ progression in the RR spectrum recorded with a laser excitation frequency lying within the contour of this electronic transition. The experimental procedure is detailed in Appendices A1 and A2. Samples of the compounds $Mo_2X_4(PMe_3)_4$ were donated by Prof. M. D. Hopkins.

UV/Visible ABS Spectra

UV/Visible ABS spectra of the compounds, as the appropriate transparent halide disk (KCl, KBr or CsI) were recorded at 77 K in the region of the $^1(\delta^* \leftarrow \delta)$ transition as detailed in Appendix A2. It was found, however, that dispersion effects in the baseline of these spectra were large (see Appendix A3). Despite the normal correction for the rising baseline due to scattering and dispersion being performed, it could not be guaranteed that the detailed vibronic structure on the ABS band was not altered by this process. Therefore, the previously published ABS spectra of the compounds as 2-methlypentane glasses at 77 K were also scanned and digitised to be used for fitting. In this way, it was possible to check

that the baseline deducted from the powder ABS spectrum had not altered in any way the relative intensities of the vibronic components in the spectrum.

On comparison, the glass and powder ABS spectra for each compound were seen to have very similar widths and spacing of the vibronic peaks. It could therefore be assumed that only the background differed between the two spectra and that any parameter values calculated for a fit of the glass ABS data would also be valid for the powder medium. Thus, for these compounds, only these glass ABS data were used in the SOS fitting calculations.

The glass ABS spectra are shown in Figs. 4.3 - 4.5. The close similarity of the structure in the glass and powder ABS spectra of $Mo_2Cl_4(PMe_3)_4$, is shown in Fig. 4.6. For brevity, only the comparison of the two spectra for the chloride compounds is shown here.

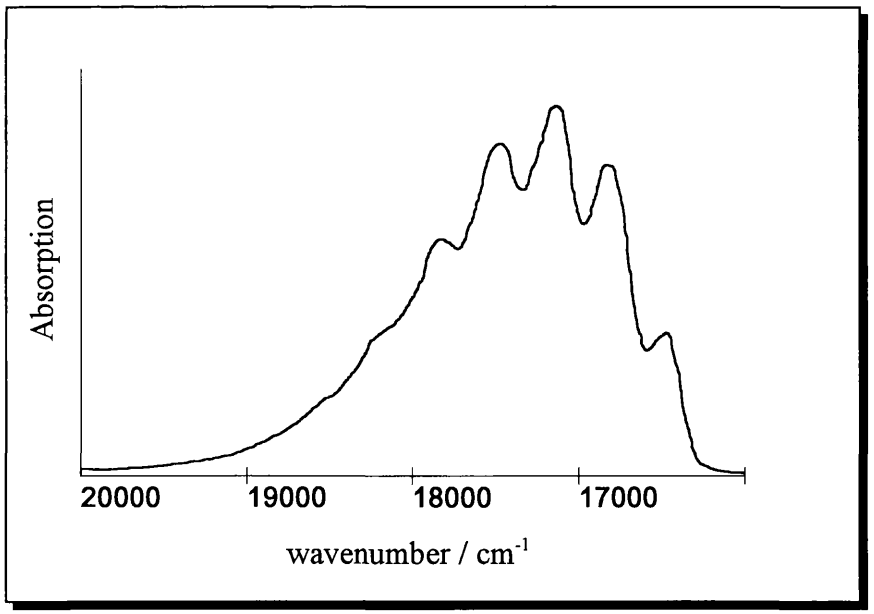

Fig. 4.3 UV/Visible ABS spectrum of $Mo_2Cl_4(PMe_3)_4$ as a 2-methylpentane glass at 77 K (scanned and digitised from ref. 4.12)

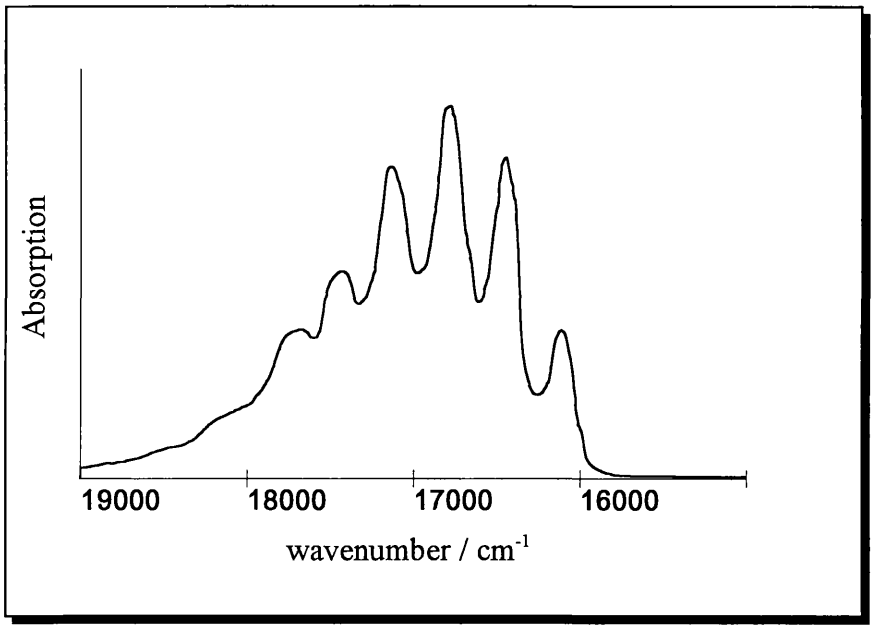

Fig. 4.4 UV/Visible ABS spectrum of $Mo_2Br_4(PMe_3)_4$ as a 2-methylpentane glass at 77 K (scanned and digitised from ref. 4.12)

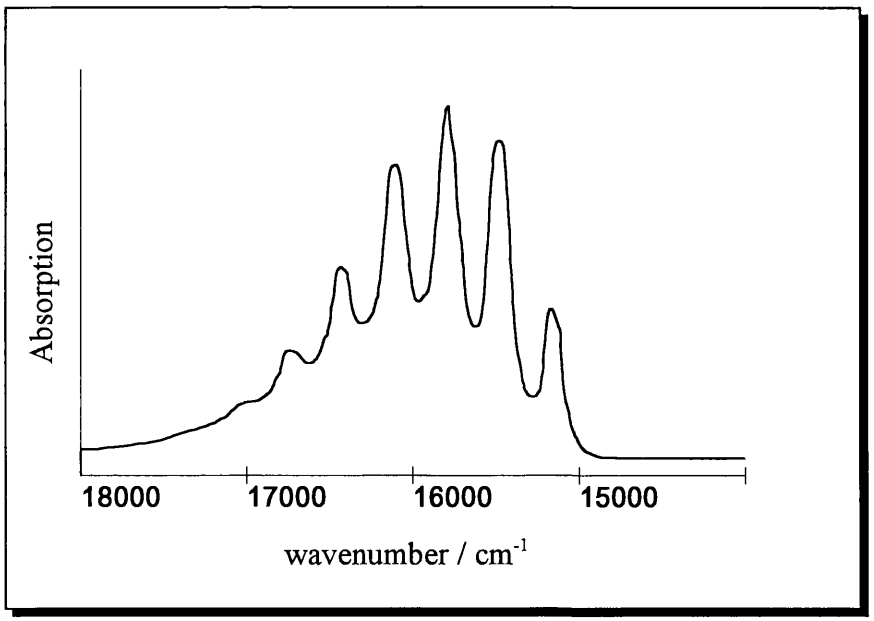

Fig. 4.5 UV/Visible ABS spectrum of $Mo_2I_4(PMe_3)_4$ as a 2-methylpentane glass at 77 K (scanned and digitised from ref. 4.12)

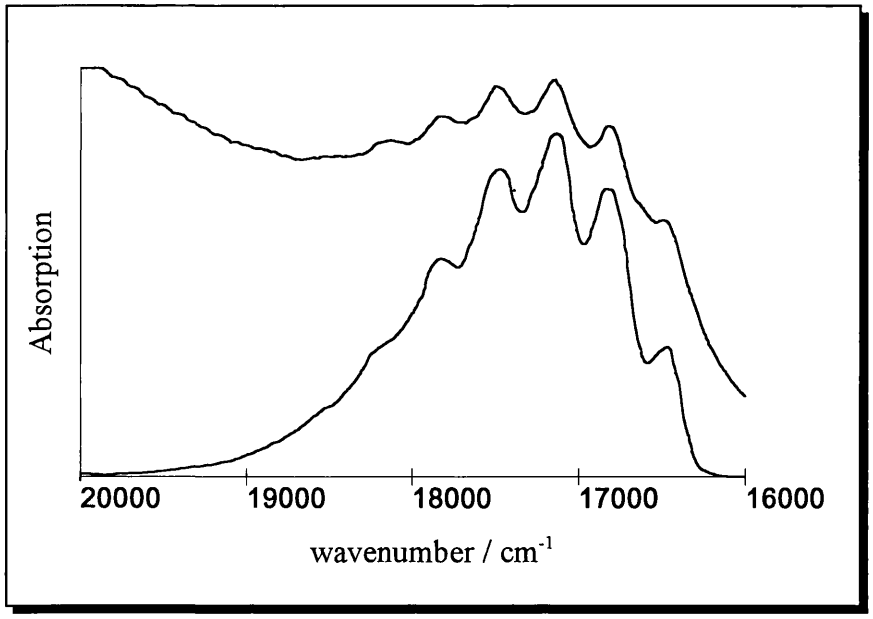

Fig. 4.6 Comparison of UV/Visible ABS spectrum of $Mo_2Cl_4(PMe_3)_4$ as a 2-methylpentane glass at 77 K (lower) and as KCl powder disk at 77 K (upper).

In all cases, the spectra were utilised as a series of evenly spaced *x* - *y* data points, in cm^{-1} units.

RR Spectra

RR spectra of the compounds as pressed halide disks (KCl, KBr or CsI) were recorded as detailed in Appendix A1. For $Mo_2Cl_4(PMe_3)_4$ and $Mo_2Br_4(PMe_3)_4$ spectra were recorded at both 295 K and 77 K; for $Mo_2I_4(PMe_3)_4$, which was known to degrade slowly with time, spectra were recorded only at 77 K. The relative intensity ratios of the first four harmonics of the $n\nu_1$ progression were measured as detailed in Appendix A1: the measurements were averaged over several spectra and a standard deviation of less than 10 % was found in each case. The excitation frequency ($\tilde{\nu}_0$) was necessarily high in each case, in order that the higher harmonics would not be obscured by strong fluorescence. The values for $\tilde{\nu}_0$ were 19,453 cm^{-1} ($Mo_2Cl_4(PMe_3)_4$ and $Mo_2Br_4(PMe_3)_4$) and 17,599 cm^{-1} ($Mo_2I_4(PMe_3)_4$). The spectra are shown in Figs. 4.7 - 4.9.

The relative intensities were corrected for spectral response of the spectrometer, but not for ν^4 scattering since this is included in the SOS calculation. The corrected relative intensity ratios of the $n\nu_1$ progression are shown for each compound in Table 4.1.

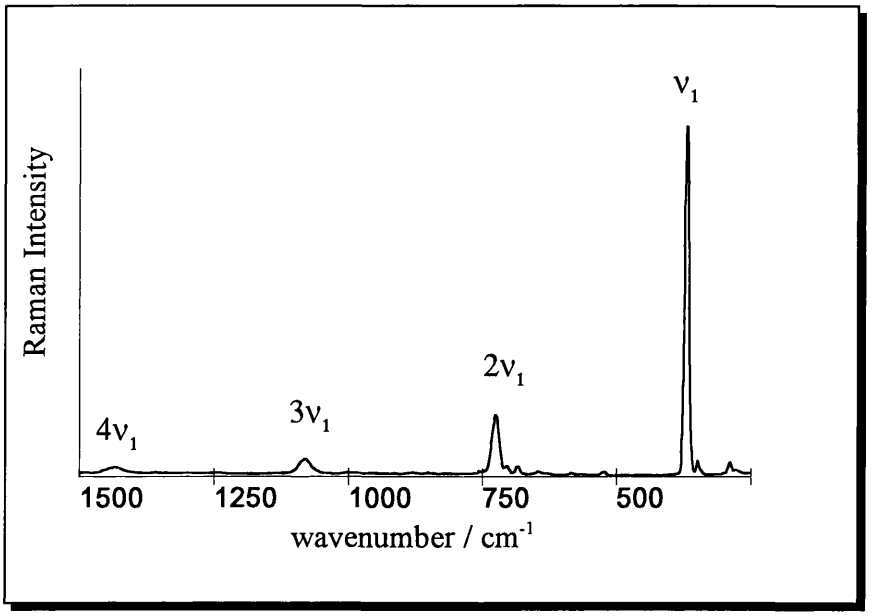

Fig. 4.7 RR Spectrum of $Mo_2Cl_4(PMe_3)_4$ as a pressed KCl disk at 77 K; $\tilde{\nu}_0$ = 19,453 cm^{-1}

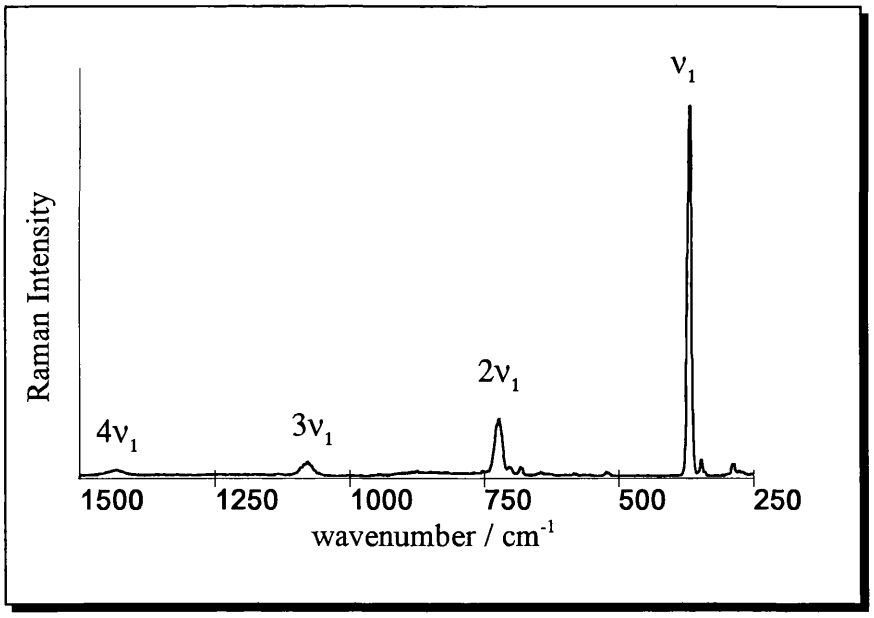

Fig. 4.8 RR Spectrum of $Mo_2Br_4(PMe_3)_4$ as a pressed KBr disk at 77 K; $\tilde{\nu}_0$ = 19,453 cm^{-1}

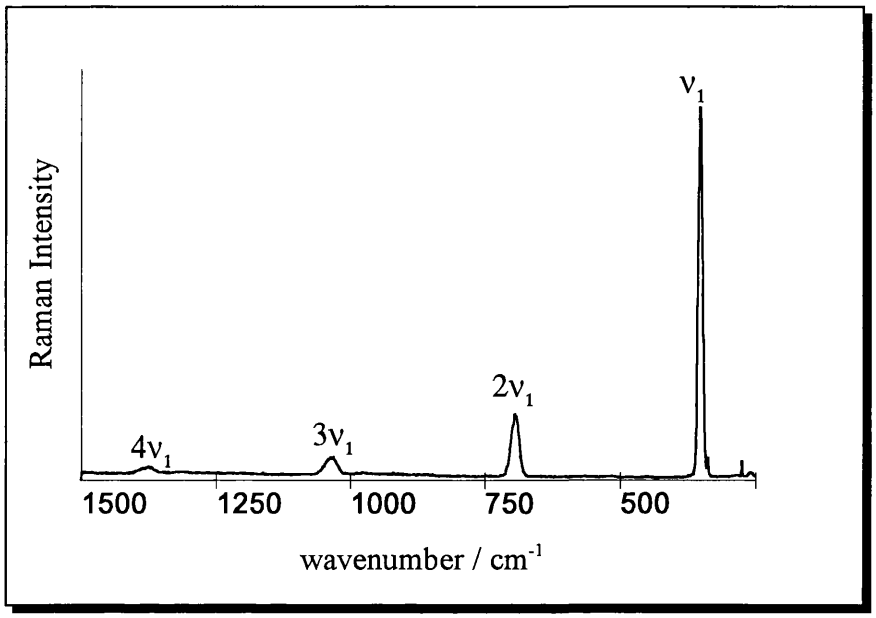

Fig. 4.9 RR Spectrum of $Mo_2I_4(PMe_3)_4$ as a pressed CsI disk at 77 K; $\tilde{\nu}_0$ = 17,599 cm^{-1}

	$Mo_2Cl_4(PMe_3)_4$		$Mo_2Br_4(PMe_3)_4$		$Mo_2I_4(PMe_3)_4$
$\tilde{\nu}_g$ / cm^{-1}	355		353		343
	77 K	295 K	77 K	295 K	77 K
$I(\nu_1)$	100	100	100	100	100
$I(2\nu_1)$	29	31	25	30	33
$I(3\nu_1)$	11	13	9	11	14
$I(4\nu_1)$	6	7	4	5	6

Table 4.1 Relative Intensity Ratios of the n = 1 to 4 members of the $n\nu_1$ progression of $Mo_2X_4(PMe_3)_4$ compounds (X = Cl, Br, I) corrected for spectral response of the spectrometer. **Errors ≤ 10%.**

SOS Calculations

In order to carry out the SOS calculations, the previous estimates of the values of $\tilde{\nu}_e$ for the ν_1 mode of each of the compounds, taken from vibronic spacing the

glass ABS spectra, were taken into account. These measurements gave values of $\tilde{\nu}_e$ = 335 cm^{-1} ($Mo_2Cl_4(PMe_3)_4$) [4.12], 340 cm^{-1} ($Mo_2Br_4(PMe_3)_4$) [4.12] and 320 cm^{-1} ($Mo_2I_4(PMe_3)_4$) [4.12]. The SOS calculations were carried out in the manner described in section 3.2, with both visual and numerical fitting procedures used.

4.3 Results

For each set of ABS and RR data, a set of parameter values corresponding to the 'best fit' was found. The parameter values are shown in Table 4.2.

As with the $[M_2X_8]^{n-}$ ions, ν_1 was approximated to a ν(MM) diatomic stretch for the purposes of converting the dimensionless displacement, Δ to the bond length change δ(M-M), via Eqn. 3.1.

	$Mo_2Cl_4(PMe_3)_4$	$Mo_2Br_4(PMe_3)_4$	$Mo_2I_4(PMe_3)_4$
$\tilde{\nu}_g$ / cm^{-1}	355	353	343
$\tilde{\nu}_e$ / cm^{-1}	335	343	323
Δ	2.44	2.35	2.35
δ(MM) / pm	10.8	10.4	10.6
m	0	0	0
Γ / cm^{-1}	$90 + 32v$	$70 + 20v$	$50 + 35v - 11v^2 + 1.5v^3$
$E_{0\text{-}0}$	16,490	16,100	15,150

Table 4.2 Calculated parameter values for the ν_1 co-ordinate of $Mo_2X_4(PMe_3)_4$ compounds using RR and ABS data. v denotes the vibrational occupation number of the excited electronic state.

The corresponding fits of the calculated and experimental RR intensity ratios and glass ABS profiles are shown in Table 4.3 and Figs. 4.10 - 4.12 respectively.

	$Mo_2Cl_4(PMe_3)_4$		$Mo_2Br_4(PMe_3)_4$		$Mo_2I_4(PMe_3)_4$
	77 K	295 K	77 K	295 K	77 K
$I(\nu_1)$	100	100	100	100	100
$I(2\nu_1)$	29	32	25	30	33
$I(3\nu_1)$	13	15	11	15	17
$I(4\nu_1)$	7	8	7	9	11

Table 4.3 : Calculated RR intensity ratios for the $n\nu_1$ progression of $Mo_2X_4(PMe_3)_4$ Compounds (X = Cl, Br, I)

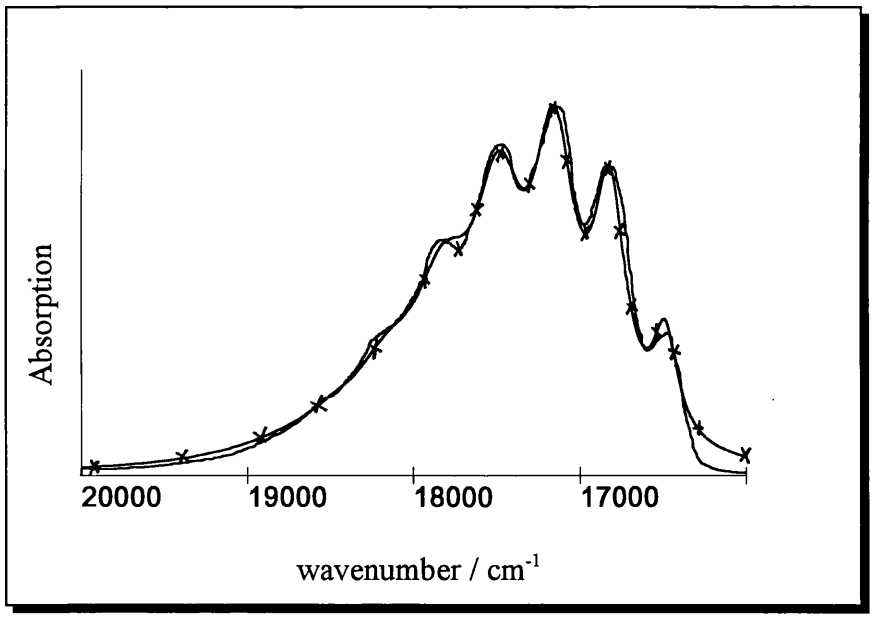

Fig. 4.10 Comparison of the experimental (—) and calculated (-*-) normalised ABS profiles for $Mo_2Cl_4(PMe_3)_4$

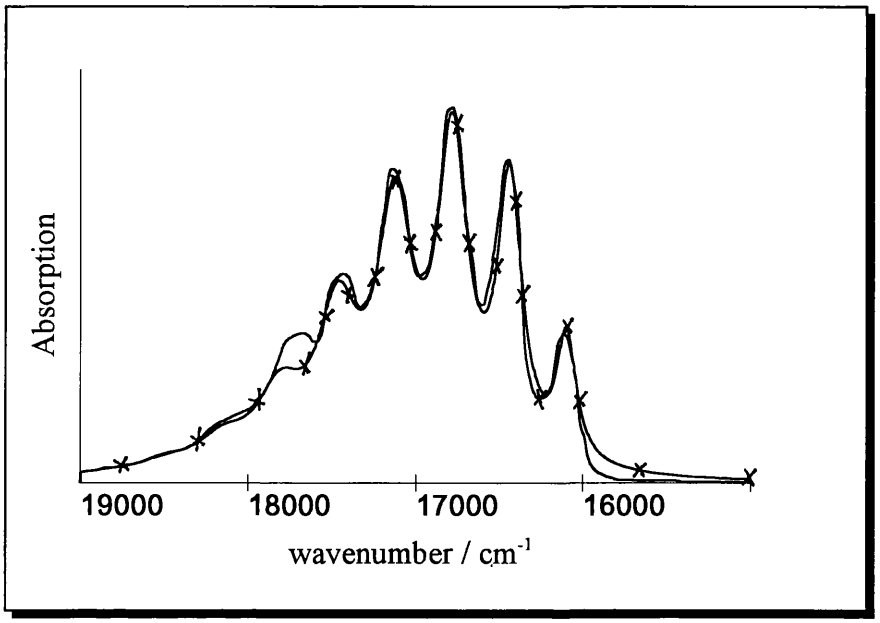

Fig. 4.11 Comparison of the experimental (—) and calculated (-*-) normalised ABS profiles for $Mo_2Br_4(PMe_3)_4$

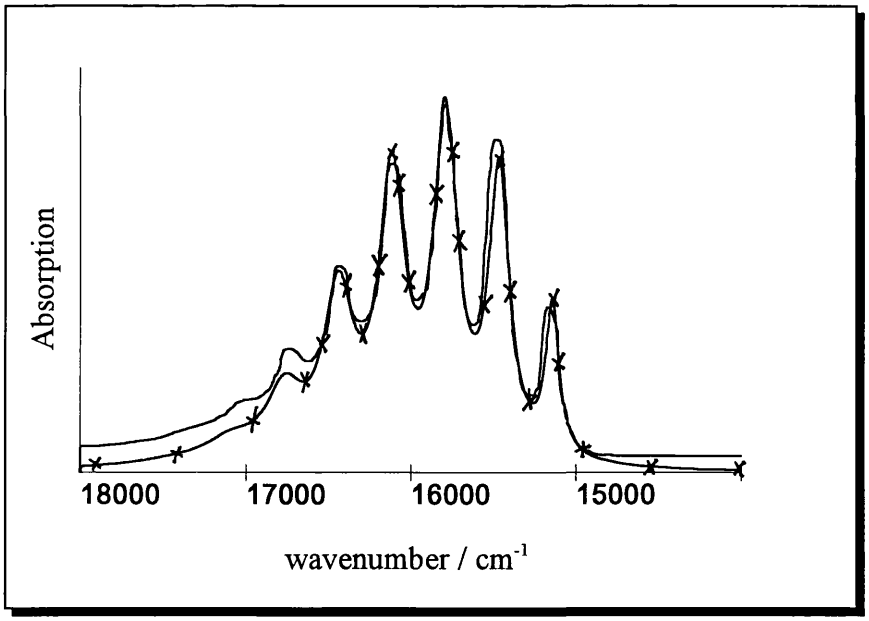

Fig. 4.12 Comparison of the experimental (—) and calculated (-*-) normalised ABS profiles for $Mo_2I_4(PMe_3)_4$

As for the $[M_2X_8]^{n-}$ ions, the error on the value of any one parameter in Table 4.2 can be estimated by keeping all the other values constant for a given fit and

changing the chosen value until the fit is significantly worsened. In this way, it is estimated that $\tilde{\nu}_e$ is known to ± 3 cm^{-1} and Γ to ± 10 cm^{-1}.

The merit of the diatomic approximation used for the conversion of Δ to the bond length change δ(M-M) will be discussed further below. It should be noted that the inclusion of Duschinsky mixing involving the ν_1 and ν_2 modes, usually assigned to the ν(MM) and ν(MX) stretches respectively, was *not* found to improve the fit in any case.

4.4 Discussion: Trends in the values of $\tilde{\nu}_e$ and δ(M-M)

In view of the previous SOS study in chapter 3 on the structurally related $[M_2X_8]^{n-}$ ions, it is useful at this stage to draw together all the results and re-examine the trends in the values of the parameters calculated.

Before doing so, however, it is necessary to assess the validity of the approximation used so far of the ν_1 mode of all the compounds to a pure ν(MM) 'diatomic' stretch. Equation (3.1) has previously been used to convert the dimensionless displacement parameter, Δ, to a meaningful bond length change, δ(MM), along the MM axis. In all of the compounds studies here, the MMX angles are greater than 90° and it is therefore expected that ν_1 contains, at least to some varying extent, some local ν(MX) character (for the $Mo_2X_4(PMe_3)_4$ series, some mixing with ν(MP) is also possible, although the wavenumber of this mode is expected to be reasonably high in comparison with the wavenumber of the ν(MM) mode). Thus, a halide dependence of the reduced mass of the vibrating species, and hence of the validity of the Δ - δ(MM) conversion, may be expected.

The G-matrix mixing of the local modes is also likely to be halide-dependent since kinetic energy coupling will be enhanced where there is a

relatively small wavenumber difference between two modes (e.g. for $Mo_2Cl_4(PMe_3)_4$ ν_1:wavenumber 355 cm and ν_2 (ν(MCl) :wavenumber 274 cm^{-1}). It is also likely to be greater for the series of compounds $Mo_2X_4(PMe_3)_4$ (X = Cl, Br or I) where the MMX angles are ~ 113° , compared to ~105° for the $[M_2X_8]^{n-}$ ions. Proper account of this mixing can only be taken of a full normal co-ordinate analysis of the compounds is made. Such analyses have previously been attempted on similar compounds [4.15, 4.16]. A further approximate analysis on these compounds has been reported [4.17] in which a valence force-field in the totally symmetric M-M, M-X and M-L (for $Mo_2X_4(PMe_3)_4$) stretching co-ordinates was assumed†. Following the fitting of the wavenumbers for the stretching modes, a relationship between the ν_1 normal co-ordinate changes and the geometric changes along the stretching co-ordinates in the excited state was found. It was seen that the bond length change along the M-M co-ordinate in the excited state was consistently very close to, but slightly less than, the values predicted form the pure diatomic calculations using Eq. (3.1). Thus, it appears that the diatomic approximation is reasonably valid in most cases, and that the ν(MM) local mode is still the dominant component of the ν_1 normal mode. However, for $Mo_2Cl_4(PMe_3)_4$ only, a non-negligible contribution of the ν(MoCl) stretch to the ν_1 mode was found, and the parameter Δ was seen to contain some displacement along the MoCl co-ordinate in the excited state [4.17].

Table 4.4 summarises the calculated values of $\tilde{\nu}_e$, Δ, δ(M-M) and Γ for all the compounds studied as well as structural information regarding the ground electronic state. These values of δ(MM) are those reported from the results of the normal co-ordinate analysis mentioned above [4.17]. Where a range of δ(MM) values is shown, this reflects the inability of the normal co-ordinate analysis calculation to fit the observed band wavenumber using a diagonal force field matrix, thus producing a range of possible force field matrices, and hence a range of acceptable geometry changes in the excited state.

† Performed by C. Svendsen at the Fysisk Institut, Odense University, Denmark.

	$[Re_2X_8]^{2-}$		$[Mo_2Cl_8]^{4-}$	$Mo_2X_4(PMe_3)_4$		
	X = Br	X = I		X = Cl	X = Br	X = I
$\tilde{\nu}_g$ / cm^{-1}	276	257	338	355	353	343
$\tilde{\nu}_e$ / cm^{-1}	255 (-7.6%)	240 (-6.6%)	336 (-0.6%)	335 (-5.6%)	343 (-2.8%)	323 (-5.8%)
Δ	2.2	2.1	3.4	2.44	2.35	2.35
δ(MM) / pm	6.5 - 8.0 (3.1%)	7.6 (3.4%)	12.5 - 15.5 (6.5%)	9.2 (4.3%)	10.1 (4.8%)	9.7 (4.6%)
δ(MX) / pm	[-2.6] - [-1.0] (-0.7%)	-1.7 (-0.6%)	[-5.3] - [-1.9] -(1.5%)	-4.4 (-1.8%)	-2.5 (-1.0%)	-2.3 (-0.8%)
δ(MP) / pm	-	-	-	-2.3	-2.1	-2.8
r(MM) /Å	2.226	2.245	2.15	2.13	2.125	2.127
m	0.08	0	0	0	0	0
Γ / cm^{-1}	225	280	280	$90 + 32v$	$70 + 20v$	$50 + 35v - 22v^2 + 9v^3$

Table 4.4 Summary of the calculated parameter values for all the compounds studied, with δ(MM) values found from a normal co-ordinate analysis. The percentage values refer to the changes in the parameter from its ground state value. Where a range of values is quoted, the percentage is calculated for the average of the range. *v* refers to the vibrational occupation number of the excited electronic state.

It is known from the previous study on the $[Re_2Br_8]^{2-}$ ion that this method observes only an eclipsed $^1\delta\delta^*$ excited electronic state; thus it should be possible to draw some conclusions about the structure and M-M bonding in this state in the different compounds studied.

One further problem with assessing any dependence of the value of δ(M-M) on the identity of the halide, X, in such a series is that the magnitudes of

δ(M-M) are very small and only one order of magnitude higher than the accuracy with which the *r*(M-M) bond lengths are known. Thus, it is necessary to ensure that any conclusions drawn from comparisons between compounds reflect real and physically significant trends. Four main observations will be discussed:

1. In general, the percentage changes in the M-M bond length, denoted henceforth %δ(MM), appear to be smaller for the Re(III) ions than for the Mo(II) compounds. (~ 3.2% Re(III); 4.3 - 6.0% Mo(II))

2. Across a halide series, such as $Mo_2X_4(PMe_3)_4$ (X = Cl, Br or I) or $[Re_2X_8]^{2-}$ (X = Br, I), the values of %δ(MM) appear to be insensitive to X.

3. The value of %δ(MM) for the $[Mo_2Cl_8]^{4-}$ ion is notably larger than for all the other compounds studied: furthermore, the percentage change in the ν_1 wavenumber is smaller than for all the other compounds.

4. The phenomenological lifetime factor, Γ, is quite large in all cases, and, for the series $Mo_2X_4(PMe_3)_4$ (X = Cl, Br or I), shows a clear dependence on the vibrational occupation number, *v*, of the excited electronic state.

4.5 Comparison of δ(MM) values for Re(III) and Mo(II) compounds

In Table 4.4, it can be seen that the percentage change in the M-M bond length in the excited state, %δ(MM), is generally larger for the Mo(II) compounds than for the Re(III) ions. The fact that this change is relatively small in all cases (< 10%) reflects the weakness of the M-M δ-bond, which is formally eliminated in this transition. In the ground electronic state, the *r*(MM) values for the Re(III) ions are also longer than in the Mo(II) analogues (*r*(ReRe) in $[Re_2Cl_8]^{2-}$:2.222 Å; *r*(MoMo) in the NH_4^+ salt of $[Mo_2Cl_8]^{4-}$: 2.150 Å).

This is usually explained [4.18] by the fact that in Re(III) complexes, the M-M bond is formed by the overlap of the 5d orbitals, as opposed to the 4d orbitals in the Mo(II) compounds. Thus, the greater number of core electrons means that the Re-Re bond is longer, despite the 5d orbitals possibly being more diffuse than the 4d, (hence improving overlap). Furthermore, in the case of these compounds, the Re atoms are formally in a higher oxidation state than the Mo atoms, and thus some contraction of the Re d orbitals is expected.

Obviously, other factors such as overall charge of the molecule, as well as the type and geometry of the ligands, differ between some of the Mo(II) and Re(III) species in Table 4.4, making comparison between them more difficult. Some insight into the expected changes in M-M bonding on changing from a second to a third row transition metal can be gained from a comparative study [4.9] of Mo-Mo and W-W bonds in the compounds $M_2Cl_4(PR_3)_4$ (M=Mo, W; R = H, Me), using PES measurements and electronic structure calculations.

It is known that quadruply bonded W dimers are more easily oxidised than their Mo counterparts: the electronic structure calculations and PES measurements confirm a higher energy for the HOMO (δ) orbital of the W compound. This would imply a weaker W-W quadruple bond, and partially account for its longer bond length (r(WW) = 2.262 Å[4.1]; r(MoMo) = 2.130 Å [4.1]). Furthermore, a red shift in the energy of the $^1(\delta^* \leftarrow \delta)$ transition is seen on going from Mo to W [4.2]. The structure calculations also indicate that, on going from Mo to W, there is a clear redistribution of M-M bonding charge in other other orbitals, often with halide character. Specifically, the calculated percentage M character in the δ orbital decreases from 72% for M = Mo to 68% for M = W.

Thus, even when no change in geometry or oxidation state accompanies a change from a second to a third row metal in a quadruply bonded metal dimer, it appears that, despite the participation of 5d rather than 4d orbitals, the $^1(\delta^* \leftarrow \delta)$ energy separation decreases and the percentage metal character in the δ orbitals

also decreases. However, it must also be remembered that two electron repulsion terms (such as K) typically decrease on going from second to third row metals. This term has also been shown [4.11] to be important in determining the final energy of the $^1(\delta \leftarrow \delta)$ transition. The M-M bond length is seen to increase on replacing Mo by W, and calculations point to a destabilisation of the M-M σ and π bonding orbitals in the third row metal complexes. It thus appears that the M-M bonding in the W compound is weaker.

Therefore, in the ground electronic state, it may be expected that the M-M bond length in the third row Re complexes will be larger than for the Mo complexes, and that the increased oxidation state in the former compounds will reinforce this trend. Furthermore, the δ bonding orbital may contain a higher percentage halide character in the case of the Re compounds, and the δ -overlap is expected to be poorer. It is therefore to be expected that, on eliminating the δ bond in the excited $^1\delta\delta^*$ state, a smaller change in the total M-M bond length will be incurred for the Re(III) ions than for the Mo(II) ions.

4.6 Comparison of δ(MM) values across a halide series

From Table 4.4, it can be seen that, for the two series $Mo_2X_4(PMe_3)_4$ (X = Cl, B or Ir) and $[Re_2X_8]^{2-}$ (X = Br or I), the percentage change in the M-M bond length (%δ(MM)) appears to be insensitive to the change in the identity of the halide.

The question of how the nature of the ligands in quadruply bonded dimetallic compounds affects the M-M bonding was discussed in detail in chapter 3 (section 3.6). From this, it was seen that the description of the M-M bonding orbitals as pure metal orbitals is not entirely valid. Indeed, electronic structure calculations indicated a non-negligible percentage halide character in the M-M δ and other bonding orbitals for the compounds studied here. This halide contribution, as well as other spectroscopic 'indicators' of M-M δ bond strength

(such as energy and intensity of the $^1(\delta \leftarrow \delta)$ transition) were seen to show a dependence on the nature of the halide in the compound. Conversely, the M-M bond length appears to be insensitive to any change in the halide, especially for the series $Mo_2X_4(PMe_3)_4$ (X = Cl, Br or I). Furthermore, only significant progressions in the ν_1 (ν(MM))mode are consistently observed in the RR spectra of these compounds in resonance with the $^1(\delta \leftarrow \delta)$ transition, indicating dominant metal character in the orbitals involved.

The variation in the energy and intensity of the $^1(\delta \leftarrow \delta)$ transition across a halide series has been explained [4.11] as being a result of a small amount of mixing between a LMCT excited state (of the appropriate symmetry) with the $^1\delta\delta^*$ excited state. This mixing is small and the $^1(\delta \leftarrow \delta)$ transition remains essentially one between metal-based orbitals. However, since the LMCT transition has a very high oscillator strength, the $^1(\delta \leftarrow \delta)$ transition can steal intensity through this mixing.

The variation in the percentage metal character in the various M-M bonding orbitals as X varies is explained from the electronic structure calculations by a variation in the energetic proximity of the X lone pair orbitals, or M-X bonding orbitals, to the M-M bonding manifold. The fact that even a reasonably large change in the calculated percentage halide character in the M-M δ bond across a series, e.g. $Mo_2X_4(PH_3)_4$ (14% X = Cl, 40%, X = I [4.8]) is insufficient to cause a change in the M-M bond length (r(MoMo) = 2.130 Å, X = Cl; r(MoMo) = 2.127 Å, X = I [4.1, 4.2]) might be explained by the constant percentage contribution [4.8] of the δ overlap population to the **total** bond overlap population across this series.

The results of the SOS calculations show that the structural insensitivity of the M-M bond to the nature of X across a halide series persists in the $^1\delta\delta^*$ excited state, despite the elimination of a bond with varying %X character. It therefore

appears that, in fact the δ bond 'strength', (as reflected in the percentage change in bond lengthening when formally broken), is similar across a halide series. This conclusion has formerly been based only on ground state *r*(MM) values, since energies and intensities of the $^1(\delta \leftarrow \delta)$ transition, as well as electronic structure calculations, seemed to indicate otherwise; in fact the latter two observations required alternative explanations for the origin of their apparent halide dependencies.

4.7 Magnitude of the parameter values for the $[Mo_2Cl_8]^{4-}$ ion.

A very clear feature of Table 4.4 is the larger value of δ(MM) (and %δ(MM)) for the $[Mo_2Cl_8]^{4-}$ ion, which is accompanied by a very small percentage change in the value of the wavenumber of the ν_1 mode. As mentioned in section 3.5, the shift of the maximum in the $^1(\delta^* \leftarrow \delta)$ ABS band from that of the $^1(\delta \leftarrow \delta^*)$ luminescence band is a qualitative indicator of the magnitude of δ(MM), and this is seen to be approximately twice as large for this Mo(II) ion as for the $[Re_2Cl_8]^{2-}$ ion [4.19]. Furthermore, the value of $\tilde{\nu}_e$ found in this SOS calculation is in close agreement with that found from the low temperature electronic absorption spectrum of $K_4Mo_2Cl_8$ [4.20].

Although the $[Re_2X_8]^{2-}$ ions are structurally more similar to the $[Mo_2Cl_8]^{4-}$ ion than is the compound $Mo_2Cl_4(PMe_3)_4$, the change in the metal, together with the change in the oxidation state for the Re complexes, make a comparison between $[Mo_2Cl_8]^{4-}$ and $Mo_2Cl_4(PMe_3)_4$ more useful. Thus, on comparing the M-M bonding in these two compounds it is seen that:

- The $^1(\delta^* \leftarrow \delta)$ transition occurs at higher energy, and is of lower intensity for the $[Mo_2Cl_8]^{4-}$ ion (Table 3.6 and [4.21]).

- Electronic structure calculations, though performed using slightly different models, would tend to predict a larger percentage metal character in the

Mo-Mo δ orbital, and other M-M bonding orbitals, for the $[Mo_2Cl_8]^{4-}$ ion than for $Mo_2Cl_4(PMe_3)_4$ [4.8 - 4.10; 4.22 - 4.25]

- Structure calculations also predict [4.8] a certain amount of delocalisation of M-M bonding character (σ, π and δ) among other orbitals in $Mo_2Cl_4(PMe_3)_4$.

- *r*(MoMo) is marginally shorter for $Mo_2Cl_4(PMe_3)_4$ (*r*(MoMo) = 2.130 Å) than for may of the salts of the $[Mo_2Cl_8]^{4-}$ ion (*r*(MoMo) = 2.150 Å, NH_4^+ salt)

- The MoMoX bond angles in $Mo_2Cl_4(PMe_3)_4$ are ~ 113° compared to ~ 105° in the $[Mo_2Cl_8]^{4-}$ ion.

It is possible that the substitution of four trimethylphosphine ligands for four chloride ligands, and the resultant reduction in overall charge of the compound mean that the effective charge on the Mo atoms is lower for $Mo_2Cl_4(PMe_3)_4$ than for the $[Mo_2Cl_8]^{4-}$ ion. While an estimate of the relative donor capabilities of the Cl and $(PMe_3)_4$ ligands is difficult, the greater amount of charge distribution and percentage halide character in the M-M bonding orbitals in the compound $Mo_2Cl_4(PMe_3)_4$ (as indicated by the electronic structure calculations) may point to a greater amount of covalency in this case. Any such mixing of Cl orbitals and M-M bonding orbitals is likely to be enhanced by the larger MMX angle in $Mo_2Cl_4(PMe_3)_4$.

If the formal charge on the Mo atoms is lower in the compound $Mo_2Cl_4(PMe_3)_4$, then it would be expected that the d orbitals would be slightly more diffuse and hence better overlap would be expected in the M-M bond, resulting in a shorter Mo-Mo bond length. At the same time, however, the stabilisation of the M-M bonding orbitals would mean that the LMCT transition, which is thought to mix with the $^1(\delta^* \leftarrow \delta)$ transition, may move lower in energy.

Hence the mixing of the type proposed in Fig. 3.20 may increase, causing a red shift and increase in intensity of the $^1(\delta^* \leftarrow \delta)$ transition. Closer energetic proximity of the M-M bonding orbitals with the ligand orbitals would then also cause the calculated reduction in the percentage metal character in the M-M bonding orbitals for this compound, when compared to the $[Mo_2Cl_8]^{4-}$ ion.

Taking into account these observations, there appear to be a number of possible explanations for the larger value of %δ(MoMo) for the $[Mo_2Cl_8]^{4-}$ ion:

1. The greater percentage metal character in the M-M δ bond for the $[Mo_2Cl_8]^{4-}$ ion (89% [4.22]], compared with 78% for $Mo_2Cl_4(PMe_3)_4$ [4.8]) means that breaking the δ bond will cause a larger change in the M-M bond length in the former compound. However, within the series $Mo_2X_4(PMe_3)_4$ (X = Cl, Br or I), a very large reduction in percentage metal character is calculated (78% X = Cl, 53% X = I) [4.8]. This is not reflected in a change in the values of %δ(MM) in the $^1\delta\delta^*$ state.

2. A large amount of Duschinsky mixing between the ν_1 and ν_2 normal modes in the $^1\delta\delta^*$ excited state occurs for $[Mo_2Cl_8]^{4-}$, which has not been detected by the SOS calculation. Inclusion of Duschinsky mixing was not found to be necessary to fit the data for either of the two compounds in question.

The presence of Duschinsky mixing between two modes in the excited state, however, results in the simultaneous enhancement of the two modes in the RR spectrum (section 1.4). For both the $[Mo_2Cl_8]^{4-}$ ion and for $Mo_2Cl_4(PMe_3)_4$, a small amount of enhancement of the ν_2 mode is seen in the RR spectrum in resonance with the $^1(\delta^* \leftarrow \delta)$ transition. Two points must be noted about this observation: first, the enhancement is a necessary, but not sufficient condition for Duschinsky mixing between two modes - therefore it does not definitely indicate Duschinsky mixing is present, and second, the progression in the ν_2 mode is very

short (≤ 2 quanta) in comparison with that in the ν_1 mode (≤ 11 quanta [4.26]). Hence, any such mixing, if present, is likely to be small.

3. The M-M δ bond has a larger contribution to the overall M-M bond strength in the $[Mo_2Cl_8]^{4-}$ ion than for $Mo_2Cl_4(PMe_3)_4$. If this were the case, the greater importance of a relatively 'weak' component of the bond might be reflected in a longer MM bond length for the former species. It is possible that the uniformity of the percentage contribution of the δ overlap to the total M-M bonding overlap [4.8] in the series $Mo_2X_4(PMe_3)_4$ (X = Cl, Br or I) may be the reason for the observed insensitivity of either *r*(MoMo), or %δ(MM) to a change in X. Therefore, this contribution may also be the reason for the larger %δ(MM) value for the ion $[Mo_2Cl_8]^{4-}$. Unfortunately, no estimates of the Mulliken overlap populations for the σ, π and δ components of the M-M bond in this ion are available for comparison with those calculated for the $Mo_2X_4(PH_3)_4$ series.

4. The difference between the parameter values of the two compounds can be ascribed to the large change in the overall charge of the species on replacing four Cl^- ligands by four $(PMe)_3$ ligands.

The $^1\delta\delta^*$ excited state can be thought of, in the Valence Bond (VB) treatment, as having a large degree of ionic character [4.11, 4.17]. The VB description of the four states arising from two electrons in the δ/δ^* manifold is as follows: With one electron in each d_{xy} orbital (on each metal), with spins opposed, the M-M bond is covalent and non-polar, corresponding to the ground $^1\delta^2$ state. The δ bond is weak and therefore the aligning of the spins on the electrons parallel causes very little energy loss; thus the $^3\delta\delta^*$ state lies close in energy to the ground state. The two excited states, $^1\delta\delta^*$ and $^1(\delta^*)^2$ have a large degree of ionic character, with both electrons in the d_{xy} orbital of the same metal, with paired spins. The $^1(\delta^*)^2$ state has a symmetric combination of d_{xy} orbitals, while the $^1\delta\delta^*$ state has an antisymmetric combination. When bonding is very weak, these states correlate to the MO configurations.

Thus, the $^1\delta\delta^*$ state is represented schematically as:

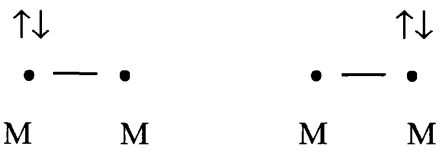

The creation of a state with ionic character within an ion of overall charge -4 may cause different perturbations to the M-M bonding than in a neutral compound. Thus, the repulsions between the Cl^- ions, or between the Mo atoms may be larger, producing a larger change in the Mo-Mo bond length as a result.

It is difficult at this stage to discount completely any of the above possibilities as an explanation for the large bond length change observed for the $[Mo_2Cl_8]^{4-}$ ion, except to note that the first possibility is least plausible, given the uniformity of the %δ(M-M) values for the $Mo_2X_4(PMe_3)_4$ series of compounds. It also seems unlikely, from current RR data, and from the SOS calculations themselves, that significant Duschinsky mixing is present, although a small amount could reinforce any other effect tending to increase the bond length change on excitation to the $^1\delta\delta^*$ state. The questions raised by these calculations merit further work, with, if possible, the $[Mo_2Br_8]^{4-}$ ion also being investigated. This has, up to now, proved difficult, as will be discussed in chapter 6. Other Mo(II) compounds with varying degrees of M-M δ bonding may also provide interesting results for comparison with those obtained in this work.

It is possible that a combination of the large negative charge on the $[Mo_2Cl_8]^{4-}$ ion, together with, perhaps, and inherent larger contribution of the δ bond to the overall M-M bond strength in this ion, could produce a larger bond length change than for the similar $Mo_2Cl_4(PMe_3)_4$ compound.

Thus far, only the values of the parameter δ(MM) have been considered in the discussion of trends among the compounds. An initial consideration of the calculated values of $\tilde{\nu}_e$, and the percentage changes in the wavenumber of this mode from the ground state value, may point to an apparently contradictory trend to that seen for the parameter δ(MM). Thus, the compounds showing the largest %δ(MM) also show the smallest percentage change in the wavenumber of the mode. The especially small change in mode wavenumber observed for the $[Mo_2Cl_8]^{4-}$ ion may appear to indicate that in fact the δ bond does not play an unusually large part in the overall M-M bond in this complex, and thus that it is the charge difference between $Mo_2Cl_4(PMe_3)_4$ and the $[Mo_2Cl_8]^{4-}$ ion which is the major reason for the difference in their calculated parameter values.

However, the parameter Δ, and hence the bond length change δ(MM), represents the *primary* geometric change which can accompany an electronic transition: this term corresponds to linear electron-phonon coupling, while a change in the mode wavenumber is a manifestation of quadratic electron-phonon coupling. The previous discussions and comparisons were based on the premise that the bond length change is the dominant structural change in the molecule on excitation, and that intuitive reasoning about the relationship between the force constant value and the bond length changes may not be entirely valid. Certainly it is seen that a relatively large change in force constant in the ground state in the series $Mo_2X_4(PMe_3)_4$ (X = Cl, Br or I), where $\tilde{\nu}_g$ = 355 cm^{-1} for X = Cl and 343 cm^{-1} for X = I, is not reflected in a large change in Mo-Mo bond length (*r*(MoMo) = 2.130 Å; X=Cl, 2.127 Å, X = I). This is also borne out in the excited state, where different percentage changes in the mode wavenumber are observed across the series, with very similar percentage changes in the bond length being calculated.

Simple relationships relating force constants for stretching modes of pseudo-diatomic species to the diatomic bond lengths [4.27] have also been found to be inappropriate for the ν_1 (ν(MM)) mode of quadruply bonded dimetallic

compounds [4.2]. The recent normal mode analysis [4.17] has shown that the pseudo-diatomic approximation is, in fact, reasonably valid for this vibrational co-ordinate for most of these compounds. Thus simple relationships relating bond lengths and mode frequencies must obviously be treated with some caution in these cases and thus it may be more reliable to base conclusions upon trends in the former parameter, rather than on the latter. It may be possible that other factors, such as repulsions between the ligands in the excited state, charge of the species, and the number and 'rigidity' of the counter-ions in the lattice may affect the reaction of the environment around the molecule to any change in the metal-metal bond length, and possibly affect the force constant.

On the basis of the evidence of the SOS calculations, and the available spectroscopic and theoretical studies of these compounds to date, it can, at present, only be concluded that the behaviour of the $[Mo_2Cl_8]^{4-}$ ion is different to that of $Mo_2Cl_4(PMe_3)_4$.

4.8 The Phenomenological Lifetime Factor, Γ

This factor is included in the theoretical treatment of the ABS and RR processes (chapter 2) in order to take account of the finite lifetime of the excited state. This finite lifetime is reflected in a broadening ("homogeneous broadening" represented by a factor Γ in cm^{-1}) of the bands in the ABS spectrum and also affects the intensity ratios of the overtones in a RR progression.

The two main mechanisms for decay from the excited vibronic states of the molecules studied here are spontaneous emission, which gives rise to natural lifetime broadening, and non-radiative decay via many low frequency lattice modes in the solid or solution matrix. However, natural lifetime broadening for an electronic transition is expected to be only ca. 10^{-4} cm^{-1} as a result of the long lifetime of the excited electronic state (typically of the order of ns). As discussed in section 3.5, the timescale of the vibrational decay via non-radiative routes

involving lattice modes is expected to be of the order of a vibrational period (< 10^{-12} s), thus necessitating that RR scattering take place on a very fast timescale. The broadening resulting from this process would then be expected to be of the order of ca. 5 cm^{-1}.

Thus, it is clear from the calculated values of Γ in Table 4.6 that other processes must account for its large magnitude. These are the multiphonon processes associated with the extra degrees of freedom arising from other modes in these systems. These include low frequency lattice modes which can, in addition to acting as sinks for non-radiative decay from the excited state, be excited simultaneously in ABS. Thus, in effect, each vibrational level in the excited electronic state is broadened to incorporate a manifold of states corresponding to the vibrational level itself plus various degrees of excitation in the other modes. This then has the effect of broadening each vibronic band in the ABS spectrum, and of averaging the intensity ratios in the RR spectrum.

Since this broadening does not arise from factors which affect the lifetime of the excited state, but is nevertheless incorporated into Γ in the theory for convenience, Γ is termed the *phenomenological* lifetime factor, rather than the homogeneous lifetime factor. Owing to the reduced resolution because of broadening of the vibronic structure in the ABS spectrum, a Lorentzian distribution was assumed to be adequate to represent this factor, as any discrepancy between this and a more appropriate Gaussian distribution would not be detectable

From Table 4.6, it is seen that Γ is, in general, larger for the $[M_2X_8]^{n-}$ ions than for the series $Mo_2X_4(PMe_3)_4$ (X = Cl, Br or I). This may reflect the greater number of lattice modes in the case of the negatively charged ions, where counter-ions are also present in the matrix.

Finally, it is seen from Table 4.6 that, in order to fit the data for the series $Mo_2X_4(PMe_3)_4$ (X = Cl, Br or I), the value of Γ was required to be dependent on

the vibrational occupation number of the excited electronic state (v). Such a dependence, if present for the $[M_2X_8]^{n-}$ ions, could not be observed owing to the large amount of broadening of the vibronic bands in the ABS spectrum. This v - dependence is thought to arise because of the energy-dependence of the transition probability. This is expected to increase with energy, and thus Γ is also expected to be dependent on v.

4.9 Conclusions

The SOS method has been found to be applicable to the ν_1 co-ordinate of the $[M_2X_8]^{n-}$ ions and $Mo_2X_4(PMe_3)_4$ series (X = Cl, Br or I) in the $^1\delta\delta^*$ excited state. Values for the structural parameters along the ν_1 co-ordinate in this excited state have been found and show good agreement with previous measurements, or estimations, where available.

From the results on the ion $[Re_2Br_8]^{2-}$, it has been possible to conclude that the timescales of the ABS and RR experiments permit observation of an eclipsed $^1\delta\delta^*$ excited state only, regardless of the medium in which the ion is held. Furthermore, it has been proposed that the potential of the excited state for these molecules is a function of the torsion angle of the ligand groups about the M-M axis, with minima corresponding to eclipsed and staggered conformations. The conversion from eclipsed to staggered minimum takes place as a result of vibrational decay in the excited state, and thus this latter conformation cannot be observed on the timescale of a conventional RR experiment. However, nanosecond TR^3 pump-probe experiments may produce spectra of the excited state characteristic of the relaxed, staggered conformation.

Thus, a direct comparison has been possible of the parameter values calculated for the $[M_2X_8]^{n-}$ ions and those calculated for the compounds $Mo_2X_4(PMe_3)_4$ (X = Cl, Br or I), where such twisting is thought to be prevented by the large phosphine ligands. In each case, the values are those of an eclipsed excited state.

A comparison of the percentage changes in the metal-metal bond length in the excited state between the Re(III) and Mo(II) compounds appears to indicate a larger δ-overlap, and hence a larger bond length change in the $^1\delta\delta^*$ state, for the Mo(II) species. This is probably a reflection of the contraction of the d-orbitals (which form the M-M δ-bond) in the Re(III) compounds, as a result of the higher oxidation state of the metal. The extra core electrons in a third row metal are also expected to increase the M-M bond length, and hence reduce the δ-overlap.

A comparison of the same percentage changes in the M-M bond length across a halide series such as $[Re_2X_8]^{2-}$ (X = Br, I) or $Mo_2X_4(PMe_3)_4$ (X = Cl, Br or I) has shown that this change is independent of the nature of X. This is in contrast to other spectroscopic parameters, such as the energy and intensity of the $^1(\delta^* \leftarrow \delta)$ transition which are seen to vary strongly as X becomes more reducing. Electronic structure calculations also point to a variable contribution of the halides to M-M δ bonding on these systems. However, the M-M bond length in the ground state appears relatively indifferent to the identity of the halide. From the SOS results, it can be concluded that the M-M bond length in the excited electronic state, where the δ-bond has formally been broken, is also independent of the nature of X. Thus it appears that the δ bond strength is actually quite uniform across a halide series, despite the apparent increased role of the halides in the M-M bonding as X becomes more reducing. It has been suggested that one reason for this may be the insensitivity to the nature of X of the calculated percentage contribution of the δ - overlap population (Mulliken population) to the total M-M bond overlap population.

The behaviour of the $[Mo_2Cl_8]^{4-}$ ion in the $^1\delta\delta^*$ state has been seen to be slightly anomalous, with a very high percentage change in the M-M bond length in comparison to the analogous $Mo_2Cl_4(PMe_3)_4$. It seems plausible at this stage to assume that the differences in charge and number of cations, as well as possibly a larger percentage contribution of the δ-bond overlap population to the total bond

overlap population in the case of $[Mo_2Cl_8]^{4-}$, may be important in determining the bond length change in the excited state.

The calculated values for the phenomenological lifetime factor, Γ, have highlighted the important role of multiphonon processes in these systems. It has also been possible to resolve a dependence of Γ on the vibrational quantum number of the excited electronic state for the series $Mo_2Cl_4(PMe_3)_4$ (X = Cl, Br, I). It has also been found that NC coupling can largely be neglected for these systems.

Finally, it is interesting to assess the consistency of the porposed model for the potential energy of the $^1\delta\delta^*$ state with data from emission spectra and kinetics studies of these compounds. Both the emission and transient absorption experiments probe a vibrationally relaxed excited state, and therefore, if twisting about the M-M axis can occur, the results may be characteristic of a staggered conformation in the $^1\delta\delta^*$ state. Thus, a low quantum yield for emission and poor overlap and mirror image relationship between the $^1(\delta^* \leftarrow \delta)$ ABS and $^1(\delta \leftarrow \delta^*)$ emission is expected. This has been observed for the $[M_2X_8]^{n-}$ ions in the solid state [4.19]. By contrast, the emission and ABS spectra of the compounds $Mo_2X_4(PMe_3)_4$ (X = Cl, Br or I) and $Mo_2Cl_4(PBu_3)_4$ (for which the barrier to rotation about the M-M axis in the $^1\delta\delta^*$ state would be higher) show good overlap and mirror symmetry, and the quantum yields of emission are correspondingly high [4.12, 4.28]. However, there remains some debate about the possibility of twisting in the solid state, or in these sterically hindered $Mo_2X_4(PMe_3)_4$ (X = Cl, Br or I) compounds. Nevertheless, the model proposed in chapter 3, which would permit the emission and kinetics studies to arise from the relaxed excited state, is not inconsistent with these emission and kinetics studies.

It can be concluded that the SOS study of the $^1\delta\delta^*$ excited state of these compounds has provided a much clearer insight into its structure and behaviour, and has allowed previously confusing experimental results to be understood.

Chapter 5

Attempted Application Of The Overtone Transform (OT) Method To Study The Structure Of The $^1A_{2u}$ Excited Electronic State Of Quadruply-Bonded $[M_2X_8]^{n-}$ Ions

The Overtone Transform method (OT) is the second of the studied approaches used to link the absorption profile of a particular resonant electronic transition to the relative intensities of the members of a vibrational mode progression in the RR spectrum. In doing so it yields, in principle, structural information relating to changes in the chosen vibrational mode (and co-ordinate) in the resonant excited electronic state.

The theoretical basis for the OT method was outlined in chapter 2. The final equations (Eqns (2.85) and (2.86)) relate the relative intensity ratios of the bands of a given totally symmetric mode progression in the RR spectrum to the resonant absorption band profile (ABS) and to three structural parameters of the vibrational mode in the resonant excited electronic state. These parameters are $\tilde{\nu}_e$ (the wavenumber of the mode in the resonant excited electronic state), δ (related to a displacement between the PE curves of the ground and excited states along the co-ordinate of interest), and a linear non-Condon (NC) coupling parameter, m. The significance of these parameters is explained in greater detail in chapter 2.

These OT equations also highlight one of the key differences between the OT and SOS approaches: in the OT method, the experimental ABS profile is used as *input* to the calculation of the RR intensity ratios; in the SOS method, the two types of data are fitted simultaneously in a 'pure simulation' calculation. Nevertheless, the experimental data required for application of the OT method remain easily accessible: an ABS profile of the resonant electronic transition and the relative intensity ratios of the first four harmonics of the mode in the RR spectrum are sufficient to yield values for the three structural parameters. For the same reasons as outlined in chapter 3, REPs are avoided where possible as the source of RR intensity data.

The purpose of this study is twofold: first, to use the OT method to obtain structural information about a molecule in an excited electronic state, and second, in so doing, to assess the performance and applicability of the method in the particular case chosen. The molecules chosen for study must adhere to any restrictions enforced by the method ensuring that any discrepancy between expected and calculated results arises solely from problems with the OT method, rather than from any unsuitability of the molecule. These restrictions arise from both the assumptions and approximations used in the theoretical development, and from the availability and accuracy of the experimental data. These issues will be discussed further in sections 5.1 and 5.2 respectively.

The metal-metal quadruple bond in the $[M_2X_8]^{2-}$ ions serves as a useful vehicle for this combined purpose. First, the ν_1 mode and the resonant $^1\delta\delta^*$ ($^1A_{2u}$) excited state appear to fit well to the restrictions and assumptions of the method. Second, some information on the values of the structural parameters to be calculated is available (or able to be estimated) from other sources. For example, vibronic structure on the low temperature electronic absorption spectrum can give an estimate for $\tilde{\nu}_e$, thus allowing the performance of the OT method to be assessed.

Even when a molecule is 'well-behaved' with respect to the criteria laid down by the method, further problems in its application cannot be ruled out. The final equations of the OT theory (Eqns (2.85) and (2.86)) cannot be solved analytically to yield expressions for $\tilde{\nu}_e$, δ, and m for the vibrational mode. Therefore, a *numerical* solution must be found by allowing values of each of the three parameters to vary simultaneously over a reasonable range and finding the best fit between the experimental and calculated RR intensity ratios. The effect of such a 'multidimensional grid search' on the location and accuracy of solution parameter values is still to be assessed. This will be discussed further in section 5.3. A schematic diagram of the OT method, highlighting the role of the experimental absorption spectrum as input into the calculation, is shown in Fig. 5.1.

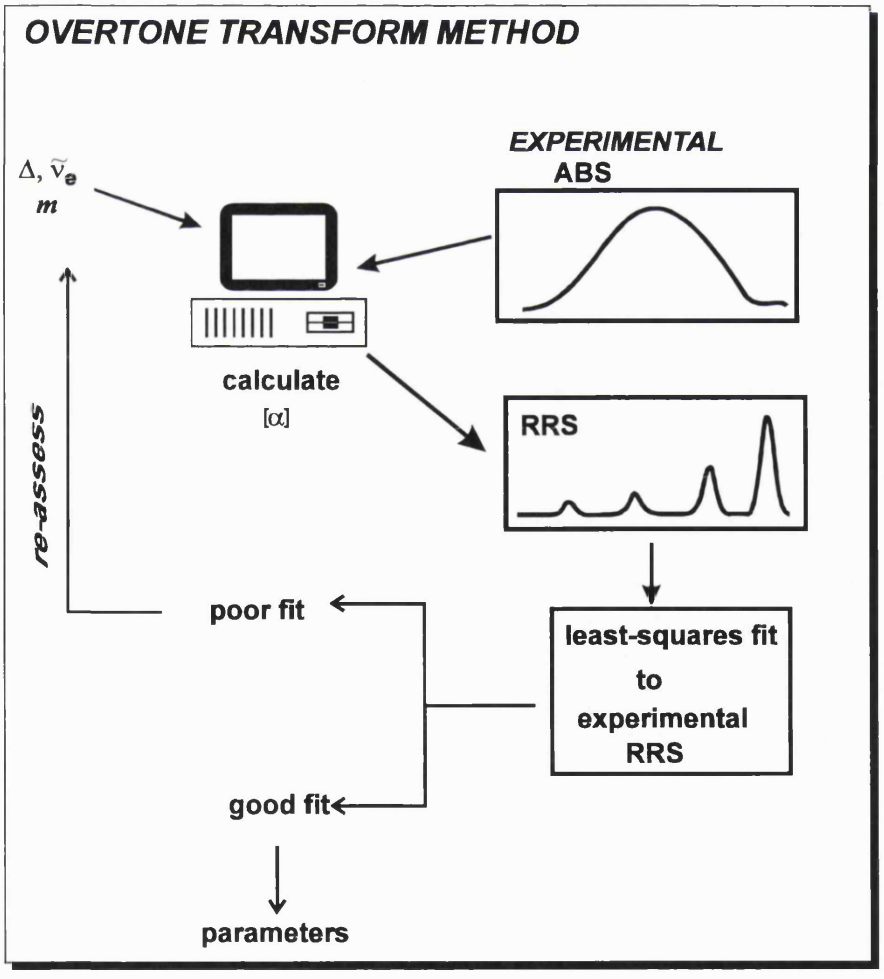

Fig 5.1 Schematic diagram of the OT method.

5.1 Assumptions and Approximations of the OT Theory

The theoretical development of the OT method (chapter 2) may be assumed (within the limits defined) to be correct. However, as detailed in chapter 2, the approximations and assumptions employed therein necessarily restrict the nature of the molecule to be studied. The criteria which must be met are discussed in chapter 2 and are summarised below:

(I) Only totally symmetric normal co-ordinates may be considered.

(II) The vibrational normal mode (corresponding to the co-ordinate of interest) must not mix with any other modes in the resonant excited state (i.e. 'Duschinsky mixing' involving this mode must be absent).

(III) The ground state wavenumber of the vibrational mode of interest must be sufficiently high for the 'effective-zero temperature' approximation, outlined in chapter 2, to hold. The experimental consequence of this assumption is that samples must usually be held in the solid state at low temperatures (~ 77 K).

(IV) The resonant electronic state must be single, non-degenerate and harmonic, and non-adiabatic couplings, which may cause a breakdown of the Born-Oppenheimer approximation, must be absent.

(V) The change in vibrational wavenumber of the mode of interest in the excited electronic state must be sufficiently small for the condition:

$$d^2 = \left(\frac{\tilde{\nu}_e - \tilde{\nu}_g}{\tilde{\nu}_e + \tilde{\nu}_g}\right)^2 << 1$$

where $\tilde{\nu}_e$ is the mode wavenumber in the excited electronic state (e) and $\tilde{\nu}_g$ is the analogous wavenumber in the ground state (g). In practice, this condition is

effectively met if :

$$\left|\frac{\tilde{\nu}_e - \tilde{\nu}_g}{\tilde{\nu}_e + \tilde{\nu}_g}\right| \leq 0.01$$

(VI) Non-Condon (NC) coupling involving the chosen vibrational mode must be sufficiently small for the assumption of only linear NC coupling to be valid. From theory, m^2 must be small in comparison to 1. In practice this condition is met if $|m| \leq 0.1$.

The restrictive effect of these criteria was illustrated in chapter 2 by the two examples of the S_2^- ion in ultramarine and by I_2. Thus, any molecule must be carefully assessed on the basis of the above points before application of the OT method.

5.2 Experimental Restrictions and Assumptions

Application of the OT method requires two sets of experimental data: the resonant absorption band profile (ABS) in the format of a series of *x-y* data points, and the ratios of the integrated RR intensities of the first four harmonics of the progression in the mode of interest. These ratios must be corrected for all frequency-dependent factors except the molecular scattering factor, as explained in Appendix A1.

The first *experimental* restriction on the molecule to be studied by the OT method is therefore that it shows a well-separated band in the absorption spectrum within the visible region of accessible laser lines, such that, by irradiating within the contour of this band, a progression up to the fourth harmonic in the mode of interest is seen. Clearly the particular excited electronic state to which the absorption corresponds must meet the theoretical criteria outlined in the section 5.1. The 'effective-zero temperature' assumption (5.1.III) usually also requires that the molecules studied may be held in the solid state and

that the spectra be recorded at liquid N_2 temperatures. This has the further benefit of enhancing any detail on the spectra.

Provided these experimental data are available, it then remains only to optimise their quality. Minimisation procedures for experimental error, together with corrections for frequency-dependent factors other than the molecular scattering, are detailed in Appendices A1-A3. The problems associated with the correction for baseline scattering and reflection in the ABS spectrum of a pressed disc of a compound have been discussed in Appendix A3. The profiles used here are those which have been corrected accordingly.

5.3 The Multidimensional Grid Search Method

The procedure which has been adopted for finding the optimum values of the parameters $\tilde{\nu}_e$, δ and m for a given mode is to minimise the value of a function $F(\tilde{\nu}_e, \delta, m)$, which describes the least-squares fit between the experimental and calculated RR intensity ratios [5.1]. $F(\tilde{\nu}_e, \delta, m)$ is defined as:

$$F(\tilde{\nu}_e, \delta, m) = \sum_{i=2}^{4} \left[\left(\frac{|\alpha_i(\tilde{\nu}, \delta, \tilde{\nu}_e, m)|^2}{|\alpha_1(\tilde{\nu}, \delta, \tilde{\nu}_e, m)|^2} \right)_{\text{calc}} - \left(\frac{\text{REP}_i(\tilde{\nu})}{\text{REP}_1(\tilde{\nu})} \right)_{\text{exp}} \right]^2 \qquad (5.1)$$

where $\tilde{\nu}$ denotes the excitation wavenumber.

The values of the parameters are allowed to take specified values within a pre-defined 'search range': the three parameters are then varied simultaneously and a minimum in $F(\tilde{\nu}_e, \delta, m)$ is sought. For brevity, $F(\tilde{\nu}_e, \delta, m)$ will henceforth be denoted F and its dependence on $\tilde{\nu}_e$, δ, and m will remain implicit.

For example, if values of $\tilde{\nu}_e$, δ and m are sought for a mode with $\tilde{\nu}_g$= 300 cm^{-1}, where a displacement (δ) of approximately 5 pm is expected, a typical search range would be:

Parameter	Start Value	End Value	Step (S)
$\tilde{\nu}_e$/ cm^{-1}	300	250	-5
δ / pm	0	10	0.5
m	0	0.1	0.01

Thus, 2000 points would be searched in this case.

The search ranges of the three parameters can be thought of as constituting a three-dimensional grid as shown in Fig. 5.2.; within this grid, the function F must be minimised.

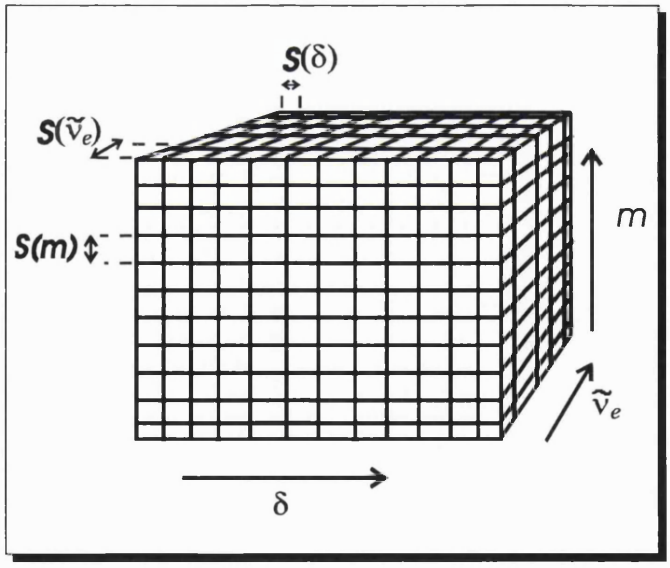

Fig. 5.2 The mutidimensional parameter grid. $S(\tilde{\nu}_e)$ denotes the step size for the parameter $\tilde{\nu}_e$, $S(\delta)$ denotes the step size for the parameter δ and $S(m)$ is the step size for the parameter m.

Such a multidimensional grid search procedure poses immediate problems:

(i)The fitting function, F, is a complicated function of all three parameters. Therefore, multiple *sets* of values of $\tilde{\nu}_e$, δ and m (denoted $\{\tilde{\nu}_e, \delta, m\}$), which produce a minimum in F, will exist. It can therefore never be guaranteed that any particular $\{\tilde{\nu}_e, \delta, m\}$ set constitutes a unique solution. It is hoped that many of the solution sets will correspond to values of the parameters lying outside a sensible physical range, and thus these sets may be eliminated. For example, if the resonant electronic transition corresponds to the promotion of an electron from a bonding molecular orbital to an anti-bonding orbital, then a *decrease* in the length of that particular bond on going to the excited state is not expected. Therefore, for the mode corresponding to the bond stretch only positive values of δ would be considered.

(ii)A sensible 'search range' across which each of the parameter values will be varied, must be pre-defined. In doing so, a reliance of the calculation on 'external' information, such as vibronic structure on the ABS profile (or its first derivative), which may indicate the expected magnitude of $\tilde{\nu}_e$, will arise. While such information may frequently be available, and indeed is desirable if a molecule is to be used to 'test' the OT method, this dependence may limit the usefulness of the method for 'blind' cases.

(iii)A suitable 'step size', S, defining the increment by which the value of the parameter is sequentially changed during the search, must be defined for each parameter. Clearly, the value of S will eventually limit the resolution and accuracy with which the final solution value of that parameter can be quoted. For this reason, small increments (S) would be preferable. However, reducing the size of S increases the number of points in the grid and the calculations can become excessively slow. Furthermore, some degree of consistency between the level of error on the experimental data and the level of resolution sought by the grid search procedure must be achieved. It would clearly be entirely inconsistent to use a digitised absorption spectrum with a resolution of 10 cm^{-1} in the

calculation and subsequently search for $\tilde{\nu}_e$ values with $S(\tilde{\nu}_e) = 0.5$ cm^{-1}.

(iv)The visualisation of the function F in the three-dimensional parameter grid space, and hence the location of minima in this function, is not a straightforward problem. One approach which has been adopted elsewhere [5.2] is to search the entire grid and retain only the absolute lowest value of F together with its grid position. Once found, further fine searches around this grid point may be made. However, since F is a complex function of all three parameters, more than one solution set $\{\tilde{\nu}_e, \delta, m\}$ will exist, i.e. there will be more than one position in the three-dimensional grid where a minimum will be found. These different minima, while all 'solutions', may have F values differing perhaps in only the third or fourth decimal place and, since the calculational error in F is not known, these other minima must also be retained and assessed on the basis of the likelihood of their $\{\tilde{\nu}_e, \delta, m\}$ values. However, the procedure outlined above will the retain only the absolute minimum in F and hence the other possible minima will be missed. A broader view of the trends in F as each of the parameters is varied must be taken; this will allow further problems, such as the location of very sharp minima, to be seen.

5.4 New Procedure for finding solution parameter values $\{\tilde{\nu}_e, \delta, m\}$

The procedure adopted in this work for finding minima in the least-squares fitting function, F, and hence solution sets of parameter values $\{\tilde{\nu}_e, \delta, m\}$, aims to allow a broader view of the behaviour of the function F as the three parameters are varied and hence to address some of the problems outlined in section 5.3.

Before the search procedure can begin, a suitable 'search range' for each of the three parameters must be defined, thus setting up the 3-D grid. These ranges must take into account estimates of the magnitude of the parameter values, where available, from 'external' experiments as well as the level of accuracy of the data.

For the NC factor, m, it is known from theory (criterion 5.2(VI)) that the upper and lower limits on m are 0.1 and -0.1 respectively. A step size $S(m)$ = 0.01 is expected to be small enough to allow a reasonable accuracy in m without excessively reducing the speed of the calculations by creating too many grid points.

The upper and lower limits on the values of δ must be decided on by taking into account external information about the electronic transition. For example, if the transition takes an electron from a bonding to an anti-bonding orbital, only positive values of δ for that co-ordinate are searched. Once the limiting values of δ have been set, the step $S(\delta)$ is set to 0.5 pm. This is in reasonable agreement with the accuracy usually quoted on crystallographic measurements of bond lengths.

In order to set a range for the wavenumber in the excited state, $\tilde{\nu}_e$, external information must again be used to decide on the magnitude and sign of any mode frequency change. Furthermore, the step size, $S(\tilde{\nu}_e)$, *must* be consistent with the accuracy of the experimental absorption profile. The ABS profile is digitised and used in the calculation in the form of a series of evenly-spaced x-y points. The program written to perform the OT calculations [5.2] allows an upper limit of 500-600 data points in the ABS profile; beyond this the calculations become excessively slow. This means that the absorption is only definitely known at particular wavenumbers, these being separated by a step size S(ABS) as shown in Fig. 5.3.

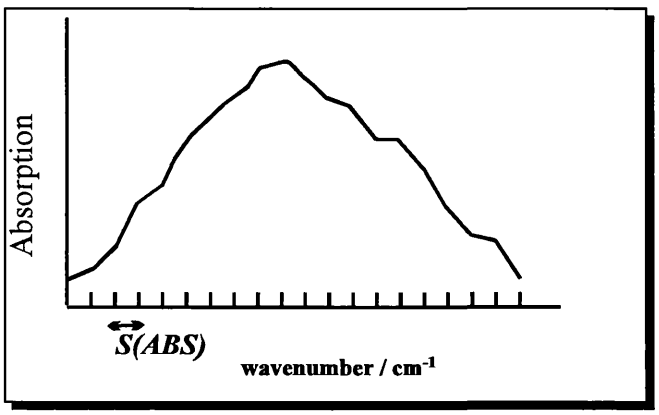

Fig 5.3 Schematic diagram of ABS spectrum showing S(ABS)

Between these defined points, the ABS must be calculated by interpolation. It would therefore be inconsistent to search for a $\tilde{\nu}_e$ value with a step size much less than $\frac{S(\text{ABS})}{2}$, the approximate error in each ABS point. Therefore, $S(\tilde{\nu}_e)$ is set to a convenient number of the order of $\frac{S(\text{ABS})}{2}$ or $\frac{S(\text{ABS})}{3}$.

A further limit on the search range of $\tilde{\nu}_e$ is that the criterion (5.1 V) must hold at all times:

$$\left|\frac{\tilde{\nu}_e - \tilde{\nu}_g}{\tilde{\nu}_e + \tilde{\nu}_g}\right| \leq 0.1$$

Once the search 'grid' has been defined, the method of searching and visualising the function F must be found. The new procedure adopted here is set out below and illustrated schematically in Fig. 5.4.

Step A: Initially, m is set to 0 and thus the search range is limited to two dimensions. For this value of m, a range of δ and $\tilde{\nu}_e$ values is searched in the following way.

Step B: For each $\tilde{\nu}_e$ value, the complete range of δ values is searched and the δ value corresponding to the minimum in F is found. This value is denoted $\delta_{\min}(\tilde{\nu}_e)$ for that particular $\tilde{\nu}_e$ value; the corresponding F value is then denoted $F_{\min}(\tilde{\nu}_e, \delta_{\min}(\tilde{\nu}_e))$. Again, for brevity, this quantity will be referred to as $F_{\min}$ and its parametric dependence assumed.

Step C: The value of $\tilde{\nu}_e$ is then changed by the amount $S(\tilde{\nu}_e)$ and the process repeated. Thus, a series of $\delta_{\min}(\tilde{\nu}_e)$ and $F_{\min}$ values is built up for all the possible values of $\tilde{\nu}_e$ and a table can be drawn up.

Step D: From this table, a plot of $F_{\min}$ vs $\tilde{\nu}_e$ shows the trend in the values of the fitting function corresponding to the $\delta_{\min}(\tilde{\nu}_e)$ as $\tilde{\nu}_e$ is varied. The $\tilde{\nu}_e$ value at which

the lowest F_{min} is seen is then denoted $(\tilde{\nu}_e)_{min}$ and the corresponding δ_{min} value, $\delta_{min}((\tilde{\nu}_e)_{min})$. Thus, the solution set for $m = 0$ is then $\{(\tilde{\nu}_e)_{min}, \delta_{min}((\tilde{\nu}_e)_{min}), 0\}$.

Step E: This search process is illustrated in Fig. 5.4. It is repeated for all the possible values of m, so that a 3-D picture of the grid may be built up.

An advantage of this method is that more than one minimum may be seen: a plot of $\tilde{\nu}_e$ vs. F_{min} (step D) may show more than one minimum - the $\delta_{min}(\tilde{\nu}_e)$ values corresponding to these minima in F_{min} may then be found (from the table in Step C) and so the grid position of a number of minima can be seen. Similarly, a plot of F vs. $\delta(\tilde{\nu}_e)$ for a particular $\tilde{\nu}_e$ may show more than one minimum; again each of the minima may be followed through so that the exact grid position can be found.

If the plot in Step D in Fig 5.4 shows no actual minima, but rather a 'bumpy plateau', it may be assumed that no actual minima in F can be found within this search range of $\tilde{\nu}_e$ and δ, for that particular value of m : all possible sets of values of $\{\tilde{\nu}_e, \delta, m\}$ for this value of m fit the experimental data equally well and so no real minimum in the fitting function can be found. This would imply that the method is insufficiently sensitive in this case.

5.5 Results of OT calculations on the M-M Co-ordinate of $[M_2X_8]^{n-}$ Ions ($[Re_2Br_8]^{2-}$, $[Re_2I_8]^{2-}$ and $[Mo_2Cl_8]^{4-}$)

The system chosen for study here, as in the case of the SOS method, is the quadruply-bonded M-M co-ordinate of the $[M_2X_8]^{n-}$ ions ($[Re_2Br_8]^{2-}$, $[Re_2I_8]^{2-}$ and $[Mo_2Cl_8]^{4-}$). The resonant electronic transition is that which takes an electron from the highest occupied molecular orbital of the metal-metal bonding system, the δ-orbital, to the antibonding δ^* orbital ($^1A_{2u} \leftarrow {}^1A_{2g}$, or $^1(\delta^* \leftarrow \delta)$), as explained

Fig. 5.4 Schematic Diagram of procedure for finding minima in OT method

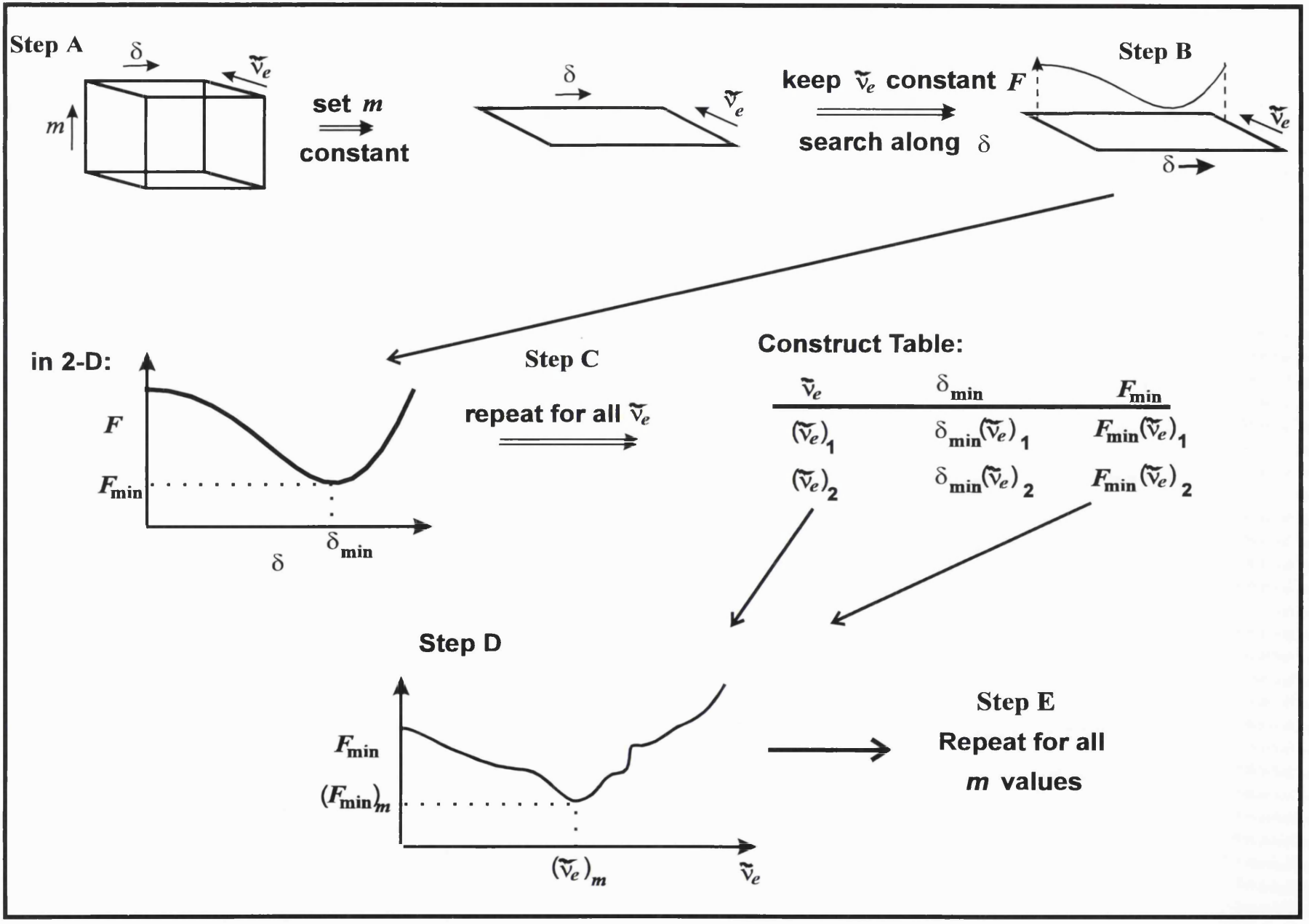

in chapters 1 and 3. The RR spectrum recorded with an excitation frequency within the contour of this $^1\delta^* \leftarrow \delta$ band shows in each case a long progression in a vibrational mode assigned to a totally symmetric M-M stretch (ν(M-M), or ν_1). Thus the OT method will be used to attempt to find structural changes along the M-M co-ordinate in the $^1A_{2u}$ excited state: $\tilde{\nu}_e\{\nu_1\}$, δ(M-M) and a NC factor, *m*, relating to this co-ordinate. These will be denoted $\tilde{\nu}_e$, δ and *m* henceforth and their relation to this co-ordinate assumed.

This system appears to meet the criteria required for application of the OT method (as outlined in sections 5.1 and 5.2):

(I) ν_1 is a totally symmetric mode in the D_{4h} point group

(II) Owing to the presence of a strong progression in this mode only in the RR spectrum, ν_1 is not thought to mix significantly with any other modes in the $^1A_{2u}$ state.

(III) The wavenumber of the ν_1 mode in each ion is sufficiently high (between 250 and 350 cm^{-1}) for the condition $\frac{N(2\nu_1)}{N(\nu_1)} << 0.01$ at 77 K. While this condition also holds at room temperature for these ions, the quality of the spectra is enhanced on lowering the temperature to 77 K.

(IV) The $^1A_{2u}$ excited state is a single, non-degenerate state which is not strongly dissociative.

(V) Using estimates of the values of $\tilde{\nu}_e(M_2)$ for the $[Re_2Br_8]^{2-}$ and $[Mo_2Cl_8]^{4-}$ ions from vibronic structure on low temperature UV/Vis absorption spectra, the condition $\left|\frac{\tilde{\nu}_e - \tilde{\nu}_g}{\tilde{\nu}_e + \tilde{\nu}_g}\right| \leq 0.1$ is estimated to hold well. It is expected that a similar percentage change in the value of the wavenumber for ν_1 in $[Re_2I_8]^{2-}$ to that in $[Re_2Br_8]^{2-}$ will be seen; if this is the case, the above criterion will also hold.

(VI) The extent and pattern of the vibrational progression of the ν_1 mode in the RR spectrum of each ion indicate that the major contribution to the resonance enhancement is likely to be through normal Condon mechanisms (A-term scattering); thus the retention of only a linear NC term appears to be valid.

It should be noted that the parameter δ is calculated from the Manneback relationships using a specified value for the reduced mass of the vibrating species. The problems associated with approximating the ν_1 mode of these systems to a local ν(M-M) stretch, and hence to adopting a reduced mass of an M_2 diatomic, have been outlined in Chapters 3 and 4. It is likely that there a small contribution to this normal mode from the ν(MX) local mode and thus the reduced mass of the system would be altered accordingly. However, for the purposes of comparison with the original SOS results in section 3.4 (based on the same diatomic approximation), the ν_1 mode of these molecules will be treated as a local ν(M-M) stretch throughout this study. Any corrections to the calculated values of δ are expected to be small (Chapter 4), and, by searching a wide range of possible δ values, any major discrepancies would be expected to become apparent.

These systems therefore appear to adhere well to the theoretical criteria of the OT method and all the required experimental data are easily accessible in each case. Clearly, the same precautions and considerations of the possible errors in the data as those outlined in Chapter 3 must be made.

Furthermore, with some estimates of the values of $\tilde{\nu}_e$ for the ν_1 mode for two of the ions, from vibronic structure on low temperature UV/Vis spectra [5.3, 5.4], and predictions of the corresponding values of δ from empirical force constant rules [5.5] , these systems also provide a good opportunity to test the performance of the OT method. Aside from the considerations of testing the method, the $^1A_{2u}$ excited state of these $[M_2X_8]^{n-}$ ions is of interest structurally, as outlined in section 1.7.

Experimental Data

The experimental data used in the OT calculations are those which were also used in chapter 3 for the SOS calculations on these ions. The ABS profiles of the $^1(\delta^* \leftarrow \delta)$ transition are shown in Fig. 3.4 - 3.6: these were recorded, manipulated and baseline-corrected as detailed in Appendices A1-A3. However, in order to use the available OT program, the number of *x-y* data points was reduced to approximately 500, thus altering the interval between the evenly spaced points.

The relative intensity ratios of the first four members of the $n\nu_1$ progression in the RR spectra were measured as described in Appendix A1. The RR spectra, recorded at 77 K, are shown for the three ions in Figs. 3.8 - 3.11. In the case of the OT method, the relative intensities were corrected for ν^4 scattering as well as spectral response (see Appendix A2 and A3). Table 5.1 shows the final corrected intensity ratios measured at 77 K, for the three ions $[Re_2Br_8]^{2-}$, $[Re_2I_8]^{2-}$ and $[Mo_2Cl_8]^{4-}$:

	$[Re_2Br_8]^{2-}$	$[Re_2I_8]^{2-}$	$[Mo_2Cl_8]^{4-}$
$\tilde{\nu}_L$ / cm^{-1}	15,453	13,297	19,435
$\tilde{\nu}_g$(M-M) / cm^{-1}	275	257	338
$I(\nu_1)$	100	100	100
$I(2\nu_1)$	41	45.6	56.3
$I(3\nu_1)$	24.8	23.3	35.5
$I(4\nu_1)$	14.8	18.4	26.5

Table 5.1 Relative RR intensity ratios for the $[M_2X_8]^{n-}$ ions at 77 K, corrected for ν^4 scattering and spectral response of the instrument. Error ~ 10%.

$[Re_2Br_8]^{2-}$

In order to define the search range of each of the three parameters $\tilde{\nu}_e$, δ and *m* for the ν_1 mode, any previous estimatess of some of these values were taken into account. From vibronic structure on the low temperature UV/Vis absorption band corresponding to the $^1(\delta^* \leftarrow \delta)$ transition, $\tilde{\nu}_e$ has been estimated as 255 cm^{-1}[5.3]

and the corresponding bond length change, δ, was calculated to be ~ 8 pm [5.5], using empirical force constant rules. Reduction of the experimental ABS profile to a suitable number of data points necessitated a step size between consecutive *x*-*y* points (*S*(ABS)) of 9.4 cm^{-1}. It was therefore decided to search for $\tilde{\nu}_e$ values from that of $\tilde{\nu}_g$ (276 cm^{-1}) to 228 cm^{-1} , the lowest value allowed by condition (5.2V) , in steps of (-)3 cm^{-1} $\left(\sim\frac{S(\mathrm{ABS})}{3}\right)$. δ was varied between 0.0 and 20.0 pm, with $S(\delta) = 0.5$. m was varied between its limiting values (±0.1) with $S(m) = 0.01$. This search range is summarised in Table 5.2; it is sufficiently broad so as not to bias the calculation towards the expected result, but also adheres to the approximations and resolution limits outlined in sections 5.1 - 5.3.

Parameter	Start Value	End Value	Step Size (*S*)
$\tilde{\nu}_e$/ cm^{-1}	276	228	-3
δ / pm	0	20	0.5
m	0.1	-0.1	0.01

Table 5.2 Search range for excited state parameter values for $[Re_2Br_8]^{2-}$

Throughout the calculation, the vibrating system is assumed to be an M_2 pseudo-diatomic; thus the reduced mass is taken to be 93 a.m.u. The calculation and search procedure was carried out as outlined in section 5.4, with m set initially to 0.0 for the first 2-D search. For each value of $\tilde{\nu}_e$ in the search range, a plot of $\delta(\tilde{\nu}_e)$ vs. F was constructed (Step B). A typical plot is shown in Fig. 5.5, for $\tilde{\nu}_e$= 255 cm^{-1}.

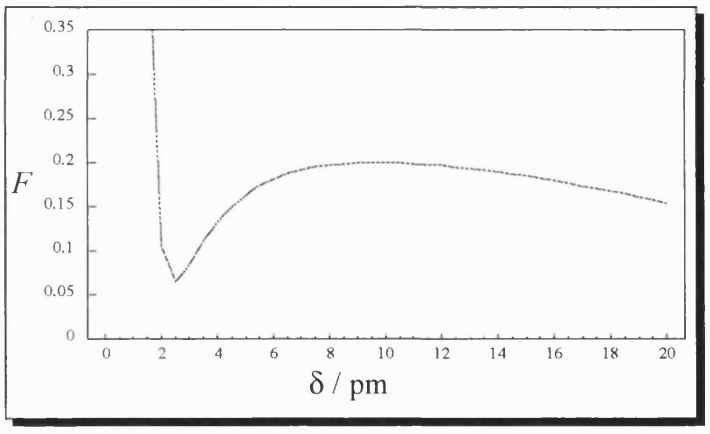

Fig 5.5 $[Re_2Br_8]^{2-}$: $m = 0$, $\tilde{\nu}_e$= 255; δ vs. F (Step B)

From this plot, the value of $\delta_{min}(255)$ is seen to be 2.5 pm, and the corresponding F_{min} value is 0.0648. By varying $\tilde{\nu}_e$ a table showing values of $\delta_{min}(\tilde{\nu}_e)$ and F_{min} at each $\tilde{\nu}_e$ was constructed (Step C) (Table 5.3). It should be noted that for some values of $\tilde{\nu}_e$, δ_{min} occurred at either 0.0 or 20.0 pm, i.e. there was no minimum in F for this value of $\tilde{\nu}_e$ in the pre-defined search range.

$\tilde{\nu}_e$ / cm^{-1}	δ_{min} / pm	F_{min}
228	6	0.06489
231	6	0.06555
234	5.5	0.06424
237	5	0.06469
240	4.5	0.06436
243	4	0.06353
246	3.5	0.06487
249	5	0.06819
252	3	0.06692
255	2.5	0.06481
258	2	0.0649
261	2	0.07683
264	1.5	0.07042
267	1	0.06452
270	1	0.11162
273	0.5	0.11171
276	-	-

Table 5.3 - $[Re_2Br_8]^{2-}$: Table of $\tilde{\nu}_e, \delta_{min}(\tilde{\nu}_e), F_{min}$; $m = 0$.

From this table, a plot of F_{min} vs. $\tilde{\nu}_e$ is constructed to find minima in F_{min} (Step D). This plot is shown in Fig. 5.6.

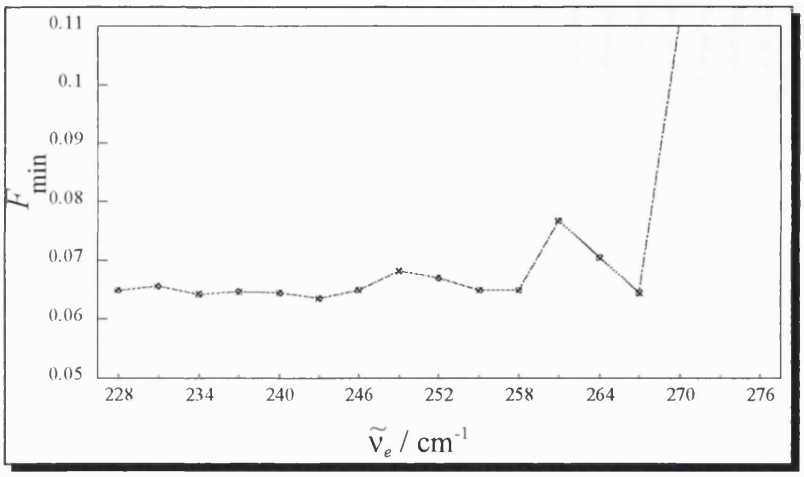

Fig 5.6- $[Re_2Br_8]^{2-}$: Plot of $\tilde{\nu}_e$ vs. F_{min} ; $m = 0.0$ (Step D)

This plot shows a 'bumpy plateau', with many combinations of $\{\tilde{\nu}_e, \delta_{min}(\tilde{\nu}_e)\}$ below 258 cm^{-1} giving low values of F_{min}. The lack of any clear trend in such a plot would imply that the technique is insufficiently sensitive in this case.

This 2-D search procedure was repeated for all 21 possible values of m - thus 21 tables equivalent to Table 5.3 were produced and the plots analogous to Figs 5.6 were assessed. Thus, for $m = 0.01$, a plot of $\tilde{\nu}_e$ vs. F_{min} (Step D) shows a slight preference for $\tilde{\nu}_e = 243$ cm^{-1}. This plot, analogous to Fig. 5.6, is shown in Fig 5.7.

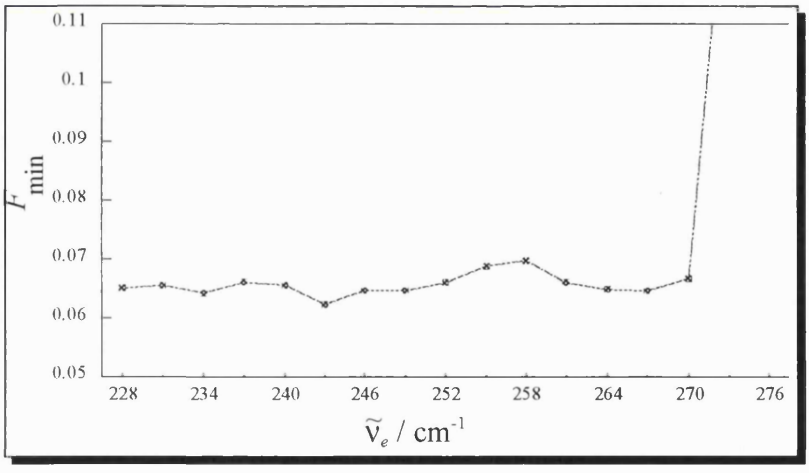

Fig 5.7; $[Re_2Br_8]^{2-}$: $m = 0.01$; $\tilde{\nu}_e$ vs. F_{min}

It is seen that, for some values of *m*, the general values of *F* are much larger than at other values of *m* and these *m* values are therefore discounted. Furthermore, very high values of $\tilde{\nu}_e$ can also be ruled out by most plots of $\tilde{\nu}_e$ vs. F_{min} (e.g. Fig. 5.6 $\tilde{\nu}_e > 267$ cm^{-1}). In general a bumpy plateau was seen in all these plots (Step D). However, if they are overlaid, for various values of *m*, a clear preference for $\tilde{\nu}_e = 243$ cm^{-1} is seen (Fig 5.8).

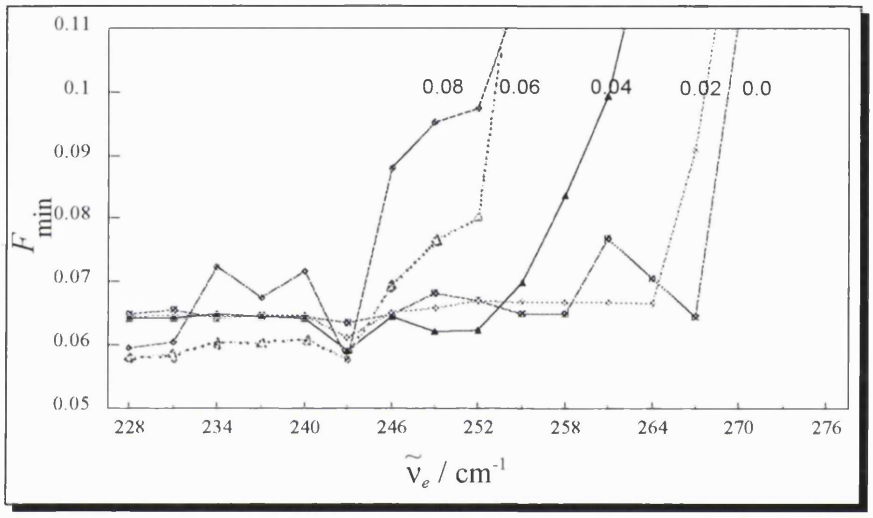

Fig 5.8: $[Re_2Br_8]^{2-}$ overlay of plots of $\tilde{\nu}_e$ vs. F_{min} with *m* varied

Hence, concentrating on this value of $\tilde{\nu}_e$ alone, a plot of *m* vs. $F_{min}(\tilde{\nu}_e = 243$ cm$^{-1})$ can be constructed (Fig. 5.9).

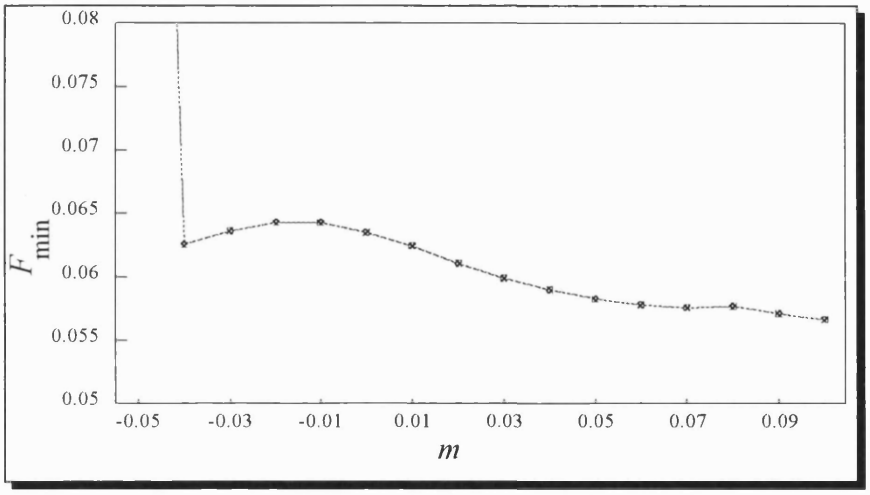

Fig. 5.9 $[Re_2Br_8]^{2-}$:Plot of *m* vs. F_{min} for $\tilde{\nu}_e = 243$ cm^{-1}

Unfortunately no clear trend is seen in this plot. Therefore, for this pre-defined search range for the three parameters, it appears that the only clear preference is for a value of $\tilde{\nu}_e$ = 243 cm^{-1} , giving a clear minimum in F for a wide range of m values. This value is neither consistent with that found from the SOS method in chapter 3, nor with the previous estimate [5.3] of (both 255 cm^{-1}). Furthermore, the corresponding values of the other two parameters cannot be specified. The convoluted procedure required to visualise and analyse the trends in the fitting function, F, as each of the three parameters is varied, certainly complicates the process of finding solution sets of parameter values. It is, however, a necessary procedure, as can be seen by a very low value of F (e.g. m = 0.06, $\tilde{\nu}_e$ = 228 cm^{-1}) not actually corresponding to a minimum in F. Thus, the overall trends in F must be visualised: in this case, the lack of any obvious trends in the crucial plots shown above would imply a large degree of insensitivity in the OT method.

The possible reasons for the failure of the method will be dealt with in section 5.6, where the effect of any errors in the experimental data will be assessed.

$[Re_2I_8]^{2-}$

The definition of the search range for each of the three parameters ($\tilde{\nu}_e$, δ, m) was complicated in this case by the lack of any previous estimates or measurements thereof. However, similar percentage changes in the mode wavenumber and the Re-Re bond length to those estimated for $[Re_2Br_8]^{2-}$ [5.3, 5.5] may be expected.

It was therefore decided to search for $\tilde{\nu}_e$ values from that of $\tilde{\nu}_g$(257 cm^{-1}) to 213 cm^{-1} (the lowest value allowed by condition (5.1 V) in section). Since the reduction of the ABS profile of the $^1(\delta^* \leftarrow \delta)$ band to an appropriate number of data points led to a step size, S(ABS) of 6.5 cm^{-1}, the interval between $\tilde{\nu}_e$ values, $S(\tilde{\nu}_e)$, was chosen to be (-)2 cm^{-1}. As for $[Re_2Br_8]^{2-}$, m was varied between 0.1 and -0.1 with $S(m)$ = 0.01. δ was varied between 0.0 and 20.0 pm with $S(\delta)$ = 0.5. This search range is summarised in Table 5.4:

Parameter	Start value	End Value	Step Size (S)
$\tilde{\nu}_e$ / cm^{-1}	257	213	-2
δ / pm	0	20	0.5
m	0.1	-0.1	0.01

Table 5.4 Search range for excited state parameters for $[Re_2I_8]^{2-}$

As before, the system was approximated to an M_2 pseudo-diatomic with a reduced mass of 93 a.m.u. The calculation was carried out in an exactly analogous way to that for $[Re_2Br_8]^{2-}$, and, to avoid unnecessary repetition, the method will be only summarised here. Step A was to set m to 0.0 and δ was varied across its range for each of value of $\tilde{\nu}_e$ (Step B). Plots were constructed for each $\tilde{\nu}_e$ value and values of $\delta_{min}(\tilde{\nu}_e)$ and the corresponding F_{min} were found. By varying $\tilde{\nu}_e$, tables such as Table 5.5 (analogous to Table 5.3) were constructed for each value of m (Step C).

$\tilde{\nu}_e$ / cm^{-1}	δ_{min} / pm	F_{min}
213	6	0.08823
215	5.5	0.08825
217	5.5	0.08985
219	5	0.088
221	4.5	0.08979
223	4.5	0.08879
225	4	0.08861
227	4	0.09042
229	3.5	0.08812
231	3.5	0.09279
233	3	0.08808
235	3	0.09583
237	2.5	0.08826
239	2.5	0.09965
241	2	0.08844
243	2	0.10455
245	1.5	0.08838
247	1.5	0.11148
249	1	0.08815
251	1	0.12363
253	0.5	0.09685
255	0.5	0.1587

Table 5.5 $[Re_2I_8]^{2-}$: table of $\tilde{\nu}_e$ vs. δ vs. F ; m = 0.0

For certain values of m and $\tilde{\nu}_e$, 'double minima' were seen in the original plot of $\delta(\tilde{\nu}_e)$ vs. F. In such cases, both these minima were taken into account for future plots. Only values of $\tilde{\nu}_e$ up to 255 cm^{-1} are shown as no minimum was seen for $\tilde{\nu}_e$ = 257 cm^{-1}.

For each m value, a plot of $\tilde{\nu}_e$ vs. F_{min} was constructed in an attempt to observe minima in the fitting function (Step D). For some values of m, several 'dips' in F_{min} were seen, but no one value of $\tilde{\nu}_e$ could be picked out. These tables and plots were repeated for all values of m and plots of $\tilde{\nu}_e$ vs. F_{min} were overlaid for different values of m (Step E) up to m = 0.05, as shown in Fig. 5.10. Beyond this m value, and for negative m values, no minima in F were seen within the δ range at *any* value of $\tilde{\nu}_e$ (i.e. there were no entries in the tables corresponding to Table 5.5)

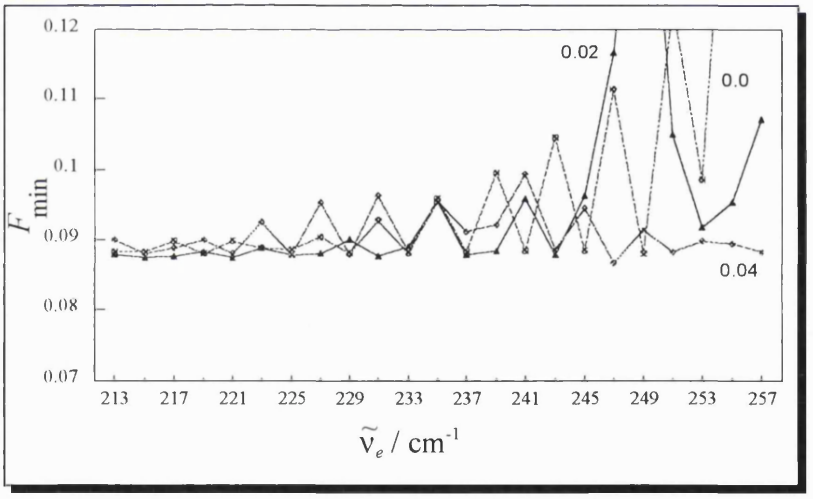

Fig 5.10 $[Re_2I_8]^{2-}$: Overlay plot of $\tilde{\nu}_e$ vs. F_{min} at different m .

By contrast to the case for $[Re_2Br_8]^{2-}$, no clear value of $\tilde{\nu}_e$ corresponding to a consistently low F_{min} value as m is varied is seen. Consequently, no attempt to find the corresponding δ_{min} and m values in an analogous way to Fig 5.9 was made.

In this case, no conclusions may be drawn about the possible solution sets for the parameter values: the insensitivity of the method caused it to reveal no trends in the fitting function as each of the parameters is varied.

$[Mo_2Cl_8]^{4-}$

Although the value of $\tilde{\nu}_e$ for the ν_1 mode in the $^1\delta\delta^*$ state has previously been measured as 336 cm^{-1}[5.4], no other measurements or estimates of any of the other parameter values have been made for this ion. It was therefore decided to define a search range for the three excited-state parameters which was consistent with those used for the structurally analogous $[Re_2X_8]^{2-}$ ions.

$\tilde{\nu}_e$ was varied between the value of $\tilde{\nu}_g$(338 cm^{-1}) to 278 cm^{-1} (the lowest value allowed by condition (5.1 V)). Owing to a required step size of 13.4 cm^{-1} in the ABS spectrum, $S(\tilde{\nu}_e)$ was taken to be (-)5 cm^{-1}. A smaller step size would be inconsistent with the experimental data. The search range is summarised in Table 5.6.

Parameter	Start Value	End Value	Step Size (S)
$\tilde{\nu}_e$ / cm^{-1}	338	278	-5
δ / pm	0	20	0.5
m	0.1	-0.1	0.01

Table 5.6 Search range for excited state parameters for $[Mo_2Cl_8]^{4-}$

The calculation and search procedure was carried out as outlined in section 5.4 and again, only the final results will be summarised here.

By varying $\tilde{\nu}_e$ and repeatedly plotting $\delta(\tilde{\nu}_e)$ vs F, Table 5.7 was constructed for m = 0.0 (Step C).

$\tilde{\nu}_e$ / cm^{-1}	δ_{min} / pm	F_{min}
278	7	0.19575
283	6	0.1961
288	5.5	0.19601
293	5	0.1992
298	4	0.19895
303	3.5	0.1845
308	3	0.19615
313	2.5	0.19641
318	2	0.19788
323	1.5	0.19982
328	1	0.2023
333	0.5	0.20532
338	-	-

Table 5.7 $[Mo_2Cl_8]^{4-}$: table of $\tilde{\nu}_e$ vs. δ_{min} vs. F_{min} for $m = 0.0$

This process was repeated for different values of m. For $m = 0.0$, a plot of $\tilde{\nu}_e$ vs. F_{min} (step D) shows a clear minimum in F at $\tilde{\nu}_e = 303$ cm^{-1}. Similar plots were constructed for the different values of m, and some of these plots are overlaid in Fig 5.11. It can be seen that a value of $\tilde{\nu}_e = 303$ cm^{-1} consistently corresponds to a minimum in F_{min}.

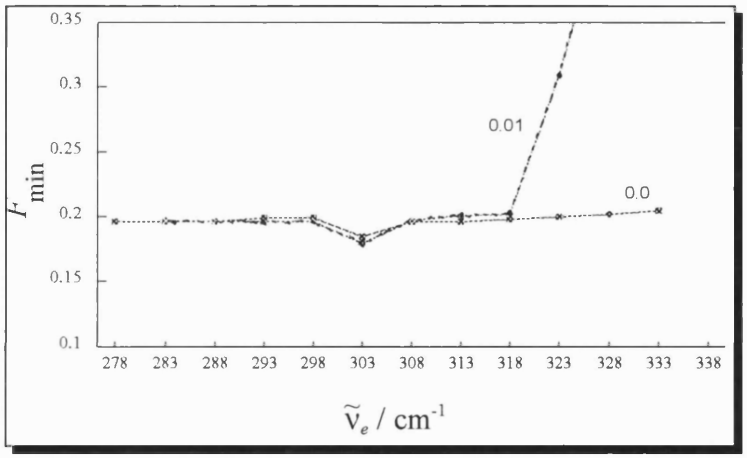

Fig 5.11 $[Mo_2Cl_8]^{4-}$:Overlay of plots of $\tilde{\nu}_e$ vs. F_{min} for $m = 0.0$ and 0.01

Only two values of m are included in the above plot for clarity. For values of m below 0.0, no minima were found in the original plots of $\delta(\tilde{\nu}_e)$ vs. F for any value of $\tilde{\nu}_e$.

Having therefore located a definite 'preferred' value of $\tilde{\nu}_e$, the corresponding values of the other two parameters were then sought. Thus, looking only at $\tilde{\nu}_e$ = 303 cm^{-1} a plot of m vs. $F_{min}(\tilde{\nu}_e = 303)$ was constructed (Fig. 5.12)

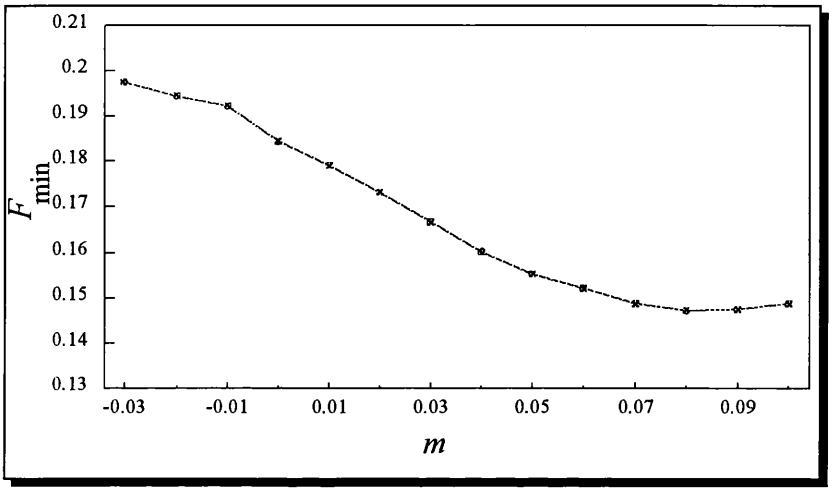

Fig 5.12 $[Mo_2Cl_8]^{4-}$: Plot of m vs. F_{min} for $\tilde{\nu}_e$ = 303 cm^{-1}

From Fig 5.12 it is clear that higher values of m are preferred, with $\tilde{\nu}_e$ held constant at 303 cm^{-1}. Possibly m = 0.08 is identifiable as a minimum, but with an F value only very slightly lower than those for m = 0.07 or 0.09. This would place $\delta \sim 10 - 11$ pm. Consequently, several sets of parameter values {$\tilde{\nu}_e$ = 303 cm^{-1}, $\delta_{min}(303)$, m) provide good fits. However, definite values of the two parameters δ and m cannot be extracted by this method.

It should be noted that the values of the fitting function, F, are, in general, much higher for this Mo(II) ion than for the two Re(III) ions above. The reason for this is not clear. It must also be noted that the value of $\tilde{\nu}_e$ suggested by this analysis (303 cm^{-1}) is not consistent either with the value predicted from the SOS method (336 cm^{-1}) , nor that which was previously estimated from experiment [5.4] (336 ± 3 cm^{-1}).

$[Mo_2Cl_8]^{4-}$: A Second Calculation

In order to try and assess whether the OT method is at least self-consistent, a second set of intensity ratios for the $n\nu_1$ progression in the RR spectrum of $[Mo_2Cl_8]^{4-}$ was measured, with excitation wavenumber 19,200 cm^{-1} (also within the contour of the resonant $^1(\delta^* \leftarrow \delta)$ ABS band). This checking procedure is not available for the two $[Re_2X_8]^{2-}$ ions, since only one laser line in the visible region is able, in each case, to produce a RR spectrum with a progression up to the fourth harmonic in ν_1. Using other laser lines, the higher harmonics are obscured by fluorescence.

The relative intensity ratios for $[Mo_2Cl_8]^{4-}$ at 19,200 cm^{-1} were measured and corrected as detailed in Appendix A1, and are summarised in Table 5.8.

	Relative Intensity
$I(\nu_1)$	100
$I(2\nu_1)$	64.6
$I(3\nu_1)$	44.8
$I(4\nu_1)$	41

Table 5.8 RR Intensity ratios for the $n\nu_1$ progression (n = 1 to 4) of $[Mo_2Cl_8]^{4-}$ recorded with an excitation wavenumber 19,200 cm^{-1}.

These intensities, together with the same ABS profile as used in the first calculation on this ion, were used in an analogous OT calculation. The search range for the parameters was the same as summarised in Table 5.7. The results were analysed in an exactly analogous manner to that described above, and in section 5.4. It was hoped to see some verification of the value of $\tilde{\nu}_e$ found in the previous calculation on this ion.

In this case, however, minima in the plots of δ vs. F (steps B and C) at different $\tilde{\nu}_e$ values, were found only for m = 0.0 and 0.01. Tables such as Table 5.9, (for m = 0.0) were constructed (Step C) for m = 0.0 and 0.01.

$\tilde{\nu}_e$ / cm^{-1}	δ_{min} / pm	F_{min}
278	6.5	0.3697
283	5.5	0.37009
288	5	0.36794
293	4.5	0.36857
298	4	0.3701
303	3.5	0.37301
308	3	0.33605
313	2.5	0.37991
318	2	0.68446
323	1.5	0.68974
328	1	0.39499
333	0.5	0.40063
338	-	-

Table 5.9 $[Mo_2Cl_8]^{4-}$ Table of $\tilde{\nu}_e$ vs. δ_{min} vs. F_{min} for m = 0.0

For the case of m = 0.01, values of $\tilde{\nu}_e$ below 308 cm^{-1} produced two apparent minima in the plot of $\delta(\tilde{\nu}_e)$ vs. F. Both minima were analysed in the usual way. From the above tables, an overlay plot of $\tilde{\nu}_e$ vs. F_{min} for different values of m (0.0 and 0.01) was constructed (Fig. 5.13). This clearly shows a value of 308 cm^{-1} for $\tilde{\nu}_e$ corresponds consistently to the lowest value of the fitting function.

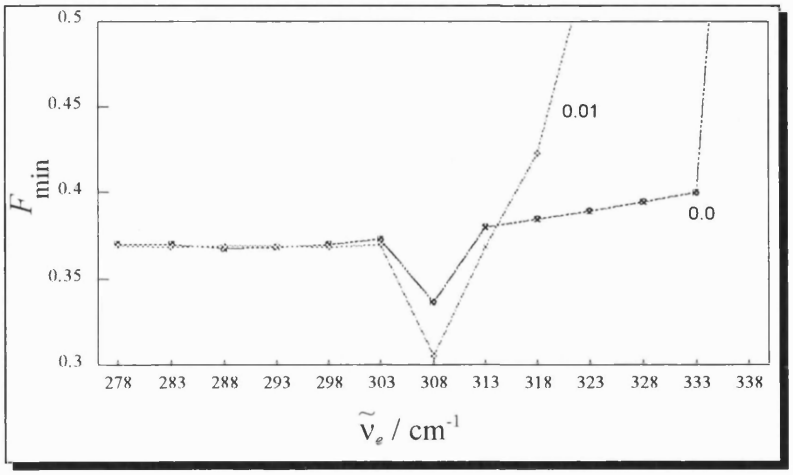

Fig 5.13 $[Mo_2Cl_8]^{4-}$: Overlay of plots of $\tilde{\nu}_e$ vs F_{min} with m varied

If $\tilde{\nu}_e$ is then set to 308 cm^{-1} the trend in $F_{min}(\tilde{\nu}_e = 308)$ with varying m can be analysed in order to try to locate values for the remaining two parameters. These plots are shown in Figs 5.14.

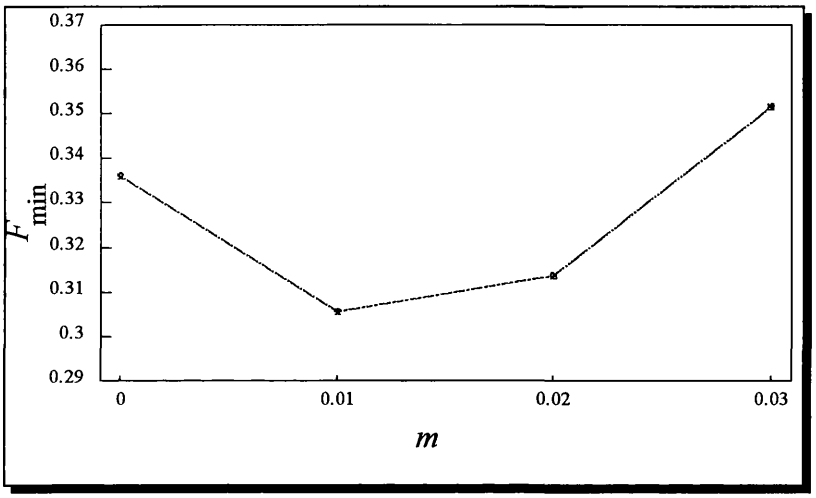

Fig 5.14 $[Mo_2Cl_8]^{4-}$: Plot of m vs. F_{min} for $\tilde{\nu}_e$ = 308 cm^{-1}

From Fig 5.14, it appears that the value m = 0.01, with $\delta_{min}(308)$ = 15.0 pm is the best possible fit. It should be noted, however, that the magnitude of the fitting function, F, corresponding to this parameter set (0.3057), is almost twice as large as any of those seen in the previous calculation using RR intensity ratios recorded with a different excitation lines. The value of $\tilde{\nu}_e$ predicted from this calculation (308 cm^{-1}) corresponds quite well to that found from the previous calculation (303 cm^{-1}). With a high value of $S(\tilde{\nu}_e)$ (5 cm^{-1}) being required by the experimental ABS spectrum, agreement of the two values of $\tilde{\nu}_e$ to within 5 cm^{-1} is considered good. However, the preferred values of the remaining two parameters differ between the calculations. It is therefore hard to assess the consistency of the OT calculations on this basis, except to say that the one parameter ($\tilde{\nu}_e$) reasonable consistency between the two calculations was found.

It should be noted, however, that the predicted solution parameter set for this calculation {$\tilde{\nu}_e$ = 308 cm^{-1}, δ = 15.0 pm, m = 0.01} shows consistency with the SOS result only in the magnitude of δ (δ_{SOS} = 15.2 pm).

It is obvious from the above calculations on the three ions that some aspect of the OT method is either erroneous or insufficiently sensitive to allow proper location of the best combination of parameter values for the excited electronic state of these ions. There are three possible areas which could be sources of potential problems.

I The Multidimensional Grid Search

The limitations of this process have been discussed in section 5.3. At present, the program available to carry out OT calculations can only be used in this form. The new procedure adopted in section 5.4 for searching for minima in the fitting function is believed to be the most thorough and clear way of finding solution sets of parameters without sacrificing either consistency with experimental data and the assumptions of the method, or the running speed of the calculations.

II Errors on Experimental Data

The apparent insensitivity of the method (showing equally good fits over a wide range of possible parameter values) may indicate that the calculation requires experimental data of higher accuracy than is, as yet, realistically attainable. For this reason, the effect on the OT calculation of errors in *both* types of experimental data (RR and ABS) will be studied in sections 5.6 and 5.7.

III The $[M_2X_8]^{n-}$ Ions

These may not fit as well as was first thought to the assumptions and limits of this method. The suitability of the ν_1 mode of these ions to study by the OT method was discussed earlier. Even if one of the approximations (such as the diatomic approximation for the ν_1 mode) were slightly inappropriate, this would not account for the inability of the method to find solution sets of parameter values: comparison with the parameter values calculated by the SOS method, within the same approximations, should be possible. However, in order to try and eliminate any possible underlying lack of suitability, 'model' systems, generated by the SOS method, within the limits of the OT method assumptions, are used as the basis of OT calculations in section 5.8. Since it cannot be guaranteed that the SOS method is itself 'correct', these calculations cannot pronounce the OT method as 'correct' or 'incorrect'. They will merely show any consistency, or lack thereof, between the two methods on the basis of an 'ideal' model system for which the data cannot be distorted by experimental factors, and for which the criteria of the OT method are rigorously met. It should, however, be noted that the SOS method has apparently succeeded in finding structural parameters for the ν_1 mode and co-ordinate of the $[M_2X_8]^{n-}$ ions in the $^1A_{2u}$ state (chapter 3); clearly, the OT method has failed in this respect.

5.6 Effect of Errors in RR Experimental Data on the OT Calculation

An estimate of the effect on the OT calculation of any errors in the RR intensity ratios can be made by altering the ratios used in the preceding section (Table 5.1) and considering any differences between the results of the calculations.

The RR intensity ratios for the first four harmonics of the ν_1 mode were calculated as averages over 4 - 6 RR spectra. A typical standard deviation on these ratios was 10 %. Therefore, the effect of a 10% change in the experimental RR intensities on the calculation should be assessed for each of the three ions. If a major change in the results is seen, it can be concluded that the method requires RR data of a higher accuracy than is yet available.

The error on the relative intensity of any single harmonic is ± 10%. For a set of four measurements (i.e. three *relative* intensities), therefore, these errors can occur in several combinations (i.e. +10% on all, or -10% on all, or some combination thereof). It was decided to study the effect on the calculation of four possible combinations of RR intensity errors. For each of the three ions, the experimental RR intensity ratios were altered as follows:

Experimental Intensity Ratios	Test 1	Test 2	Test 3	Test 4
$I(\nu)$	$I(\nu)$	$I(\nu)$	$I(\nu)$	$I(\nu)$
$I(2\nu)$	$I(2\nu)$ + 10%	$I(2\nu)$ - 10%	$I(2\nu)$ + 10%	$I(2\nu)$ -10%
$I(3\nu)$	$I(3\nu)$ + 10%	$I(3\nu)$ - 10%	$I(3\nu)$ - 10%	$I(3\nu)$ + 10%
$I(4\nu)$	$I(4\nu)$ + 10%	$I(4\nu)$ -10%	$I(4\nu)$ + 10%	$I(4\nu)$ +10%

Table 5.10 Error Combinations on RR Data used to test the OT method

For the purposes of these tests, no error in the ABS profile was included. Thus, for each ion, the altered intensity ratios were used as the basis of four new calculations, using the identical search ranges for each of the three parameters to those detailed in section 5.5. It was, however, decided that the effect of these

errors could be adequately assessed by looking at the simplest 2-D grid with *m* set to 0.0.

Overlay plots of $\tilde{\nu}_e$ vs. $F_{\min}$ (m = 0.0) for the case of no errors and for Tests 1 - 4 are shown in Figs. 5.15 $[Re_2Br_8]^{2-}$, 5.16 $[Re_2I_8]^{2-}$ and 5.17 $[Mo_2Cl_8]^{4+}$.

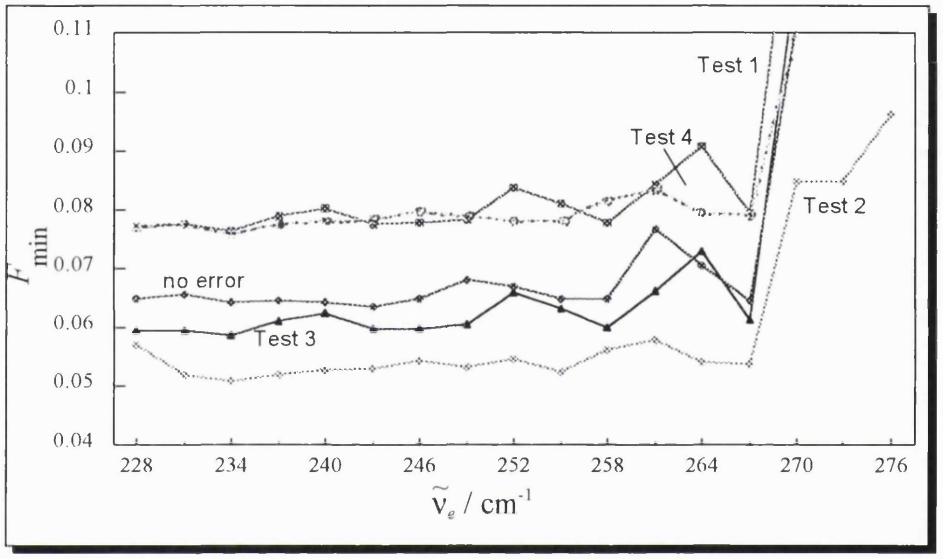

Fig 5.15 $[Re_2Br_8]^{2-}$: overlay of plots of $\tilde{\nu}_e$ vs. $F_{\min}$ for different errors on Raman intensities

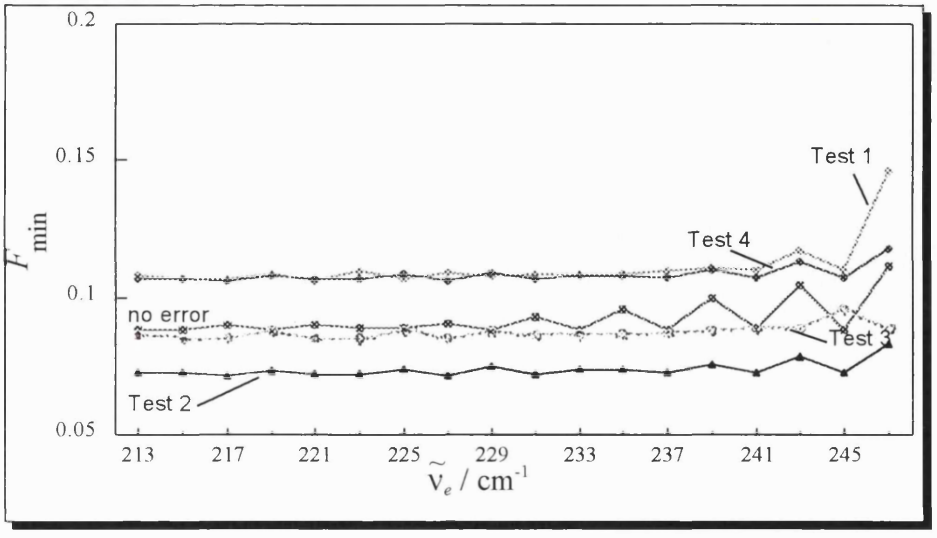

Fig 5.16 $[Re_2I_8]^{2-}$: overlay of plots of $\tilde{\nu}_e$ vs. $F_{\min}$ for different errors on Raman intensities

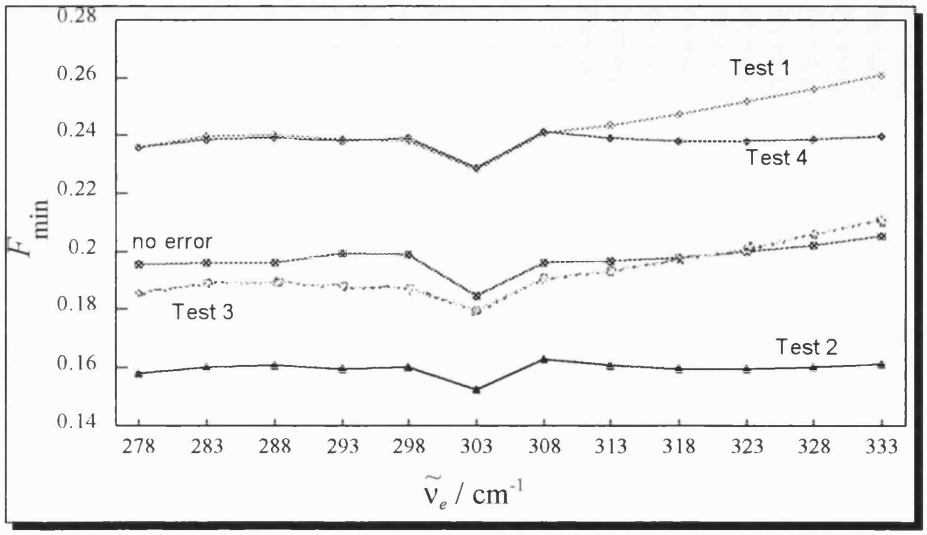

Fig 5.17 $[Mo_2Cl_8]^{4-}$: overlay of plots of $\tilde{\nu}_e$ vs. F_{min} for different errors on Raman intensities.

The plots of $\tilde{\nu}_e$ vs. F_{min} are seen to be largely indifferent to the addition of errors. This is most clearly seen in Fig. 5.17. In general, the average values of the fitting function are larger when a +10% error is added to each of the intensity ratios (Test 1). However, for all tests on the $[Re_2X_8]^{2-}$ ions the plots show no definitive mnimum, and thus the insensitivity of the method seems unaffected by the addition of RR errors.

Hence, it can be concluded that the calculations are not very sensitive to a 10% change in the RR intensity ratios. This would indicate that the experimental data are not at fault when considering the apparent failure of the method to locate parameter values for the $[M_2X_8]^{n-}$ ions. Therefore, other areas of the calculation must be investigated for possible sources of error.

5.7 Effect of Errors in ABS Profile on the OT Calculation

The experimental absorption profile, ABS, is used as input into the OT calculation rather than being fitted in a least-squares manner, as are the RR data. Specifically, the function $\Phi(\omega)$, the complex polarizability, is computed from the

experimental ABS via Eqn (2.83), and is subsequently used in the calculation. The calculations are performed using frequency values in angular units (ω) which are then converted in the usual way to the $\tilde{\nu}$ values. Φ(ω) is given by

$$\Phi(\omega) = \frac{2}{\pi} P \int_0^{\infty} \frac{ABS(\omega')}{\omega'^2 - \omega^2} d\omega' + i\frac{ABS(\omega)}{\omega} \qquad (5.2)$$

where ω is the angular laser excitation frequency (= $2\pi c\tilde{\nu}_L$) and P denotes the Cauchy principal value.

During the calculation, functions of the type $\Phi(\omega - s\omega_2)$ are computed, where ω_2 is the angular mode frequency in the excited state ($\omega_2 = 2\pi c\tilde{\nu}_e$) and s is an integer. These functions are related to the n^{th} order Raman correlators, $\alpha_n^{NC}(\omega)$, via equations (2.85) and (2.86). Finally, the ratios of the squares of the moduli of the Raman correlators, $\frac{|\alpha_n^{NC}(\omega)|^2}{|\alpha_{n'}^{NC}(\omega)|^2}$ are computed to give the ratios of the frequency-dependence of the RR intensities of the nth and n' th order harmonic bands (effectively the REPs for the n^{th} and n'^{th} harmonics). Then, with ω set to the experimental laser frequency, a comparison with the experimentally measured intensity ratios can be made.

From Eqn. (5.2), it is clear that Φ(ω) has a real (Re) and an imaginary (Im) part. The modulus, $|\Phi(\omega)|^2$ is then:

$$|\Phi(\omega)|^2 = |Re[\Phi(\omega)]|^2 + |Im[\Phi(\omega)]|^2 \qquad (5.3)$$

i.e.$|\Phi(\omega)|$ is the curve corresponding to the sum of the squares of the two curves Re[Φ(ω)] and Im[Φ(ω)]. The function $\Phi(\omega - s\omega_2)$ has real and imaginary parts corresponding to the curves Re[Φ(ω)] and Im[Φ(ω)] *downshifted* in frequency by an amount $s\omega_2$. Thus $|\Phi(\omega - s\omega_2)|^2$ is then the sum of the squares of these two downshifted curves.

With the experimental ABS used in this way in the OT calculations, it is clear that the effect of any errors in ABS on the calculation may be modelled by examining their effect on the function $\Phi(\omega)$. In this way, the need to carry out a full transform calculation, including a multidimensional grid search (which is itself a possible source of error) is avoided and the effect of any ABS errors may be seen more clearly.

The method of computation of $\Phi(\omega)$ from the experimental ABS(ω) in the present OT method is not known, as the source code of the program is not available for inspection. However, a previously published method [5.6] was used and adapted to write a program in C++ for calculating $\Phi(\omega)$. Details of this calculational procedure and program are given in Appendix A6.

In order to minimise any complicating effects on the error calculation of a complicated structured ABS, a series of model Lorentzians was generated in order to perform initial tests for errors. Details of this program are given in Appendix A5.

Two possible sources of error on the ABS(ω) data were investigated:

(i) The effect of the **step size** between adjacent points in the ABS(ω) spectrum
and
(ii) The effect of varying the '**tail length**' of the Lorentzian.

(i) Effect on the Calculation of $\Phi(\omega)$ of the Step Size, S(ABS), in the ABS Spectrum.

In order to perform this test, four Lorentzians were generated which were identical apart from differing step sizes, S(ABS) between adjacent x points. The centre of the Lorentzians was chosen to be in a wavenumber region typical of

many inorganic species (15,000 - 20,000 cm^{-1}), and the step sizes, S(ABS), were also typical of those required by the restriction on the number of data points enforced by the OT method (20-50 cm^{-1}). The properties of the four test Lorentzians are summarised in Table 5.11.

	Start Value / cm^{-1}	End Value / cm^{-1}	S(ABS)
Curve 1	15,000	20,000	20
Curve 2	15,000	20,000	25
Curve 3	15,000	20,000	33.3
Curve 4	15,000	20,000	50

Table 5.11 Properties of Lorentzians used to test effect of step size on the calculation of $\Phi(\omega)$.

These curves are shown in Fig 5.18.

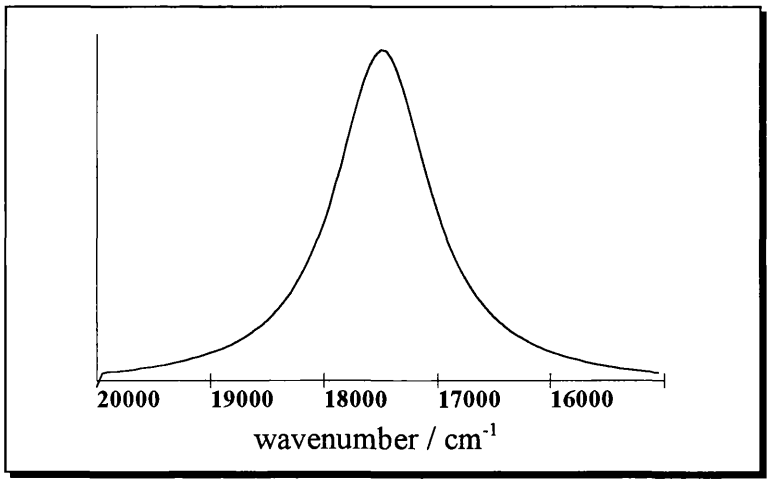

Fig 5.18 Shape of Lorentzian Curves 1 - 4 used to test the effect of step size on the calculation of $\Phi(\omega)$.

Zero points (as required by the procedure for calculating $\Phi(\omega)$, Appendix A6), were added to the ends of these curves (e.g. at 14,980 and 20,020 cm^{-1} in Curve 1). For each curve, the imaginary and real parts of $\Phi(\omega)$, as well as the modulus, $|\Phi(\omega)|$ were calculated and compared.

Figure. 5.19 shows the imaginary parts of $\Phi(\omega)$ for each of the four curves. As can be seen, they are identical and can be overlaid exactly. Similarly, the real parts of $\Phi(\omega)$ are identical (Fig. 5.20). Finally, the moduli, $|\Phi(\omega)|$, which are of the form used in the OT calculation, are all identical for the four curves (Fig 5.21) and can be overlaid as shown.

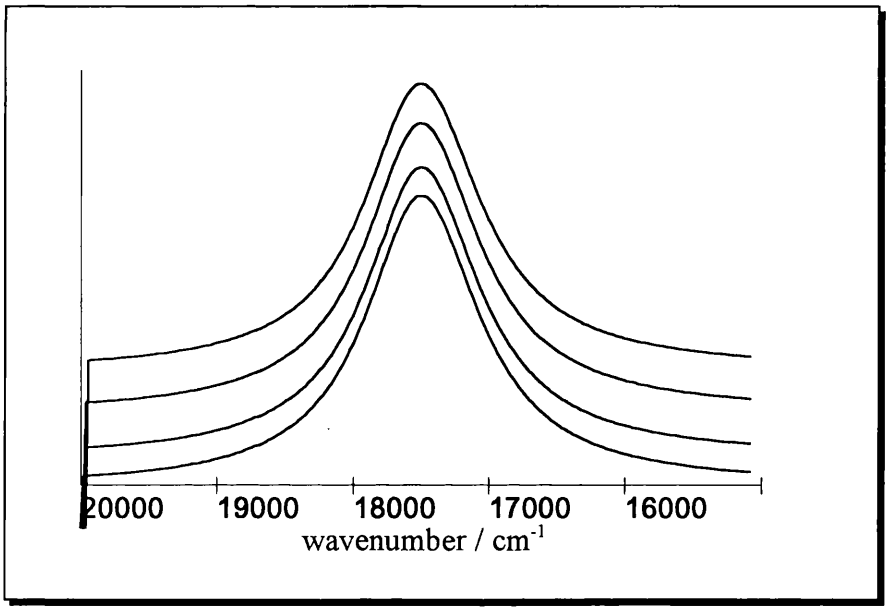

Fig 5.19 Stack Plot of Im [$\Phi(\omega)$] for Curves 1 - 4

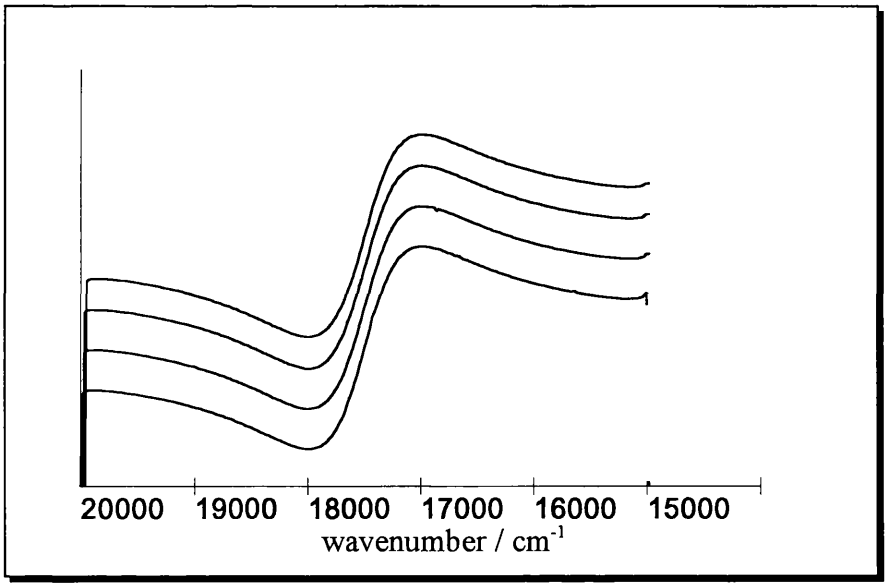

Fig 5.20 Stack Plot of Re [$\Phi(\omega)$] for Curves 1 - 4

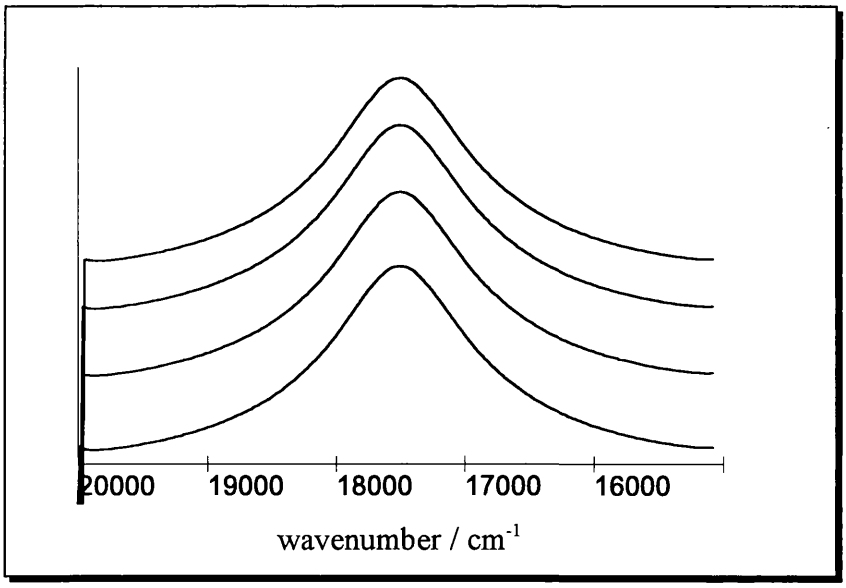

Fig 5.21 Stack Plot of $|\Phi(\omega)|$ for Curves 1 - 4

From this, it may be concluded that altering S(ABS) does not affect the calculation of $\Phi(\omega)$. Clearly, the curves used here are unstructured, whereas a typical experimental ABS spectrum may have some structure of width of the order of 200 - 300 cm^{-1}. However, provided that the step size in the ABS spectrum, S(ABS), is not so large as to distort the structure, then the arguments applied in the case of unstructured Lorentzians used here, should hold. Any effect of such a large S(ABS) would be clearly seen in the ABS spectrum: these are recorded with the maximum resolution (Appendix A2) and then reduced to an appropriate number of data points, thus increasing S(ABS). Any deviation of the 'reduced points' ABS from that originally recorded would be obvious at this stage, so that an excessively large S(ABS) would naturally be avoided.

The step sizes used in the above tests are of the order of, or indeed larger than, those typical of the experimental curves (section 5.4), while the actual curve width and positions are typical of an experimental curve for the complexes under study. From this, it may be concluded that the error arising in the calculation of $\Phi(\omega)$ from the non-zero step size between adjacent points in the ABS spectrum is negligible, although the magnitude of S(ABS) certainly has an effect on the multidimensional grid search (section 5.5). It should, however, be noted, that the

procedure used here for calculation of $\Phi(\omega)$ may be different from that used in the actual OT program; furthermore, the manipulation of $\Phi(\omega)$ thereafter in the calculation has not been considered in detail. However, the latter should merely correspond to a shifting of the initially calculated curves by integral amounts of $\tilde{\nu}_e$ (the excited state mode wavenumber = $\omega_e/2\pi c$); this is not expected to introduce any errors. The former problem may only be addressed if the actual procedure of calculating $\Phi(\omega)$ used in the calculations (section 5.4 and 5.5) were available; however, serious discrepancies between the two methods of calculation are not anticipated.

(ii) Effect on the calculation of $\Phi(\omega)$ of a variable tail length on ABS curve

In order to perform this test, five different normalised Lorentzian curves were generated, this time with equal step size, S(ABS), but with varying tail lengths. The properties of the five curves are summarised in Table 5.12.

	Start Value / cm^{-1}	End Value / cm^{-1}	Step Size S(ABS)
Curve a	14,975	20,025	25
Curve b	15,175	19,825	25
Curve c	15,375	19,625	25
Curve d	15,575	19,425	25
Curve e	15,775	19,225	25

Table 5.12 Properties of Curves used to test the effect of variable tail lengths on the calculation of $\Phi(\omega)$

Thus, if curve c is the 'central' curve, then up to 400 cm^{-1} is added or subtracted to each end in the different curves; in effect, sections of curve e are successively 'chopped' while still retaining the central band in order to see the importance of the tails.

As in the previous calculation (i), zero points were added at the ends of each curve to facilitate calculations. For each curve, the imaginary part

Im[Φ(ω)], real part Re[Φ(ω)], and modulus, |Φ(ω)| of Φ(ω) were calculated. Curves a and e are shown in Fig. 5.22.

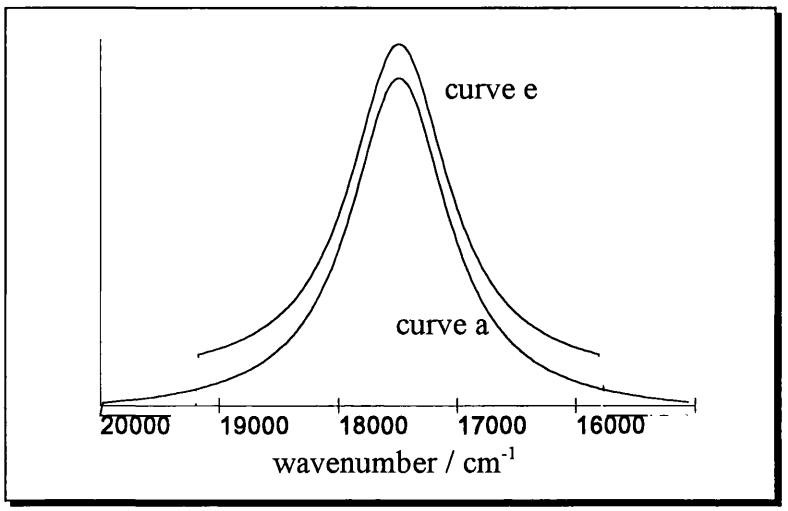

Fig. 5.22 Curves a and e used to test the effect of tail lengths on the calculation of Φ(ω).

A comparison of the imaginary parts of Im[Φ(ω)] for all five curves overlaid shows that, as the tails of the curves are 'chopped', the peak of the Im[Φ(ω)] is slightly raised and the curve broadens slightly. This point is best illustrated by an overlay plot of Im[Φ(ω)] for the two 'extreme' cases, curves a and e. This is shown in Fig 5.23.

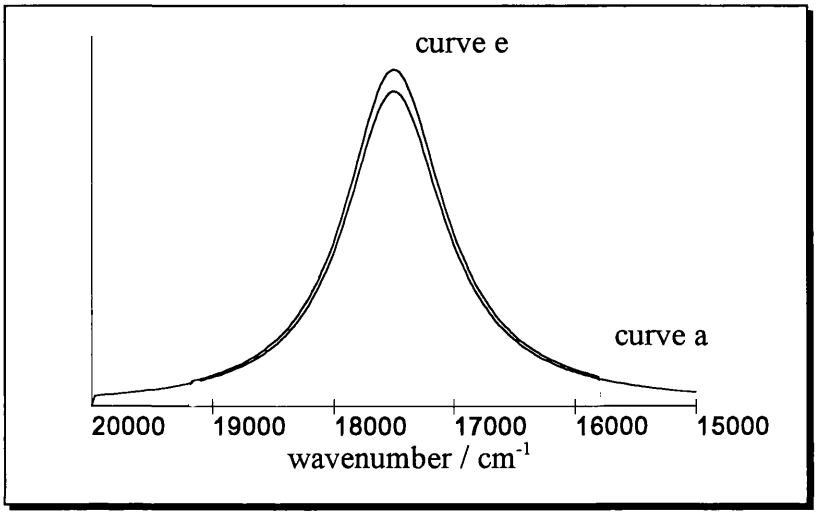

Fig 5.23 Plot of Im[Φ(ω)] for curves a and e

A comparison of the Re[Φ(ω)] of the five curves is shown in Fig. 5.24. Again, a similar trend is seen as the tails of the curves become shorter.

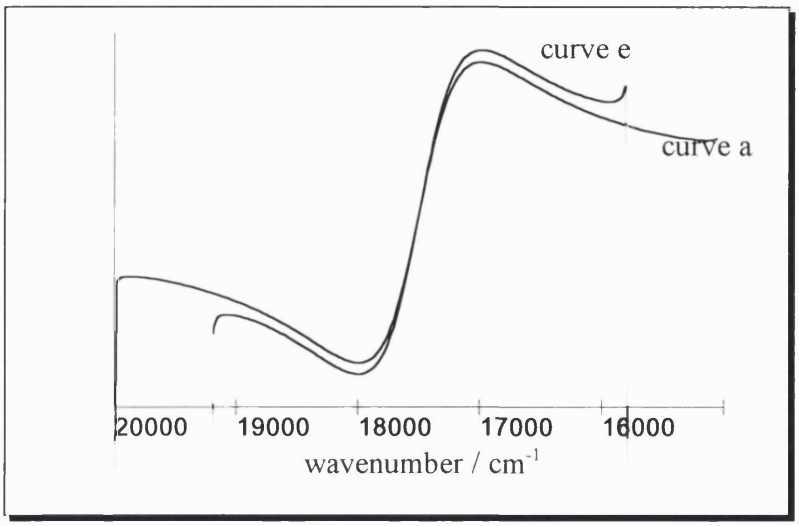

Fig 5.24 Plot of Re[Φ(ω)] for curves a and e.

As expected, the moduli, |Φ(ω)| are not identical when overlaid. In going from curve a to curve e, the maximum height of the curve |Φ(ω)| increases, as does the width. Furthermore, at the extremes of the curve (start and finish point), curve e deviates upwards away from the slope of curve a. Again, this is best illustrated by a comparison of the curves |Φ(ω)| for curves a and e (Fig. 5.25)

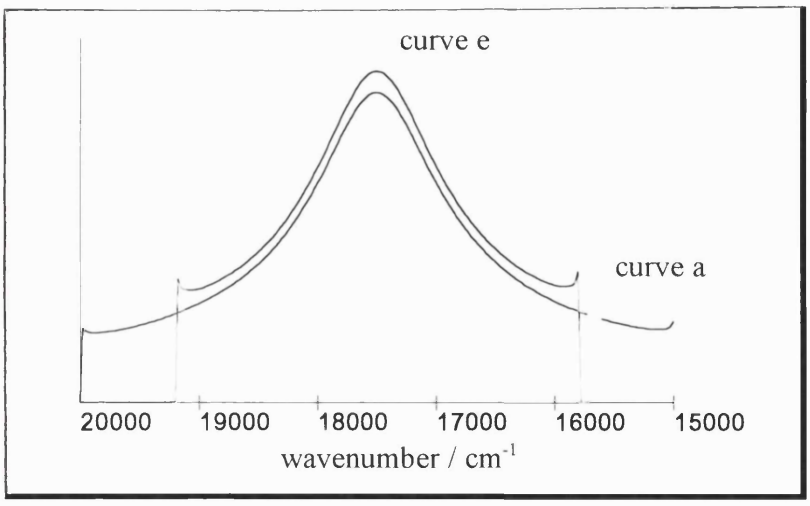

Fig 5.25 Plot of |Φ(ω)| for curves a and e.

Thus it would appear that varying the length of the 'tails' on either side of an ABS band has an effect on the calculation of $|\Phi(\omega)|$. It is estimated that curve c represents typical ABS data available for inorganic coloured compounds, with tails of 2125 cm^{-1} from the centre of the band. In curves a and e, the tails are 400 cm^{-1} longer and shorter respectively. Often long tails are not available due to the presence of a nearby second electronic absorption band. In some cases a complete ABS band, including tails cannot be recorded owing to the cut-off of the detector or source light intensity at certain wavelengths. Obviously, to maximise the chance of success of the OT method, the maximum tail length on the experimental ABS band should be given; this may possibly require modelling of the tails (where the baseline is absent and/or obscured by another band). However, this then has the severe disadvantage of increasing the value of *S*(ABS), in order for more ABS data to be included using the same number of data points. This then necessitates a wider grid search for $\tilde{\nu}_e$ values. At present, the program requires evenly spaced *x*-*y* data points; if some weighting could be added, such that more points of the ABS profile were sampled over the area of the peak, rather than the tails, then this may improve the workings of the calculation.

Although these calculations were performed using simple Lorentzian bands, the conclusions would be valid for all types of ABS curves. The experimental curves used for the $[M_2X_8]^{n-}$ ions in section 5.5 contained the maximum tail length possible, subject to a reasonable size of *S*(ABS). Without further modification of the OT program, it is not clear whether tails on the experimental ABS data are affecting the outcome of the OT calculations on these compounds.

Thus, one possible source of the error or failure of the present OT method may have been found. However, whether the effect of ABS tails on the calculation of $\Phi(\omega)$ is a large enough effect to account for the failure of the method in section 5.5 to locate any solution sets, is not clear. It may only be concluded from the present investigation that the maximum tail length possible on

the ABS band, subject to a sensible S(ABS) size, should be used as input in the OT calculations.

5.8 The Use of SOS-generated 'Model' Systems to Test the OT Method

The ideal molecules or systems for testing the performance of the OT method are those for which the assumptions (theoretical and experimental) hold rigorously, and for which error-free experimental data may be recorded. In this way any unsuitability of the system to this kind of calculation would be eliminated as a possible source of calculation failure.

For the OT method, such molecules would ideally be diatomics, with a single, totally symmetric vibrational mode, thus precluding the possibility of Duschinsky mixing. The resonant excited state would be a single, non-degenerate harmonic state. The change in frequency of the mode on excitation to the excited state would be sufficiently small for condition (5.1 V) to hold, and the ground state frequency of the mode would be sufficiently high for the 'effective zero temperature' condition hold to hold. Non-Condon coupling in the system would be small enough to ensure that only linear terms need be considered.

Real molecules for which all of these conditions (sections 5.1 and 5.2) are *known* to hold, are few; only in diatomics can the possibility of Duschinsky mixing be completely eliminated; however, as noted in sections 5.1 and 5.2, typical diatomics such as I_2 and S_2^- ion are unsuitable for other reasons.

For this reason, the SOS method has been used to generate ABS profiles and RR progression intensity ratios for a single vibrational mode in nine different 'model systems'. The systems were generated using different combinations of the structural parameters of the excited electronic state which the OT method is

designed to extract (i.e. $\tilde{\nu}_e$, δ and m). The ability of the OT method to recover these known parameters can then be tested.

Variations in the model system data were also achieved by maintaining a given combination of excited state parameter values $\{\tilde{\nu}_e, \delta, m\}$, while varying the 'experimental' conditions under which the generated 'experimental' data (RR and ABS) were produced e.g. by varying the temperature of the system or the excitation frequency for the RR spectrum. Again, these data were used in OT calculations to try and recover the values of $\tilde{\nu}_e$, δ and m. In this way, the response of the OT method to variation in experimental conditions can be monitored.

Clearly, such tests using data generated by another method (SOS) will not *prove* that the OT method actually succeeds or fails: they will merely show any consistency or lack thereof, between the two calculational methods. However, given the lack of any real, 'ideal' molecules with which to test the methods, coupled with the proven ability of the SOS method and contrasting inability of the OT method to produce sensible excited state parameter values $\tilde{\nu}_e$, δ and m, for $[M_2X_8]^{n-}$ ions (chp 3), such a comparison is certainly valid and useful.

Basic Properties of the Model Systems

The basic properties of each of the model systems were chosen such that, at all times, the strict assumptions of the OT method were valid. A single, resonant excited electronic state was chosen, with a zero-zero transition energy (denoted $E_{0\text{-}0}$ in the SOS method) within the typical visible range (14,000 cm^{-1}). Only a single vibrational mode was considered, precluding the possibility of mode-mixing in the excited state. The vibrating species was assumed to be a 'pseudo-diatomic' of reduced mass 50 a.m.u., similar to the value for a pure Mo_2 dimer. The ground state wavenumber of this mode was chosen to be 300 cm^{-1}, also typical of a symmetric Mo-Mo stretch in a quadruply bonded dimolybdenum species.

The phenomenological lifetime factor, Γ, was taken to be 200 cm^{-1} throughout. The ABS profile was generated between 12,000 and 17,000 cm^{-1}: thus, typical tail lengths on the ABS were used and these were made as long as possible, subject to allowing a reasonable value of S(ABS). Both start and end points lie well out of the actual ABS band; it is assumed that any effect due to the tails of the ABS is negligible. An even spacing between points, S(ABS) of 10 cm^{-1} was taken; again, this is typical for 'real' experimental data.

A constant value of 5 pm for the parameter δ was taken for all the model systems. This corresponds to a value of Δ, the dimensionless displacement used in the SOS method, of 1.05, according to the equation (3.1):

$$\Delta = \left(\frac{\omega_g \mu}{\hbar}\right)^{\frac{1}{2}} \delta$$

where ω_g is the angular frequency of the mode in the ground electronic state (= $2\pi c\tilde{\nu}_g$) and μ is the reduced mass of the vibrating species (50 a.m.u.). The common properties of all the systems are summarised in Table 5.13.

Reduced Mass /	50
$E_{0\text{-}0}$ / cm^{-1}	14,000
$\tilde{\nu}_g$ / cm^{-1}	300
Γ / cm^{-1}	200
Start Point of ABS /	12,000
End Point of ABS /	17,000
S(ABS)	10
δ / pm	5

Table 5.13 Summary of the common properties of the SOS-generated model systems used to test the OT method.

Experimental data for nine different model systems, based on these common properties, were then generated by either varying the values of $\tilde{\nu}_e$ and m (δ being held constant throughout), or by varying the temperature or laser

excitation frequency used to obtain the experimental data. A summary of the remaining properties of the nine different systems is given in Table 5.14.

System	δ/ pm	$\tilde{\nu}_g$ / cm^{-1}	$\tilde{\nu}_e$ / cm^{-1}	m	T / K	$\tilde{\nu}_L$ / cm^{-1}
1	5	300	300	0	0	14,500
2	5	300	276	0	0	14,500
3	5	300	276	0.05	0	14,500
4	5	300	300	0	77	14,500
5	5	300	276	0	77	14,500
6	5	300	276	0	0	13,500
7	5	300	276	0	0	14,000
8	5	300	276	0	0	14,500
9	5	300	276	0	0	15,000

Table 5.14 Properties of the model systems used to test the OT method.

For each of these systems, the ABS profile and the relative intensity ratios of the first four harmonics of the band due to the diatomic stretching mode in the RR spectrum, recorded with excitation wavenumber $\tilde{\nu}_L$, were generated. The RR intensity ratios were corrected for ν^4 scattering as required by the OT method. These data were then used as normal input in OT calculations and a search for the solution parameter values $\{\tilde{\nu}_e, \delta, m\}$ was carried out. The data for all the systems are shown in Figs. 5.26 and Table 5.15 respectively.

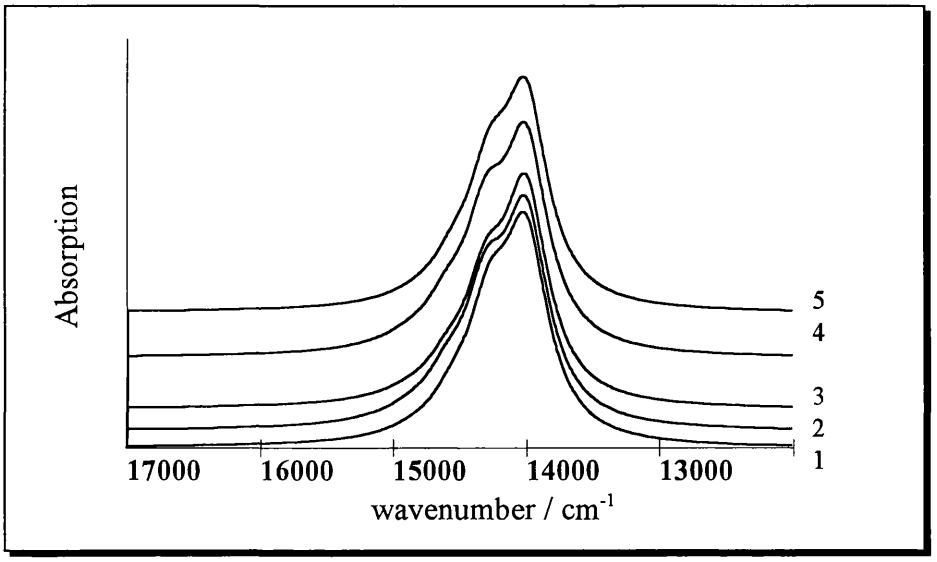

Fig 5.26 ABS curves for SOS-generated systems 1 - 5 (ABS curves for systems 6 - 9 are identical to that for system 2).

	System 1	System 2	System 3	System 4	System 5	System 6	System 7	System 8	System 9
$I(\nu)$	100	100	100	100	100	100	100	100	100
$I(2\nu)$	49.2	34.4	55.1	49.1	34.4	9.6	25	34.4	18.2
$I(3\nu)$	39.5	26.4	50	39.4	26.4	1	5.3	26.4	8.2
$I(4\nu)$	17.3	14.3	24.7	17.4	14.4	0.1	1	14.3	3

Table 5.15 RR Intensity Ratios for Systems 1-9 (generated by SOS method and corrected for ν^4)

System 1: $\tilde{\nu}_e = 300$ **cm^{-1}; δ=5 pm, $m = 0$**

This corresponds to the simplest kind of structural change possible in the excited electronic state: linear electron-phonon coupling (a simple bond length change in this case).

In order for the OT calculations to be performed, a search range for the parameters $\tilde{\nu}_e$, δ and m was defined. Since both $\tilde{\nu}_e$ and m were unchanged, the simplest search range was then to set $\tilde{\nu}_e = 300$ cm^{-1} , $m = 0.0$ and vary δ from 0.0 to 20.0 pm, with $S(\delta) = 0.5$, i.e. a 1-D search.

The output from the calculation was analysed in the same way as for the $[M_2X_8]^{n-}$ ions (section 5.5). Since only one parameter was being varied, a plot of δ vs. F (step B in Fig. 5.4) should show any minima; this plot is shown in Fig. 5.27.

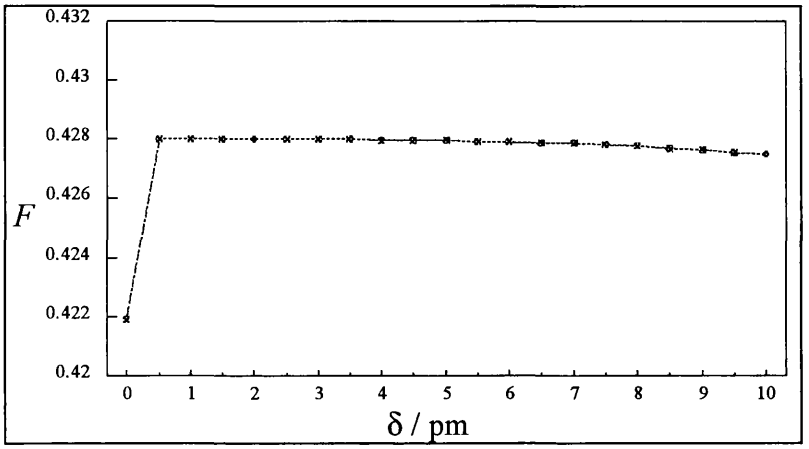

Fig 5.27 System 1 : Plot of δ vs. F

No minima in F were seen, other than at δ=0.0(which is not considered a true minimum). Thus, there is an immediate lack of consistency between the SOS and OT methods on even the most basic system.

System 2: $\tilde{\nu}_e$ = 276 cm^{-1}, δ = 5 pm, m = 0.0

This system included the second type of structural change accommodated by the OT method: a change in the mode wavenumber in the excited electronic state. The magnitude of this change is well within the limits imposed by condition (5.1 V). The generated data were used as the basis of an OT calculation, with the following pre-defined search range for each of the parameters:

Parameter	Start Value	End Value	Step Size (S)
δ / pm	0	10	0.5
$\tilde{\nu}_e$ / cm^{-1}	300	252	-3
m	0	0	0

The step size, $S(\tilde{\nu}_e)$, was chosen to be approximately one third of S(ABS) of the generated ABS spectrum, which in this case was 10 cm^{-1}. $\tilde{\nu}_e$ was allowed to take successively lower values until the condition (5.1 V) no longer held. A plot of $\tilde{\nu}_e$ vs. $F_{\min}$ should reveal any minima: this plot is shown in Fig 5.28.

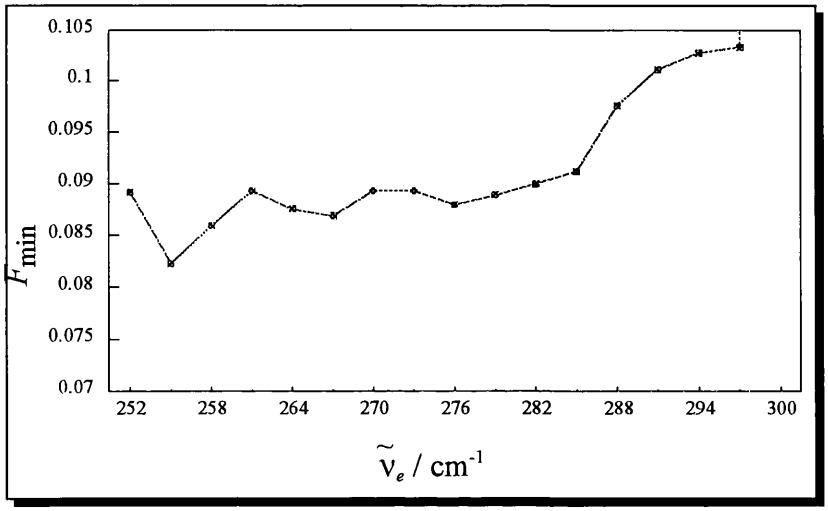

Fig 5.28: System 2: plot of $\tilde{\nu}_e$ vs. $F_{\min}$

The plot shows a 'bumpy plateau': a value of $\tilde{\nu}_e$ = 255 cm^{-1} produces a slight dip in F, but the value of this function does not dip as significantly at the actual value of $\tilde{\nu}_e$ (276 cm^{-1}). Overall, a single clear minimum in F between values of 258 and 285 cm^{-1} for $\tilde{\nu}_e$ cannot be identified and thus a similar problem to that which occurred with the $[M_2X_8]^{n-}$ ions also occurs here. Therefore no definite solution sets of parameters were able to be identified in this range.

System 3: $\tilde{\nu}_e$ = 276 cm^{-1}, δ = 5.0 pm, m = 0.05

This system encompasses all of the possible structural changes along the normal co-ordinate in the excited electronic state, which are allowed by the OT method. The generated data was used as input to an OT calculation. The search range defined for each parameter was identical to that in system 2, except that m was now varied between -0.1 and +0.1 in steps of 0.01. This range is the usual m range taken in the previous OT calculations on the $[M_2X_8]^{n-}$ ions.

The output from the grid search was analysed in the usual way. A plot of $\tilde{\nu}_e$ vs. F_{min} (step D) was constructed for all m values. Some of these plots are overlaid as shown in Fig. 5.29. Only values of $\tilde{\nu}_e$ > 264 cm^{-1} are shown: for most values of m, only these values produced a minimum in the plot of δ vs F.

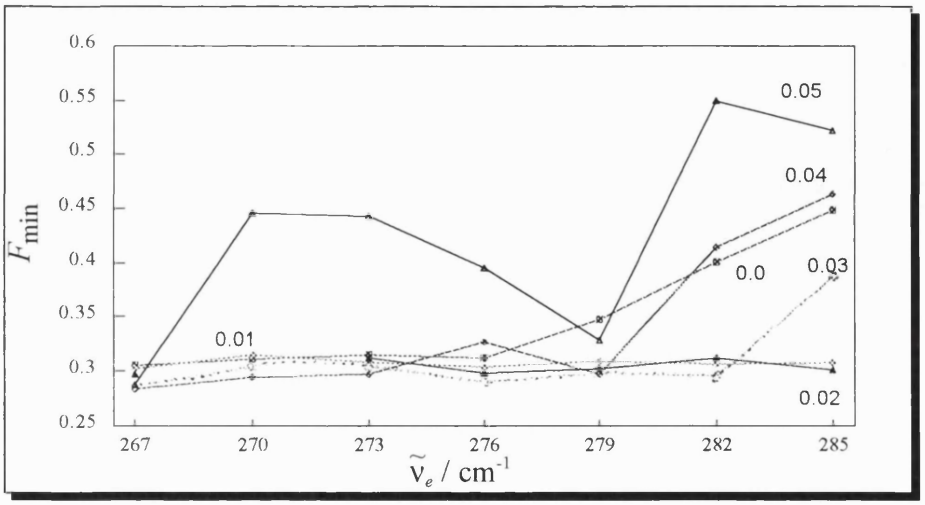

Fig 5.29: System 3: Plot of $\tilde{\nu}_e$ *vs.* F for various m

From this plot, it is clear that the most distinctive minimum occurs for m = 0.05, with $\tilde{\nu}_e$ = 279 cm^{-1}. The value of δ corresponding to this grid position is 5.5 pm. This is in quite good agreement with the actual values, and this may indicate that experimental data used for the real molecules may be the source of the failure of the OT method. However, it is notable that the *actual* lowest value of F_{min} in this search would give a different value (m = 0.04, $\tilde{\nu}_e$ = 267 cm^{-1}) and that this does not correspond to a minimum in F. It should also be noted that the values of F_{min} for m = 0.05 are consistently larger (i.e. the fit is poorer) than for lower values of m. Thus, the OT method has being fairly successful at finding values for two of the parameters, but the minimum corresponding to these values does not correspond to a minimum in the third parameter (m). It appears that the OT method shows limited success in reproducing some of the parameter values for the most complex system. Moreover, the importance of considering general trends in the magnitude of F rather than absolute values of F has been illustrated.

System 4: $\tilde{\nu}_e$ = 300 cm^{-1}, δ = 5 pm, m = 0.0, T = 77 K

This system is analogous to System 1, except that the experimental data were generated using an 'experimental' temperature of 77 K. In this way, the effectiveness of the 'zero-temperature' approximation in the OT method could be assessed.

It was therefore expected that the output of the OT calculation on the two sets of data would be almost identical. The results were analysed in the usual way: with only δ being varied, $\tilde{\nu}_e$ and m were set to their known values and a plot of δ vs. F (step B) should reveal any minima. A comparison of this plot for the two systems (1 and 4) is shown in Fig 5.30.

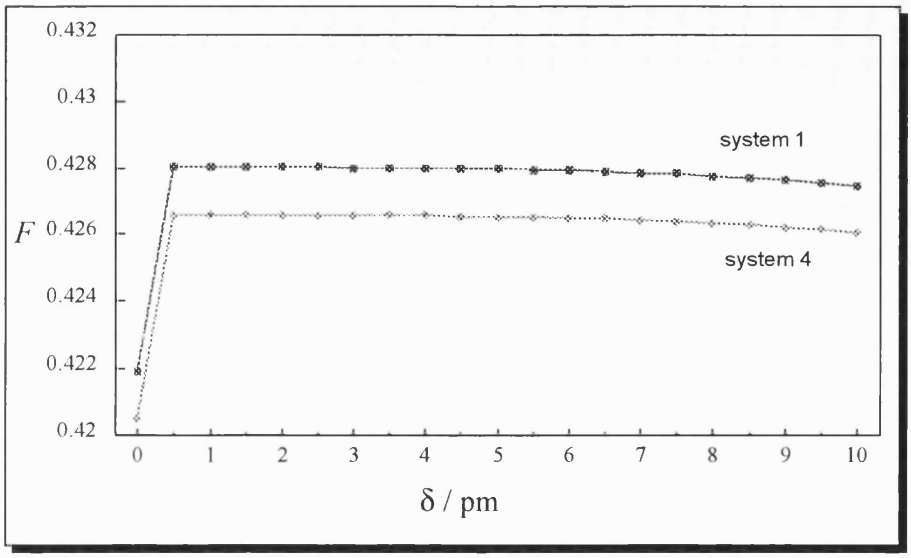

Fig 5.30 : comparison of the plots of δ vs. F for systems 1 and 4.

As can be seen from this plot, the breaking of the strict zero-temperature approximation appears to have little effect on the OT calculation for a mode of ground state wavenumber 300 cm^{-1} (typical for real experimental data). While no actual solution can be found for either system within the pre-defined search range, this comparison has shown that the breakdown in the strict zero-temperature condition is unlikely to have been the cause of the apparent failure of the OT method in the case of the $[M_2X_8]^{n-}$ ions, for which the data were recorded at ~ 77 K.

System 5: $\tilde{\nu}_e$ = 276 cm^{-1}, δ = 5 pm, m = 0.0, T = 77 K

This system is identical to system 2, but, as in the case above, the 'experimental' data were generated at 77 K. The generated ABS profile and RR intensity ratios are again very similar to those of system 2 seen in Fig. 5.27.

The plots of $\tilde{\nu}_e$ vs. F_{min} for systems 2 and 5 is shown in Fig 5.31, and it is clear that the temperature again has no effect on the OT calculation.

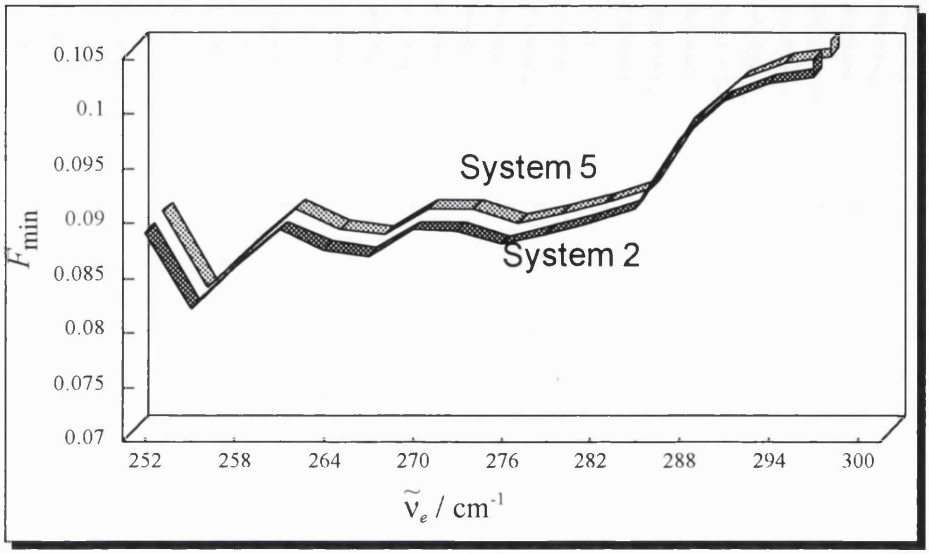

Fig. 5.31 comparison of the plots of $\tilde{\nu}_e$ vs. F for systems 1 and 4

Systems 6 - 9: Variation of the Laser Excitation Frequency Throughout the ABS Band

The four systems (6-9) have identical parameter values to those of system 2: $\tilde{\nu}_e$ = 276 cm^{-1}, δ = 5.0 pm and m = 0.0. Furthermore, the temperature at which the 'experimental' data for these systems was generated was also 0 K (as for system 2). The only difference between the systems is that the RR data were generated using four different values of $\tilde{\nu}_L$, all within the contour of the resonant ABS band. The four values of $\tilde{\nu}_L$ are:

System	$\tilde{\nu}_L$ / cm^{-1}
6	13,500
7	14,000
8	14,500
9	15,000

Thus, the ABS profile generated for all the systems is the same. However, the RR intensity ratios differ between the systems (see Table 5.15)

These data were then used in OT calculations, using the same search range for the parameter values as those used for system 2:

	Start value	End value	Step size, S
$\tilde{\nu}_e$ / cm^{-1}	300	252	-3
δ / pm	0	10	0.5
m	0	0	0

Thus, by varying $\tilde{\nu}_L$ (and therefore the RR intensity ratios), the effect of the position of the incident laser frequency on the OT method and the consistency between the two methods can be assessed.

The output from the calculations was analysed in the usual way. The plots of $\tilde{\nu}_e$ vs. F_{min} (step D) were constructed for each system : an overlay of these is shown in Fig. 5.32.

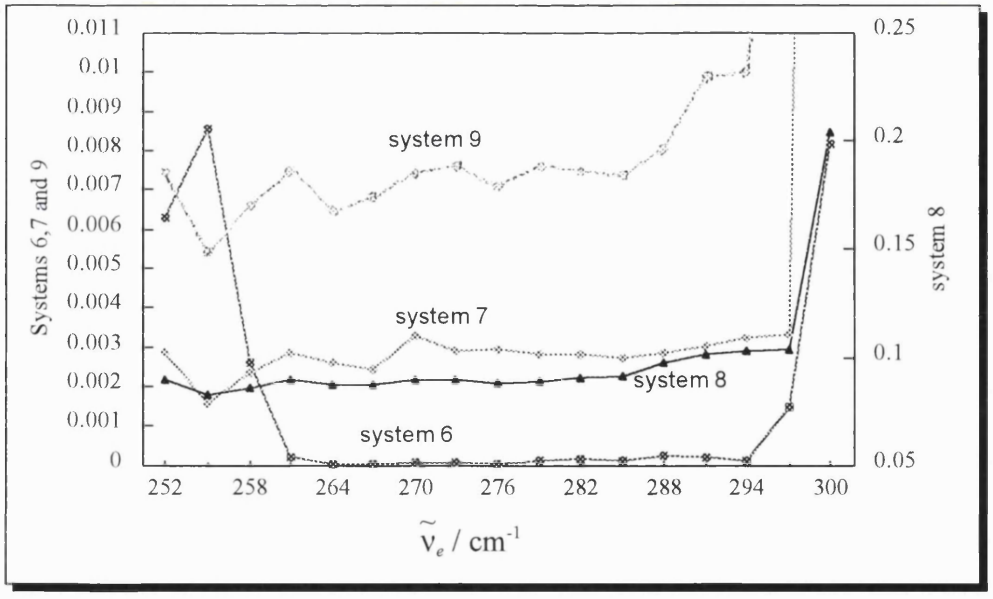

Fig 5.32 Comparison of plots of $\tilde{\nu}_e$ vs. F_{min} for systems 6 - 9

It is obvious from Fig 5.32, that there is no agreement between the curves for the different systems, despite their physical properties being identical. Moreover, only for system 9 is a clear preference for a certain $\tilde{\nu}_e$ value (255 cm^{-1}) observed.

The plot for system 9 also shows a slight dip in F_{min} at $\tilde{\nu}_e$ = 276 cm^{-1}, with a corresponding value of δ = 5.0 pm (the 'correct' value). Clearly, however, this is not the most striking minimum in the plot and it is only possible to assign it as the best minimum in the light of knowing the expected values of the parameters.

For the other systems, especially 6 and 8, the insensitivity of F_{min} to $\tilde{\nu}_e$ remains the most striking feature of these plots. It should be noted that the values of F_{min} are significantly lower when $\tilde{\nu}_L$ falls below the value of $E_{0\text{-}0}$ (system 6) then when it is above $E_{0\text{-}0}$(systems 8 and 9). The reason for this is not clear - it would be expected that the harmonic approximation is likely to hold for excitation to all the vibronic levels attainable in all the systems. Furthermore, all the systems generated by the SOS method, were so done using the harmonic approximation as an assumption. However, this remains an important observation, since it appears that the fitting function is, in general, lower for RR data recorded with an excitation frequency at the red end of the resonant ABS profile. By contrast, the only system where location of the correct value of $\tilde{\nu}_e$ was possible was one for which $\tilde{\nu}_L$ fell at the blue end of the ABS spectrum.

Overall, it can be concluded that an attempt to find consistent parameter values using the above calculations would prove extremely difficult if the expected values were not already known. Only in the case of the most complex system (system 3) was there some success in recovering the known strucutral parameters.

5.9 Conclusions

The above study has shown that, while in theory the OT method is widely applicable, many problems with its implementation remain. Certainly transform processes are more suitably applied in a mode-by-mode approach to systems where many normal modes are involved in the ABS and RR spectra. In this way,

the advantage of 'reading' multimode information from the ABS is better utilised. However, the ν_1 co-ordinate of $[M_2X_8]^{n-}$ adheres to all the restrictions imposed by this method, and is unlikely to be the cause of the failure of the method. Furthermore, parameter values for the error-free 'model' systems, generated by the SOS method also proved difficult to find by this method.

It appears that the OT method is insufficiently sensitive to allow proper location of the excited state parameter values. This insensitivity probably arises form two sources: first, the necessity to read the ABS means that the number of data points therein is restricted, and this has repercussions when performing the mulitdimensional grid search. The fewer the number of ABS points, the larger value of S(ABS) and hence the coarser the necessary search for $\tilde{\nu}_e$ values. With the convoluted procedure required to visualise and find solution sets of parameters using the current OT program, the set-up of the grid may be crucial to the final sensitivity of the fitting function, F, to each of the unknown parameters.

Second, it has been seen that the calculation of the complex polarizability, $\Phi(\omega)$, from the experimental ABS, is dependent on the length of the tails on either side of the band. Furthermore, owing to the zero-temperature approximation, and the requirement for averaging over all orientations precluding the use of polarised single-crystal data, most ABS spectra are recorded in a powder medium at low temperatures. With the problems associated with baseline scattering and dispersion in a powder sample, it may be expected that, while visual fitting of such spectra (e.g. in the SOS method) is feasible, the use of these data as an accurate starting point for a numerical calculation may be unreasonable. It can only be concluded that the ABS data should be recorded with the highest accuracy possible, and that the maximum tail lengths on the ABS spectrum should be used, subject to a sensible number of data points. Where possible, glass ABS spectra would avoid the problems of baseline effects, and may sharpen the resolution of the spectrum, but with RR spectra in the form of a glass experimentally

unachievable at present, and many of the compounds studied here being unstable in solution, this option is rarely available.

Thus, it must be finally concluded that, at present, the implementation of the OT method remains problematic and it is unsuitable for general application. It is likely to be of most use in a situation where very many modes are excited in the ABS band, such that the benefit of reading this multimode information from the ABS spectrum is more apparent. The resonance enhanced Raman modes could then be treated individually, with the multimode information remaining implicit in the ABS. However, even in the cases studied here, where a single mode dominates the RR and ABS spectra, the OT method should, in principle, be applicable. The failure of application reported here must question the usefulness of the method at its current stage of development.

Chapter 6

A Spectroscopic Study of $Cs_4Mo_2Br_8$

In chapters 3 and 4, it was seen that the SOS method can be applied successfully to study the structures of quadruply bonded dimetallic species in the $^1\delta\delta^*$ excited electronic state. From the studies on the ions $[Re_2Br_8]^{2-}$, $[Re_2I_8]^{2-}$ and $[Mo_2Cl_8]^{4-}$, and on the series of compounds $Mo_2X_4(PMe_3)_4$ (X = Cl, Br or I), new insights into the nature of the metal-metal (M-M) δ bonding in these types of molecules were achieved. In particular it was noted that the structural distortions along the M-M axis of the $[Mo_2Cl_8]^{4-}$ ion in this $^1\delta\delta^*$ state were unusual, and it was suggested that this may be a result of the high charge of the ion or of a greater contribution than usual of the δ bond to the total M-M quadruple bond in this ion.

A comparative study of the structurally analogous ion $[Mo_2Br_8]^{4-}$ could therefore provide further information on the reasons for this observed behaviour, and could also reinforce findings concerning the variation in δ bond characteristics as a halide series is traversed.

Furthermore, it has previously been reported that the RR spectrum of the $[Mo_2Br_8]^{4-}$ ion in resonance with the $^1(\delta^* \leftarrow \delta)$ transition shows an interesting temperature dependence. At ~ 77 K, the intensities of the overtones in the ν_1 (ν(MoMo)) progression are seen to be random, with some overtones having higher intensities than the fundamental band [6.1]. This phenomenon, known as intensity cross-over, has never been adequately explained.

Thus, in this chapter, the attempted synthesis and spectroscopic study of the $[Mo_2Br_8]^{4-}$ ion are reported.

6.1 Synthesis

The $[Mo_2Br_8]^{4-}$ ion has only once been reported as the Cs^+ salt in a straightforward synthesis via the reaction of $Mo_2(O_2CCH_3)_4$ and CsBr in the presence of conc. HBr [6.2]. A purple solid was collected and the RR and far IR spectra were also reported. However, no microanalysis or crystal structure were available to confirm the proposed formula of $Cs_4Mo_2Br_8$.

Later workers synthesised the NH_4^+ salt via the compound $(NH_4)_4Mo_2(SO_4)_4.2H_2O$, which can be prepared from the octachloride, $(NH_4)_5Mo_2Cl_9.H_2O$ [6.3]. The sulphate is then treated with conc. HBr to give a purple crystalline product, $(NH_4)_4Mo_2Br_8$. The availability of single crystals of this salt allowed confirmation of the usual D_{4h} molecular symmetry for the $[Mo_2Br_8]^{4-}$ ion [6.3]. This compound was also investigated spectroscopically and UV/Vis absorption, far IR and RR spectra were reported [6.4]. A band observed at ~ 18,000 cm^{-1} in the UV/Vis spectrum was assigned to the $^1(\delta^* \leftarrow \delta)$ transition. The RR spectrum in resonance with this band showed unusual intensity cross-over in the ν_1 (ν(MoMo)) mode progression at 77 K [6.1]. Furthermore, several combination bands which were absent from the RR spectrum at 295 K appeared in the equivalent low temperature spectrum.

In this work, attempts to synthesise the sulphate $(NH_4)_4Mo_2(SO_4)_4.2H_2O$ as a precursor to $(NH_4)_4Mo_2Br_8$ were unsuccessful. For this reason, the Cs^+ salt was prepared by the following reaction:

$$4CsBr + Mo_2(O_2CCH_3)_4 + 4HBr \rightarrow Cs_4Mo_2Br_8 + 4CH_3CO_2H$$

0.6 g $Mo_2(O_2CCH_3)_4$ were ground finely with 1.7 g CsBr and the mixture added to 10 cm^3 ice-cold conc. HBr. The mixture was held at 0 °C with stirring for 12 - 15 min. A dark purple precipitate was filtered, rinsed with cold ethanol and dried with ether.

The reaction was allowed to proceed for only 12-15 min in order to avoid any oxidation of the product to $Cs_3Mo_2Br_8H$ [6.5], an orange-brown H-bridged species which has been reported to form in this synthesis if the reaction time is too long.

It was found that this purple precipitate was reasonably air-sensitive, degrading to a brown colour on long exposure to air. Consequently, it was stored under N_2 at all times. At this stage, it was supposed that the purple compound was $Cs_4Mo_2Br_8$, and thus attempts were made to record the experimental data necessary for the application of the SOS method to the $^1\delta\delta^*$ excited state, i.e. the ABS spectrum of the $^1(\delta^* \leftarrow \delta)$ transition and the RR spectrum in resonance with this band.

6.2 Electronic Absorption Spectrum

The UV/Vis ABS spectrum of $(NH_4)_4Mo_2Br_8$ has been reported previously [6.4], with the $^1(\delta^* \leftarrow \delta)$ transition maximising at ~ 18,000 cm^{-1}.

The purple compound, prepared as above, was made into a transparent alkali halide (KBr) disk, as detailed in Appendix A2. UV/Vis spectra were then recorded in the region 400 - 800 nm (see Appendix A2) at 295 and at 77 K.

These are shown in Fig. 6.1, where correction for baseline scattering and dispersion effects (Appendix A3) have been performed.

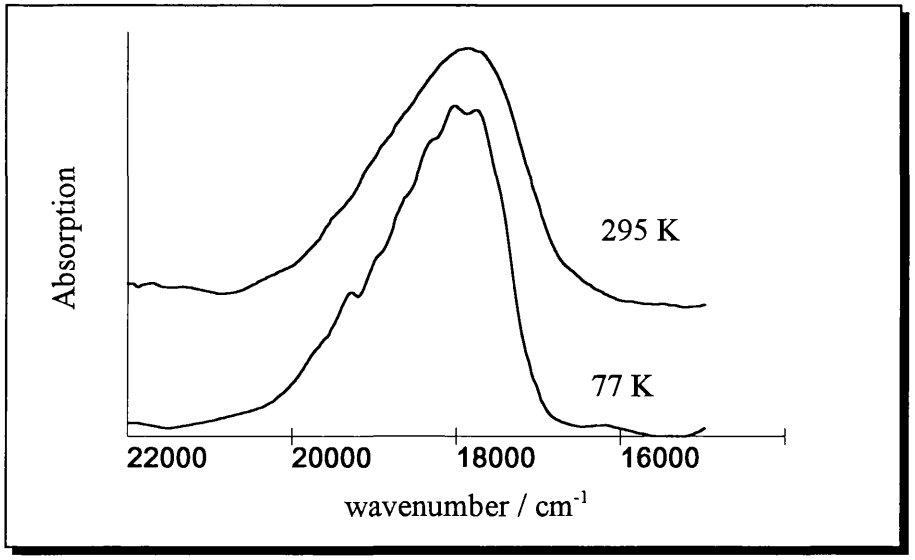

Fig. 6.1 UV/Vis ABS spectrum of the compound $Cs_4Mo_2Br_8$ in the region of its $^1(\delta^* \leftarrow \delta)$ transition. Correction for baseline scattering and dispersion effects have already been performed.

In this region, there appears to be only one band with a maximum at ~ 18,000 cm^{-1}, assigned to the $^1(\delta \leftarrow \delta)$ transition. This is in good agreement with the value reported for $(NH_4)_4Mo_2Br_8$. Some vibronic structure was observed on the spectrum recorded at 77 K. The spacing of this structure is difficult to determine on the basis of peak positions of a relatively short and poorly resolved progression, but appears to be in the order of ~ 320-325 cm^{-1}. In the ABS spectrum of $(NH_4)_4Mo_2Br_8$, a spacing 320 cm^{-1} was reported, and this was assigned to the wavenumber of the ν_1 mode in the $^1\delta\delta^*$ (denoted $\tilde{\nu}_e$). From RR spectroscopy, the corresponding value for the ground state ($\tilde{\nu}_g$) was found to be 336 cm^{-1}.

It appears at this stage that there is good agreement between the observed ABS spectrum for the purple compound and that reported previously for $(NH_4)_4Mo_2Br_8$.

6.3 Resonance Raman Spectra

RR spectra of the sample were recorded in the form of a pressed halide (KBr) disk, as described in Appendix A1. Excitation by a laser line with a wavenumber lying within the contour of the electronic ABS band observed in Fig. 6.1 (17,599 cm^{-1}) produced a long progression in a mode of wavenumber 333 cm^{-1}. This was assigned the symmetric $\nu_1(\nu(Mo\text{-}Mo))$ stretch on the basis of comparison with the RR spectrum reported for $(NH_4)_4Mo_2Br_8$, which shows a similar progression in a mode of wavenumber 336 cm^{-1}. The difference in wavenumber of this mode for different salts of the same ion is not unexpected: for example, the wavenumber of the ν_1 mode in $Cs_4Mo_2Cl_8$ is 340 cm^{-1} compared with 338 cm^{-1} for the corresponding NH_4^+ salt [6.6]. It should be noted that in this case, however, the Cs^+ salt band shows the higher wavenumber: for the ion $[Mo_2Br_8]^{4-}$ it appears that the reverse is true. The RR spectrum of $Cs_4Mo_2Br_8$ is shown in Fig. 6.2.

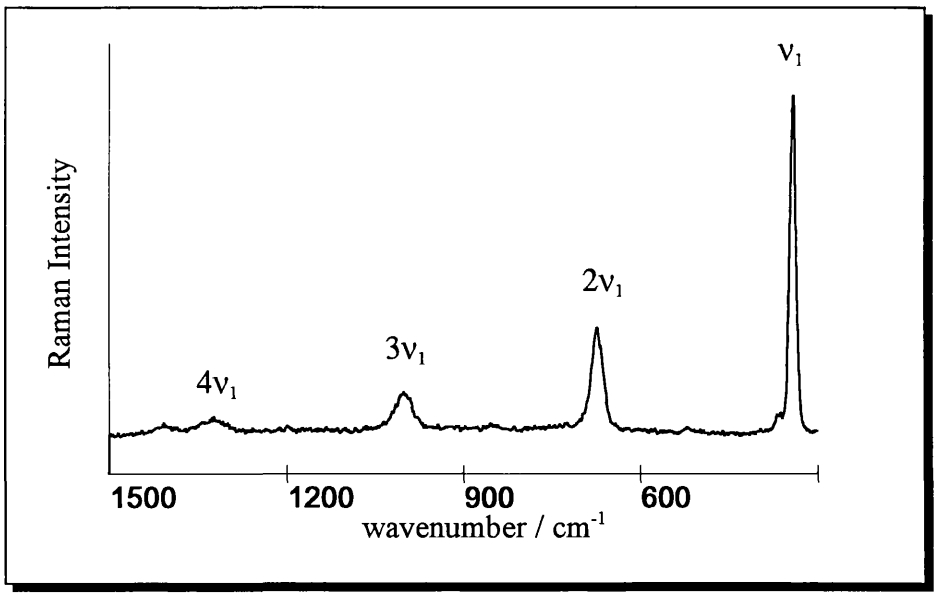

Fig. 6.2 RR spectrum of $Cs_4Mo_2Br_8$ as a pressed KBr disk at 295 K. Excitation wavenumber 17,599 cm^{-1}.

On lowering the temperature of the sample to ~77 K, and recording a RR spectrum with the same excitation wavenumber, an additional progression in a second mode, of wavenumber 355 cm^{-1} was seen. A large fluorescence band was also seen at this temperature, starting at ~16,400 cm^{-1} and maximising at ~ 15,000 cm^{-1}. This spectrum is shown in Fig. 6.3.

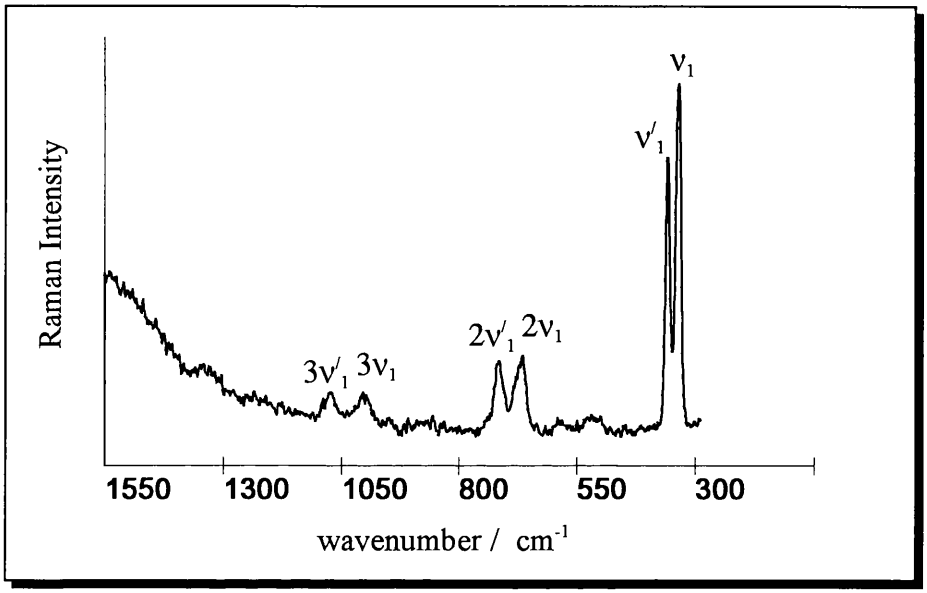

Fig. 6.3 RR spectrum of $Cs_4Mo_2Br_8$ as a pressed KBr disk at 77 K. Excitation wavenumber 17,599 cm^{-1}.

The wavenumbers of the bands observed in this spectrum are shown in Table 6.1: it is seen that the 'new' bands appearing at ~77 K cannot be assigned to a combination band of ν_1 with another mode, but constitute an actual progression in a mode of wavenumber 355 cm^{-1}.

Wavenumber / cm^{-1}	Assignment
333	ν_1
355	ν_1'
664	$2\nu_1$
712	$2\nu_1'$
997	$3\nu_1$
1072	$3\nu_1'$

Table 6.1 Observed band wavenumbers in the RR spectrum of $Cs_4Mo_2Br_8$ as a pressed KBr disk at 77 K. Excitation wavenumber 17,599 cm^{-1}.

It has previously been reported that the RR spectrum of $(NH_4)_4Mo_2Br_8$ at 77 K (excitation wavenumber 17,599 cm^{-1}) also shows some bands which are not observable at 295 K [6.1]. These were assigned to progressions in 31 + $n\nu_1$, 141 + $n\nu_1$, 293 + $n\nu_1$ and $n\nu_1$-78 cm^{-1}. It can be seen form Table 6.1 that the progression observed here does not match any of these assignments.

On warming the sample, the spectrum seen at 295 K (Fig. 6.2), with only one progression in the 333 cm^{-1} mode, is completely recovered, and the fluorescence disappears.

The behaviour of the two bands (and progressions) as the wavenumber of the excitation was varied across the ABS band was investigated at both 295 and 77 K. These spectra are shown in Figs. 6.4 (295 K) and 6.5 (~77 K). It can be seen that, at all excitation wavenumbers, the fundamental band or progression in the mode of wavenumber 355 cm^{-1} is strongly observed at ~77 K *only*. A small shoulder on the fundamental band of wavenumber 333 cm^{-1}, corresponding to the 355 cm^{-1} band, is seen at 295 K when excitation wavenumber of 17,599 cm^{-1} is used.

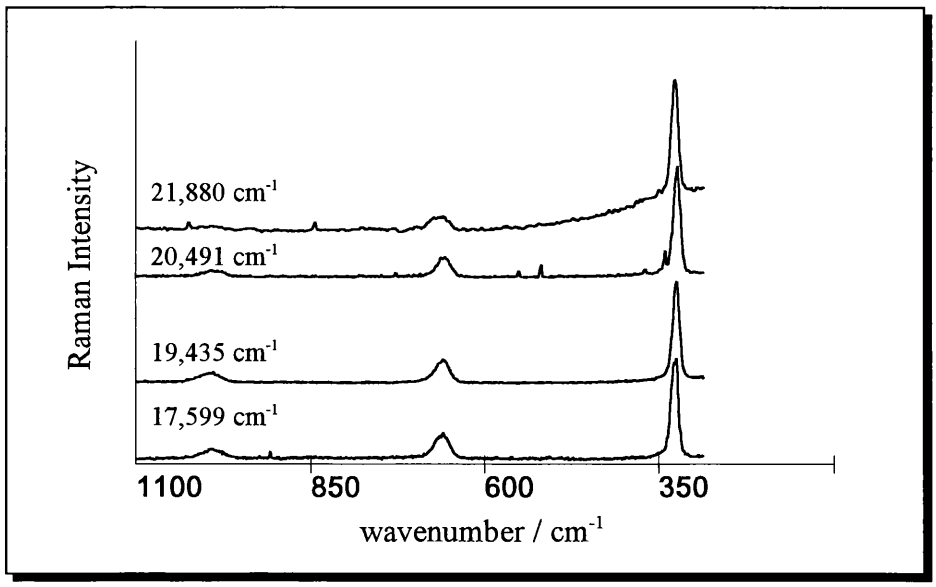

Fig. 6.4 RR spectra of $Cs_4Mo_2Br_8$ as a pressed halide (KBr) disk at 295 K, using excitation wavenumbers across the observed $^1(\delta \leftarrow \delta)$ ABS band. The intensity scale is not normalised.

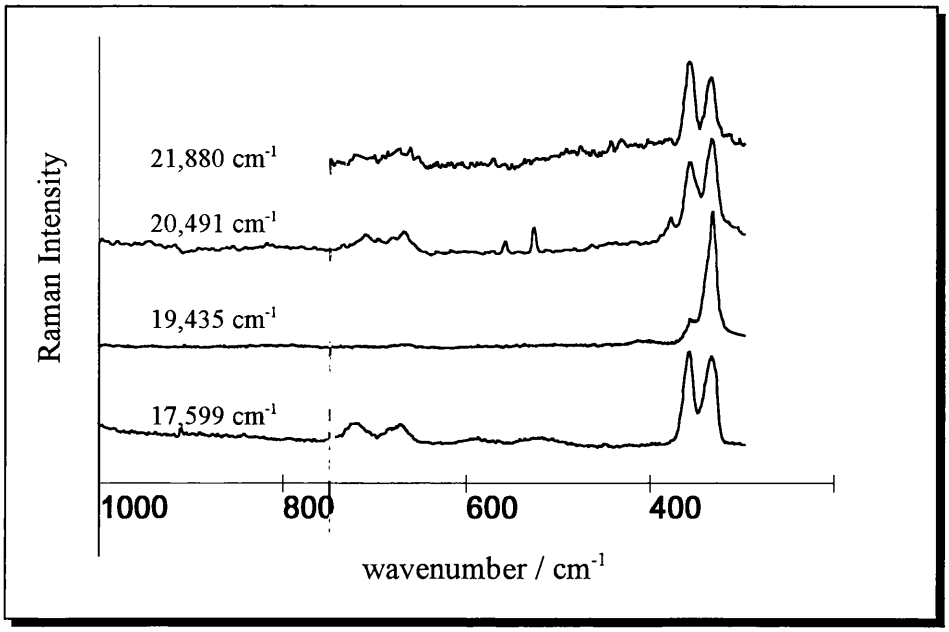

Fig. 6.5 RR spectra of $Cs_4Mo_2Br_8$ as a pressed halide (KBr) disk at ~77 K, using excitation wavenumbers across the observed $^1(\delta \leftarrow \delta)$ ABS band. The intensity scale is not normalised.

From these spectra (Fig. 6.5), it appears that the band at 355 cm^{-1} shows resonance enhancement in the same region as that in which the band at 333 cm^{-1} is enhanced. However, it is notable that the relative intensities of the two bands is not constant, suggesting that excitation profiles of the two bands at 77 K would not be coincident. In particular, it appears that the band at 355 cm^{-1} is strongly resonance enhanced at 17,599 cm^{-1}, but less so at 19,453 cm^{-1}; however, when the excitation wavenumber is raised further, enhancement is seen to be strong again. This type of apparently random variation in intensity of a band as the excitation wavenumber is varied is also seen for the ν_1 mode of $(NH_4)_4Mo_2Br_8$ at 77 K. It thus appears that the two species present here have slightly different electronic structures.

By way of reference, the analogous spectra of $Cs_4Mo_2Cl_8$ were recorded at both temperatures. No behaviour similar to that of the "$Cs_4Mo_2Br_8$" is seen with any excitation line. This is shown in Fig. 6.6, where the spectra have been recorded at both temperatures, using an excitation wavenumber of 17,599 cm^{-1}.

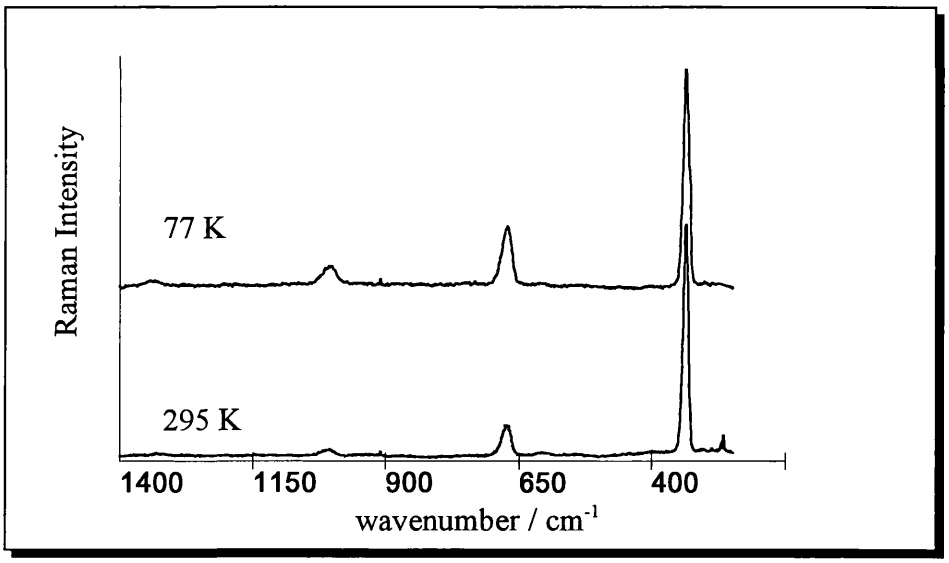

Fig. 6.6 RR spectra of $Cs_4Mo_2Cl_8$ as a pressed halide (KCl) disk at 295 and ~77 K, using excitation wavenumber 17,599 cm^{-1} (arbitrary intensity scale).

A pressed disk of $Cs_4Mo_2Br_8$ with KBr and K_2SO_4 was prepared, in order that the intensity of the bands in the RR spectrum could be referenced against the sulphate band observed at 981 cm^{-1}. RR spectra of this disk were recorded at 295 K and 77 K using the 17,599 cm^{-1} excitation line, and are shown in Fig. 6.7.

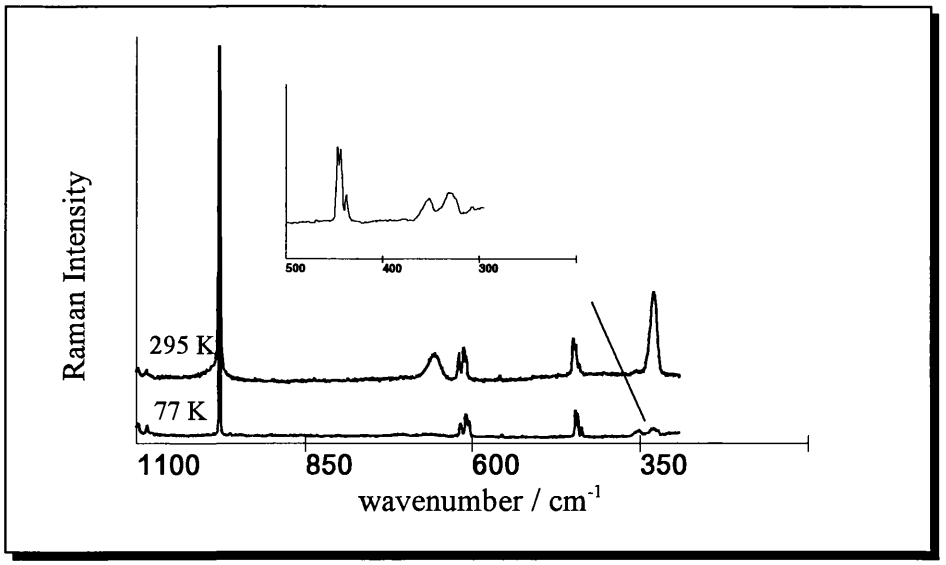

Fig. 6.7 RR spectra of $Cs_4Mo_2Br_8$ as a pressed halide (KBr) disk , incorporating K_2SO_4, at 295 K and ~77 K. Excitation wavenumber 17,599 cm^{-1}. The intensity of the 981 cm^{-1} sulphate bands in both spectra has been normalised.

It can be seen that the intensity of the band at 333 cm^{-1} in the RR spectrum decreases relative to that of the sulphate band at 981 cm^{-1} (the standard), on lowering the temperature from 295 to 77 K. However, the inclusion of the K_2SO_4 in the pressed powder disk was found to reduce significantly the quality of the RR spectra. For this reason, no quantitative measure of the drop in intensity of the 333 cm^{-1} band as the temperature is lowered was possible. However, it does appear that the combined intensity of the two bands at 355 and 333 cm^{-1} at 77 K is less than that of the 333 cm^{-1} band alone at 295 K (relative to the intensity standard).

At this stage, it is not clear whether the species with a band of wavenumber 355 cm^{-1} (denoted species *a*) is present at room temperature, with its RR spectrum being unobservable, or whether there is a conversion from the species with a band of wavenumber 333 cm^{-1} (species *b*) to species *a* as the temperature is lowered. Certainly, the RR spectrum at 295 K appears to be a simple progression in the ν_1 mode of an $[Mo_2X_8]^{4-}$ ion in resonance with the $^1(\delta^* \leftarrow \delta)$ transition. Furthermore, the progressions of both species *a* and *b* at 77 K are also typical of this type of progression, with the fluorescence band being strong only for species *a*.

It is clear that investigations using alternative techniques are required to establish whether the sample is a mixture of two different compounds, and whether or not they are both present at room temperature.

6.4 Infra-red Spectra

Far IR

A far IR spectrum of "$Cs_4Mo_2Br_8$" was recorded at 295 K, with the sample held in a wax disk using a Nicolet FT spectrometer. It has not yet been possible to record this spectrum at lower temperatures. Bands were observed in the region 400 - 100 cm^{-1} and the spectrum can be modelled to a sum of Lorentzians with

band wavenumbers and intensities shown in Table 6.2. The spectrum is shown in Fig. 6.8.

Assignment [spacing]	Wavenumber / cm^{-1}	Assignment [spacing]
a	356 w	
[49]	333 w	*b*
a	307 vw	[42]
[65]	291 vw	*b*
a	242 s, sh	[70]
[53]	222 s	*b*
a	189 m, sh	[50]
[65]	172 m, sh	*b*
a	124 mw	[61]
	111 mw	*b*

Table 6.2 Observed band wavenumbers and intensities of the far IR spectrum of $Cs_4Mo_2Br_8$, together with assignments. The figures in parentheses indicate the spacing between bands in a series.

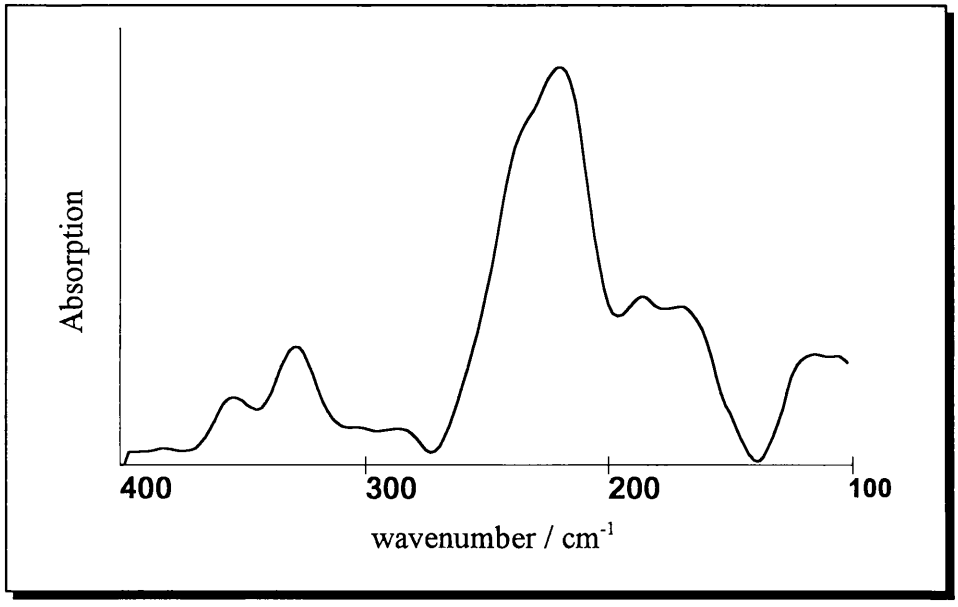

Fig. 6.8 Far IR spectrum of $Cs_4Mo_2Br_8$ as a wax disk at 295 K.

The spectrum appears to be the sum of the spectra due to two species, assigned *a* and *b* in Table 6.2. The highest wavenumber bands in each case (356 cm^{-1} and

333 cm^{-1}) can be assigned to the totally symmetric ν_1 (ν(Mo-Mo)) stretching mode, and these values correspond to those observed in the RR spectra at 77 K. For a centrosymmetric molecule of symmetry D_{4h}, this band should be forbidden in the IR spectrum, but appears weakly in this case. Similarly, in the IR spectra of salts of the ion $[Mo_2Cl_8]^{4-}$, a band due to the ν_1 mode is also weakly observable.† All other bands in the spectrum also appear to be the sum of two components. The fit of the combined spectra modelled and assigned to species *a* and *b*, to the recorded spectrum is shown in Fig. 6.9.

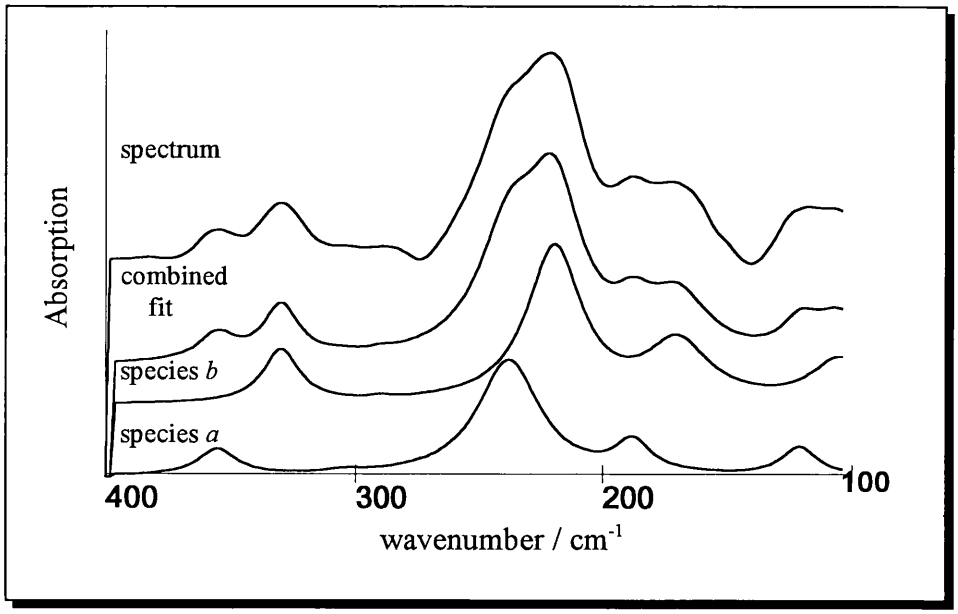

Fig. 6.9 Modelled far IR spectra of species *a* and *b* present in $Cs_4Mo_2Br_8$, together with the fit of the combined spectrum to the original recorded spectrum.

The observation that the spacing between successive bands in the spectrum of species *a* is very similar to that between the analogous bands in the spectrum of species *b* strongly supports the interpretation of the recorded spectrum as a sum of spectra due to two different species.

Previous reports of the far IR spectra of any of the salts of the $[Mo_2Br_8]^{4-}$ ion have been incomplete [6.1, 6.2]. It is reported that bands are observed at 251 (m) and 223 (s) cm^{-1} in the spectrum of the Cs^+ salt [6.2] and at 181, 170 and

† see Fig. 6.10

96 cm^{-1} in the spectrum of the $(NH_4)^+$ salt [6.1]. However, no spectrum has been published to enable visual comparison with that shown in Fig. 6.8.

Thus it would appear that both these species are in fact present at 295 K, but that the RR spectrum of species *a* is unobservable at this high temperature. Furthermore, modelling of the far IR spectrum appears to show that the two species are extremely similar, with the spacing between bands assigned to series *a* are very close to those assigned between bands assigned to series *b*.

By way of reference, the equivalent far IR spectrum of $Cs_4Mo_2Cl_8$ as a wax disk at 295 K was also recorded and is shown in Fig. 6.10, together with a fit generated by modelling the bands to Lorentzian components. The wavenumbers of the bands in the fit are shown in Table 6.3.

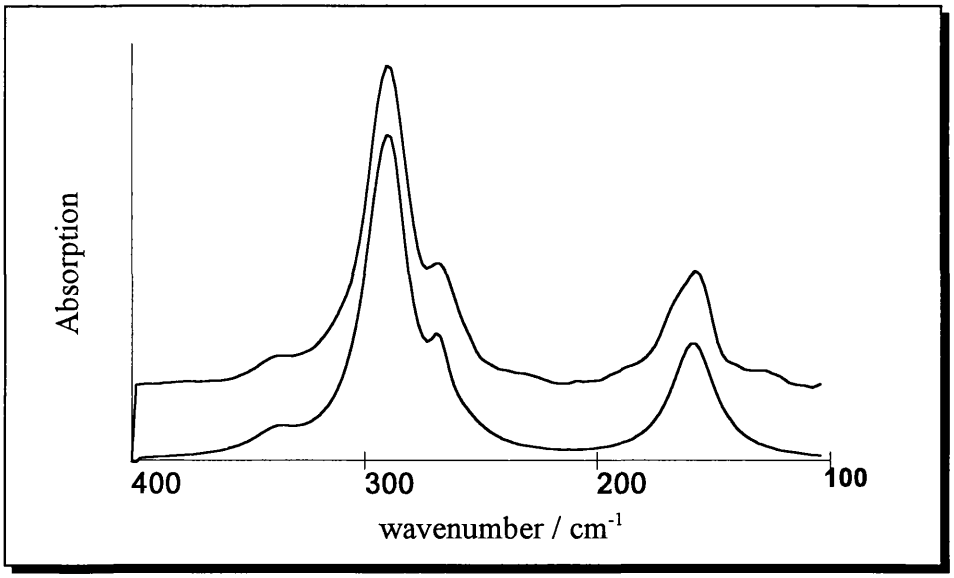

Fig. 6.10 Far IR spectrum of $Cs_4Mo_2Cl_8$ as a wax disk at 295 K, together with a fit of the spectrum to Lorentzian band components.

Wavenumber / cm^{-1}	Intensity
340	w
294.5	vs
290	m, sh
271	sh
259	s
161	s

Table 6.3 Wavenumbers and intensities of bands modelled to fit the IR spectrum of $Cs_4Mo_2Cl_8$.

Previously, bands were observed in the spectrum of this compounds at 336(w), 295 (vs), 286(s), 272(w), 260(sh) and 161(s) cm^{-1} [6.6]. Thus the agreement with the current band wavenumbers and intensities is good. It is notable that the number and pattern of the bands in this spectrum are very similar to those observed for both of the two species in '$Cs_4Mo_2Br_8$' (Fig. 6.9), although obviously the spacing between bands will be markedly different for Mo-X stretching vibrations in the octachloride and octabromide compounds. However, the simplicity of the spectra assigned to the two species *a* and *b* in the compound $Cs_4Mo_2Br_8$, and the close similarity of the pattern of bands observed in these spectra to that observed for $Cs_4Mo_2Cl_8$ suggest that *a* and *b* are simple, highly symmetric quadruply bonded M-M species.

Mid IR

A mid IR spectra of $Cs_4Mo_2Br_8$ as a pressed halide (KBr) disk was also recorded in the region 600 - 3000 cm^{-1}. However, no previous reports of mid IR spectra of any salt of the $[Mo_2Br_8]^{4-}$ ion are available for comparison. The presence of water was confirmed, but it was not possible to assign it as bound or unbound. Attempts to dry the compound further, in order to remove any unbound water, resulted in degradation of the sample. In general, bands were observed at

wavenumbers analogous to those in the mid-IR spectrum of $Cs_4Mo_2Cl_8$, which was also recorded for reference. Some weak bands assignable to the starting material, $Mo_2(O_2CCH_3)_4$, were also observed.

Notably, no bands assignable to a ν(Mo-H-Mo) stretching mode were observed, which might be the case of either of the species were the oxidised compound $Cs_3Mo_2Br_8H$. This band has previously been reported at ~1245 cm^{-1} [6.5].

6.5 Other Characterisation Experiments

Other forms of characterisation were attempted in order to try and identify the species *a* and *b*. In many cases, characterisation was hindered by the air sensitivity of the compound, and its rapid decomposition in solution.

Elemental Analysis

1. Microanalysis : this was greatly hindered by the instability of the compound in solution and the availability of measurements for only one element (Br) by mass. Found %Br: 44.1; calculated %Br : 46.1 for $Cs_4Mo_2Br_8$.

2. EDAX and Electron Microprobe: these techniques were applied in order to find the ratio of the heavy elements present in the compound. It was found, however that the sample was very 'soft' to the electron beam, and decomposition occurred during these processes. Thus, results were widely varying and irreproducible.

XPS

The XPS spectrum of the compound was recorded at 295 K and at liquid nitrogen temperature. Peaks due to Cs, Br and Mo $3d_{5/2}$ shells were observed, but no change in the spectrum was observed on lowering the temperature of the sample.

The peaks due to the Mo and Br atoms were seen to reflect two different environments in roughly equal proportions. The possibility of the second Mo environment being due to the presence of the starting material $Mo_2(O_2CCH_3)_4$, was discounted by taking account of a spectrum of pure $Mo_2(O_2CCH_3)_4$. The energy of the Mo peaks in the latter spectrum were found not to match those of the Mo peaks seen in the spectrum of $Cs_4Mo_2Br_8$. However, the presence of some C peaks in the spectrum of $Cs_4Mo_4Br_8$ confirmed the presence of small amounts of $Mo_2(O_2CCH_3)_4$ as an impurity. More quantitative estimations of the ratios of the elements present were again not possible due to sample degradation during the experiment.

X-Ray Powder Diffraction

A powder XRD spectrum of the compound was recorded for comparison with that calculated from the single-crystal data published for $(NH_4)_4Mo_2Br_8$ (calculated by Dr. D. Tocher). It was found, however, that the powder pattern for the $Cs_4Mo_2Br_8$ did not match that calculated for $(NH_4)_4Mo_2Br_8$, with only very few peaks being present.

6.6 Reactivity

The reactivity of the "$Cs_4Mo_2Br_8$" has been investigated, again to allow comparison with the reactivity of other quadruply bonded dimolybdenum compounds. In a similar way to that seen for the $[Mo_2Cl_8]^{4-}$ ion, the compound is observed to undergo rapid reaction in donating solvents, suggesting that ligand exchange occurs. A summary of the main reaction is given in Table 6.4.

All solutions were found to be unstable and it has not yet been possible to isolate and characterise any of the products formed. However, it is notable that very similar reactions to those described above are seen for the $[Mo_2Cl_8]^{4-}$ ion.

Solvent	Colour of solution	λ_{max} / nm
CH_3CN	blue	607
acetone	purple	-
DMF	dark red	-
dil. HBr	pink	505.2
dil. HBr + CH_3CN	purple	553.6
conc. HCl	pink	514.5

Table 6.4 Summary of the reactions of the compound $Cs_4Mo_2Br_8$ with a variety of solvents.

6.7 Discussion

The synthesised compound "$Cs_4Mo_2Br_8$" appears to contain two species *a* and *b*, each with a strong Mo-Mo bond. From the far IR spectra (section 6.4), it is seen that the two species are present at room temperature. Furthermore, they appear to be reasonably symmetric having a simple pattern in the far IR spectrum similar to that seen for $Cs_4Mo_2Cl_8$. The similarity of the pattern and spacings of the series of bands assigned to each species indicates that they are structurally very similar.

The XPS spectrum also shows that two Mo and Br environments are present at room temperature in approximately equal proportions, and that this proportion does not change at low temperatures.

The RR and fluorescence of the species denoted *a*, (with ν(MoMo) = 355 cm^{-1}), in resonance with the $^1(\delta^* \leftarrow \delta)$ transition, appear to be weak (possibly even disallowed) at room temperature. However, they are observed strongly at ~ 77 K. Changing the excitation frequency appears to show that resonance with the band assigned to the $^1(\delta^* \leftarrow \delta)$ transition occurs for both species at ~ 18,000 cm^{-1}. However the REPs of the fundamental band of the ν_1 mode progression for the two species appear not to be exactly coincident.

The fact that the temperature dependence of the species *a* is observed only in its fluorescence and RR spectra may indicate that this species (with a band of wavenumber 355 cm^{-1}) is eliminated at 295 K as a result of the laser excitation, or that the *excited* electronic state of this species is not accessible at this temperature. It is difficult to draw any conclusions about the nature of the excited state from the ABS spectrum. Certainly a band assignable to the $^1(\delta^* \leftarrow \delta)$ is observed and occurs in the same region as that observed for $(NH_4)_4Mo_2Br_8$ [6.1, 6.4]. However, because of thermal broadening and the problems associated with scattering and dispersion in the baseline of powder ABS spectra (Appendix A3), greater detail on the ABS band cannot be observed. It is impossible to rule out that the observed band could consist of two components, or to tell if the vibronic structure observed at 77 K is characteristic of one or more progressions of similar spacing. Ideally, a single crystal or glass ABS spectrum would show whether or not the band observed at around 18,000 cm^{-1} was composed of one or more components. However, the instability of the compound in solution (section 6.6) prevents such a spectrum form being recorded. Thus it is not possible to say at present whether species *a* is being destroyed during, or is merely unobservable in, the RR experiment at 295 K

The failure of further characteristic methods (section 6.5) as a result of the sensitive nature of the sample, means that proper identification of the two species is not possible.

The RR spectrum of the compound recorded with excitation wavenumber 17,599 cm^{-1} at 295 K, is very similar to that reported for the compound $(NH_4)_4Mo_2Br_8$ at the same temperature: no strong fluorescence band is observed in either spectrum, and the wavenumbers of the ν_1 mode of species *b* are very similar (333 cm^{-1} Cs^+ salt, 336 cm^{-1} NH_4^+ salt). Therefore, if it can be assumed that the species observed at room temperature in the RR spectrum (species *b*) in the compound is, in fact, $Cs_4Mo_2Br_8$, then there remain several possibilities for the

identity of the species *a*, with ν_1 fundamental band of wavenumber 355 cm^{-1}, for which the RR spectrum is observable only at 77 K:

1. $Mo_2(O_2CCH_3)_4$

This is the starting material for the synthesis reaction and its presence as an impurity has been confirmed by XPS studies. Some bands attributable to this species are also observed in the mid-IR spectrum of the purple. The far IR spectrum of $Mo_2(O_2CCH_3)_4$ is also reported to show bands at 366, 334 and 223 cm^{-1} [6.2], near to some of the bands in Fig. 6.8 and Table 6.2. However, the XPS study showed that the amount of this impurity is likely to be small. This is further reinforced by the RR spectrum, which might be expected to show a band attributable to the ν_1 fundamental of $Mo_2(O_2CCH_3)_4$ at 406 cm^{-1} [6.7] if large amounts of this compound were present.

Furthermore, the reported maximum in the $^1(\delta \leftarrow \delta)$ transition in the electronic ABS spectrum of $Mo_2(O_2CCH_3)_4$ is ~ 23,000 cm^{-1} [6.8]: hence strong resonance enhancement of the ν_1 mode would not be expected with excitation lines of 17,599 or 19,543 cm^{-1}.

It may be possible that small amounts of $Mo_2(O_2CCH_3)_4$ are present and can be detected in the mid-IR and XPS spectra. However, that amount present is expected to be sufficiently small so as not to affect the far IR or RR spectra.

2. $Cs_3Mo_2Br_8H$

It has previously been reported that this brown compound forms during the synthetic reaction described in section 6.1, approximately 45 min after the formation of an initial purple transient [6.5]. Thus, the reaction time during the synthetic reaction was kept deliberately short.

The brown compound $Cs_3Mo_2Br_8H$ was originally formulated as $Cs_3Mo_2Br_7$ [6.9], and other salts of the supposed $[Mo_2X_7]^{3-}$ ions (X = Cl or Br) were isolated [6.10, 6.11]. However, on account of its diamagnetism it was later reformulated as $Cs_3Mo_2Br_8H$ [6.5], and has been structurally characterised [6.12]. The molecule is seen to have C_{2v} symmetry and contains both bridging H and Br atoms: the mid-IR spectrum revealed a band which was assigned to the ν(Mo-H-Mo) stretch at 1245 cm^{-1}[6.5]. The presence of bridging atoms between the metals in this kind of compound leads to debate about the presence of an actual metal-metal bond. It can be seen from Figs. 6.2 and 6.3, that the ABS and RR spectra of the compound prepared here ("$Cs_4Mo_2Br_8$") are characteristic of dimetallic species with a strong M-M bond. This may indicate that $Cs_3Mo_2Br_8H$ is not a likely assignment for the identity of the species present in the sample in question. Furthermore, the compound "$Cs_4Mo_2Br_8$" is seen to have a dark purple colour, rather than the orange-brown reported for $Cs_3Mo_2Br_8H$.

The clearest indication, however, that species *a* in the prepared sample is not $Cs_3Mo_2Br_8H$ comes from its IR spectra. In the mid-IR, no band at or near 1245 cm^{-1}, the value reported for the ν(Mo-H-Mo) stretching mode in $Cs_3Mo_2Br_8H$ [6.5], is observed. Furthermore, the lowering of the molecular symmetry in the bridged species (C_{2v} rather than D_{4h} for an $[M_2X_8]^{n-}$ ion) would be reflected in a complex far IR spectrum. The simplicity of the far IR spectrum for both species present in the compound "$Cs_4Mo_2Br_8$" (Fig. 6.9), and the similarity of these spectra to that recorded for $Cs_4Mo_2Cl_8$ (Fig. 6.10), indicate a high molecular symmetry for each species. In addition, a RR spectrum of $Cs_3Mo_2Br_8H$ has previously been reported [6.13] and shows many unassignable bands in the region < 400 cm^{-1}. By contrast, the spectrum of the compound "$Cs_4Mo_2Br_8$" (Fig. 6.3) is relatively simple.

3. $Cs_2Mo_2Br_6(OH_2)_2$

Since the only other ligand in the reaction mixture is water, the possibility that ligand exchange may have occurred must be considered. The $(mpH)^+$ and $(pyH)^+$

salts of the $[Mo_2X_6(OH_2)_2]^{2-}$ ions (X = Cl or Br) have previously been reported [ref] and their IR and RR spectra measured [6.14]. The wavenumber of the ν_1 (ν(MM)) mode for the case when X = Br has been found to be 350 cm^{-1}, in reasonable agreement with that of species (*a*) in question here, taking into account the difference in cations. However, the RR and fluorescence of this compound appear to be strong at both 295 and 77 K; furthermore, the fluorescence appears to start at ~18,100 cm^{-1}, approximately 1,700 cm^{-1} higher than that due to species *a* in the "$Cs_4Mo_2Br_8$" sample. While different salts of this di-aquo ion will undoubtedly differ to some extent, it would be expected that their spectra would be largely similar.

Further evidence against the identification of the second species as $Cs_2Mo_2Br_6(OH_2)_2$ is the lack of similarity between its far IR spectrum and that reported for the $(mpH)^+$ salt of $[Mo_2Br_6(OH_2)_2]^{2-}$. In general the far IR spectra of these di-aquo ions are seen to be more complicated than the simple pattern observed in Fig. 6.8, reflecting their lower symmetry. Furthermore, no band assignable to ν(Mo-O), reported to occur at ~ 380 cm^{-1} for the $(mpH)^+$ ion, has been observed in the region 600 - 100 cm^{-1}.

4. A different crystallographic unit of $Cs_4Mo_2Br_8$

The similarity of two series in the far IR spectrum would indicate structural similarity between the two species present in this compound; furthermore their RR spectra at low temperature are similar, save for the presence of fluorescence for species *a*. The similarity of all the recorded spectra to those of the analogous $Cs_4Mo_2Cl_8$ compound would also indicate that the two species contain the $[Mo_2Br_8]^{4-}$ ion, and it has already been seen that the NH_4^+ salt of this ion shows interesting temperature dependence in its RR spectrum [6.1].

It has previously been reported that two different crystallographic units occurred in $K_3Mo_2(SO_4)_4.3^1/_2H_2O$ (MM bond order 3.5) [6.15], one of which corresponds to discretely packed units, the other to molecules packed in infinite

chains. Furthermore, it has been seen that the two species have values of ν(Mo-Mo) differing by ~12 cm^{-1}[6.16], and that two distinct progressions are observed in a low temperature single-crystal ABS spectrum of the ($\delta^* \leftarrow \delta$) transition [6.17]. It may be possible that a similar situation exists here. Possibly the different species may incorporate water molecules in different ways, or have different packing arrangements in the lattice. The assignment of the second species to a slightly different unit of the $[Mo_2Br_8]^{4-}$ ion with some unexplained temperature-dependent behaviour associated with the $^1\delta\delta^*$ excited electronic state thus remains the most likely possibility, based on the available evidence.

6.8 Conclusions

It has not yet been possible to apply the SOS method to the $^1\delta\delta^*$ state of the $[Mo_2Br_8]^{4-}$ ion owing to the observation of two separate species in the sample of $Cs_4Mo_2Br_8$ prepared. The temperature dependent behaviour of the species *a* in the RR spectrum is, to the best of the knowledge of the author, unknown for any other quadruply bonded dimetallic compound of this type. It appears that this species is a dimolybdenum species, since the far IR, RR and mid-IR spectra are all similar to those recorded for $Cs_4Mo_2Cl_8$.

This very interesting, but as yet unexplained observation merits much further work. The synthesis and spectroscopic investigation of other salts of this ion would be very beneficial in determining whether the behaviour observed is unique to the Cs^+ salt. Furthermore, a RR spectrum recorded on a multichannel instrument, with variable temperature facility on the sample chamber, would allow better characterisation of the temperature dependence of the RR spectrum of the species *a*. Further XRD spectra of different salts of the ion may also be useful. However, with these experiments not yet possible, it is only possible to speculate that the observations may reflect two differing structural units of the $[Mo_2Br_8]^{4-}$ present simultaneously in the Cs^+ salt.

Appendix A1

The RR Experiment: Measurement of Band Intensity Ratios

A1.1 Experimental Arrangement

Both Innova I70 Ar^+ and Coherent I301 and CR3000K Kr^+ ion lasers were used as sources of monochromatic light for the excitation of Raman spectra. A range of lines in the visible region is available from these lasers. Typical power of the beam at the sample was 20 - 50 mW. Light from the lasers was brought to a focus on the sample by a series of lenses and mirrors; the scattered light from the sample was collected at 90° as shown in Fig. A1(a).

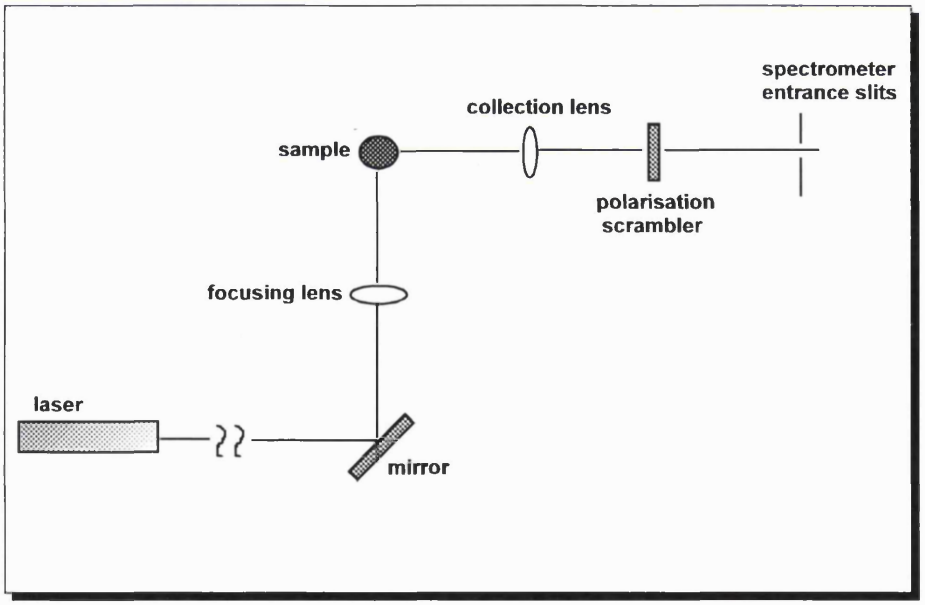

Fig. A1(a) Schematic diagram of the optical arrangement of the RR experiment

The 90° degree scattered light is focused on the entrance slits of the spectrometer using an achromatic collection lens. Before entering the spectrometer, the scattered light passed through a polarisation scrambler; this is

required because of the different response of the spectrometer gratings to light of different polarisations.

Solid powder samples were held on a copper block at the end of a cold finger in a cryostat as shown in Fig. A1(b). Indium wire was used to ensure good thermal contact between the copper block and the cold finger. For spectra recorded at 77 K, the sample chamber was evacuated and the cold finger filled with liquid nitrogen prior to the recording of the spectrum.

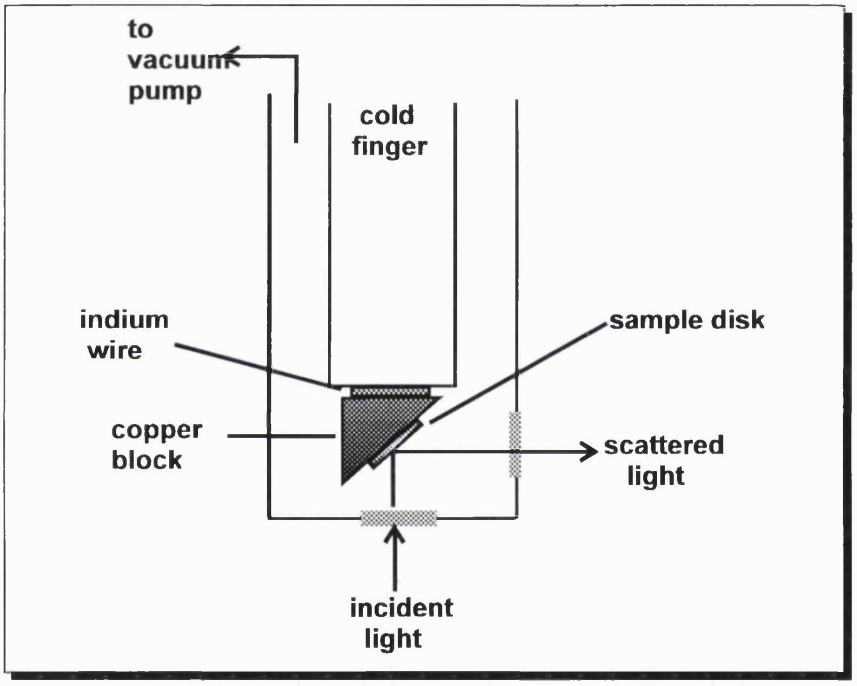

Fig. A1(b) Diagram of sample chamber for solid disk samples

Solution samples were held in a spinning cell, shown schematically in Fig. A1(c). This was employed to prevent overheating of the sample.

The spectrometer used for recording the RR spectra was a Spex 1401 double monochromator with 1200 line gratings blazed at 20,000 cm^{-1} fixed on a Czerny-Turner mount. The photomultiplier used as a detector was an RCA C31034A tube, from which the signal was fed via amplifiers to a 80286 PC computer. A data collection program written by Dr. S. Best was used to record the data in binary files.

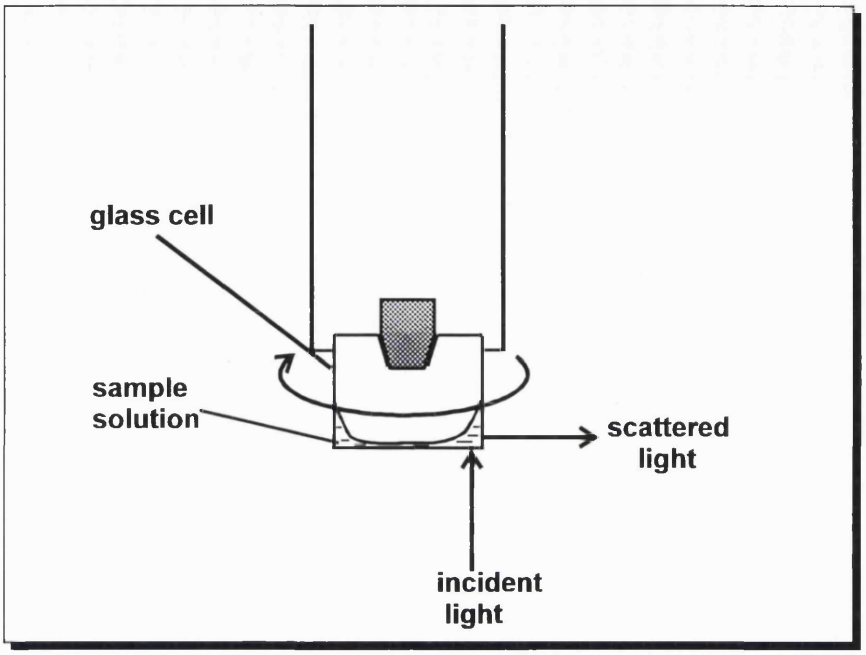

Fig. A1(c) Diagram of sample chamber for solution samples.

A1.2 Sample Preparation

Solid State Spectra

Samples of the compounds were ground finely and mixed with the appropriate dry alkali halide. The mixture was ground finely again and pressed into a 6 mm disk. At all times the sample was kept as dry as possible and grinding was prolonged to maximise the homogeneity of the resulting disk. Very thin disks were prepared in order to ensure good thermal conduction and also to minimise the path length of the light through the sample (hence lowering self-absorption (see section A1.4)). For low temperature spectra, samples were mounted on the copper block attached to the cold finger of the cryostat. The sample chamber was evacuated and the cold finger was filled with liquid nitrogen. This was then allowed to stabilise, and then refilled immediately prior to optimisation of the collection optics ('peaking up') and collection of the spectra. In this way, any loss of focus due to the boil off of the liquid nitrogen could be minimised.

Solution Spectra

Solutions of samples were freshly prepared and transferred to the glass cell for fitting into the rotating column of the spinning cell apparatus (Fig. A1(c)). All solvents were freshly distilled.

A1.3 Measurement of Band Intensities and Positions

Positions of bands in the RR spectra were referenced to the position of the laser line. Where a laser plasma line also fell within the region of the spectrum, the calibration was also checked against its position. Calibration using the standard emission lines from a Ne lamp source or the positions of solvent bands in solution spectra were also used.

The intensity of a band in a spectrum was measured as the integrated area under the peak, using cubic baseline modelling. The program used to perform this analysis was written by Dr. L. Allers of King's College London. The intensity of the fundamental band, $I(\nu)$, of the chosen progression in the mode of frequency ν, (or wavenumber, $\tilde{\nu}$) was used as an internal intensity reference in each case. The following treatment is given in terms of frequency (ν): in practice, band positions are usually measured in wavenumbers ($\tilde{\nu}$). However, the exact same treatment is applicable in this case. The relative intensities of successive members of the mode progression were then measured ($\frac{I(2\nu)}{I(\nu)}$, $\frac{I(3\nu)}{I(\nu)}$ etc.) for subsequent use in the SOS and OT calculations. For each compound, at a given excitation frequency, several spectra were recorded (usually 6) and the intensity ratios were averaged. A standard deviation of less than 10 % was normally achieved.

A1.4 Corrections to the Experimentally Measured Intensity Ratios

In order for the experimentally determined intensity ratios (A1.3) to be used in the OT or SOS calculations, they must first be corrected for a number of

frequency-dependent factors. The theoretical intensity ratios (derived in chapter 2) depend only on the ratios of the frequency-dependent molecular scattering parameters, $I'(\nu)$. In general, however, the *observed* intensity of a recorded band in a Raman experiment, $I(\nu)$ is given by [A.1]:

$$I(\nu) = P_0\, C\, \nu^4\, S(\nu)\, A(\nu)\, I'(\nu) \qquad \text{....A1(1)}$$

where: P_0 is the power of the incident radiation at the sample

C is the concentration of scatterers

$S(\nu)$ is the overall spectral response of the spectrometer

$A(\nu)$ is the self-absorption of the scatterer at frequency ν

$I'(\nu)$ is molecular scattering parameter

Hence, the observed intensity ratio $\frac{I(n\nu)}{I(\nu)}$ is given by:

$$\frac{I(n\nu)}{I(\nu)} = \frac{P_0\, C\, (n\nu)^4\, S(n\nu)\, A(n\nu)\, I'(n\nu)}{P_0 C\, \nu^4\, S(\nu)\, A(\nu)\, I'(\nu)} \qquad \text{....A1(2)}$$

For the spectra recorded here, the power of the laser is assumed to be constant throughout a single spectrum (frequent checks on the power output of the laser were made). The concentration, C, of scatterers was also assumed to be constant. Hence the desired intensity ratio is given by:

$$\frac{I'(n\nu)}{I'(\nu)} = \frac{I(n\nu)}{I(\nu)} \times \frac{\nu^4}{(n\nu)^4} \times \frac{S(\nu)}{S(n\nu)} \times \frac{A(\nu)}{A(n\nu)} \qquad \text{....A1(3)}$$

The correction for ν^4 is facile and is performed only for OT calculations, since this factor is included in the SOS treatment.

Self-Absorption [$A(\nu)$]:

The absorption of the scattered light by the sample itself can arise when spectra are recorded on resonance, since the frequency of the scattered light lies within an electronic ABS band. Iganiki et al [A.2] have shown that a suitable correction for $A(\nu)$ involves:

$$\frac{A(\nu)}{A(\nu')} \approx \frac{\varepsilon(\nu')}{\varepsilon(\nu)} \times \frac{1-\exp(-\varepsilon(\nu)C\,l)}{1-\exp(-\varepsilon(\nu')C\,l)} \qquad \text{....A1(4)}$$

where C is the concentration, $\varepsilon(\nu)$ the molar extinction coefficient at the frequency ν and l is the path length of the light through the sample.

Obviously, for spectra recorded in the solid-state, no estimation of the local concentration in the solid is available. Furthermore, an estimation of the path length is difficult, but this can be minimised by achieving a tight focus of the laser beam on the sample. Self-absorption is further minimised by making the disks as thin as possible (thus reducing l) and diluting the concentration of the sample with the appropriate alkali halide. No other formal correction for self-absorption is possible.

For spectra recorded in solution, the above correction was again difficult to compute, since the path length of the light through the sample in the spinning cell was not known. Again, low concentrations were used and the path length was minimised in order to reduce the effect of this absorption. It is then possible, in solution, to check if these minimisation procedures have been sufficient to prevent significant self-absorption by looking at the relative intensities of solvent bands and comparing with those seen in a spectrum of pure solvent (recorded at the same excitation frequency). Obviously, in a RR spectrum, the scattered light giving rise to solvent bands is also of an absolute frequency which lies within the contour of an electronic ABS band of the sample (solute), and so will be subject to self-absorption. However, in a spectrum of pure solvent, no absorption occurs. Thus, for the solution spectra recorded in this work, the concentration of sample was kept sufficiently low so as to ensure that the ratios of solvent bands in the RR spectrum were the same as in the equivalent spectrum of pure solvent, to within 5%.

Spectral Response [$S(\nu)$]

The efficiency of the diffraction grating in the monochromator and the response of the PM tube are in general not independent of the frequency of the light incident upon them. Thus, the system used to record spectra has also an intrinsic spectral variation.

The usual procedure used to correct for this non-constant 'instrumental' response is to record a spectrum of the emission of a standardised tungsten lamp. The emissivity of such a lamp, when operating at a known temperature, current and voltage, is well-documented. Division of the recorded tungsten emission spectrum by its known emission curve produces an instrumental spectral response function, $S(\nu)$, which is then normalised. In subsequent Raman spectra, the recorded spectrum is actually the product of a 'real' spectrum and $S(\nu)$. Thus, the measured ratios of band intensities at frequencies ν and ν' $(\frac{I(\nu)}{I(\nu')})$ must be multiplied by the ratio $\frac{S(\nu')}{S(\nu)}$, in order to obtain the 'real' intensity ratios.

The spectral response of the spectrometer was measured as outlined above. A program was written in BASIC to calculate $S(\nu)$ for all ν values within the range of the spectral response curve. Thus, for all the measured intensity ratios, the fraction $\frac{S(\nu')}{S(\nu)}$ could be easily found.

A1.5 Effect of the Slit Width on Raman Band Intensities

In an ideal experiment arrangement, the scattered light would be brought to a focus on infinitely narrow entrance slits on the spectrometer. The optical arrangement within the spectrometer then reflects that of a perfectly parallel beam incident on the diffraction grating, such that the diffracted light is brought to a focus again on the exit slits. In this situation, for a given (monochromatic) wavelength of light, only one particular angular setting of the grating will allow the light to leave the exit slits, resulting in a delta function at the wavelength in the recorded spectrum.

However, in practice, the slits must have a finite width in order to allow sufficient light to pass through. If it assumed that the image focused on the exit slits is still infinitely narrow, then it can be seen that there exists an angular range, $\delta\theta$, of settings of the grating which will allow diffracted light to pass through and onto the exit slits. This results in a box function in the resulting recorded spectrum, as shown in Fig. A1(d).

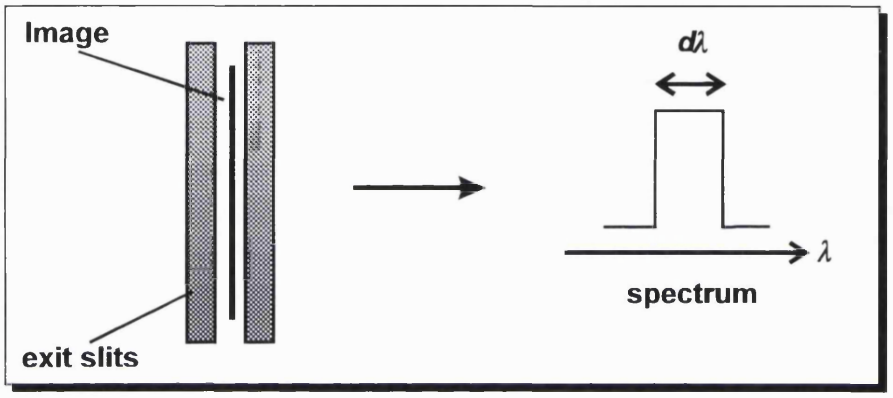

Fig. A1(d) The effect on the spectrum of having an infinitely narrow entrance slit width and a finite exit slit width

It can be shown that the width of this box function depends directly on the exit slit width, w, the angular range, $\delta\theta$, and inversely on the path length, L, of the spectrometer:

$$d\lambda \propto \frac{w\,\delta\theta}{L} \qquad \text{.....A1(5)}$$

In all the spectra recorded in this work, however, the entrance and exit slits were set to the same width. In this case, the image produced on the exit slits is the same width as the slits and results in a triangular function in the recorded spectrum as shown in Fig. A1(e).

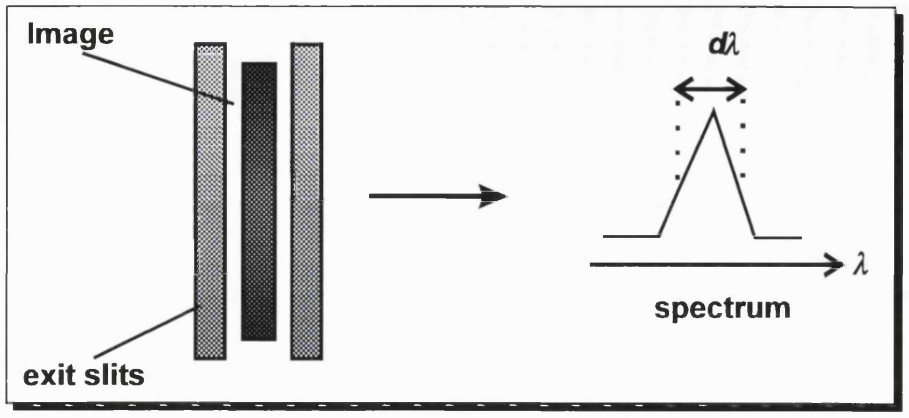

Fig. A1(e) The effect on the spectrum of having finite (equal) entrance and exit slit widths

Thus, the effect of non-zero slit widths on the spectrum of monochromatic light is to broaden the resulting signal to a triangular function, hence altering its apparent intensity. Obviously, the scattered light corresponding to a band in a Raman spectrum is not perfectly monochromatic, as it is broadened by lifetime effects, Doppler broadening, inhomogeneous and thermal broadening. However, the band can be thought of as a series of monochromatic lines. The effect of the slit widths on such a distribution can be seen as the convolution of the triangular function with the band, such that, at each wavelength, a triangular function is produced. In total, the band is broadened and has a triangular shape.

However, in order for this slit width to broaden the Raman band significantly, the width of the triangular function, $d\lambda$, must be comparable to the width of the Raman band. For this reason, the slits were kept as narrow as possible (subject to sufficient throughput of light). In all spectra, bandshapes were checked to ensure that no triangular peaks were seen. It was then assumed that the slit width had not significantly broadened the band and therefore that its intensity was unaffected.

In this work, Raman Excitation Profiles (REP) have been avoided as the source of intensity data. For REP measurements, an internal standard, e.g. potassium sulphate, is included in the sample disk. The ratio of the intensity of the fundamental band of the molecule to that of the designated band of the standard is then measured and corrected as normal. This process is then repeated using different excitation frequencies throughout the contour of the resonant ABS band. However, between measurements at different excitation frequencies, the sample must be removed from the path of the beam and replaced. For solid compounds it is difficult to ensure that the same spot on the inhomogeneous disk is again at the focus of the beam. Furthermore, the long time required to perform such an experiment compared with the method of taking ratios of intensities of successive harmonics of a given mode, means that sample degradation can often take place. Ensuring that all other factors save those shown in equation A1(1) are constant between spectra recorded at different excitation frequencies is very difficult. For this reason, where a sufficient number of overtones of a progression are observed, the method of taking ratios of their relative intensities is greatly preferred.

Appendix A2

The Absorption Experiment

A2.1 The Experimental Arrangement

All the absorption spectra used in this work were calculated from the measured *transmission* spectra. In general, for a beam of light of intensity I and wavelength λ, incident upon an absorbing material, the change in intensity, dI, on passing through a thickness dl is given by:

$$dI(\lambda) = - A(\lambda)\, I\, dl \qquad \text{....A2(1)}$$

where $A(\lambda)$ is defined as the absorption coefficient. This represents the absorption of a material and is usually wavelength dependent. Integration of equation A2(1) yields:

$$I(l, \lambda) = B \exp(-A(\lambda)\, l) \qquad \text{....A2(2)}$$

where B is a constant. Clearly, at $l = 0$, $I(l, \lambda) = I(0, \lambda)$ and hence:

$$I(l, \lambda) = I(0, \lambda) \exp(-A(\lambda)\, l) \qquad \text{....A2(3)}$$

Experimentally, the transmission spectrum, $I(l, \lambda)$ is recorded and divided by the spectrum $I(0, \lambda)$ of the unimpeded light (i.e. a 'background' spectrum with no sample in the path of the beam).

Thus

$$\frac{I(l,\lambda)}{I(0,\lambda)} = \exp(-A(\lambda)l) \qquad \text{....A2(4)}$$

and

$$\ln\left[\frac{I(l,\lambda)}{I(0,\lambda)}\right] = -A(\lambda)l \qquad \text{....A2(5)}$$

Thus, from this, a spectrum of the absorption $A(\lambda)$ of the material as a function of wavelength of the incident light can be obtained.

In general, the absorption coefficient $A(\lambda) = \varepsilon(\lambda)C$ where $\varepsilon(\lambda)$ is the molar extinction coefficient and C is the concentration of the absorbing species. All the absorption spectra used in this work were computed in this way and were normalised to unit area. It should be noted that the scale on the 'absorption' axis is therefore taken to be arbitrary. This is especially important for solid-state spectra, where the deduction of the scattering background means that the final scale on the absorption coefficeint axis is not related to that used for measurement, but reflects instead the normalised intensity. Thus the axis label is simply 'absorption' in each case.

Solid State Spectra

Transparent pressed alkali halide disks of the compounds were mounted onto the end of a cold finger in a glass cryostat with quartz windows. For spectra at 77 K, the cryostat chamber was evacuated and the cold finger filled with liquid nitrogen immediately prior to recording of the spectrum.

Transmission spectra were measured on a Spex 1702 monochromator at King's College London. The light source used was a tungsten strip lamp with an optical fibre feedback loop to keep the light level constant.

Absorption spectra were then computed as described above, and subsequently normalised.

Solution Spectra

Dilute solutions of compounds were prepared and placed in a quartz cuvette. The background spectrum ($I(0, \lambda)$) was run through a cuvette filled with solvent only. All the spectra were recorded on an AVIV 17 spectrometer and the absorption spectra computed as above and finally normalised.

A2.2 Sample Preparation

Solid State Spectra

Sample compounds were held in pressed alkali halide disks. The careful preparation of these disks was found to be crucial in the determining the quality of the final spectrum. The appropriate alkali halide was first ground very finely and then dried under vacuum overnight. The compound was ground under a stream of dry N_2 gas and then the two powders mixed in the appropriate concentration so as to give a transparent disk. The mixture was ground again under N_2 and a 6 mm disk pressed and stored in a dessicator before use. In every case, the minimum delay between disk preparation and spectrum recording was sought so as to minimise the chance any water adsorbing onto the surface of the disk. The particle size in the disk was required to be sufficiently small to ensure good homogeneity and also to try to minimise surface scattering (see Appendix A3).

Solution Spectra

All solvents were freshly distilled and the solutions were prepared immediately prior to recording of the spectra.

A2.3 Data Manipulation

All absorption spectra, calculated as detailed in section A2.1, were found in units of wavelength. In order to use the ABS spectra in both the OT and SOS calculations, conversion to units of cm^{-1} were required.

A simple program was written to perform this conversion. Following this calculation, the spectra had then to be converted to evenly spaced data points by a linear interpolation program. Finally, a normalising and scaling program allowed a variable number of evenly spaced data points to be obtained and the spectra to be normalised with respect to the area under the ABS band.

For the SOS calculation, there is no limit on the number of data points used in the calculation and so a number around 2,000 was used. For the OT method, the program used [A.3] dictated that the maximum number of data points in the ABS spectrum was between 500 and 600.

For spectra recorded in pressed powder discs, the background is not independent of wavelength, and the baseline is seen to rise towards the blue end of the spectrum. Contributions to this baseline arise from reflection and scattering of light both at the surface and within the disk. These problems are treated in more detail in Appendix A3.

Appendix A3

Baseline Effects in Powder Absorption Spectra

A3.1 General

The baseline observed in the ABS spectrum (calculated from the transmission spectrum) of a pressed powder disk sample is never flat, unlike those observed in spectra of solutions or glasses. The background is seen to rise towards the blue end of the spectrum, and this indicates that there is increasing deviation of the light away from the direction of normal transmission (and hence away from the detector) as the frequency of the light increases. This apparent decrease in transmission results in a *rise* in the baseline of the computed ABS spectrum towards higher frequencies.

It is likely that, for the pressed powder samples, several factors contribute to this baseline effect in a complex way. While each individual contribution may be modelled, their total effect cannot be treated numerically. Contribution to the baseline could arise from the following processes:

- Reflection of light at the surface of the disk
- Scattering of light by the molecules in the sample
- Scattering of light at the interface between compound and alkali halide in the disk
- Fluorescence

Reflectance

Reflection of the incident light at the surface of the disk will reduce the transmission through the disk and lead to an apparent increase in absorption. If this reflectance is independent of frequency, then this should have the effect of a simple upwards shift in the level of the baseline in the resulting ABS spectrum.

The reflection is made up from a specular and a diffuse part, the latter showing some frequency dependence. The relative amounts of these two kinds of reflection is dependent on the particle size at the surface of the disk.

This contribution is complex in its frequency dependence. However, it might be expected that, since scattering of light is involved, a ν^4 dependence on the frequency, ν, may be observed. Since this kind of reflection would not occur to the same level in a solution or a glass sample, it may indicate that it is indeed a contributor to the observed rising baseline in a solid state (powder) spectrum.

Molecular Scattering

Light transmitted into the disk may be scattered by the molecules in the powder. If this scattering is elastic, it may be expected to show the usual ν^4 dependence on the frequency (ν) of the light. However, with concentrations of sample very low and the power of the incident light weak in an ABS experiment (compared with that used in a scattering experiment (e.g. Raman)), this factor is also not expected to affect markedly the baseline of the ABS spectrum. Further evidence this effect being weak is that it will be equally present in ABS spectra recorded in solution and glass media, where no such baseline effects are seen.

Interface Scattering

In a pressed powder disk, it is inevitable that small particles or clumps of compound and alkali halide are present beneath the surface of the disk. Despite thorough mixing and grinding of the two powders together, the final disk will have a certain amount of inhomogeneity, resulting in interfaces being present between 'clumps' of alkali halide and of sample. These interfaces, between materials of different refractive indices, may act as strong sources of scattering within the disk, as shown in Fig. A3(a).

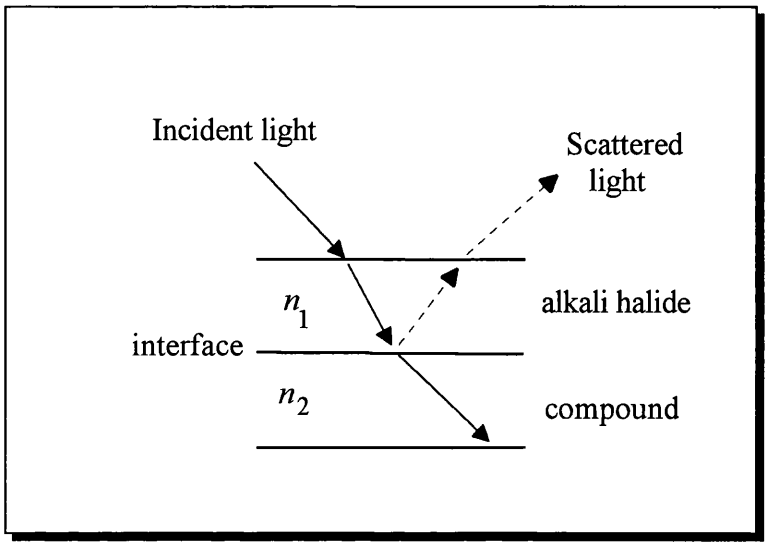

Fig. A3(a) : Interface scattering of light at the alkali halide/compound boundary. *n* denotes the refractive index of the medium

No such interfaces are present in solution, nor in a glass medium since the molecules of the compound are evenly dispersed through the molecules of the solvent. In these cases, any scattering from the within the sample arises purely from molecular scattering and is therefore weak. This may indicate that interface scattering is a major source of the observed baseline effects in powder ABS spectra.

Fluorescence

All of the compounds studied here fluoresce to some extent when irradiated within the contour of the ABS band being recorded in the ABS spectra. It is therefore possible that some of this fluorescence (which will occur at the red end of the spectrum) may be detected during the ABS experiment. The effect of the detection of fluorescence would be to apparently increase transmission, thus decreasing the apparent ABS. However, since the overlap of the ABS and fluorescence occurs only at the red end of the ABS spectrum, this effect will not

account for the overall baseline observed. It may, however, add a complicating deviation at the low frequency end.

It seems likely therefore that scattering, either at the surface, or at interfaces within the disk, is the major source of the rising baseline in powder ABS spectra. To understand better the observed frequency dependence of this baseline, the frequency dependence of elastic scattering must first be considered.

A3.2 Frequency Dependence of Elastic Scattering

The elastic scattering, or irradiance, $I(\theta)$ at an angle θ from an oscillating dipole p (= qd) where d is the distance between the charges q, is given by [A.4]:

$$I(\theta) = \frac{p^2\omega^4\sin^2\theta}{32\pi^2c^3\varepsilon_0 r} \qquad \text{....A3(1)}$$

where ω is the angular frequency of the scattered light, ε_0 is the permittivity of a vacuum and r is the radial distance form the dipole.

Thus, immediately, the ω^4 (or ν^4) dependence of the scattered light is seen, and, if this were the only source of frequency dependence for the scattered light then a baseline rising towards the blue end of the spectrum in accordance with this law would be expected.

However, the initial polarisation or induced dipole p is also frequency dependent. For a non-polar molecule, p represents the induced dipole in the molecule when placed in the electric field of the incident light. This is proportional to the molecular, $\alpha(\omega)$, as described in chapter 1.

From the optical theorem, it is seen that the absorption cross-section is proportional to the *imaginary* part of $\alpha(\omega)$. Thus the elastic scattering cross-section must be proportional to the *real* part of $\alpha(\omega)$, the frequency dependence of which is governed by the denominator $\frac{1}{\omega_0 - \omega - i\Gamma}$, where ω_0 is an electronic transition frequency and Γ is a damping factor. As ω approaches ω_0, the real part of $\alpha(\omega)$ follows the same pattern as the real part of $\Phi(\omega)$ (the complex polarizability) and is shown in Fig. A3(b) and detailed in chapter 5.

This anomalous behaviour of $\alpha(\omega)$ in the region of an electronic transition is the origin of the observed anomalous dispersion of the refractive index of a material (n).

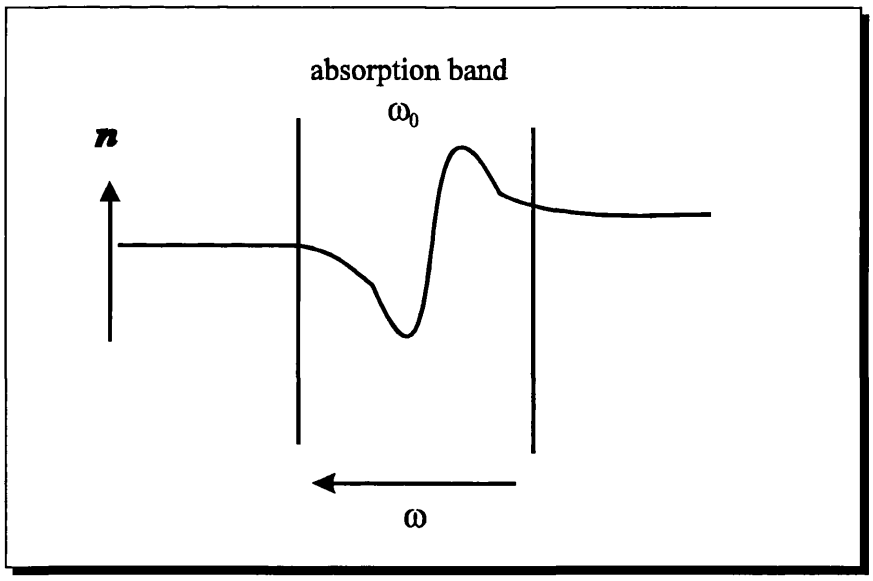

Fig. A3(b) Anomalous dispersion of the refractive index of a medium in the region of an ABS band

For alkali halides, the electronic transition frequencies lie far in the UV region of the spectrum and so no such anomalous scattering behaviour from these compounds is expected. However, for the coloured compounds studied here, it may be expected that some anomalous pattern of background scattering may be observed in the region of an electronic absorption band. These factors, together

with contributions from reflection and possibly fluorescence, serve to produce a complex rising background in the powder ABS spectrum, with often the baseline extrapolated on one side of the band not matching that extrapolated on the other. An example of this is shown in section A3.3.

A3.3 $Mo_2Cl_4(PMe_3)_4$: An Example

An example of the importance of the baseline in such ABS spectra is given by the compound $Mo_2Cl_4(PMe_3)_4$. A structured ABS band is observed in the UV/Vis spectrum, centred around 17,000 cm^{-1}. The spectrum recorded at 77 K in the form of a pressed KCl disk shows the usual discontinuity of extrapolated baselines on the red and blue ends of the band. However, the recorded ABS spectrum of the glass at 77 K has a flat baseline. These two spectra are shown in Fig. A3(c) (the latter spectrum was scanned and digitised form ref [A.5]).

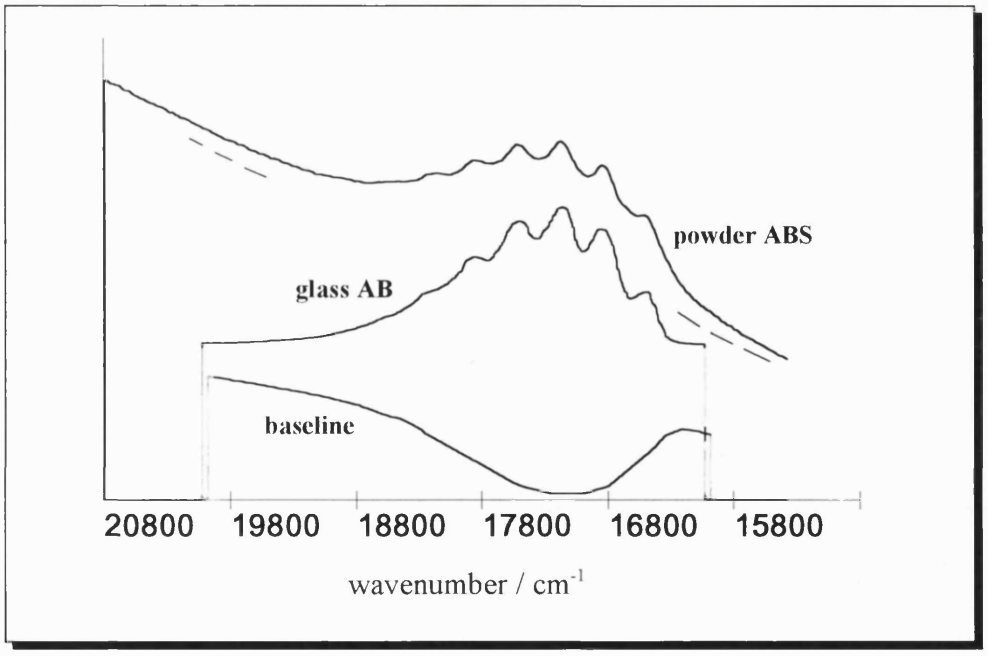

Fig. A3(c) Powder and Glass ABS spectra of $Mo_2Cl_4(PMe_3)_4$ at 77 K

If the two ABS bands are matched to approximately the same integrated area and their difference taken, the effective baseline for the pressed powder spectrum may

be seen. This baseline, also shown in Fig. A3(c), is that which would have been required to be deducted from the original powder ABS spectrum in order for consistency with the vibronic band intensity pattern observed in the glass spectrum to be achieved.

It can be seen from Fig. A3(c) that there is an obvious deviation of this baseline away from a $\tilde{\nu}^4$ dependence, and, at the red end of the band, an effect similar to that seen in Fig. A3(b).

Thus, great care must be taken when subtracting background baselines from powder ABS spectra. For the cases where vibronic structure is minimal, the removal of a general baseline may be sufficient to produce a final ABS reasonably close to the actual ABS band. In many cases, comparison with the appropriate glass spectrum is not available as the compound may degrade in solution. In these cases, the optimum baseline, based on the contributions above and the extrapolated baselines on either side of the ABS band, may have to suffice.

Where there is sharp vibronic structure, however, the exact nature of the baseline deducted may alter the relative intensity ratios of the vibronic pattern. Where possible, glass ABS spectra should then be used. If this is not available, the procedure described above for the case of no vibronic structure is followed. It should be noted, however, that this part of the collection and manipulation of experimental data remains open to a relatively unknown error.

Appendix A4

Data manipulation and Handling Programs

A4.1 Experimental Data

RR data

RR band intensity ratios measured from the recorded spectra were corrected for a number of frequency-dependent factors, as detailed in Appendix A1. The correction required for the normalised spectral response of the instrument is multiplication by the ratio $\frac{S(\nu)}{S(\nu')}$, where $S(\nu)$ is the value of the instrumental response function at the frequency ν. This value is calculated from the recorded spectrum of a standardised tungsten lamp.

In order to compute these correction ratios, a program was written in BASIC to interpolate between the known points of the $S(\nu)$ curve. Since the number of points in the original curve is quite large, a simple linear interpolation was taken to be adequate.

ABS data

ABS spectra were first computed from transmission spectra, recorded in units of wavelength (nm), as detailed in Appendix A2. A simple BASIC program was written to convert the data to a series of unevenly spaced points in units of cm^{-1}. Linear interpolation was then used again to scale this data to the appropriate number of evenly spaced points, ready for use in either the OT or SOS calculations.

A4.2 Generation of Lorentzian Curves for Testing the OT Method

In chapter 5, a number of tests of the OT method were performed using idealised Lorentzian curves as the basis of the calculation. These curves were generated in a simple BASIC program using the formula:

$$y(x) = \frac{a}{(x-E)^2 + b^2} \qquad \text{....A4(1)}$$

where a is an intensity factor, E is the centre of the band and b is a damping or width factor.

These parameters were varied according to the desired characteristics of the Lorentzian and in this way, identical curves with different tail lengths (x ranges) or different step sizes (different number of points for the same x range) could be obtained. A typical curve employed values of a = 250,000, E = 17,500 and b = 500.

A4.3 Scanning and Digitising of Published Spectra

In chapter 4, digitised ABS spectra of $Mo_2X_4(PMe_3)_4$ compounds, recorded in the form of 2-methylpentane glasses, were used for SOS calculations. This was necessary because of the difficulties encountered in removing the baseline in the corresponding powder ABS spectra.

The published glass spectra were scanned and each saved as a Windows bitmap. A program was written in Visual Basic for Windows to enable conversion of these bitmaps to a series of x-y data points.

The procedure followed was first to note carefully the start and end points of the spectrum in the appropriate units (e.g. cm^{-1}). These are assigned x_S ans x_F respectively. The spectra were horizontally aligned and all the axes removed, leaving only the curve itself.

The program operated on the following scheme. The start and end points of the spectrum were input, together with the required number of data points. Starting at the top left hand corner of the bitmap, the map was searched downwards, pixel by pixel, until a black pixel (denoting the beginning of the curve) was found. If no black pixel was found then a move one pixel to the right was made, and the search repeated (see Fig. A4(a)). On finding the first black pixel, its x-value is assigned to the start values x_S the spectrum, and its y value zero.

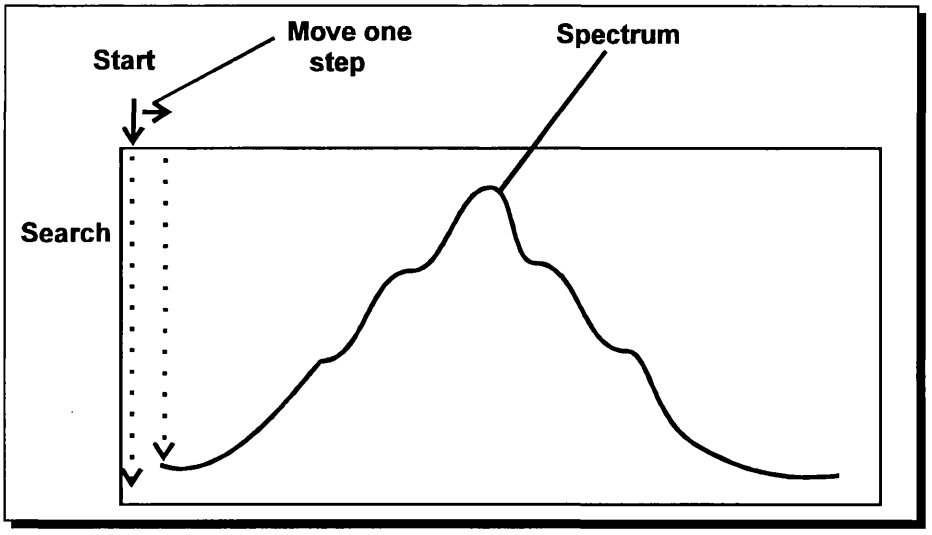

Fig. A4(a) Schematic diagram of the digitising routine for scanned bitmaps

The end point is found in a similar way, starting from the top right hand corner of the bitmap. Its x position is assigned x_F (that of the end of the spectrum), and its y value 0.

Once the start and end points have been located, the number of points is used to calculate a step size (in pixels) and also an actual step size (Δx) in, say, cm^{-1}. Starting at the top at end of the spectrum again, a move of one step size (in pixels) is made and a search downwards for a black pixel resumed. Once found, its x position can be calculated as being $x_S + \Delta x$, and its y value can be found relative to that at the start of the spectrum. The process is repeated until the end of the spectrum is reached. Finally, the spectrum is normalised.

Appendix A5

Calculation of the Complex Polarisability Φ(ω)

A5.1 General and Computational Method

In the OT method, the experimental absorption spectrum, ABS(ω), is read and the complex polarisability, Φ(ω), is calculated for subsequent use in the calculation. In order to test the effect of various aspects of the ABS data on the OT calculation, their effect on the function, Φ(ω) has been modelled.

From chapter 2 (eqn. (2.83)), Φ(ω) is defined as:

$$\Phi(\omega) = \frac{2}{\pi} P \int_0^\infty d\omega' \frac{ABS(\omega)}{\omega'^2 - \omega^2} + i\frac{ABS(\omega)}{\omega} \qquad \text{....A5(1)}$$

The exact routine for calculating Φ(ω) in the OT program used in chapter 5 [A.3] is, however, not known. For this reason, an alternative program was used, with a calculational procedure based on one published by Chan et al [A.6].

According to [A.6], Φ(ω) is defined as:

$$\Phi(\omega) = P \int_{-\infty}^{\infty} d\omega' \, I(\omega')(\omega' - \omega)^{-1} + i\pi I(\omega) \qquad \text{....A5(2)}$$

where $I(\omega)$ is the normalised lineshape function defined by

$$I(\omega) = \left[\int d\omega' \frac{ABS(\omega')}{\omega'} \right]^{-1} \frac{ABS(\omega)}{\omega} \qquad \text{....A5(3)}$$

The above definition is consistent with that in A5(1) if it is assumed that $\omega\omega' \approx \omega^2$ for the entire range, and that the ABS(ω) in A5(1) is normalised. Furthermore, the differing factor of π between A5(1) and A5(2) stems form alternative definitions of scattering cross-sections in two methods. Such differences between the two methods are not expected to affect the shape of the function $\Phi(\omega)$.

Thus, using the definitions in A5(2) and A5(3), the following procedure is carried out in order to calculate $\Phi(\omega)$ from a particular ABS(ω) curve.

i. The ABS curve is extrapolated to zero at either end of the spectrum, either by the addition of tangential straight line tails, or by simply adding zero points. This latter process will not affect the remainder of the calculation as only integrated areas are computed.
ii. At this stage, the 'experimental' data consists of an array of N frequencies $\{\omega_i\}$ and an array of N corresponding ABS values, $\{ABS_i\}$, with $ABS_1 = ABS_N = 0$.
iii. The normalised absorption lineshape function $I(\omega)$ is then computed at each of the ω_i according to equation A5(3). This produces an array $\{I_i\}$ of N $I(\omega)$ values, with $I_1 = I_N = 0$, and $I(\omega)$ taken to be linear between adjacent frequencies.
iv. According to A5(2), the imaginary part of $\Phi(\omega)$ ($Im[\Phi(\omega)]$), is simply $\pi I(\omega)$ and this is then computed for all the frequencies, ω_i.
v. The real part of $\Phi(\omega)$ ($Re[\Phi(\omega)]$) is then the Hilbert transform:

$$H(\omega) = P \int_{-\infty}^{\infty} d\omega' \, I(\omega')(\omega' - \omega)^{-1}$$

where P denoted the principal part. Since $I(\omega)$ has been approximated to a series of straight line segements, Chan et al have shown that the contibution of any segment is given by:

$$H_i = I_{i+1} - I_{i-1} + I_i \ln\left(\frac{\omega_{i+1} - \omega_i}{\omega_i - \omega_{i-1}}\right) + \sum_{j=1}^{i-2} h_{ij} + \sum_{j=i+1}^{N-1} h_{ij}$$

where $H_1 = I_2 + \sum_{j=2}^{N-1} h_{1j}$, $H_N = -I_{N-1} + \sum_{j=1}^{N-2} h_{Nj}$ and the h_{ij} are given by:

$$h_{ij} = I_{j+1} - I_j + \left[I_{j+1} + \left[\frac{\omega_i - \omega_{j+1}}{\omega_{j+1} - \omega_j}\right] \times (I_{j+1} - I_j)\right] \ln\left[\frac{\omega_{j+1} - \omega_i}{\omega_j - \omega_i}\right]$$

These H_i are calculated to give Re[Φ(ω)].

vi. With the arrays Im[Φ(ω)] and Re[Φ(ω)] obtained, the modulus |Φ(ω)| can be computed from:

$$|\Phi(\omega)|^2 = (\mathrm{Im}[\Phi(\omega)])^2 + (\mathrm{Re}[\Phi(\omega)])^2$$

A5.2 C++ Program to Calculate Φ(ω)

The format of the ABS data used as input for this program is ASCII *x-y* data points with the *y* value on the line below the corresponding *x* value. The end zero points are added automatically by the program. In the code listed below, x[i] denotes the $\{\omega_i\}$ values, y[i] the $\{ABS_i\}$values and Iv[i] the $\{I_i\}$ values.

```
#include <io.h>
#include <stdio.h>
#include <conio.h>
#include <math.h>
#include <fcntl.h>
#include <graphics.h>
#include <stdlib.h>
#include <dos.h>

void main (void) {

  int gdriver=DETECT,gmode,ymax,xmax,c;
  float x [800],y [800],iv [800],im[800];
  float hn [800], hi [800], hj [800],h1[800];
  float re[800],modfi [800],un;
  float ing,oneovering,hsum,hisum,h1sum,hnsum;
  char filename [12], inln [80],buffer[80];
  int n,i,j,k,p,u;
```

```
  FILE *infile;

  printf("Enter the Filename\n");
  gets(filename);
  infile= fopen(filename,"r");
  fgets(inln,80,infile);
  i=atoi(inln);
  u = i;
  for (n=1;n<=i;n++) {
    fgets(inln,80,infile);
    x[n]=atof(inln);
    fgets(inln,80,infile);
    y[n]=atof(inln);
  }

  fclose(infile);

  // Calculate the normalised lineshape function
  for (j=1;j<i;j++) {
    ing += ((x[j+1] - x[j])/2) * (y[j]/x[j]+y[j+1]/x[j+1]);
  }
  oneovering=1.0/ing;
  for (k=1;k<i;k++) {
    iv[k] = oneovering * (y[k]/x[k]);
    im[k] = 3.1415926*iv[k];
  }
  iv[1]=0;
  iv[i]=0;

  //Calculate the real part of the polarizability
  for (p=2;p<i;p++) {
   hsum= 0;
   hisum= 0;
    printf ("%i \n",p);
    for (j=1;j<p-1;j++) {
      hi[j] = iv[j+1] - iv[j] + (iv[j+1] +
            ( (x[p] - x[j+1]) / (x[j+1] - x[j]) ) *
               (iv[j+1] - iv[j])) * log((x[j+1] -
x[p])/(x[j]-x[p]));
      hsum += hi[j];
    }
    for (j=p+1;j<i;j++) {
      hj[j] = iv[j+1] - iv[j] + (iv[j+1] +
            ( (x[p] - x[j+1]) / (x[j+1] - x[j]) ) *
               (iv[j+1] - iv[j])) * log((x[j+1] -
x[p])/(x[j]-x[p]));
      hisum += hj[j];
    }
    re[p] = iv[p+1] - iv[p-1] +
          (iv[p] * log((x[p+1] - x[p])/(x[p] - x[p-1]))) + hsum +
hisum;
  }

  for (j=2;j<i;j++) {
    h1[j] = iv[j+1] - iv[j] + (iv[j+1] +
            ( (x[1] - x[j+1]) / (x[j+1] - x[j]) ) *
            (iv[j+1] - iv[j])) * log((x[j+1] - x[1])/(x[j]-x[1]));
```

```
    h1sum += h1[j];
  }
  re[1] = iv[2] + h1sum;

  for (j=1;j<i-1;j++) {
    hn[j] = iv[j+1] - iv[j] + (iv[j+1] +
            ( (x[i] - x[j+1]) / (x[j+1] - x[j]) ) *
            (iv[j+1] - iv[j])) * log((x[j+1] - x[i])/(x[j]-x[i]));
    hnsum += hn[j];
  }
  re[i] = -iv[i-1] + hnsum;

  //calculate the array of moduli of polarisability
  for (p=1;p<=u;p++) {
    modfi[p] = sqrt((im[p]*im[p]) + (re[p]*re[p]));
  }

  printf ("\n Save imaginary part File? (y/n):");
  p=getche();
  if (p=='y' | p=='Y') {
     printf("\n Enter the  imaginary part Output Filename:");
     scanf ("%s",&filename);
     infile= fopen(filename,"w");
       for (n=1;n<=i;n++) {
       fprintf(infile," %f %f \n",x[n],im[n]);
       }

     }
  fclose(infile);

  printf ("\n Save real part File? (y/n):");
  p=getche();
  if (p=='y' | p=='Y') {
     printf("\n Enter the  real part Output Filename:");
     scanf ("%s",&filename);
     infile= fopen(filename,"w");
     for (n=1;n<=i;n++) {
       fprintf(infile," %f %f \n",x[n],re[n]);
     }
  }
  fclose(infile);

  printf ("\n Save polarisability modulus File? (y/n):");
  p=getche();
  if (p=='y' | p=='Y') {
     printf("\n Enter the polarisability modulus Output
Filename:");
     scanf ("%s",&filename);
     infile= fopen(filename,"w");
       for (n=1;n<=i;n++) {
       fprintf(infile," %f %f \n",x[n],modfi[n]);
       }
  }
  fclose(infile);
}
```

References

Chapter 1

1.1 G. H. Atkinson in *Advances in Infrared and Raman Spectroscopy*, ed. R.J. H. Clark and R. E. Hester, Heyden, London, 1982, **9**, 1.

1.2 J. R. Schoonover, R. F. Dallinger, P. M. Killough, A. P. Sattelberger and W. H. Woodruff, *Inorg. Chem.*, 1991, **30**, 1093.

1.3 G. Herzberg, *Spectra of Diatomic Molecules*, Van Nostrand, New York, 1950.

1.4 A. C. Albrecht, *J. Chem. Phys.*, 1961, **34**, 1476

1.5 J. Tang and A. C. Albrecht in *Raman Spectroscopy*, ed. H. Syzmanski, Plenum, New York, 1970, **2**, 33.

1.6 P. M. Champion and A. C. Albrecht, *J. Chem. Phys.*, 1980, **72**, 6498.

1.7 D. C. Blazej and W. L. Peticolas, *J. Chem. Phys.*, 1980, **72**, 3134.

1.8 S. Hassing and O. Sonnich Mortensen, *J. Chem. Phys.*, 1980, **73**, 1078.

1.9 V. I. Hizhnyakov and I. Tehver, *Phys. Stat. Sol.*, 1967, **21**, 755.

1.10 V. I. Hizhnyakov and I. Tehver, *J. Raman Spec.*, 1988, **19**, 383.

1.11 V. I. Hizhnyakov and I. Tehver, *J. Raman Spec.*, 1993, **24**, 653.

1.12 J. B. Page in *Light Scattering in Solids VI*, ed. G. Güntherodt and M. Cardona, Springer, Berlin, Heidelberg, New York, 1991, chp 2, 17.

1.13 J. B. Page and D. L. Tonks, *J. Chem. Phys.*, 1981, **75**, 5694.

1.14 E. J. Heller, *Acc. Chem. Res.*, 1981, **11**, 368.

1.15 D. J. Tannor and E. J. Heller, *J. Chem. Phys.*, 1982, **77**, 202.

1.16 S. -Y. Lee and E. J. Heller, *J. Chem. Phys.*, 1979, **71**, 477.

1.17 E. J. Heller, R. L. Sundberg and D. J. Tannor, *J. Phys. Chem.*, 1982, **86**, 1822.

1.18 A. Meyers, *PhD Thesis*, University of California, Berkeley, 1984.

1.19 C. D. Cowman and H. B. Gray, *J. Am. Chem. Soc.*, 1973, **95**, 8177.

1.20 J. R. Schoonover, R. F. Dallinger, P. M. Killough, A. P. Sattelberger and W. H. Woodruff, *Inorg. Chem.*, 1991, **30**, 1093.

1.21 M. D. Hopkins and H. B. Gray, *J. Am. Chem. Soc.*, 1984, **106**, 2468.

1.22 F. Duschinsky, *Acta. Physiochim. USSR.*, 1973, **1**, 551.

1.23 G. Herzberg and E. Teller, *Z. Phys. Chem.*, 1933, **B21**, 410.

1.24 A. Smekal, *Naturwissenschaften*, 1923, **11**, 873.

1.25 C. V. Raman and V. S. Krishnan, *Nature*, 1928, **121**, 501.

1.26 G. Landesberg and L. Mandelstam, *Naturwissenschaften*, 1928, **16**, 557.

1.27 G. Plazcek in *Rayleigh and Raman Scattering, Handbuch der Radiologie*, ed. E. Marx, Akademische Verlagsgesellschaft, Leipzig, 1934, **2**.

1.28 M. Wolkenstein and M. Eliashevich, *J. Phys. USSR.*, 1945, **9**, 326.

1.29 D. A. Long, *Raman Spectroscopy*, M^{c}Graw Hill, 1977.

1.30 P.P. Shorygin and L. L. Krushinkii, *Opt. Spectrosc.*, 1961, **11**, 12.

1.31 H. A. Kramers and W. Heisenberg, *Z. Phys.*, 1925, **31**, 681.

1.32 P. A. M. Dirac, *Proc. Royal Soc.*, London, 1927, **114**, 710.

1.33 *Advances in Infrared and Raman Spectroscopy*, ed. R. J. H. Clark and R. E. Hester, Heyden, London, Vols. 1 - 14.

1.34 R. J. H. Clark, *J. Chem. Phys. Soc. (UCL)*, 1976, **73**, 4.

1.35 S. P. Best, R. J. H. Clark, M. A. M. Daniels, C. A. Porter and R. Withnall, *Studies in Conservation*, 1995, **40**, 31.

1.36 D. L. Rosseau, J. M. Friedman and P. F. Williams, *Top. Curr. Phys.*, 1979, **11**, 203.

1.37 R. J. H. Clark, T. J. Dines and L. H. Ferris, *J. Chem. Soc., Dalton Trans.*, 1982, p. 2237.

1.38 R. J. H. Clark, T. J. Dines and G. P. Proud, *J. Chem. Soc., Dalton Trans.*, 1983, p. 2019.

1.39 R. J. H Clark and B. Stewart, in *Structure and Bonding*, ed. J. D. Dunitz et al., Springer: Berlin, Heidelberg, 1979, **36**, 2.

1.40 R. J. H. Clark and T. J. Dines, *Angewandte Chemie (Int. Ed. English)*, 1986, **25**, 131.

1.41 P. W. Atkins, *Molecular Quantum Mechanics*, 2nd Edition, Oxford University Press: Oxford, New York, 1983.

1.42 J. D. Jackson, *Classical Electrodynamics*, 2nd Edition, Wiley: New York, 1975.

1.43 C. Manneback, *Physica*, 1951, **XVII**, 1001.

1.44 R. J. H. Clark, T. J. Dines and M. Kurmoo, *Inorg. Chem.*, 1983, **22**, 2766.

1.45 R. J. H Clark and B. Stewart, *J. Am. Chem. Soc.*, 1981, **103**, 6593.

1.46 N. R. D'Urso, *PhD Thesis*, University of London, 1981.

1.47 M. J. Stead, *PhD Thesis*, University of London, 1983.

1.48 R. J. H. Clark and T. J. Dines, *Molecular Physics*, 1981, **42**, 193.

1.49 B. R. Stallard, P. M. Champion, P. R. Callis and A. C. Albrecht, *J. Chem. Phys.*, 1983, **78**, 712.

1.50 D. L. Tonks and J. B. Page, *J. Chem. Phys.*, 1982, **76**, 5820.

1.51 D. L. Tonks and J. B. Page, *Chem. Phys. Lett.*, 1979, **66**, 449.

1.52 C. K. Chan, *J. Chem. Phys.*, 1984, **81**, 1614.

1.53 D. L. Tonks and J. B. Page, *J. Chem. Phys.*, 1988, **88**, 738.

1.54 H. M. Lu and J. B. Page, *J. Chem. Phys.*, 1990, **92**, 7038.

1.55 C. K. Chan and J. B. Page, *J. Chem. Phys.*, 1983, **79**, 5234.

1.56 M. C. C. Ribeiro, W. J. Barreto, M. L. A. Temperini and P. S. Santos, *J. Phys. Chem.*, 1993, **97**, 12153.

1.57 J. R. Cable and A. C. Albrecht, *J. Chem. Phys.*, 1986, **84**, 1969.

1.58 J. R. Cable and A. C. Albrecht, *J. Chem. Phys.*, 1986, **84**, 4745.

1.59 F. A. Cotton, N. F. Curtis, C. B. Harris, B. F. G. Johnson, S. J. Lippard, J. T. Mague, W. R. Robinson and J. S. Wood, *Science*, 1964, **145**, 1305.

1.60 F. A. Cotton and S. J. Lippard, *J. Am. Chem. Soc.*, 1964, **86**, 4497.

1.61 A. S. Kotel'nikova and V. G. Troner, *Russ. J. Inorg. Chem.*, 1958, **3**, 268.

1.62 V. G. Kuznetzov and P. A. Koz'min, *J. Struct. Chem.*, 1963, **4**, 49.

1.63 F. A. Cotton and C. B. Harris, *Inorg. Chem.*, 1965, **4**, 330.

1.64 F. A. Cotton, N. F. Curtis, B. F. G. Johnson and W. R. Robinson, *Inorg. Chem.*, 1965, **4**, 326.

1.65 F. A. Cotton, *Inorg. Chem.*, 1965, **4**, 334.

1.66 F. A. Cotton, N. F. Curtis and W. R. Robinson, *Inorg. Chem.*, 1965, **4**, 1696.

1.67 F. A. Cotton, C. Oldham and W. R. Robinson, *Inorg. Chem.*, 1965, **5**, 1798.

1.68 J. V. Brencic and F. A. Cotton, *Inorg. Chem.*, 1969, **8**, 7.

1.69 J. E. Armstrong, D. A. Edwards, J. T. Mague and R. A. Walton, *Inorg. Chem.*, 1979, **18**, 1172.

1.70 J. D. Eakins, D. G. Humphries and C. E. Mellish, *J. Chem. Soc.*, 1963, p. 6012.

1.71 A. P. Mortola, J. W. Moskowitz, N. Rösch, C. D. Cowman and H. B. Gray, *Chem. Phys. Lett.*, 1975, **32**, 283.

1.72 F. A. Cotton, P. E. Fanwick, J. W. Fitch, H. D. Glicksman and R. A. Walton, *J. Am. Chem. Soc.*, 1979, **101**, 1752.

1.73 F. A. Cotton, *Chem. Soc. Rev.*, 1983, **12**, 35.

1.74 F. A. Cotton and R. A. Walton, *Multiple Bonds Between Metal Atoms*, 2nd Edition, Clarendon Press: Oxford, 1993.

1.75 F. A. Cotton, B. A. Frenz, B. R. Stults and T. R. Webb, *J. Am. Chem. Soc.*, 1976, **98**, 2768.

1.76 F. A. Cotton, L. M. Daniels and K. Vidysagar, *Polyhedron*, 1988, **7**, 1667.

1.77 F. A. Cotton, J. H. Matonic and D. de O. Silva, *Inorg. Chim. Acta.*, 1995, **234**, 115.

1.78 J. San Filippo, *Inorg. Chem.*, 1972, **11**, 3140.

1.79 L. R. Morris, R. J. Porcja, J. W. Nicoletti, J. San Filippo and H. B. Jenkins, *J. Am. Chem. Soc.*, 1980, **102**, 1923.

1.80 W. C. Trogler, C. D. Cowman, H. B. Gray and F. A. Cotton, *J. Am. Chem. Soc.*, 1977, **99**, 2993.

Chapter 2

2.1 A. C. Albrecht, *J. Chem. Phys.*, 1961, **34**, 1476.

2.2 J. Tang and A. C. Albrecht, in *Raman Spectroscopy*, ed. H. Syzmanski, Plenum: New York, 1970, **vol 2**, p. 33.

2.3 P. M. Champion and A. C. Albrecht, *J. Chem. Phys.*, 1980, **72**, 6498.

2.4 D. C. Blazej and W. Peticolas, *J. Chem. Phys.*, 1980, **72**, 3134.

2.5 V. I. Hizhnyakov and I. Tehver, *Phys. Stat. Solidi*, 1967, **21**, 755.

2.6 (a).V. I. Hizhnyakov and I. Tehver, *J. Raman Spec.*, 1988, **19**, 383
(b) V. I. Hizhnyakov and I. Tehver, *J. Raman Spec.*, 1993, **24**, 653.

2.7 A. C. Albrecht, R. J. H. Clark, D. Oprescu, S. J. R. Owens and C. Svendsen, *J. Chem. Phys.*, 1994, **101**, 1890.

2.8 J. B. Page in *Light Scattering in Solids VI*, ed. G. Güntherodt and M. Cardona, Springer, Berlin, Heidelberg, New York, 1991, chp 2, 17.

2.9 S. -Y. Lee and E. J. Heller, *J. Chem. Phys.*, 1979, **71**, 4777.

2.10 E. J. Heller, R. L. Sundberg and D. J. Tannor, *J. Phys. Chem.*, 1982, **86**, 1822.

2.11 E. J. Heller, *Acc. Chem. Res.*, 1981, **11**, 368.

2.12 J. D. Jackson, *Classical Electrodynamics*, 2nd Edition, Wiley: New York, 1975.

2.13 O. S. Mortensen and S. Hasssing in *Advances in Infrared and Raman Spectroscopy*, ed. R. J. H. Clark and R. E. Hester, 1980, **6**, 1.

2.14 C. Svendsen, *Private Communication*, Odense University, 1995.

2.15 D. J. Tannor and E. J. Heller, *J. Chem. Phys.*, 1982, **77**, 387.

2.16 C. Manneback, *Physica*, 1951, **XVII**, 1001.

2.17 R. J. H. Clark, T.J. Dines and M. Kurmoo, *Inorg. Chem.*, 1983, **22**, 2766.

2.18 D. L. Rosseau, J. M. Friedman and P. F. Williams, *Top. Curr. Phys.*, 1979, **11**, 203.

Chapter 3

3.1 F. A. Cotton, N. F. Curtis, C. B. Harris, B. F. G. Johnson, S. J. Lippard, J. T. Mague, W. R. Robinson and J. S. Wood, *Science*, 1964, **145**, 1305.

3.2 F. A. Cotton and C. B. Harris, *Inorg. Chem.*, 1965, **4**, 330.

3.3 J. G. Norman and H. J. Kolari, *J. Chem. Soc., Chem. Commun.*, 1974, **96**, 303.

3.4 J. G. Norman and H. J. Kolari, *J. Am. Chem. Soc.*, 1975, **97**, 33.

3.5 A. P. Mortola, J. W. Moskowitz, N. Rösch, *Int. J. Quantum Chem. Symp. No. 8,* 1974, 161.

3.6 A. P. Mortola, J. W. Moskowitz, N. Rösch, C. D. Cowman and H. B. Gray, *Chem. Phys. Lett.*, 1975, **32**, 283.

3.7 F. A. Cotton, L. M. Daniels and K. Vidysagar, *Polyhedron*, 1988, **7**, 1667.

3.8 J. V. Brencic and F. A. Cotton, *Inorg. Chem.*, 1969, **8**, 7.

3.9 W. K. Bratton, F. A. Cotton, M. Debeau and R. A. Walton, *Coord. Chem.*, 1971, **1**, 121.

3.10 J. San Filippo and H. J. Sniadoch, *Inorg. Chem.*, 1973, **12**, 2326.

3.11 R. J. H. Clark and M. L. Franks, *J. Am. Chem. Soc.*, 1976, **98**, 2763.

3.12 R. J. H. Clark and M. L. Franks, *J. Am. Chem. Soc.*, 1975, **97**, 2691.

3.13 F. A. Cotton, J. H. Matonic and D. de O. Silva, *Inorg. Chim. Acta.*, 1995, **234**, 115.

3.14 F. A. Cotton, N. F. Curtis, B. F. G. Johnson and W. R. Robinson, *Inorg. Chem.*, 1965, **4**, 326.

3.15 C. D. Cowman and H. B. Gray, *J. Am. Chem. Soc.*, 1973, **95**, 8177.

3.16 G. Peters and W. Preetz, *Z. Naturforsch.*, 1979, **1767**, 346.

3.17 W. Preetz and L. Rudzik, *Angewandte Chemie, Int. Ed. Engl.*, 1979, **18**, 150.

3.18 W. C. Trogler, D. K. Erwin, G. L. Geoffroy and H. B. Gray, *J. Am. Chem. Soc.*, 1978, **100**, 1160.

3.19 R. J. H. Clark in *Inorganic Chemistry towards the 21st Century*, A. C. S. Symposium Series, ed. M. Chisholm, Washington, 1983, **211**, 509.

3.20 R. J. H. Clark and M. J. Stead, *Inorg. Chem.*, 1983, **22**, 2124.

3.21 R. J. H. Clark and N. R. D'Urso, *J. Am. Chem. Soc.*, 1978, **100**, 3088.

3.22 H. W. Huang and D. S. Martin, *Inorg. Chem.*, 1985, **96**, 24.

3.23 P. E. Fanwick, D. S. Martin, F. A. Cotton and T. R. Webb, *Inorg. Chem*, 1977, **16**, 2103.

3.24 P. J. Hay, *J. Am. Chem. Soc.*, 1982, **104**, 7007.

3.25 W. C. Trogler, E. I. Solomon and H. B. Gray, *Inorg. Chem.*, 1977, **16**, 3031.

3.26 V. M. Miskowski, R. A. Goldbeck, D. S. Kliger and H. B. Gray, *Inorg. Chem.*, 1979, **19**, 86.

3.27 M. D. Hopkins and H. B. Gray, *J. Am Chem. Soc.*, 1984, **106**, 2468.

3.28 C. G. Morgante and W. S. Struve, *Chem. Phys. Lett.*, 1979, **63**, 344.

3.29 I. F. Fraser and R. D. Peacock, *Chem. Phys. Lett.*, 1987, **B7**, 583.

3.30 J. R. Winkler, D. G. Nocera and T. L. Netzel, *J. Am. Chem. Soc.*, 1986, **108**, 4451.

3.31 J. R. Schoonover, R. F. Dallinger, P. M. Killough, A. P. Sattelberger and W. H. Woodruff, *Inorg. Chem.*, 1991, **30**, 1093.

3.32 S. D. Conradson, A. P. Sattelberger and W. H. Woodruff, *J. Am.Chem. Soc.*, 1988, **101**, 1309.

3.33 P. E. Fanwick, S. M. Tetrick and R. A. Walton, *J. Am. Chem. Soc.*, 1985, **107**, 5009.

3.34 F. A. Cotton, B. G. DeBoer and M. Jeremic, *Inorg. Chem.*, 1970, **9**, 2143.

3.35 J. V. Brencic and F. A. Cotton, *Inorg. Chem.*, 1970, **9**, 346.

3.36 A. B. Brignole and F. A. Cotton, *Inorg. Synth.*, 1972, **13**, 81.

3.37 H. D. Glicksman and R. A. Walton, *Inorg. Chem.*, 1978, **17**, 3199.

3.38 W. Preetz, G. Peters and L. Rudzik, *Z. Naturforsch*, 1979, **34b**, 1240.

3.39 A. Meyers, *PhD Thesis*, University of California, Berkeley, 1984.

3.40 R. M. Tubino, E. Mulazzi and J. L. Birman, *J. Raman Spec.*, 1984,**15**, 141.

3.41 B. S. Hudson and L. D. Ziegler, *J. Chem. Phys*, 1983, **79**, 1197.

3.42 M. D. Hopkins, H. B. Gray and V. M. Miskowski, *Polyhedron*, 1987, **6**, 705.

3.43 M. D. Hopkins, W. P. Schaefer, M. J. Bronikowski, W. H. Woodruff, V. M. Miskowski, R. F. Dallinger and H. B. Gray, *J. Am. Chem. Soc.*, 1987, **109**, 408.

3.44 F. A. Cotton, B. A. Frenz, B. R. Stults and T. R. Webb, *J. Am. Chem. Soc.*, 1976, **98**, 2768.

3.45 F. A. Cotton, M. W. Extine, T. R. Felthouse, B. W. S. Kolthammer and D. G. Lay, *J. Am. Chem. Soc.*, 1981, **103**, 4040.

3.46 J. G. Norman and H. J. Kolari, *J. Chem. Soc. Chem. Commun.*, 1975, p. 649.

3.47 B. E. Bursten, F. A. Cotton, P. E. Fanwick and G. G. Stanley, *J. Am. Chem. Soc.*, 1983, **105**, 3082.

3.48 L. Noodleman and J. G. Norman, *J. Chem. Phys.*, 1979, **70**, 4903.

3.49 F. A. Cotton, J. L. Hubbard, D. L. Lichtenberger and I. Shim, *J. Am. Chem. Soc.* 1982, **104**, 679.

3.50 M. C. Milletti, *Polyhedron*, 1993, **12**, 401.

3.51 A. Sierraalta, *Chem. Phys. Lett.*, 1994, **227**, 557.

3.52 J. G. Norman, H. J. Kolari, H. B. Gray and W. C. Trogler, *Inorg. Chem.*, 1977, **16**, 87.

3.53 D. L. Lichtenberg and C. H. Blevins, *J. Am. Chem. Soc.*, 1984, **106**, 1636.

3.54 T. Ziegler, *J. Am. Chem. Soc.*, 1985, **107**, 4453.

3.55 V. K. Ceylan, C. Sourriseau and J. V. Brencic, *J. Raman Spec.*, 1985, **16**, 128.

Chapter 4

4.1 F. A. Cotton, M. W. Extine, T. R. Felthouse, B. W. S. Kolthammer and D. G. Lay, *J. Am. Chem. Soc.*, 1981, **103**, 4040.

4.2 M. D. Hopkins, W. P. Schaefer, M. J. Bronikowski, W. H. Woodruff, V. M. Miskowski, R. F. Dallinger and H. B. Gray, *J. Am. Chem. Soc.*, 1987, **109**, 408.

4.3 M. D. Hopkins, V. M. Miskowski, P. M. Killough, A. P. Sattelberger, W. H. Woodruff and H. B. Gray, *Inorg. Chem.*, 1992, **31**, 5368.

4.4 F. A. Cotton and C. B. Harris, *Inorg. Chem.*, 1965, **4**, 330.

4.5 F. A. Cotton, B. G. DeBoer and M. Jeremic, *Inorg. Chem.*, 1970, **9**, 2143.

4.6 F. A. Cotton, L. M. Daniels and K. Vidysagar, *Polyhedron*, 1988, **7**, 1667.

4.7 J. V. Brencic and F. A. Cotton, *Inorg. Chem.*, 1969, **8**, 7.

4.8 M. C. Milletti, *Polyhedron*, 1993, **12**, 401.

4.9 F. A. Cotton, J. L. Hubbard, D. L. Lichtenberger and I. Shim, *J. Am. Chem. Soc.* 1982, **104**, 679.

4.10 A. Sierraalta, *Chem. Phys. Lett.*, 1994, **227**, 557.

4.11 M. D. Hopkins, H. B. Gray and V. M. Miskowski, *Polyhedron*, 1987, **6**, 705.

4.12 M. D. Hopkins and H. B. Gray, *J. Am Chem. Soc.*, 1984, **106**, 2468.

4.13 V. M. Miskowski, R. A. Goldbeck, D. S. Kliger and H. B. Gray, *Inorg. Chem.*, 1979, **19**, 86.

4.14 J. R. Schoonover, R. F. Dallinger, P. M. Killough, A. P. Sattelberger and W. H. Woodruff, *Inorg. Chem.*, 1991, **30**, 1093.

4.15 W. K. Bratton, F. A. Cotton, M. Debeau and R. A. Walton, *Coord. Chem.*, 1971, **1**, 121.

4.16 E. M. Larson, T. M. Brown and R. B. Von Dreele, *Acta Cryst.*, 1986, **B42**, 533.

4.17 C. Svendsen, *Private Communication*, Odense University, 1995.

4.18 F. A. Cotton and R. A. Walton, *Multiple Bonds Between Metal Atoms*, 2nd Edition, Clarendon Press: Oxford, 1993.

4.19 W. C. Trogler, E. I. Solomon and H. B. Gray, *Inorg. Chem.*, 1977, **16**, 3031.

4.20 P. E. Fanwick, D. S. Martin, F. A. Cotton and T. R. Webb, *Inorg. Chem*, 1977, **16**, 2103.

4.21 W. C. Trogler, D. K. Erwin, G. L. Geoffroy and H. B. Gray, *J. Am. Chem. Soc.*, 1978, **100**, 1160.

4.22 J. G. Norman and H. J. Kolari, *J. Am. Chem. Soc.*, 1975, **97**, 33.

4.23 J. G. Norman and H. J. Kolari, *J. Chem. Soc., Chem. Commun.*, 1974, **96**, 303.

4.24 J. G. Norman and H. J. Kolari, *J. Chem. Soc. Chem. Commun.*, 1975, p. 649.

4.25 L. Noodleman and J. G. Norman, *J. Chem. Phys.*, 1979, **70**, 4903.

4.26 R. J. H. Clark and M. L. Franks, *J. Am. Chem. Soc.*, 1975, **97**, 2691.

4.27 S. D. Conradson, A. P. Sattelberger and W. H. Woodruff, *J. Am. Chem. Soc.*, 1988, **101**, 1309.

4.28 J. R. Winkler, D. G. Nocera and T. L. Netzel, *J. Am. Chem. Soc.*, 1986, **108**, 4451.

Chapter 5

5.1 A.C. Albrecht, R. J. H. Clark, D. Oprescu, S.J. R. Owens and C. Svendsen, *J. Chem. Phys*, 1994, **101**, 1890.

5.2 D. Oprescu, *PhD Thesis*, University of London, 1996.

5.3 C. D. Cowman and H. B. Gray, *J. Am. Chem. Soc.*, 1973, **95**, 8177.

5.4 P. E. Fanwick, D. S. Martin, F. A. Cotton and T. R. Webb, *Inorg. Chem*, 1977, **16**, 2103.

5.5 J. R. Schoonover, R. F. Dallinger, P. M. Killough, A. P. Sattelberger and W. H. Woodruff, *Inorg. Chem.*, 1991, **30**, 1093.

5.6 C. K. Chan and J. B. Page, *J. Chem. Phys.*, 1983, **79**, 5234.

Chapter 6

6.1 N. R. D'Urso, *PhD Thesis*, University of London, 1981.

6.2 A. P. Ketteringham and C. P. Oldham, *J. Chem. Soc, Dalton Trans.*, 1973, p. 1067.

6.3 J. V. Brencic, I. Leban and P. Segedin, *Z. Anorg. Allg. Chemie*, 1976, **427**, 85.

6.4 R. J. H. Clark and N. R. D'Urso, *J. Am. Chem. Soc.*, 1978, **100**, 3088.

6.5 F. A. Cotton and B. J. Kalbacher, *Inorg. Chem.*, 1975, **15**, 523.

6.6 R. J. H. Clark and M. L. Franks, *J. Am. Chem. Soc.* 1975, **97**, 2691.

6.7 J. San Filippo and H. J. Sniadoch, *Inorg. Chem*, 1973, **12**, 2326.

6.8 M. C. Manning and W. C. Trogler, *Inorg. Chem.*, 1982, **21**, 2797.

6.9 J. V. Brencic, D. Dobcnick and P. Segedin, *Monat. Chemie*, 1974, **105**, 351.

6.10 J. V. Brencic and F. A. Cotton, *Inorg. Chem.*, 1970, **9**, 351.

6.11 J. San Filippo and H. J. Sniadoch, *Inorg. Chem.*, 1974, **13**, 2121.

6.12 A. Bino, *Inorg. Chim. Acta*, 1985, **L7**, 101.

6.13 J. San Filippo and M. A. Schaefer-King, *Inorg. Chem.*, 1976, **15**, 1228.

6.14 V. K. Ceylan, C. Sourisseau and J. V. Brencic, *J. Raman Spec.*, 1985, **16**, 128.

6.15 F. A. Cotton, B. A. Frenz, E. Pedersen and T. R. Webb, *Inorg. Chem.*, 1975, **14**, 391.

6.16 A. Loewenshuss, J. Shamir and M. Arden, *Inorg. Chem.*, 1976, **15**, 238.

6.17 P.E. Fanwick, D.S. Martin, T.R. Webb, G. A. Robbins and R.A. Newman, *Inorg. Chem.*, 1978, **17**, 2723.

Appendices

A.1 D. P. Strommen and K. Nakamoto, *Laboratory Raman Spectroscopy*, Wiley: New York, 1984.

A.2 F. Iganiki, M. Tasumi and T. Miyazawa, *J. Mol. Spec.*, 1974, **50**, 286.

A.3 D. Oprescu, *PhD Thesis*, University of London, 1996.

A.4 E. Hecht, *Optics*, 2nd Edition, Addison-Welsey, 1987.

A.5 M. D. Hopkins and H. B. Gray, *J. Am. Chem. Soc.*, 1984, **106**, 2468.

A.6 C. K. Chan and J. B. Page, *J. Chem. Phys.*, 1983, **79**, 5234.